

**DIFFERENTIAL EFFECTS OF PIGMENT EPITHELIUM DERIVED
FACTOR AND EPIDERMAL GROWTH FACTOR ON ISCHEMIA-
REPERFUSION INJURY IN RATS;**

A MAGNETIC RESONANCE IMAGING STUDY AT 3 TESLA

**DISSERTATION ZUR ERLANGUNG DES
NATURWISSENSCHAFTLICHEN DOKTORGRADES
DER BAYERISCHEN JULIUS-MAXIMILIANS-UNIVERSITÄT WÜRZBURG**



VORGELEGT VON

DEEPU PILLAI

AUS THRISSUR, INDIEN

WÜRZBURG 2011

Eingereicht am:.....

Mitglieder der promotionskommission:

Vorsitzender: Prof. Dr. Thomas Dandekar

Gutachter: PD Dr. Felix Schlachetzki.

Gutachter: Prof. Dr. Erich Buchner.

Tag des Promotionskolloquiums:

.....

Doktorurkunde ausgehändigt am:

.....

To my parents and family.....

Contents

Acknowledgements	1
Zusammenfassung	5
Summary	9
1.0. Introduction. Part I.	
1.1. Stroke.....	13
1.2. The case for extended neuroprotection.....	16
1.3. Neuroprotection, a retrospective analysis.....	20
1.4. Novel therapeutic approaches and emerging concepts.....	24
1.5. The concept of the neurovascular unit.....	28
1.5.1. The endothelium.....	29
1.5.2. The extra-cellular matrix.....	31
1.5.3. Perivascular astrocytes.....	32
1.5.4. Neurons and axons.....	34
1.5.5. Pericytes and microglia.....	34

1.6. The blood brain barrier.....	36
1.6.1. The BBB phenotype.....	38
1.7. Neurotrophic growth factors.....	42
1.7.1. Protective effects of neurotrophic growth factors in ischemic brain injury.....	47
1.7.2. The epidermal growth factor.....	48
1.7.2.1. Neurotrophic properties of EGF.....	51
1.7.3. The pigment epithelium derived factor.....	52
1.7.3.1. Structural properties of PEDF.....	54
1.7.3.2. Binding and signal transduction.....	55
1.7.3.3. Trophic properties of PEDF.....	58
1.7.3.4. Neuroprotective properties of PEDF.....	58
1.7.3.5. PEDF as a potent anti-angiogenic factor.....	60

2.0. Introduction. Part II.

2.1. Elementary concepts of nuclear magnetic resonance imaging.....	62
2.1.1. Establishment of a net magnetization.....	62
2.1.2. Fundamental principles of nuclear magnetic resonance.....	69
2.1.3. Relaxation characteristics.....	75

2.1.3.1. T ₁ relaxation.....	75
2.1.3.2. T ₂ and T ₂ [*] relaxation and spin echoes.....	79
2.1.3.3. Spatial allocation of resonant frequencies.....	85

3.0. Aim and Objectives.

3.1. Aim.....	93
3.2. Objectives.....	93

4.0. Materials and methods.

4.1. Establishment of small animal magnetic resonance imaging strategies on a 3 tesla clinical dedicated head magnetic resonance scanner.....	95
4.1.1. The MR system.....	95
4.1.2. The phased array radio frequency coil system.....	96
4.1.3. In-vivo MRI.....	97
4.1.3.1. Configuration and optimization of sequence parameters.....	97
4.1.3.2. Determination of tissue relaxation characteristics.....	101
4.1.3.3. Determination of the optimal parallel imaging reconstruction algorithm: GRAPPA or mSENSE?.....	102
4.1.3.4. Anatomical characterization of a rat brain.....	102
4.1.3.5. MR imaging of a rat model of ischemic stroke.....	103

4.1.3.6. MR imaging of a rat model of intra-cerebral haemorrhage.....	107
4.1.3.7. MR imaging of rat spinal cord injury models.....	108
4.1.3.8. MR imaging of a mouse model of Glioblastoma.....	110
4.1.4. Data analysis.....	112
4.2. Serial magnetic resonance imaging to determine the blood brain barrier permeability changes and the dynamic fluxes in vasogenic oedema formation following ischemia-reperfusion injury in rats.....	114
4.2.1. Experimental design.....	114
4.2.2. Surgical procedure.....	114
4.2.3. Magnetic resonance imaging.....	115
4.2.4. Data analysis.....	115
4.3. Trophic properties of epidermal growth factor and pigment epithelium derived factor on selected indices of neurovascular injury following ischemia-reperfusion injury in rats.....	117
4.3.1. Evaluation of blood-brain barrier permeability for macromolecules.....	117
4.3.1.1. Experimental design.....	117
4.3.2. Treatment regimen with EGF and PEDF.....	118
4.3.2.1. Experimental design.....	119
4.3.2.2. Magnetic resonance imaging.....	120

4.3.2.3. Data analysis.....120

5.0. Results.

5.1. Establishment of small animal magnetic resonance imaging strategies on a 3 tesla clinical dedicated head magnetic resonance scanner.....123

5.1.1. Configuration and optimization of sequence parameters.....123

5.1.2. 3D-MPRAGE characterization of brain anatomy.....126

5.1.3. The rat model of cerebral ischemia.....128

5.1.4. The rat model of intra-cerebral haemorrhage.....130

5.1.5. The rat model of cervical and thoracic spinal cord injuries.....131

5.1.6. The mouse model of glioblastoma.....134

5.2. Serial magnetic resonance imaging to determine the blood brain barrier permeability changes and the dynamic fluxes in vasogenic oedema formation following ischemia-reperfusion injury in rats.....137

5.2.1. Bi-phasic BBB opening and progression of brain volume with leaky BBB following ischemia-reperfusion injury as investigated by post-contrast T₁-sequences.....138

5.2.2. Ipsilateral and remote oedema formation as investigated by the temporal profile of transverse relaxation times.....141

5.3. Trophic properties of epidermal growth factor and pigment epithelium derived factor on selected indices of neurovascular injury following ischemia-reperfusion injury in rats.....	144
5.3.1. Evaluation of blood-brain barrier permeability for macromolecules.....	144
5.3.2. Trophic properties of EGF and PEDF on ischemia-reperfusion injury.....	144
5.3.2.1. Effect of EGF and PEDF on the infarct volume.....	145
5.3.2.2. Effect of EGF and PEDF on the T_2 -values within the infarct region.....	147
5.3.2.3. Effect of EGF and PEDF on the T_2 -value x infarct volume product (T_{2vol}) up to 48 hours.....	148
5.3.2.4. Effect of EGF and PEDF on the T_2 -values at the ipsilateral cortex.....	149
5.3.2.5. Effect of EGF and PEDF on the T_2 -values at the contralateral striatum.....	150
5.3.2.6. Effect of EGF and PEDF on the susceptibility weighted T_2^* -values at the infarct region.....	152
5.3.2.7. Effect of EGF and PEDF on the susceptibility weighted T_2^* - values at the contralateral region.....	153
5.3.2.8. Effect of EGF and PEDF on the T_1SI_{diff} values at the ipsilateral striatum.....	155

5.3.2.9. Effect of EGF and PEDF on the T_1SI_{diff} values at the contralateral striatum.....	156
---	-----

6.0. Discussion.

6.1. Establishment of small animal magnetic resonance imaging strategies on a 3 tesla clinical dedicated head magnetic resonance scanner.....	158
6.1.1. Imaging of the rodent model of cerebral ischemia.....	161
6.1.2. Imaging of the rodent model of intra-cerebral haemorrhage.....	163
6.1.3. Imaging of the rodent model of spinal cord injuries.....	164
6.1.4. Imaging of the mouse glioblastoma model.....	166
6.2. Serial magnetic resonance imaging to determine the blood brain barrier permeability changes and the dynamic fluxes in vasogenic oedema formation following ischemia-reperfusion injury in rats.....	168
6.2.1. MR imaging of BBB permeability characteristics.....	169
6.2.2. Oedema development in relation to BBB permeability.....	172
6.2.3. Biphasic BBB permeability; A surrogate marker for the ‘new penumbra’?..	175
6.2.4. Summary.....	176
6.3. Trophic properties of epidermal growth factor and pigment epithelium derived factor on selected indices of neurovascular injury following ischemia-reperfusion injury in rats.....	178
6.3.1. Effect of EGF and PEDF on the infarct volume.....	178

6.3.2. Effect of EGF and PEDF on oedema formation and resorption at the infarct region.....	182
6.3.3. Effect of EGF and PEDF on oedema formation and resorption at distant sites remote from infarcted region.....	184
6.3.4. Altered metabolic state at the infarct site as mapped by susceptibility weighted (T_2^*) sequences.....	186
6.3.5. Altered metabolic state at the contralateral striatum as mapped by susceptibility weighted (T_2^*) sequences.....	188
6.3.6. Temporal profile of blood brain barrier permeability characteristics at the ipsilateral striatum as detected by post-contrast T_1 imaging.	189
6.3.7. Temporal profile of T_1SI_{diff} changes at the contralateral striatum.....	192
6.3.8. Concluding remarks and future directives.....	194
References.....	196
List of Abbreviations.....	225
List of Publications.....	230
Curriculum vitae.....	232
Declaration.....	233

Acknowledgements

At this moment of thanksgiving, I would like to express my deepest gratitude and heart-felt thanks to all the people and organizations that have extended me all the advice, help and resources to complete this little work to a meaningful conclusion.

*It's rather a privilege to express my sincere gratitude and thankfulness to my esteemed research guide **PD. Dr. Med. Felix Schlachetzki**, Department of Neurology, Regensburg University Medical Centre, Regensburg. His constant encouragement, valuable suggestions and timely advice have been a source of strength to me. I thank him for the freedom of thought, expression, abundant moral support and trust during the entire course of my associations with him.*

*I express my deepest gratitude and will remain grateful to **Prof. Dr. Med. Ulrich Bogdahn**, Director, clinic and polyclinic for Neurology, Regensburg University Medical Centre, Regensburg, for his timely help, care and attention to my affairs and also in providing me with the necessary facilities during the tenure of this work,*

*I extend my thankfulness to **Prof. Dr. Dr. Martin J. Müller**, former Dean, Faculty of Biology, Julius-Maximilians-Universität Würzburg, Würzburg, for considering and granting me this very opportunity to pursue my doctoral work at the faculty of biology.*

*I will remain deeply indebted to **Prof. Dr. Erich Buchner**, Department of Genetics and Neurobiology, Julius-Maximilians-Universität Würzburg, Würzburg, for all his kind support, guidance and generosity that has been bestowed upon me, without which such an endeavor could have never been possible.*

*In the first place, if it has not been for a chance communication between me and **Dr. Michael S. Dittmar**, Department of Anaesthesiology, Regensburg University Medical Centre, Regensburg, this thesis would have never taken its present material shape. Apart from all that, I am deeply indebted to him for his invaluable scientific insights, timely help and support that had been instrumental in the execution of this work,*

*It had been a matter of immense pleasure to be associated with none other than **Prof. Dr. Med. Gerhard Schuierer**, Center for Neuroradiology, Regensburg University Medical Centre, Regensburg, for being benefitted directly out of his sheer knowledge, experience and expertise in the field of magnetic resonance, imaging without which this work would have been incomplete.*

*I remain grateful to **Prof. Dr. Mark Greenlee**, Department of Experimental Psychology, University of Regensburg, Regensburg, for all the help and support that was provided to me during the course of this work,*

*I am thankful to **PD Dr. Gyula Kovacs** and **Mr. Markus Raabe**, Department of Experimental Psychology, University of Regensburg, Regensburg, for being at my side to sort out all the little technical troubles which I have faced every now and then.*

*I remain indebted to **Dr. Robin Heidemann**, Max Planck Institute for Human Cognitive and Brain Sciences, Leipzig, for his invaluable help and guidance in matters regarding the concepts of magnetic resonance imaging.*

*I also extend my thankfulness and gratitude to **Dr. Nagesh Shanbhag**, **Mr. Dobri Baldaranov**, **Mr. Josef Mayr** and **Mr. Praveen Kumar** for their invaluable help and timely support and on whom I had relied heavily for the successful execution of this work, Their support contributed enormously and had literally made my life a lot easier.*

*These three people have always reinstated my faith in humanity. **Dr. Michael Gruber**, Department of Anaesthesiology, Regensburg University Medical Centre, Regensburg, even though did not have anything to do with me or my work, has always been the first person at my side, whenever, I am faced with a technical trouble at the laboratory. He had always been extremely reliable and dependable and moreover his eagerness to help others has always taught me a lesson or two. Along the same lines, it's a matter of immense pleasure and pride to remember two of my friends who were nothing but pillars of strength from my initial days of life here at Regensburg. **Mr. Waqar Hayat** and **Dr. Parykshit Saikja** will always be remembered for their utmost selfless help and support during this rather stormy part of my life.*

*My heartfelt thanks are due to **Ms. Brigitte Rinke**, **Dr. Amit Tyagi**, **Mr. Ralf Koeber**, **Dr. Kiran Pawar**, **Ms. Petra Leukel**, **Dr. Sridhar Chirasani**, **Mr. Paul Ramm**, **Mr. Massimiliano Caioni**, **Mr. Maruf Hassan**, **Ms. Eva Maria Storr**, **Mrs. Anette Lohmeier**, **Ms. Doris Melchner** and **Dr. Mahesh Kandasami**; my colleagues and friends at our laboratory who has proven a lot many times to be extremely dependable and generous with me for every other little problem with which I have often bothered them.*

*This work could have been impossible without the generous financial support from **Bayerische Forschungsstiftung** and the **Bavarian State Ministry of Sciences, Research and the Arts**, "**ForNeuroCell**" for which I will always remain thankful.*

*No other person on this planet would have suffered as much as my beloved wife **Mrs. lekshmi** for having been to put up with all my idiosyncrasies and irrational temperaments that have been often taken out on her. I would take this opportunity to say sorry and also thank her for being a wonderful display of love, care, patience and utmost understanding throughout these trying times.*

I remain grateful to my extended family members including my in-laws for all their love, affection, support and well wishes which had kept me going throughout these trying times.

Last on this page, but first on my mind are the enormous sacrifices of two individuals, who in the twilight of their lives had to bear with the very fact that their only son might be away for years to come. This work and all my future endeavours will just be a material manifestation of their extension of blessings towards my being. A word of Thanks does not mean and cannot contain any thing here.....

28-03-2011

Regensburg

Deepu R. Pillai

Zusammenfassung

Schlaganfall ist nach Herzinfarkt und Krebs die dritthäufigste Todesursache weltweit und 1/6 aller Menschen erleiden mindestens einen Schlaganfall in ihrem Leben. Wichtiger ist jedoch, dass Schlaganfallerkrankungen die führende Ursache für dauerhafte Behinderungen darstellen. Ungefähr ein Drittel dieser Patienten, die die ersten 6 Monate überleben sind auf die Hilfe anderer angewiesen. Die enorme Wichtigkeit des Schlaganfalls begründet sich zudem dadurch, dass schon jetzt die sozioökonomischen Kosten 6% der gesamten Gesundheitsausgaben betragen und die globale Lebenserwartung weiter steigen wird. Der ischämische Hirninfarkt ist der mit 80% vorherrschende Schlaganfalltyp und resultiert aus thrombotischen und embolischen Verschlüssen der großen hirnversorgenden Arterien und deren Ästen (insbesondere der A. cerebri media).

Die wichtigste Komplikation mit hoher Mortalität nach einem ischämischen Schlaganfall ist Entwicklung eines raumfordernden vasogenen Ödems. Veränderungen der Permeabilität der Blut-Hirn-Schranke (BHS) begleitet die Ödementwicklung und Analyse der zeitlichen BHS-Permeabilität können wichtige Erkenntnisse über den natürlichen Verlauf eines Hirninfarkts und die Aktivierung kompensatorischer Mechanismen, die in Reparaturvorgänge münden, liefern.

Verschiedene Modelle des akuten ischämischen Schlaganfalls mit Nagetieren wurden entwickelt um die Schlaganfalltherapie des Menschen weiter zu entwickeln. Sie sind momentan unersetzliche Instrumente in der Schlaganfallforschung.

Die hier vorgestellte Arbeit setzt sich aus 3 abgeschlossenen sequentiellen Teilprojekten zusammen. Das erste Teilprojekt befasst mit der Etablierung von der nicht-

invasiven Kleintierbildgebung auf einem klinischen 3 Tesla Kernspintomographen. Diese Arbeit bildet die Grundlage für das in vivo Monitoring der pathologischen Veränderungen nach Schlaganfall in einem identischen Versuchstier nachverfolgt werden kann und so die eigene Kontrolle darstellt.

Gewebs relaxometrische Messungen wurden initial durchgeführt um die transverse (T_2), longitudinal (T_1) und transverse (T_2^*) Relaxationszeit (aufgrund der magnetischen Suszeptibilitätseffekte) in kortikalen und striatalen Hirnregionen der Nagetiere zu bestimmen. Statistisch signifikante Unterschiede in der T_2^* -Werte konnte zwischen der kortikalen und Striatalen Regionen des Gehirn von Nagetieren gefunden werden. Hierdurch konnten bestehende Messprotokolle vom Menschen auf die Nagetiere optimiert und für die Untersuchungen des Schlaganfalls genutzt werden. Diese Vorarbeiten erlauben klinisch relevante Veränderungen wie eine veränderte Diffusion und Perfusion nach ischämischen Schlaganfall zu verfolgen.

Basierend auf diesen Vorarbeiten wurde die örtliche und zeitliche Charakterisierung der bi-phasischen BHS-Öffnung und der Ödementwicklung nach experimenteller I/R der Ratte mittels serieller Magnetresonanztomographie (MRT) untersucht. Hier diente die T_2 -Relaxometrie zur Ödemquantifizierung und wurde 1 Stunde nach Beginn der zerebralen Ischämie, unmittelbar nach Reperfusion und im Intervall von weiteren 4, 24 und 48 Stunden durchgeführt. Eine T_1 -gewichtete Sequenz wurde vor und nach Gabe von Kontrastmittel an den drei letztgenannten Zeitpunkten zeigte den bi-phasischen Verlauf der BHS-Öffnung 4 und 48 Stunden nach Reperfusion. Eine signifikante Reduktion der BHS Permeabilität 24 Stunden war zum einem mit einer Erhöhung des Gesamtvolumens der gestörten BHS und zum anderen mit Maximum der Ödementwicklung assoziiert. Darüber hinaus konnte 48 Stunden nach Reperfusion bereits eine Resorption des Ödems

anhand der T_2 -Relaxometrie gemessen werden während die zweite Phase der biphasischen BHS-Öffnung auftrat.

Zusätzlich trat 4 Stunden nach Reperfusion eine Ödembildung auch der nicht-ischämischen Striatum auf, welche in unterschiedlichem Maße über die Studiendauer persistierte. Dies spricht dafür, dass Ischämie und Reperfusion Effekte auf das gesamte Gehirn haben können. Zusammenfassend sprechen die Beobachtung dafür, dass der zeitlichen Entwicklung des Hirnödems verschiedene Mechanismen der erhöhten Blut-Hirn-Schranken Permeabilität zu Grunde liegen.

Zwei Wachstumsfaktoren, der, Pigment epithelium abstammende Wachstumsfaktor (PEDF) und der epidermale Wachstumsfaktor (EGF), mit deutlich unterschiedlichen trophischen Eigenschaften wurden auf ihre positiven Effekte im etablierten Tiermodell der zerebralen I/R hin untersucht. Dabei wurden serielle MRT Untersuchungen bis hin zu einer Woche genutzt. Beide Wachstumsfaktoren führten im Modell zu einer signifikanten Neuroprotektion, die sich in einer Reduktion des Infarktolumens gegenüber einer Kontrolle mit Kochsalz zeigte.

PEDF allerdings hatte gegenüber EGF eine potentere Wirkung und zeigte darüber hinaus und noch deutlicher als EGF eine signifikante Verminderung der Ödembildung. Allerdings zeigte eine Behandlung mit diesen großmolekularen Proteinen zumindest nach 24 Stunden auch eine Neigung zur Ödembildung in vom Schlaganfall nicht betroffenen Hirnarealen, deren Signifikanz allerdings noch unklar ist. T_2^* -gewichtete Relaxationsmessungen können dazu genutzt werden, um metabolische Veränderungen, die aus neuroprotektiven Therapieansätzen bzw. zellulärer Proliferation bzw. Neurogenese entstehen, zu quantifizieren. Hier zeigten insbesondere mit PEDF behandelte Versuchstiere

eine hochsignifikante Reduktion der T_2^* -Werte, welche als Hinweis auf eine erhöhte metabolische Aktivität gewertet werden können.

Insgesamt zeigten alle Behandlungsgruppen (Kochsalzkontrollen, EGF und PEDF) behandelte Tiere signifikant erhöhte T_2^* -werte auf des kontralateralen Striatums, welche auf eine weitreichende metabolische Suppression hindeuten, wie sie normalerweise bei einer Reihe von traumatischen Hirnerkrankungen gefunden werden können. Ein weiterer Befund ist, wie erwartet, die ausgedehnte Verminderung der BHS-Durchgängigkeit durch PEDF über die gesamte Dauer der Untersuchung hinweg.

Diese Studie unterstreicht den Nutzen nicht-invasiver Bildgebungsstrategien, ohne die die Untersuchung der benötigten Parameter in einem longitudinalen Design nicht möglich wäre. Ausblickend müssen diese gut mittels MRT charakterisierten Prozesse durch immunhistologische und funktionelle Untersuchungen gestützt und nachfolgend publiziert werden.

Summary

Stroke, after myocardial infarction and cancer is the third most common cause of death worldwide and 1/6th of all human beings will suffer at least one stroke in their lives. Furthermore, it is the leading cause for adult disability with approximately one third of patients who survive for the next 6 months are dependent on others. Because of its huge socioeconomic burden absorbing 6% of all health care budgets and with the fact that life expectancy increases globally, one can assume that stroke is already, and will continue to be, the most challenging disease. Ischemic stroke accounts for approximately 80% of all strokes and results from a thrombotic or embolic occlusion of a major cerebral artery (most often the middle cerebral artery, MCA) or its branches

Following acute ischemic stroke, the most worrisome outcome is the rapidly increasing intra-cranial pressure due to the formation of space-occupying vasogenic oedema which can have lethal consequences. Permeability changes at the Blood-Brain Barrier (BBB) usually accompanies the oedematous development and their time course can provide invaluable insight into the nature of the insult, activation of compensatory mechanisms followed by long term repair.

Rodent models of focal cerebral ischemia have been developed and optimized to mimic human stroke conditions and serve as indispensable tools in the field of stroke research.

The presented work constituting of three separate but complete works by themselves are sequential, where, the first part was dedicated to the establishment of non-invasive small animal imaging strategies on a 3 tesla clinical magnetic resonance scanner. This

facilitated the longitudinal monitoring of pathological outcomes following stroke where identical animals can serve as its own control. Tissue relaxometric estimations were carried out initially to derive the transverse (T_2), longitudinal (T_1) and the transverse relaxation time due to magnetic susceptibility effects (T_2^*) at the cortical and striatal regions of the rodent brain. Statistically significant differences in T_2^* -values could be found between the cortex and striatal regions of the rodent brain. The derived tissue relaxation values were considered to modify the existing imaging protocols to facilitate the study of the rodent model of ischemic stroke. The modified sequence protocols adequately characterized all the clinically relevant sequels following acute ischemic stroke, like, the altered perfusion and diffusion characteristics.

Subsequent to this, serial magnetic resonance imaging was performed to investigate the temporal and spatial relationship between the biphasic nature of BBB opening and, in parallel, the oedema formation after I/R injury in rats. T_2 -relaxometry for oedema assessment was performed at 1 h after ischemia, immediately following reperfusion, and at 4, 24 and 48 hours post reperfusion. Post-contrast T_1 -weighted imaging was performed at the last three time points to assess BBB integrity. The biphasic course of BBB opening with significant reduction in BBB permeability at 24 hours after reperfusion was associated with a progressive expansion of leaky BBB volume, accompanied by a peak ipsilateral oedema formation. At 48 hours, the reduction in T_2 -value indicated oedema resorption accompanied by a second phase of BBB opening. In addition, at 4 hours after reperfusion, oedema formation could also be detected at the contralateral striatum which persisted to varying degrees throughout the study, indicative of widespread effects of I/R injury. The observations of this study may indicate a dynamic temporal shift in the

mechanisms responsible for biphasic BBB permeability changes, with non-linear relations to oedema formation.

Two growth factor peptides namely pigment epithelium derived factor (PEDF) and epidermal growth factor (EGF) with widely different trophic properties were considered for their beneficial effects, if any, in the established rodent model of I/R injury and studied up to one week employing magnetic resonance imaging. Both the selected, trophic factors demonstrated significant neuroprotection as demonstrated by a reduction in infarct volume, even though PEDF was found to be the most potent one. PEDF also demonstrated significant attenuation of oedema formation in comparison to both the control and EGF groups, even though EGF could also demonstrate oedema suppression. In the present work, we noticed that interventions with macromolecule protein/peptides by itself could mediate remote oedema at distant sites even though the significance of such an observation is not clear at present.

Susceptibility (T_2^*) weighted tissue relaxometric estimations were considered at the infarct region to detect any metabolic changes arising out of any neuroprotection and/or cellular proliferation / neurogenesis. PEDF group demonstrated a striking reduction of the T_2^* -values, which is indicative of an increased metabolic activity. Moreover, all the groups (Control, EGF and PEDF) demonstrated significantly elevated T_2^* -values at the contralateral striatum, which is indicative of widespread metabolic suppression usually associated with a variety of traumatic brain conditions. Moreover, as expected from the properties of PEDF, it demonstrated an extended BBB permeability suppression throughout the duration of the study.

This study underlines the merits of considering non-invasive imaging strategies without which it was not possible to study the required parameters in a longitudinal

fashion. All the observations are adequately supported by reasonably well defined mechanisms and needs to be further verified and confirmed by an immunohistochemical study. These results also need to be complemented by a functional study to evaluate the behavioural outcome of animals following these treatments. These studies are progressing at our laboratory and the results will be duly published afterwards.

1.0. Introduction. Part I.

1.1. STROKE.

Stroke, a “brain attack”, is a non-communicable disease of increasing socioeconomic importance in ageing populations. According to World Health Organization (WHO) stroke was the second commonest cause of mortality worldwide in 1990 and the third commonest cause of mortality in more developed countries, where it caused about 4.4 million deaths worldwide (1, 2). In the most recent estimates made in 1999, the number of deaths due to stroke reached 5.54 million worldwide, with two-thirds of these deaths occurring in less developed countries (3). Stroke is also a major cause of long-term disability and has enormous emotional and socioeconomic results for patients, their families, and health services (4). Lifetime costs per patient are estimated between US\$59800 and US\$230000 (5). By the year 2020, stroke and coronary-artery disease together are expected to be the leading causes of lost healthy life-years (3) .

In practice, ‘stroke’ refers to an umbrella of conditions caused by the occlusion or rupture of blood vessels supplying the brain, where the latter condition can result in Intra-Cerebral Haemorrhage (ICH). Most often, blood flow is compromised within the territory of an occluded blood vessel (focal cerebral ischemia). Less commonly, stroke results from absence of blood flow to the entire brain due to cardiac arrest (global ischemia). In all instances, stroke ultimately involves death and dysfunction of brain cells, causing neurological deficits that reflect the location and size of the compromised brain area (6). Focal ischemic stroke accounting for about 80% of stroke incidents could result from atherothrombosis (75% of the cases) or could be due to embolic sources (25% of cases).

Haemorrhagic stroke has a relatively less rate of prevalence and accounts for almost 20% of the cases (7). ICH is more than twice as common as SubArachnoid Haemorrhage (SAH) and is much more likely to result in death or major disability than cerebral ischemia or SAH (8). Pathophysiological changes in small arteries and arterioles due to sustained hypertension are generally regarded as the most important cause of ICH (9, 10). Other causes of ICH include vascular malformations, ruptured aneurysms, coagulation disorders, use of anticoagulants and thrombolytic agents, haemorrhage into a cerebral infarct, bleeding into brain tumours, and drug abuse (11). However, neither surgical nor medical treatment of ICH has been proven conclusively to benefit patient populations and current therapies focus on prevention of recurrence and treatment of complications (12).

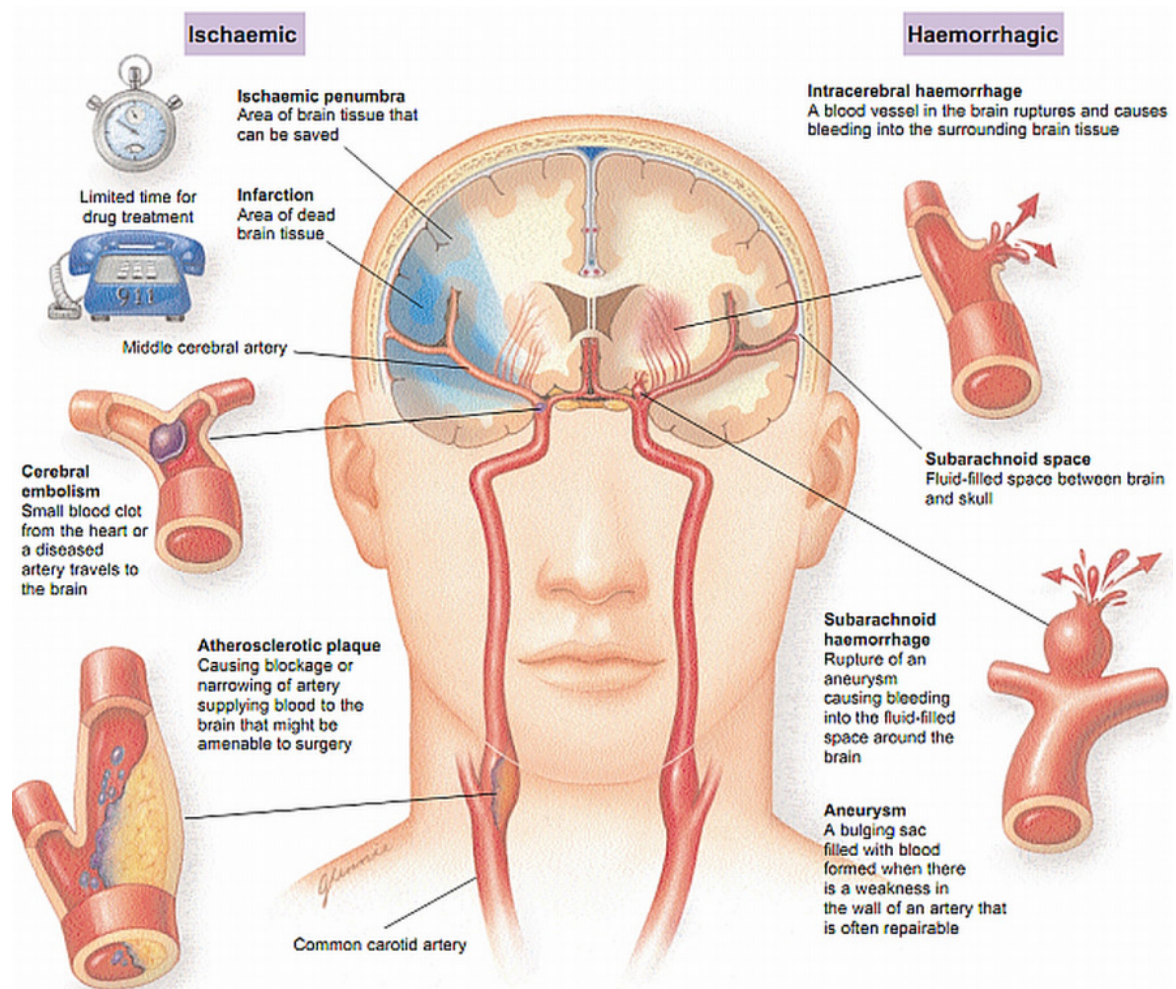


Figure 1. Schematic representation of major stroke sub-types. *Adapted from reference(13).*

Cerebral ischemia by virtue of its higher prevalence commanded extensive research efforts in the past decade with important successes and disappointing failures (14). At present there are two major approaches to the treatment of acute ischaemic stroke: thrombolysis, to try and restore blood flow to the compromised region, and neuroprotection, which involves the use of drugs to interfere with one or more of the mechanisms in the ``ischemic cascade`` and thus minimize the subsequent neurodegeneration. Successful approaches were accomplished with thrombolytic approaches, to restore blood flow of which, at least two trials has contributed enormously in the treatment of acute stroke. The first was the National Institute of Neurological Disorders and Stroke Recombinant Tissue-Type Plasminogen Activator (NINDS rt-PA) trial reported in 1995. This study demonstrated that initiation of IntraVenous (IV) rt-PA within three hours after the onset of acute ischemic stroke significantly improved outcome at three months (15).

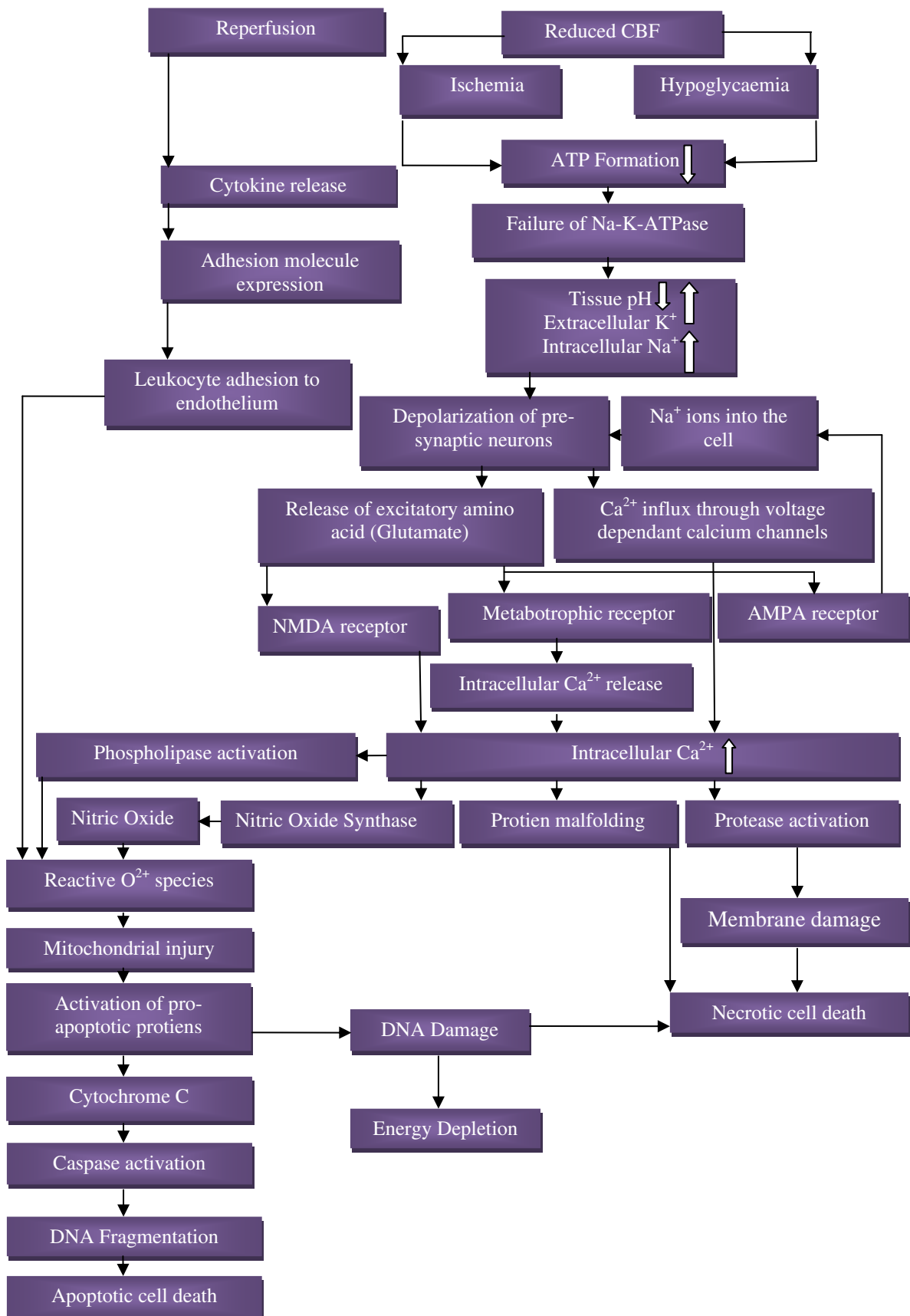
The success of this study led to the United States Food and Drug Administration (US-FDA) approval of rt-PA initiated within three hours of stroke onset as the only currently available acute stroke therapy. The second major success was with the intra-arterial pro-urokinase initiated within six hours of stroke onset in patients with angiographically documented proximal Middle Cerebral Artery Occlusion (MCAO) which also improved outcome at three months (16). A third marginally positive acute stroke trial used ancrod, initiated within 3 hours after stroke onset also improved 3-month outcome but to a lesser degree than either rt-PA initiated within 3 hours or prourokinase initiated within 6 hours (17). These successful thrombolytic therapies for acute stroke were outweighed by a large number of neuroprotective trial failures. Currently, not one of the many purported neuroprotective therapies assessed in pivotal clinical trials has demonstrated unequivocal, statistically significant improvements in clinical outcome (18).

1.2. THE CASE FOR EXTENDED NEUROPROTECTION.

Intravenous thrombolytic rt-PA treatment is an inherently risky procedure especially beyond the three hour time window as it results in haemorrhagic transformation (19). This also means that, thrombolytic procedures will only be applicable to a select few people and cannot be universally applied.

Experimental data has demonstrated the presence of a ring shaped ``ischemic penumbra`` surrounding the ischemic core, where energy failure followed by reversible ionic pump dysfunction have developed. The penumbral zone comprises of neurons which are electrically silent but with maintained ionic homeostasis or with slightly elevated extracellular potassium (K^+) for extended periods of time from the point of the ictus (20, 21). Neuroprotection evolved as a concept directly resulting from the gradual unravelling of the complexities of the ischemic cascade and aims to salvage this penumbral zone from undergoing further cell death mediated through apoptotic and necrotic pathways. This was a process that began at about the time that Olney first proposed a neurotoxic role for glutamate under ischemic conditions and continues with the description of a seemingly never ending series of interrelated pathways (22).

The common feature of the cascade was its inexorable passage to cell death unless single or multiple components could be attenuated. The sequence of events is now reasonably well known and includes early energy failure with depletion of Adenosine Tri-Phosphate (ATP), glutamate release, and its effects on the postsynaptic N-Methyl-D-Aspartate (NMDA) receptors, disruption of sodium and calcium ion homeostasis, free radical generation from mitochondria which may then destroy lipid membranes, generation of inflammatory components, endogenous thrombolysis, and the triggering of both necrotic and apoptotic cell death (Figure 2) (23).



CBF, cerebral blood flow; ATP, adenosine-tri-phosphate; NMDA, N-methyl-D-aspartate; AMPA, α -amino-3-hydroxy-5-methyl-4-isoxazolepropionic acid.

Figure 2. The ischemic cascade and reperfusion injury. Adapted from reference (24)

Each of these pathways (and many others) has been explored using pharmacological probes to observe neurochemical and other outcomes. In most instances, experimental blockade of these pathways has led to protection of cellular function and these properties of these probes have been exploited to develop ``neuroprotectants``. Further, these agents have shown to protect cells as well as volumes of tissue from ischemia and improve outcomes in animal models of stroke (25). Neuroprotection has been demonstrated at various levels ranging from individual cells, usually in culture, brain slices in which the neurovascular unit (Refer page 28) is more likely to remain intact, and, finally, in animal models of cerebral ischemia (26-30). To date, a bewildering number of such chemical compounds with proposed neuroprotectant properties has been designed and synthesized to act on all conceivable molecular targets (31).

The animal model gray matter neurochemical ischemic cascade does represent, however, the accumulated knowledge of 30 years of research. Indeed, each component of the cascade has been validated many times over in different laboratories and using different approaches. To laboratory investigators, there seems little doubt that the majority of neuroprotectants is effective in protecting the brain from ischemia. This has been demonstrated many times with different classes of compounds and using the outcome measures of a reduction in infarct volume and improved neurological scores in a number of animal models (32-37). However, the apparently simple matter of translating this into the human paradigm then, however, was never been realized till date.

A brief list of recently completed and ongoing clinical trials of neuroprotectants is summarized below (Table 1).

Drug name	Proposed mechanism of action	Clinical phase
NXY-059 (Cerovive)	Free radical scavenger	Phase III (recently terminated)
Citicholine	Neuroprotectant	Phase II/III (recently failed)
Albumin	Neuroprotectant	Phase III
DP-b99	Calcium chelator	Phase II (completed)
ONO-2506/MK-0724(Proglia)	Neurotrophic glial modulator	Phase II (recently terminated)
Cafeinol	Caffeine + ethanol	Phase II
Piclozotan(SUN-N4057)	5-HT1A receptor agonist	Phase II (recently terminated)
Encadin (NS-7)	Calcium channel blocker	Phase II
S-18986	AMPA receptor modulator	Phase II
Msc-1 (AGY-94806)	Opioid receptor sigma agonist	Phase II
BRX-345 (arimoclolol)	Heat shock protein inducer	Phase II
AX200 (G-CSF)	Growth factor	Phase II
NTx-265	Stem cell stimulator (EPO receptor agonist)	Phase II
LuAA24493	Carbamylated EPO	Phase I
ONO-2231	PARP1 inhibitor	Phase I
Neu2000	NMDA antagonist/antioxidant	Phase I
AEOL-10150	Antioxidant	Phase I
BAY-387271	Cannabinoid agonist	Phase I
HF-0220	Neuroprotective steroid	Phase I
HF-0420	Heparinoid	Phase I
MC-1	Vitamin B derivative	Phase I
SUN-N8075	Na ⁺ /Ca ⁺ channel blocker	Phase I
TS-011	Arachidonic acid modulator	Phase I
NA-1	PSD-95 inhibitor	Phase I
ILS-920	Immunophilin ligand	Phase I

Table 1. Neuroprotectants currently under development for treating ischemic stroke. *Adapted from reference (38).*

1.3. NEUROPROTECTION, A RETROSPECTIVE ANALYSIS.

Abundant literature has piled up over the last years detailing the discrepancies for the failure in translating pre-clinical data into an equivocal clinical scenario (24, 39-44). Dismal results of the so called neuroprotectants at large, time consuming and expensive clinical trials have called for a thorough review of methodologies that is followed throughout the pre-clinical and clinical development of potential drug candidates. The Stroke Therapy Academic Industry Roundtable (STAIR), a conference of academicians and industry representatives was convened to suggest such guidelines for the pre-clinical and clinical evaluation of neuroprotective drugs and to recommend potential clinical investigators the data which they should review to reassure themselves that a particular neuroprotective drug has a reasonable chance to succeed in an appropriately designed clinical trial (45-50).

It is becoming clear that the existing animal models of focal cerebral ischemia are an imperfect representation of human stroke and may be relevant only to a minority of human stroke sub-types (51). Human stroke occurs in the context of aging, hypertension, diabetes, cardiac disease such as atrial fibrillation, and with the use of concomitant medications. In addition, the gender differences may influence both stroke mechanisms and responses to therapy. Hypertension, the most prevalent risk factor for stroke, alters vascular responses to ischemia that may extend beyond the vasculature and lead to compensatory responses at the neurovascular unit (52, 53). These effects have not been well-studied in animal models, at least in part because animal models of hypertension are heterogeneous (54). Diabetes and hyperglycemia occur in one-third of acute stroke patients and are associated with worse outcome in large vessel and cardioembolic stroke but better outcomes in lacunar stroke (46). They reduce the likelihood of good recovery after recanalization therapy

through complex mechanisms that partly depend on the duration and severity of ischemia and whether parenchymal reperfusion actually occurs (55). No single animal model mimics these circumstances completely. Most preclinical testing initially involves rodents. Higher order species such as cats and primates are also available to test specific hypotheses or mechanisms. Although unproven, there may be some advantages to testing in nonhuman, gyrencephalic primates. In contrast to rodents, the descending anatomic pathways such as the corticospinal tracts in these animals have innervation patterns similar to humans (56). The primate and pig models may also be useful for testing the effects of drugs on white matter injury.

The efficacy of neuroprotective agents is typically screened in a restricted set of models ranging from in-vitro activity to promote neuronal survival and animal models involving permanent or transient ischemia. In considering the feasibility of linking animal models to human stroke, differences in brain structure must be considered. The human brain has a higher proportion of white matter relative to the rodent brain. It is unlikely that a treatment that targets only neurons and that does not also salvage white matter tracts would have widespread clinical relevance. The emerging concept of the neurovascular unit emphasizes that all the multiple cell types in the brain must be considered. It is likely that not only neurons but also glial and vascular elements in the brain need to be rescued. Furthermore, we must not only prevent cell death per se but also preserve cell function, especially the cell–cell signaling that subserves the integrity of the neurovascular unit (57). Finally, from a molecular and cellular perspective, accumulating data suggest that many of the neuroprotective targets tested in preclinical models may have a negative effect on the recovery process (58). Thus, any acute therapy must be carefully targeted to block the desired target during its deleterious phase without interfering with endogenous substrates

of recovery later on. Without understanding how and when these injury-into-repair transitions occur, it may not be possible to effectively translate acute experimental interventions into the appropriate timing, dose, and duration in clinical trials.

Nevertheless, individual rodent stroke models have been demonstrated to capture various elements of the human disease. With careful attention to size, mechanism, and purpose selected rodent models can be used to study the major targets of human neuroprotective therapies, reperfusion injury, delayed apoptotic cell death, and inflammatory cascades; or the cellular elements of neural repair (59). Further, it has also been demonstrated that physiological factors that influence ischemic damage in rodent models have clinical correlates, thus indicating the predictive relevance of these models (13). STAIR recommendations include, amongst others, that thorough investigation should be primarily completed in rats where use of animals belonging to multiple strains should be avoided as much as possible. The studies should also be conducted in a randomized, blinded fashion analogous to those methodologies followed during clinical trials (47).

In animal models, the time of stroke or ischemic onset is known precisely. Most neuroprotective studies in animals have relied on drug administration either before the ischemic insult or very soon after the onset of ischemia or at the time of reperfusion with little attention being paid to drug administration at various extended time periods following reperfusion (47, 60, 61). The window of therapeutic opportunity in animal models is not necessarily predictive of the time window in humans, but determination of relative windows is useful. There is increasing concern that the window of opportunity in humans may not be substantially longer than in smaller species. In compliance with these concerns, STAIR recommends that the time window for efficacy in the animal models

must be clearly established (47). Further, precise knowledge of the demonstration of extended efficacy of a therapeutic agent is critical for conducting clinical trials. During clinical trials, the time windows for entry in acute stroke neuroprotective trials have been longer and highly variable; in studies published between 1995 and 1999, the median time to entry was 12 hours (range, 4 hours to 12 days), with a median time to treatment of 14 hours (62). Even though therapeutic intervention within 3 hours could salvage most of the potentially reversible ischemic tissue and benefit patients, such a feat is unlikely as none of the published neuroprotective clinical trials has used a 3-hour window (45, 62).

Several studies advocates, that it is a necessity to follow animals for much longer time periods because if the compound is shown to be initially effective with a short survival time, initial beneficial effects may be lost over time (63, 64). Long-term outcome, that is, reduced infarct volume, should be evaluated to ameliorate concerns that the drug merely slows the maturation of the histopathological process. Routine histological end points cannot distinguish whether surviving neurons are functional or dysfunctional or will go on to die in a delayed fashion, and they are less predictive of long-term histology than early behavioural assessments (65). Moreover, some compounds [e.g., basic Fibroblast Growth Factor (bFGF), osteogenic protein-1] have been associated with functional improvement without affecting infarct size in animals, suggesting that they act by other mechanisms, e.g., enhancement of neural repair, rather than by neuroprotection (66, 67). Functional recovery is a major and may be the most relevant end point in clinical trials (15, 16). Therefore, it is desirable despite being difficult to demonstrate that drugs improve functional outcome after experimental ischemia. It is challenging to measure function and behaviour in brain-damaged animals, although techniques to measure these outcomes are advancing.

1.4. NOVEL THERAPEUTIC APPROACHES AND EMERGING CONCEPTS.

Most trials to date have attempted to modulate the early metabolic events in ischemia, particularly that involving glutamate activation of the calcium cascade. With a growing understanding of the pathophysiology of ischemic brain injury in the acute phase of stroke, as well as progress in understanding the mechanisms that underlie functional recovery in the sub acute stages, newer therapeutic strategies are emerging (23, 68, 69).

On the basis of the complexity of events and the disappointing results from single-agent trials, it may not be realistic to expect that a single neuroprotective agent will offer lasting therapeutic benefit. Effective neuroprotection might require “rational” polytherapy which combines drugs with different mechanisms of action, perhaps administered at different post stroke intervals, to maximize efficacy and/or extend the window for reperfusion, minimize reperfusion injury or haemorrhage, or inhibit delayed cell death (45, 70). Since the failure of several neuroprotective trials has been attributed to dose-limiting toxicity, combination therapy may permit lower doses of each agent and minimize adverse effects (71).

Synergistic effects have been demonstrated in animals when thrombolysis is combined with a number of other agents like citicoline, α -amino-3-hydroxy-5-Methyl-4-isoxazole Propionic Acid (AMPA) and NMDA antagonists amongst others (72-74). The concept of such a synergy has been reinforced by observations from a number of studies. In animal models, a combination of such neuroprotective drug entities with entirely different mechanism of actions has demonstrated protective effects. Studies include the NMDA antagonist MK-801 in combination with a γ -Amino Butyric Acid (GABA) agonist, a free radical scavenger, a calcium antagonist and citicoline (75-78).

Patients with ischemic stroke may undergo significant spontaneous recovery after their event (47). The mechanisms promoting functional recovery after ischemic stroke are not entirely clear but most likely depend on functional and/or structural reorganization of the remaining intact brain broadly termed as cerebral plasticity. Studies in stroke patients show that recovery may be robust for at least the first three months after the stroke, but further recovery may continue thereafter (47).

This prolonged time window of opportunity to intervene on the stroke recovery process offers a substantial and currently unexploited opportunity for drug development. Over the years, the focus was on the hyper acute and acute intervention, which, even though critically important, had lead us to underestimate “restorative” interventions that might enhance recovery at the sub-acute and chronic stages after stroke (79). Within minutes of ischemia, a loss of dendritic spines can be observed at excitatory synapses; re-establishment of dendritic spine synapses in surviving neurons can occur rapidly and represents a potential substrate for functional recovery (80). Ischemic cortical injury induces the expression of growth factors in peri-infarct regions, and behavioural recovery is accompanied by increased dendritic branching and synaptogenesis that peaks 2 to 4 weeks after stroke in the rat (81).

Mechanisms of neuroplasticity postulated to underlie recovery include unmasking of latent connections, redundancy that allows recruitment of alternate parallel pathways to take over lost functions, axonal sprouting from surviving neurons with formation of new synapses, and possibly even neurogenesis (68, 82-84). Intra-cisternal administration of bFGF at 24 hours post stroke or osteogenic protein-1 beginning 3 days after stroke promoted recovery in animals without affecting infarct size and stimulated new neuronal sprouting and synapse formation (67, 85, 86). Most importantly, accumulating data clearly

points to the fact that, many treatment targets have biphasic roles where initial deleterious responses transit into beneficial mechanisms for neuronal and vascular recovery (58). NMDA receptors mediate the neuroplasticity and protection against apoptosis that is afforded by environmental enrichment (87). In fact, prolonged use of NMDA receptor antagonists increases cell death in mouse models of traumatic brain injury. Some data also support a role for NMDA signalling in promoting the endogenous neurogenesis that occurs after stroke (88). Emerging molecular studies now suggest that these beneficial NMDA mechanisms may involve augmentation of protective Cyclic AMP Response Element Binding (CREB) protein signalling in neurons (89). Taken together, in retrospect, these analysis suggest that an untitrated and wholesale blockade of NMDA receptors might not have been an optimal strategy for stroke treatment (90). Data exists to demonstrate that, although Matrix Metallo-Proteinases (MMPs) disrupt neurovascular matrix and cause injury during acute stroke, they can promote neurovascular remodelling in peri-infarct cortex during the delayed stages of stroke recovery (91).

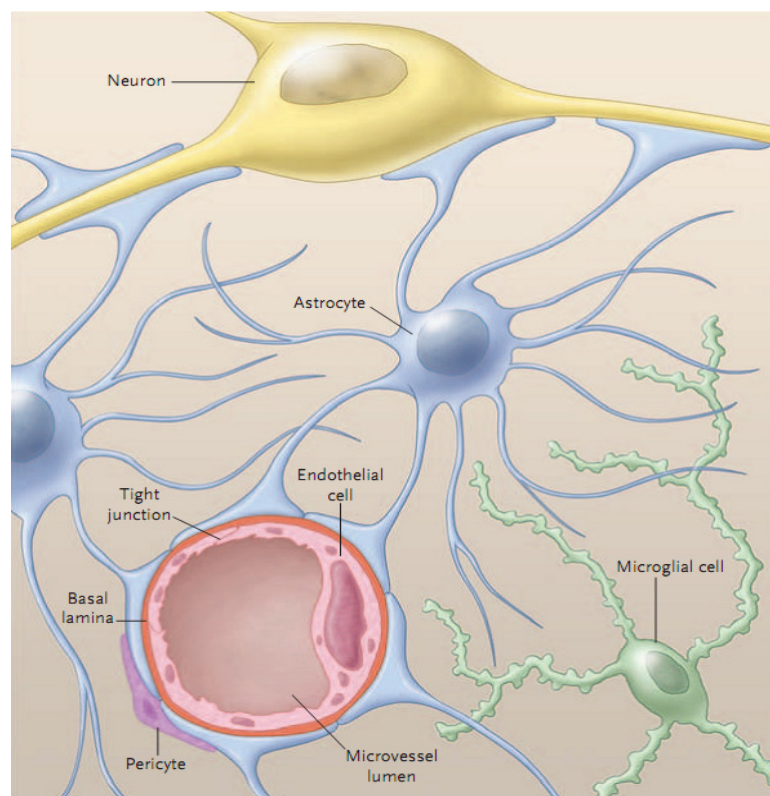
MMPs also mediate the movement of neuroblasts during the endogenous neurogenic response that is triggered after brain injury (92) . Even though inhibitors of MMPs during the first few hours after stroke reduces infarction, the same inhibitors worsen outcomes when applied several days later (93). Further, many studies have shown that select inhibitors of C-Jun-N-terminal Kinase (JNK) are neuroprotective in animal models of cerebral ischemia (94). Emerging data now suggest that JNK also has a biphasic role in terms of injury versus repair. Whereas acute over activation of this pathway triggers caspases and other cell death mediators, a delayed and regulated role for JNK may contribute to neuronal recovery. During brain development, JNK is a requisite signal for neural precursor cell migration, microtubule assembly and axonal guidance (95). An

analogous role might exist in adult brain, wherein JNK contributes to dendritic sprouting and axonal re-growth after injury (95). Evidence also exists to prove that free radicals may also participate in angiogenesis; Nitric Oxide (NO) promotes angiogenic sprouting, and Vascular Endothelial Growth Factor (VEGF) signalling requires the functional production of radicals from the reduced Nicotinamide Adenine Dinucleotide Phosphate (NADPH) oxidase pathway (96, 97).

All the above said raises a number questions including what are the molecular signals that trigger the transition from injury to repair within damaged but not yet dead brain tissue? When do these complex transitions occur? What cell types are involved? Are there effects on neurovascular coupling (98)? Even during the early stages of cerebral ischemia, a complex network of endogenous neuroprotective responses may be triggered (99-101). How do our acute therapies affect these repair mechanisms? Is there a continuum between early cellular repair and delayed neuronal plasticity and vascular remodelling? Without a full understanding of how our targets switch from deleterious to beneficial roles over time, we will not be able to maximize neuroprotection without interfering with endogenous recovery.

1.5. THE CONCEPT OF THE NEUROVASCULAR UNIT.

A general assessment of the causes for the failure of neuroprotectants to realize their promise in the clinic points to the complexity of post-ischemic brain injuries. Ischemia initiates inflammation, increases microvascular permeability and causes local haemorrhage in addition to having direct effects on cells. Ischemic stroke has such effects because it is really a vascular disorder affecting neuronal function.



The neurovascular unit comprises of neurons, the microvessels that supply them, and their supporting cells. Cerebral microvessels consist of the endothelium (which forms the blood brain barrier), the basal lamina matrix, and the end-feet of astrocytes. Microglial cells and pericytes may also participate in the unit.

Figure 3. Essential components of the neurovascular unit. *Adapted from reference(102)*

Because neurons constitute less than 5 percent of cells in cerebral gray matter, ischemia affects not only neurons but also astrocytes and other glial cells that support the neurons, the axons of neurons that relay their signals to other cells, and the microvessels that supply oxygen and nutrients to them. Neurons and microvessels respond equally

rapidly to the ischemic insult (103). These observations have led recently to a shift in perspective from a focus on the neurons alone to a focus on the complex of neurons, the microvessels that supply them, and the supportive cells (astrocytes, other glial cells, and resident inflammatory cells). This “neurovascular unit” (Figure 3) which may vary in composition and function from site to site within the brain, may be a more realistic target of ischemic injury. Injury to any part of the unit could affect the other components (102). In as much as focal ischemia of the brain is a pro-inflammatory stimulus, it is of interest to consider how the hypothetical “neurovascular unit” and its component elements might respond separately and in concert. The responses of the “unit” to inflammatory modulators generated early during focal ischemia or from other processes that affect individual component of the “unit” have not been established; although, the responses of some of the individual “unit” components have been detailed in specific experimental settings. Among the known interactions of inflammatory cytokines with the proposed neurovascular components and elements are as follows.

1.5.1. THE ENDOTHELIUM.

Under normoxic conditions the intact resting endothelium preserves anti-thrombotic and anti-inflammatory characteristics of the cerebral microvasculature, and contributes to the permeability barrier through its inter-endothelial cell cohesion receptors, components of the tight junctions, and adhesion to the subjacent basal lamina matrix. The anti-thrombotic milieu most probably involves mechanisms similar to the endothelium in other vascular beds, including the generation of adenosine, production and secretion of prostacyclin (PGI₂), and the glycocalyx surface. The anti-inflammatory properties derive from storage of leukocyte adhesion receptors (e.g. P-selectin), and the requirement for

synthesis of other receptors necessary for cell-matrix adhesion (104). Typically, thrombosis and inflammation are linked. Endothelial cells within cerebral capillaries and especially within the post-capillary venules, respond to Tumor Necrosis Factor (TNF) - α and InterLeukin (IL) - 1β by translocation of P-selectin (stored in Weibel-Palade bodies) to the luminal surface, the synthesis of Inter Cellular Adhesion Molecule (ICAM)-1 and its expression on the luminal surface, and the subsequent appearance of E-selectin on this surface (105, 106). These adhesion receptors facilitate firm adhesion of PolyMorpho Nuclear (PMN) leukocytes to the local endothelium in preparation for their transmigration into the injured neuropil (107, 108). Both the cytokines (TNF- α and IL- 1β) have been shown to down-regulate the integrin $\alpha_6\beta_1$ found on endothelial cells (109). How this impacts microvessel integrity is not known, but this could augment the processes initiated by focal ischemia that lead to the rapid loss in β_1 -integrin expression observed in vivo and in the down-regulation of matrix-dependent integrins by experimental ischemia in vitro (110, 111).

Focal ischemia stimulates loss in the solute permeability barrier established by the endothelium allowing leakage of electrolytes and plasma proteins as large as fibrinogen (~360 kDa). It have been postulated that IL- 1β facilitates oedema formation in the initial moments following the onset of focal ischemia (112). Others have suggested that oedema is associated with leukocyte infiltration (113). Furthermore, immunologic blockade of the functional β_1 -integrin subunit, expressed on epithelial cells of the dermis, produces significant local oedema within the skin, consistent with the events noted above (114). The fact that the endothelium does not detach from the basement membrane during focal ischemia implies that changes in these receptors do not fully explain the adhesion of the endothelium to the underlying matrix (110) .

1.5.2. THE EXTRA-CELLULAR MATRIX.

The cerebral microvessel wall displays rapid dynamic changes in response to focal ischemia that precede the incursion of inflammatory cells. Significant changes in the matrix integrity of the basal lamina and in matrix receptors occur simultaneously with neuron injury. The expression of the matrix constituents of the basal lamina, including laminin-1 and -5, collagen IV and cellular fibronectin decreases substantially following the onset of focal ischemia (115). The endothelial cell β_1 -integrin receptor and integrin $\alpha_6\beta_4$ on astrocyte end-feet decrease substantially in the first 60 minutes following MCAO (110, 116).

The alternate receptor family, dystroglycan, is lost from the astrocytic end-feet in the same time frame (117). It is notable that aquaporin-4 is co-distributed with dystroglycan in the luminal membrane of astrocyte endfeet (117, 118). Separation of the astrocytic end-feet from the matrix of select microvessels occurs in this period (119). This separation coincides with the accumulated fluid within the extravascular space. Proteases that could process matrix are generated rapidly within the core under the conditions of focal ischemia and belong to four families; the MMPs (e.g. pro-MMP-2 and -9, and their MMP activators), serine proteases (e.g. urokinase plasminogen activator, u-PA), cysteine proteases (e.g. cathepsin L), and heparinase (120). Members of all four families appear within 1–2 hours after MCAO in the ischemic core. Degradation of some matrix proteins has been shown to have cytokine activity, and it is possible that some of these products can also affect the integrity of the neuropil.

For instance, in the process of PMN leukocyte activation and migration, protease degradation of specific extra-cellular matrix substrates occurs with the generation of chemotactic products. Neutrophil Elastase (NE) released upon degranulation of PMN

leukocytes can cleave laminin-5 to generate a peptide capable of promoting granulocyte chemotaxis (121). Similarly MMP-8 (also released by PMN leukocytes upon activation and degranulation) can generate a Pro-Gly-Pro-containing peptide from collagen that is chemotactic for granulocytes (122). While not yet tested in the Central Nervous System (CNS), it is likely that activation and migration of PMN leukocytes through the cerebral microvasculature can generate substances from the basal lamina matrix (which contain both laminin-5 and collagen (IV)) that promote the progress of cellular inflammation post-ischemia.

1.5.3. PERIVASCULAR ASTROCYTES.

Astrocytes have important physiological properties as they relate to CNS homeostasis. Astrocytes affect neuronal function by the release of NeuroTrophic Factors (NTFs), guide neuronal development, contribute to the metabolism of neurotransmitters, and regulate extracellular pH and potassium levels (123). It has recently been appreciated that astrocytes have a dynamic role in regulating neuronal function (124, 125). Astrocytes increase the number of mature functional synapses on CNS neurons and are required for synaptic maintenance in vitro (126). This study suggests that astrocytes may actively participate in synaptic plasticity. Similarly, the ablation of reactive astrocytes leads to substantial neuronal degeneration in the injured adult CNS (127). Astrocytes have been mainly investigated as putative inducers of the Blood Brain Barrier (BBB) and are widely believed to be operating in favour of the BBB formation (128-130). Humoral factors released from astrocytes were suggested to contribute to tight junction formation (131, 132) but are not sufficient to induce and maintain BBB characteristics alone. Nevertheless, the Glial cell line Derived Neurotrophic Factor (GDNF) seems to be necessary for BBB

induction (133, 134). Inversely, IL-1 β secreted by astrocytes and induced by TNF- α via an endothelin-1 mediated mechanism has been shown to be responsible for compromising the BBB quality (135). Still, the list of all factors required for BBB induction, development, maintenance and perhaps for necessary repairs still remains incomplete.

The importance of astrocytes in this process was demonstrated by a study in which astrocyte ablation led to a failure of BBB repair and resulted in persistent vasogenic oedema (127). Interestingly, it has recently been shown that endothelial cells induce the differentiation of astrocyte precursor cells into astrocytes in vitro, which is mediated by endothelial cell production of Leukemia Inhibitory Factor (LIF) (136). Thus, soluble factors from both endothelial cells and astrocytes may contribute to the generation of the BBB. The Src-Suppressed C-Kinase Substrate (SSeCKS) in astrocytes has been reported to be responsible for the decreased expression of the angiogenic permeability factor VEGF and the increased release of the anti-permeability factor Ang-1. The SSeCKS over-expression was shown to increase the expression of tight junction molecules and to decrease the paracellular permeability in endothelial cells (137).

There is considerable evidence that astrocytes can serve immune function, can potentially present antigens, have phagocytic properties, and generate cytokines and chemokines in response to a variety of stimuli (138). Class II Major Histocompatibility Complex (MHC) molecules are expressed following stimulation with Interferon- γ (IFN- γ) and TNF- α and are inhibited by Transforming Growth Factor (TGF)- β , IFN- β , IL-1, IL-4, norepinephrine, glutamate, Vasoactive Intestinal Peptide (VIP) and nitric oxide. ICAM-1 has also been detected following stimulation with TNF- α , IL-1 and IFN- γ . The inhibitors include TGF- β , IL-6 and IL-10. Further, inconsistent data also exists to the expression of molecules like B7 and CD40 which may follow stimulation with IFN- γ (138).

1.5.4. NEURONS AND AXONS.

The impact of inflammation initiated by focal ischemia on neuron and axon viability and resultant stroke severity has been debated. The concordance of cytokine generation and leukocyte infiltration in the early hours following ischemia onset has suggested that both events can contribute to neuronal injury. The cytokines TNF- α and IL-1 β can derive from endothelial cells, astrocytes, microglia, and neurons themselves. Recent work has indicated that in isolated conditions, Dorsal Root Ganglionic (DRG) neurons can stimulate isolated PMN leukocytes to initiate their respiratory burst with free radical release leading to an increase in Ca⁺² transients in the neurons (139). One consequence is that PMN leukocyte infiltration could aggravate neuronal injury. While IL-1 β expression has been associated with neuronal injury, a recent report suggests that IL-1 β could stimulate neurite outgrowth from DRG neurons, and could support nerve regeneration (140). However, events in the peripheral circulation are not uniformly recapitulated in the CNS. The manner in which IL-1 β could mediate neuronal injury in the CNS has been the subject of vigorous discussion. One possibility is that enzymes with matrix protease activity, generated during ischemia, could promote neuron injury either directly or indirectly (141). This hypothesis has been proposed recently in conjunction with microvascular events (142).

1.5.5. PERICYTES AND MICROGLIA.

Pericytes are pluripotential cells located within the basal lamina matrix of microvessels. These cells become activated and can migrate in response to specific stimuli including focal ischemia and inflammation. Pericytes also have been shown to have some

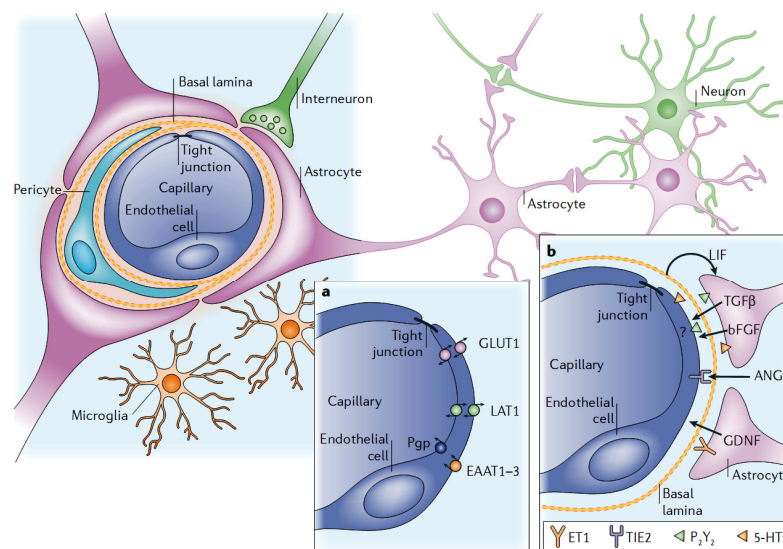
properties found in select inflammatory cells (143). Microglia being resident inflammatory cells of the CNS, derived from bone marrow stem cells and also evolving from cells of the monocyte/macrophage lineage (144). Microglia can play a number of roles in inflammatory responses of the CNS. While normally quiescent, these cells possess Fc receptors, complement receptors, receptors for a number of cytokines, chemokine receptors, CD40, Fas and Fas ligand (145). Microglia can also generate TNF- α and IL-1 β in addition to other cytokines, and are known to regulate T-cell-mediated immune processes (145). In response to activators, microglia can express pro-MMP-9. Within the first 24 hours following the onset of focal ischemia, peripheral blood cells of the monocyte / macrophage lineage enter the neuropil. At the same time microglia become activated, undergo shape change, and express markers of inflammation (146).

1.6. THE BLOOD BRAIN BARRIER.

The CNS is the most critical and sensitive system in the human body. Proper neuronal function necessitates a highly regulated extracellular environment, wherein the concentrations of ions such as Na^+ , K^+ , and Ca^{2+} must be maintained within very narrow ranges. Furthermore, the metabolic demands of nervous tissue are considerable, with the CNS accounting for approximately 20% of oxygen consumption in humans (147). The CNS is also extremely sensitive to a wide range of chemicals. Many of the substances we consume in our diet, although readily metabolized and excreted without harm to peripheral organ systems, are in fact quite neurotoxic. It is therefore essential that the interface between the CNS and the peripheral circulatory system functions as a dynamic regulator of ion balance, a facilitator of nutrient transport, and a barrier to potentially harmful molecules. This homeostatic aspect of the cerebral microcirculation, historically referred to as the BBB, performs all of these functions (148).

The BBB is a selective barrier formed by the endothelial cells that line cerebral microvessels (149). It acts as a ‘physical barrier’ because complex Tight Junctions (TJs) between adjacent endothelial cells force most molecular traffic to take a trans-cellular route across the BBB, rather than moving paracellularly through the junctions, as in most endothelia (Figure 4) (148, 150). Small gaseous molecules such as oxygen and carbon-dioxide can diffuse freely through the lipid membranes, and this is also a route of entry for small lipophilic agents, including drugs such as barbiturates and ethanol. The presence of specific transport systems on the luminal and abluminal membranes regulates the trans-cellular traffic of small hydrophilic molecules, which provides a selective ‘transport barrier’, permitting or facilitating the entry of required nutrients, and excluding or effluxing potentially harmful compounds (151). Finally, a combination of intra- and extra-

cellular enzymes provides a rather ill defined ‘metabolic barrier’. Ecto-enzymes such as peptidases and nucleotidases are capable of metabolizing peptides and ATP, respectively, whereas intra-cellular enzymes such as Mono-Amine Oxidase (MAO) and cytochrome P450 (1A and 2B) can inactivate many neuroactive and toxic compounds (152). Large hydrophilic molecules such as peptides and proteins are generally excluded, unless they can be transferred by specific receptor-mediated transcytosis, or by the less specific adsorptive-mediated transcytosis (Figure 5) (153). However, the brain endothelium has a much lower degree of endocytosis / transcytosis activity than peripheral endothelium, which contributes to the transport-barrier property of the BBB. Hence, the term BBB covers a range of passive and active features of the brain endothelium. As the TJs severely restrict entry of hydrophilic drugs, and there is limited penetration of larger molecules such as peptides, strategies for drug delivery to the CNS need to take these features into account.

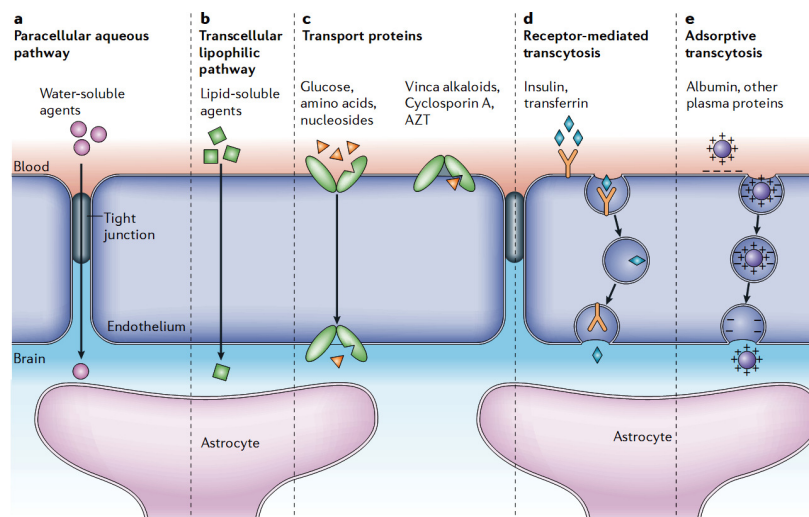


The barrier is formed by capillary endothelial cells, surrounded by basal lamina and astrocytic perivascular endfeet. Astrocytes provide the cellular link to the neurons. The figure also shows pericytes and microglial cells. **a)** Brain endothelial cell features observed in cell culture. The cells express a number of transporters and receptors, some of which are shown. EAAT1–3, excitatory amino acid transporters 1–3; GLUT1, glucose transporter 1; LAT1, L-system for large neutral amino acid transport; Pgp, P-glycoprotein. **b)** Examples of bidirectional astroglial–endothelial induction necessary to establish and maintain the BBB. Some endothelial cell characteristics (receptors and transporters) are shown. 5-HT, 5-hydroxytryptamine (serotonin); ANG1, angiopoietin 1; bFGF, basic fibroblast growth factor; ET1, endothelin 1; GDNF, glial cell line-derived neurotrophic factor; LIF, leukaemia inhibitory factor; P2Y2, purinergic receptor; TGFβ, transforming growth factor-β; TIE2, endothelium-specific receptor tyrosine kinase 2.

Figure 4. Cellular constituents of the blood brain barrier. *Adapted from reference (149).*

1.6.1. THE BBB PHENOTYPE.

Specifically, the BBB exists primarily as a selective diffusion barrier at the level of the cerebral micro vascular endothelium, characterized by the presence of tight cell-cell junctions and a lack of fenestrations. The circumference of the capillary lumen is enclosed by a single endothelial cell. Anatomically, the endothelial cells of the BBB are distinguished from those in the periphery by increased mitochondrial content, a lack of fenestrations, minimal pinocytotic activity, and the presence of TJs (154-156). Attached at irregular intervals to the abluminal membrane of the endothelium are pericytes, often divided into granular and filamentous subtypes (157). Pericytes and endothelial cells are ensheathed by the basal lamina, a membrane 30 to 40-nm thick composed of collagen type IV, heparin sulfate proteoglycans, laminin, fibronectin, and other extra-cellular matrix (ECM) proteins (158). The basal lamina is contiguous with the plasma membranes of astrocytic end-feet, which ensheath cerebral capillaries (Figure 4.).

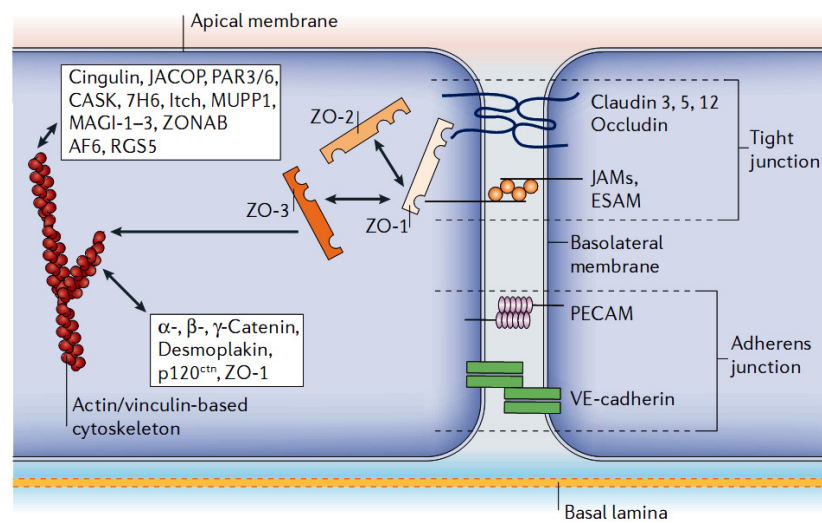


A schematic diagram of the endothelial cells that form the blood–brain barrier (BBB) and their associations with the perivascular end feet of astrocytes. The main routes for molecular traffic across the BBB are shown. **a**) Normally, the tight junctions severely restrict penetration of water-soluble compounds, including polar drugs. **b**) However, the large surface area of the lipid membranes of the endothelium offers an effective diffusive route for lipid-soluble agents. **c**) The endothelium contains transport proteins (carriers) for glucose, amino acids, purine bases, nucleosides, choline and other substances. Some transporters are energy-dependent (for example, P-glycoprotein) and act as efflux transporters. AZT, azidothymidine. **d**) Certain proteins, such as insulin and transferrin, are taken up by specific receptor-mediated endocytosis and transcytosis. **e**) Native plasma proteins such as albumin are poorly transported, but cationization can increase their uptake by adsorptive-mediated endocytosis and transcytosis. Drug delivery across the brain endothelium depends on making use of pathways **b–e**; most CNS drugs enter via route **b**.

Figure 5. Transport pathways across the blood brain barrier. *Adapted from reference (149).*

A great deal is now known about specific features of the brain endothelium that contribute to its barrier properties (whether physical or chemical) and distinguish brain endothelium from the endothelium of peripheral tissues. The TJs are more complex in the brain endothelium, seen in freeze–fracture images as a network of strands formed by intramembranous particles, and occlude the intercellular cleft more effectively (150). These junctions significantly restrict even the movement of small ions such as sodium and chloride, so that the Trans-Endothelial Electrical Resistance (TEER), which is typically 2–20 ohm.cm² in peripheral capillaries, can be >1,000 ohm.cm² in brain endothelium (159).

Among the molecules identified as making important contributions to TJ structure are the trans-membrane proteins occludin and the claudins. Occludin is a 60–65 kDa protein with a carboxy (C)-terminal domain that is capable of linking with Zonula Occludens protein-1 (ZO-1) (Figure 6). The main function of occludin appears to be in TJ regulation (148, 160). In the BBB, expression of the proteins claudin-3 (originally misidentified as claudin-1, now also referred to as 1/3), claudin-5 and possibly claudin-12 appears to contribute to the high TEER (150). Junctional Adhesion Molecules JAM-A, JAM-B and JAM-C are present in brain endothelial cells, and are involved in the formation and maintenance of the TJs. The transmembrane proteins are connected on the cytoplasmic side to a complex array of peripheral membrane proteins that form large protein complexes, the cytoplasmic plaques (Figure 6). Within the plaques are adaptor proteins with many protein–protein interaction domains, including ZO-1, ZO-2 and ZO-3; the Ca²⁺-dependent Serine protein Kinase (CASK); (Membrane-Associated Guanylate kinase with Inverted orientation of protein–protein interaction domains) MAGI-1, MAGI-2 and MAGI-3; the PARTitioning defective proteins PAR3 and PAR6; and (MULTI-PDZ-Protein 1) MUPP1.



Simplified and incomplete scheme showing the molecular composition of endothelial tight junctions. Occludin and the claudins - proteins with four transmembrane domains and two extracellular loops-are the most important membranous components. The Junctional Adhesion Molecules (JAMs) and the Endothelial Selective Adhesion Molecule (ESAM) are members of the immunoglobulin super family. Within the cytoplasm are many first-order adaptor proteins, including Zonula Occludens 1, 2 and 3 (ZO 1-3) and Ca^{2+} -dependent Serine protein Kinase (CASK), that bind to the intramembrane proteins. Among the second-order adaptor molecules, cingulin is important, and Junction-Associated Coiled-Coil protein (JACOP) may also be present. Signalling and regulatory proteins include Multi-PDZ-Protein 1 (MUPP1), the PARTitioning defective proteins 3 and 6 (PAR3/6), MAGI-1-3 (Membrane-Associated Guanylate kinase with inverted orientation of protein-protein Interaction domains), ZO-1 associated Nucleic Acid-Binding protein (ZONAB), Afadin (AF6), and Regulator of G-protein Signalling 5 (RGS5). All of these adaptor and regulatory/signalling proteins control the interaction of the membranous components with the actin/vinculin-based cytoskeleton. In epithelial cells, tight and adherens junctions are strictly separated from each other, but in endothelial cells these junctions are intermingled. The most important molecule of endothelial adherens junctions is Vascular Endothelial cadherin (VE-cadherin). In addition, the Platelet-Endothelial Cell Adhesion Molecule (PECAM) mediates homophilic adhesion. The chief linker molecules between adherens junctions and the cytoskeleton are the catenins, with desmoplakin and p120 catenin (p120^{ctn}) also involved. Itch, E3 ubiquitin protein ligase.

Figure 6. Molecular composition of endothelial tight junctions. *Adapted from reference (149).*

These help to organize the second class of plaque proteins, the regulatory and signalling molecules (including the small Guanosine Tri Phosphatases (GTPases)) and their regulators, such as the Regulator of G-protein Signalling 5 (RGS5), and the transcription regulator the ZO-1-associated Nucleic Acid Binding protein (ZONAB). A newly identified protein, Junction-Associated Coiled-coil Protein (JACOP), may anchor the junctional complex to the actin cytoskeleton. Cell-cell interaction in the junctional zone is stabilized by adherens junctions. The TJs have a valuable function not only in restricting paracellular permeability (gate function) but also in segregating the apical and basal domains of the cell membrane (fence function) so that the endothelium can take on the

polarized (apical-basal) properties that are more commonly found in epithelia, such as those of the gastrointestinal tract and kidney (150). The PAR3–atypical Protein Kinase C (aPKC)-PAR6 complex appears to be involved in regulating TJ formation and in establishing cell polarity. The brain endothelial transporters that supply the brain with nutrients include the GLUcose Transporter 1 (GLUT1), several amino acid carriers (including L-system for large neutral Amino acid Transport (LAT)-1), and transporters for nucleosides, nucleobases and many other substances (Figure 5). Several organic anion and cation transporters identified in other tissues and the choroid plexus are also proving to be expressed on the brain endothelium. Where compounds need to be moved against a concentration gradient, the energy may come from ATP (as in the ATP-Binding Cassette (ABC) family of transporters), including P-glycoprotein (Pgp and Multidrug Resistance-related Proteins, MRPs), or the Na^+ gradient created by operation of the abluminal Na^+ , K^+ -ATPase (149).

Some transporters (for example, GLUT1 and LAT1) are bidirectional, moving substrates down the concentration gradient, and can be present on both the luminal and abluminal membranes or predominantly on one. Among the efflux transporters Pgp is predominantly concentrated on the luminal membrane whereas the Na^+ dependent transporters are generally abluminal specialized for moving solutes out of the brain (161-163). They include several Na^+ -dependent glutamate transporters (Excitatory Amino Acid Transporters 1–3; (EAAT1–3) which move glutamate out of the brain against the large opposing concentration gradient ($< 1 \mu\text{M}$ in interstitial fluid compared with $\sim 100 \mu\text{M}$ in plasma) (163). The clear apical–basal polarity of brain endothelial cells noted above is hence reflected in their polarized transport function.

1.7. NEUROTROPHIC GROWTH FACTORS.

NTFs are a class of proteins that are normally present in the mammalian nervous system and are capable of promoting the survival and/or maintenance of specific neuronal populations. Further, NTFs can, in some instances, perform additional functions including stimulation of axonal growth, synaptic plasticity, neurotransmitter synthesis and release (164-166). Normal differentiation of neuronal and glial cells and their maintenance are under the control of NTFs. Among neural cells, neurons are particularly sensitive to various injuries such as ischemia, hypoxia, hypoglycemia, infection, and trauma. These vulnerabilities of neurons make it difficult to treat patients suffering from the above injuries in clinical situations. The vulnerability is found to be different even within the neuronal sub-populations (167). NTFs are also involved in the normal maintenance and survival of neuronal cells after differentiation. Constant secretion of NTFs keep cell survival signals activated and death signals inactive. For example, the presence of Nerve Growth Factor (NGF) maintains cell survival by activating cell survival factors like Bcl-2 and inhibiting death signals such as Apoptotic Protease Activating Factor (APAF)-1 and caspases (168). However, once NTFs are deprived for some reason, such as in ischemia, the balance between survival and death signals is tipped in favour of death signals that finally result in neuronal cell death. Many other stimuli such as Reactive Oxygen Species (ROS), FAS ligand and TNF activate distinct biochemical pathways that trigger a family of caspases and lead to cell death.

NTFs are usually classified into 3 or 4 subclasses based on their receptors (Table 2). NTFs that work with tyrosine kinase receptors are a major group consisting of Epidermal Growth Factor (EGF), Fibroblast Growth Factor (FGF), Hepatocyte Growth Factor (HGF), Insulin-like Growth Factor (IGF-1), neurotrophins (NGF, Brain-Derived Neurotrophic

Factor [BDNF], NeuroTrophin 3 [NT3], NeuroTrophin 4/5 [NT4/5]), Platelet-Derived Growth Factor (PDGF), VEGF, amongst others. Once these proteins bind the receptors as a monomer (FGF) or dimer (neurotrophins), the receptors form dimers and the intracellular tyrosine kinase domains are activated, those then trans-phosphorylate intracellular signal proteins that possess SH2 (Src Homology 2), SH3 or PH (Pleckstrin Homology) domain (165). GDNF and companion proteins, such as neurturin, artemin, and persephin bind receptor complex of GDNF Family Receptor alpha-1 ($GFR\alpha-1$) and c-ret as a monomer, activating the intracellular tyrosine kinase domain.

Type of receptors and neurotrophic factor family	Neurotrophic factors as ligands	Intracellular active domain	Downstream signal proteins
Tyrosine kinase receptors		Tyrosine kinase domain	SH2, SH3, PH
EGF receptor family	EGF, HB-EGF, TGF		
Eph family	Ephrin (LERK)		
FGF receptor family	FGF 1~9		
HGF receptor family	HGF, MSP		
Insulin receptor family	Insulin, IGF-1		
NGF receptor family	Neurotrophins (NGF, BDNF, NT3, NT4/5)		
PDGF receptor family	PDGF-A & B, CSF-1, Steel factor		
Ret receptor family	GDNF, Neurturin, Artemin, Persephin		
Tie family	Angiopoietin-1 & 2		
VEGF receptor family	VEGF-A,B & C, PIGF		
Cytokine receptors	CNTF, LIF, IL-2, IL-6	Intracellular portion (gp 130/LIFR)	JAK
Serine/threonine kinase receptor		Serine-threonine kinase domain	Smad 1~8
TGF- super family	BMP family: BMP2~8, OP1 & 2, GDF 5~7		
	Activin family: Activin A & B		
	TGF- family: TGF-1~3		

EGF, epidermal growth factor; HB-EGF, Heparin binding-EGF; TGF, transforming growth factor; LERK, ligand for eph related kinase; FGF, fibroblast growth factor; HGF, hepatocyte growth factor; MSP, macrophage stimulating protein; IGF, insulin like growth factor; NGF, nerve growth factor; BDNF, brain derived neurotrophic factor; PDGF, platelet-derived growth factor; CSF, colony stimulating factor; GDNF, glial cell derived neurotrophic factor; VEGF, vascular endothelial growth factor; CNTF, ciliary neurotrophic factor; LIF, leukemia inhibitory factor; IL, interleukin; LIFR, LIF receptor; JAK, janus protein tyrosine kinase; TGF; transforming growth factor; BMP, bone morphogenetic protein; OP, osteogenic protein; GDF; growth differentiation factors.

Table 2. Classification of neurotrophic factors based on their receptors. *Adapted from reference(169).*

Cytokines, such as Ciliary NeuroTrophic Factor (CNTF), LIF, and IL-2 bind dimeric or trimeric receptors and activate intracellular tyrosine kinase proteins such as JANUS protein tyrosine Kinase JAK. The TGF- super family consists of the activin family (activin-A and -B), Bone Morphogenetic Protein family (BMP 2~8), Osteogenic Proteins (OP 1~2), Growth Differentiation Factors (GDF 5~7), and TGF-family (TGF 1~3). TGF ligands bind to type 1 and 2 receptors, and the receptors form a tetrameric functional complex. Then type 2 receptors phosphorylate serine-threonine kinase domain of type 1 receptors so that the type 1 receptors activate subsequent signal systems such as SMAD.

Neurotrophins generally activate the Trk receptors (TrkA, TrkB and TrkC), which are cell-surface receptors with intrinsic tyrosine kinase activity. They can auto-phosphorylate and may for instance, after the binding of NGF to TrkA, the receptor phosphorylates several tyrosine residues within its own cytoplasmic tail (170). These phosphotyrosines in turn serve as docking sites for other molecules such as PhosphoLipase C γ (PLC γ), PhosphoInositide 3-Kinase (PI(3)K) and adaptor proteins such as Shc, and these signal transduction molecules coordinate neuronal survival (Figure. 7) (171).

A central role of the PI(3)K pathway in neuronal survival was first suggested by the observation that PI(3)K inhibitors block the survival effect of NGF (172). PI(3)K enzymes are normally present in cytosol and can be activated directly by recruitment to an activated Trk receptor, or indirectly through activated Ras. Active PI(3)K enzymes catalyse the formation of the lipid 3'- phosphorylated phosphoinositides, which regulate the localization and activity of a key component in cell survival, the Ser/Thr kinase Akt (173). Akt has three cellular isoforms of which c-Akt3/RAC-PK γ is the major species expressed in neurons (174). In addition to a centrally located kinase domain, Akt contains a PH

These results establish an essential role for Akt in neuronal survival. Akt targets several key proteins to keep cells alive, including apoptosis regulators and transcription factors (Figure 7). Bad is a pro-apoptotic member of the Bcl-2 family, which in its unphosphorylated form can bind to Bcl-x_L and thus block cell survival (176). But the activation of Akt induces the phosphorylation of Bad and promotes its interaction with the chaperone protein 14-3-3, which sequesters Bad in the cytoplasm and inhibits Bad's proapoptotic activity (177). Akt has been shown to affect, directly or indirectly, three transcription factor families: Forkhead, CREB and Nuclear Factor (NF)-κB, all of which are involved in regulating cell survival, and whereas the phosphorylation of Forkhead family members by Akt negatively regulates death promoting signals, the phosphorylation of CREB and IκB Kinase (IKK) stimulates survival pathways (178-181).

Neurotrophins also stimulate docking of the adaptor protein Shc to activated Trk receptors. This triggers the activation of the small Guanosine Tri-Phosphate (GTP) binding protein Ras and the downstream Mitogen Activated Protein (MAP) kinase cascade, which includes the subsequent sequential phosphorylation and activation of the kinases Raf, MAP kinase kinase/ERK kinase (MEK) and Extracellular signal Regulated protein Kinase (ERK) (182).

The effect of the MAP kinase pathway on survival is mediated at least partly by activation of the pp90 Ribosomal S6 Kinase (RSK) family members. Like Akt, RSK phosphorylates Bad, and both kinases might act synergistically in inhibiting Bad's proapoptotic activity. The effect of RSKs on neuronal survival is not limited to the phosphorylation of Bad; RSKs are also potent activators of the CREB transcription factor. Because CREB is known to activate transcription of bcl-2, it can stimulate cell survival

directly. Thus, although there is a divergence in the survival pathways downstream of the neurotrophin receptors, both the PI(3)K-Akt and MAP kinase pathways converge on the same set of proteins, Bad and CREB, to inhibit the apoptosis programme.

1.7.1. PROTECTIVE EFFECTS OF NEUROTROPHIC GROWTH FACTORS IN ISCHEMIC BRAIN INJURY.

Neurotrophic factors are not only essential for the survival and differentiation of normally developing neurons, but also play important roles in the protection and recovery of mature neurons under pathologic conditions (183). Wealth of data exists to show the protective effects of neurotrophins against a number of pathologies in the CNS. GDNF has been found to be protective in various injuries of the central and peripheral nervous tissue and CNTF infusion has been demonstrated to prevent learning disability and neuronal loss induced by ischemia in gerbils (184, 185).

To examine direct protective effects of NTF proteins against ischemic brain damage, topical administration of NTFs such as GDNF, NT-3, VEGF, IGF-1, and BDNF onto the ischemic brain surface have been attempted in rat models of permanent and transient focal cerebral ischemia. Topical application of GDNF greatly reduced the infarct size (48%) and brain oedema (30%) at 24 hours following permanent MCAO in rats (186). Acquired data suggest that treatment with GDNF was protective not only by reducing the apoptotic process, but also a reduction in the necrotic process and accompanying oedema (187). In transient MCAO models, treatment of ischemic rats with topical application of NT-3, VEGF, and IGF-1 ameliorated infarct sizes and was associated with a reduction in the number of Terminal deoxynucleotidyl transferase dUTP Nick End Labeling (TUNEL) and

caspase positive cells (188-190). Again, in another study, delivery of BDNF into the MCA territory through an osmotic mini-pump demonstrated a 33% reduction in total infarct volume (191). After ischemic cortical lesions, bFGF demonstrated reduction in infarct size and diminishes neuronal loss (192, 193). Other growth factors including NGF, NT-4/5 and IGF-1 have also been reported to reduce neuronal loss or infarct size in various brain regions (194-196).

1.7.2. THE EPIDERMAL GROWTH FACTOR.

EGF is a small polypeptide (molecular weight 6000 Da) that stimulates the proliferation of the epidermis and several internal epithelial tissues in vivo (197). It's a single polypeptide consisting of 53 amino acid residues, of which 6 are cysteine (198). These cysteines form three intramolecular disulfide bonds that are important for maintaining the biological activity of EGF (199, 200). EGF is synthesized as a precursor consisting of 1217 amino acid residues from which the mature form may be generated by proteolysis (201). The EGF precursor is a glycosylated transmembrane protein with an apparent molecular weight of 140–150 kDa.

The EGF Receptor (EGFR) is a 170 kDa membrane-spanning protein composed of a 130 kDa single polypeptide chain and N-linked oligosaccharides. EGFR possesses an intracellular tyrosine kinase domain, which is activated by EGF binding (202). The EGFR being a receptor tyrosine kinase, is dimerized, activated, and then autophosphorylated on its tyrosine residues following EGF binding (203). These phosphorylated tyrosine residues serve as high-affinity binding sites for several secondary signalling molecules containing the Src Homology 2 (SH2) domain, which consists of about 100 amino acid residues (204,

205). The signalling molecules containing SH2 domain which associate directly with the activated EGFR include PLC γ , Ras-GTPase-Activating Protein (Ras-GAP), Grb2, Nck, Shc and SHP-2 (206). When PLC γ is phosphorylated on its tyrosine residues its enzymatic activity increases. PLC γ binding to the activated EGFR facilitates the efficient tyrosine phosphorylation of PLC γ which results in its activation. PLC γ catalyzes the hydrolysis of the membrane phospholipid phosphatidylinositol-4,5-bisphosphate generating Di-Acyl Glycerol (DAG) and Inositol 1,4,5-trisPhosphate (IP-3) (201, 207). DAG is a physiological activator of Protein Kinase C (PKC), which is a family of ubiquitous serine/threonine protein kinases involved in growth control and tumorigenesis (208).

IP-3 induces Ca²⁺ release from intracellular stores, affecting Ca²⁺-regulated processes in the cell. On the other hand, Grb2, Nck, and Shc lack an obvious catalytic domain, and are thought to be adaptor proteins, serving as intermediates between receptor tyrosine kinases and downstream signalling molecules (201, 204, 205). Grb2 links the activated EGFR to the Ras signaling pathway. Grb2 has two Src Homology 3 domains (SH3) [11,20,36,37], which are protein–protein interaction sites found in many signalling molecules, through which Grb2 binds to the Ras guanine nucleotide releasing factor SOS (201, 204, 205).

The Grb2/SOS complex binds to the activated EGFR through the SH2 domain of Grb2, recruiting SOS to the plasma membrane where the Ras protein is located. This translocation made the exchange of Guanosine Di-Phosphate (GDP) to GTP on Ras, which in turn activates it. The activated Ras induces a kinase cascade including Raf (a serine/threonine kinase), MAP kinase kinase (MEK) (a dual specificity kinase), and MAP Kinase (MAPK) (a serine/threonine kinase) (201, 209). MAPK is activated which can translocate into the nucleus, and where it can phosphorylate and activates several

transcription factors such as Elk-1 and c-Myc (201). Shc, a SH2 domain-containing adaptor protein, binds to activated EGFR and is also tyrosine-phosphorylated in response to EGF. Phosphorylated Shc can bind to Grb2, also stimulating the Ras signalling pathway (201, 204, 206). So, Shc appears to provide an alternative route for activating the Ras pathway by offering a docking site for Grb2. In addition to the SH2 domain, Shc has a phosphotyrosine interaction domain (also called the phosphotyrosine binding domain) which associates with a phosphotyrosine residue in a manner different from that of the SH2 domain (205). Shc binding to the EGFR may be mediated by the cooperative binding of the PI and SH2 domains to two phosphotyrosine residues on the EGFR (201, 204, 207).

SHP-2 is another SH2-containing protein tyrosine phosphatase, and is thought to be allosterically activated by SH2 domain-mediated binding to target phosphotyrosine residues on the EGFR. However, the physiological substrates of SHP-2 remain unclear.

EGF stimulates PI3-K activity, although PI3-K does not bind directly to the EGFR in contrast to other growth factor receptors, such as the PDGF receptor and TrkA (an NGF receptor), which bind directly to PI3-K. ErbB-3, Cbl, and Gab1 mediate the EGF-induced activation of PI3-K. ErbB-3, which forms a heterodimer with the EGFR, is tyrosine-phosphorylated in response to EGF. Cbl is phosphorylated on tyrosine residues and associates with PI3-K in response to EGF. Cbl has two consensus binding sites for the SH2 domains of PI3-K through which Cbl appears to bind to and activate PI3-K. Gab1 displays amino-acid homology with the Insulin-Receptor Substrate-1 (IRS-1) and Gab1 is tyrosine-phosphorylated in response to EGF.

Phosphorylated Gab1 then associates with PI3-K through the SH2 domains of PI3-K. The phosphorylated Gab1 can also bind to Grb2, PLC γ , and SHP-2. PI3-K catalyzes the phosphorylation of the 3'-position of inositol in phosphatidylinositol (PLI), PLI 4-

phosphate or PI (4,5)-bisphosphate in vitro (201, 207). The 3`-phosphoinositides produced by PI3-K may have a second messenger function. EGF also activates another pathway, which involves activation of the non-receptor tyrosine kinases called Jak and the latent cytoplasmic transcription factors called STAT (Signal Transducer and Activator of Transcription). The Jak-STAT pathway was originally identified as being interferon-induced. STAT is tyrosine-phosphorylated by activated Jak, which associates with the ligand-receptor complex and then STAT moves into the nucleus where it stimulates the transcription of those target genes.

1.7.2.1. NEUROTROPHIC PROPERTIES OF EGF.

EGF promotes the neurite outgrowth and cell survival of cultured cerebral, subneocortical telencephalic and cerebellar neurons (201). It has also demonstrated prevention of high oxygen induced apoptosis in the cultured cerebral cortical neurons (210). Not only under normal culture conditions but also under pathologic conditions in vitro, EGF has been shown to protect cortical neurons against anoxia-induced damage and to attenuate the neurotoxicity of potassium cyanide or NMDA on cultured neurons (211, 212). Pre-treatment of cultured hippocampal neurons with EGF prevented nitric oxide induced neuronal damage (213). These in vitro findings raise the possibility that EGF subserves an in vivo neuroprotective function in the ischemic brain.

Continuous infusion of EGF into the lateral ventricle of gerbils starting either before or just after a 3-minute forebrain ischemia improved the behavioural score correlated well with the results of subsequent histologic examinations showing the suppression by EGF of delayed neuronal death in the hippocampal CA1 field (214). These results suggest that

EGF can act as a neuroprotective agent in brain ischemia. Although EGF has been known as a neuroprotective agent in vitro, this result shows that EGF can protect hippocampal neurons against ischemia-induced damage in vivo. The mechanism(s) by which EGF prevents delayed neuronal death in vivo is not well elucidated. The ability of EGF to protect oxidative injuries and to suppress accumulation of lipid peroxides may account partly for the mechanism of action. On the other hand, EGF rescued neurons from anoxic injury in vitro and under the anoxic environment; the enhancement of anti-oxidant enzymes by EGF may not be considered to be responsible for the neuroprotective effect (211). This clearly demonstrates that multiple pathways are involved in EGF mediated neuroprotection and the anti-anoxic action of EGF may play a significant role in rescuing ischemic neurons together with the anti-oxidant activity.

1.7.3. THE PIGMENT EPITHELIUM DERIVED FACTOR.

SERPINS (SERine Protease INhibitors) are the largest and most broadly distributed superfamily of protease inhibitors (215). To date, over 1,500 members of this family have been identified which include 36 human proteins, as well as molecules in plants, fungi, bacteria, archaea and viruses. The SERPIN family encodes two groups of proteins. The first group comprises the predominant family of protease inhibitors in mammals and regulates cascades such as inflammation, blood coagulation and extracellular matrix remodelling (216). The second group represents a substantial number of proteins which are not thought to be inhibitors of specific proteases but rather perform diverse functions such as hormone transporters, molecular chaperones or tumor suppressors (217).

Interestingly, although the function of SERPINs varies widely, these molecules share a common structure. All typically have three β -sheets (termed A, B, and C) and eight or nine α -helices (hA-hI) (Figure 8). SERPINs also possess an exposed region termed the Reactive Center Loop (RCL) that in inhibitory molecules includes the specificity determining region and forms the initial interaction with the target protease.

Pigment epithelium-derived factor (PEDF) is a 50 kDa secreted glycoprotein that belongs to the non-inhibitory SERPIN group (218). PEDF was first identified in 1987 in conditioned medium from foetal human Retinal Pigment Epithelium (RPE) cell cultures (219). PEDF is widely expressed in the nervous system but has been studied most intensively in the retina. Using a bioactivity assay, PEDF was later purified and found to be a protein that migrated as a closely spaced doublet of bands at 50 kDa in polyacrylamide gels (175). Early studies of human fetal and bovine eyes detected PEDF expression in the RPE cells of the retina and in the matrix between the RPE layer and the adjacent photo receptors (220-222).

An analysis of adult human brain and spinal cord showed significant levels of the PEDF transcript in most regions of the nervous system (220, 223, 224). In adult human, monkey and rat spinal cords, PEDF protein and mRNA were detected in motor neurons of the ventral horn and in some neurons in the dorsal horn. Ependymal cells are probably an important source of PEDF in the human CerebroSpinal Fluid (CSF), indicating that, like the retina, much of the brain might be bathed in this NTF (223). PEDF is also expressed in several non-neural tissues including skeletal muscle, bone, heart, placenta and liver (224). This is not surprising, as many growth factors that are essential for neural development are also found outside the nervous system (225).

1.7.3.1. STRUCTURAL PROPERTIES OF PEDF.

The human PEDF gene spans about 16 kb of Deoxyribo Nucleic Acid (DNA) and contains 8 exons and a 5' flanking region that is unusual because it contains a dense cluster of *ALU* repeats (224). The PEDF promoter region contains several key regulatory elements including a retinoic acid receptor motif. The PEDF gene was mapped to human chromosome 17p13, a hot spot for many retinal degenerative diseases that are characterized by loss of photoreceptor function and subsequent visual impairment such as retinitis pigmentosa, lebers congenital amaurosis and a type of cone-rod dystrophy (224, 226, 227).

The PEDF gene encodes a 418 amino acid protein with a hydrophobic signal that is characteristic of secreted proteins with a calculated molecular weight of 46.3 kDa (228). PEDF contains a single carbohydrate side chain that increases its apparent molecular weight to the 50 kDa doublet that is seen on polyacrylamide gels. PEDF has structural and sequence homology to members of the SERPIN family of proteinase inhibitors and contains an RCL that is characteristic of this family (228). However, PEDF does not have inhibitory activity against many proteinases possibly owing to differences in the sequence of the RCL (228, 229). Moreover, the RCL in PEDF is unusual because it is exposed in the native state so that the central region is largely uncovered, a feature that might allow its rapid binding to regulatory proteins (Figure 8).

The neurotrophic domains of PEDF have not been fully defined yet. A 44-amino-acid fragment of PEDF, corresponding to positions 78-121, has neuroprotective activity on motor neurons, whereas an adjacent 34-amino-acid peptide, corresponding to positions 44-77 does not (223). Whether the entire 44-amino-acid fragment is required for the

neurotrophic activity of PEDF or regulates the same pathways as the full-length protein is still unclear.

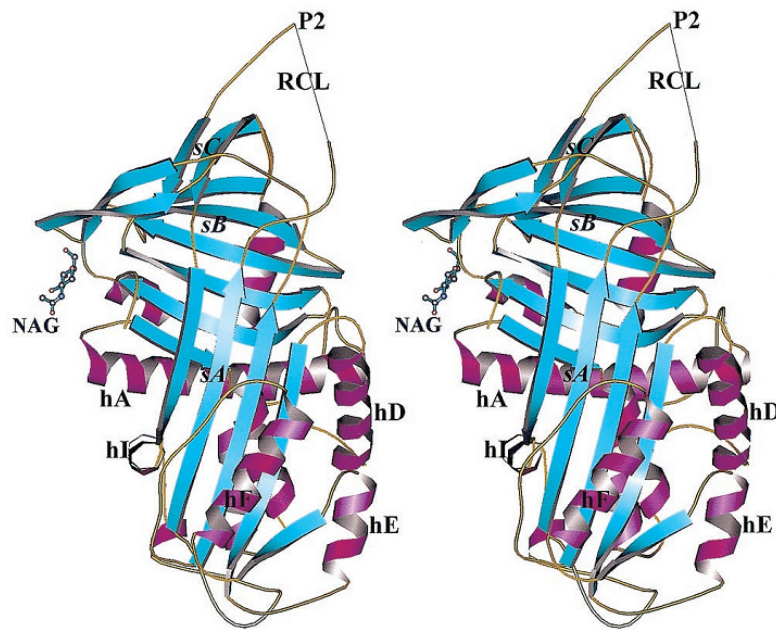


Figure 8. Stereo view ribbon diagram of glycosylated PEDF in the native typical SERPIN orientation. β -strands are cyan (sA–C), α -helices are magenta and listed in order (hA, hD–F, hI), coils and turns are gold, and the carbohydrate residue is represented as ball-and-sticks. The reactive center loop is labeled as RCL, and N-acetylglucosamine is labeled as NAG. Adapted from reference (229).

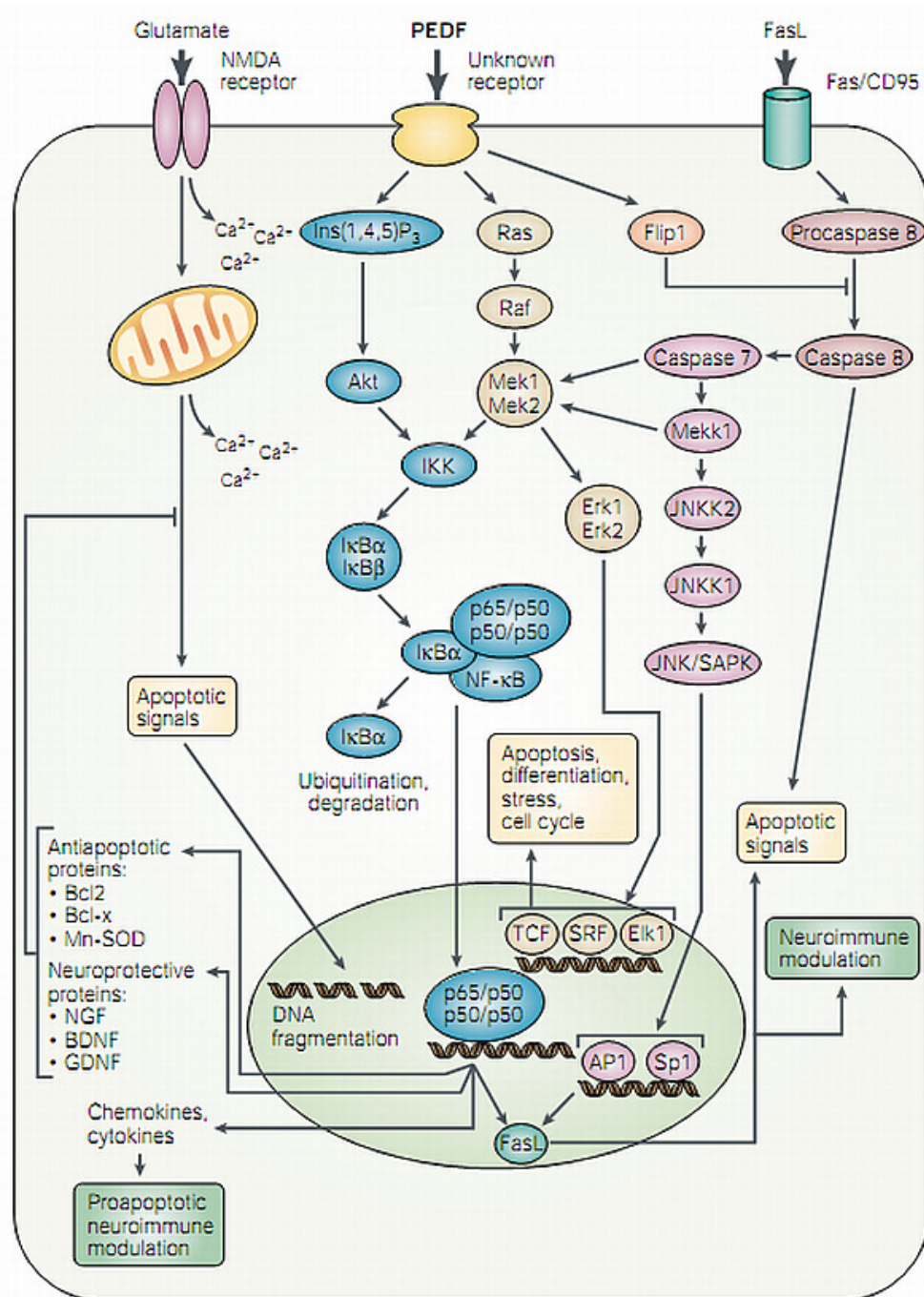
1.7.3.2. BINDING AND SIGNAL TRANSDUCTION.

Like most other growth factors, PEDF presumably binds to cell surface receptors and triggers a cascade of intracellular events, which culminate in target gene regulation and activity. Radiolabelled [125 I] PEDF binds to a single class of binding sites on retinoblastoma and cerebellar granule cells with K_d values of 1.7–3.6 nM and 3.2 nM, respectively, indicating that the activity of PEDF might be mediated by its interaction with a single receptor type (230). In addition, a single class of binding sites was detected with a K_d of 2.5–6.5 nM on retinal membranes (231). A recent study showed that PEDF promotes activation of NF- κ B, a transcription factor that in turn induces the expression of antiapoptotic genes and/or NTFs in cerebellar granule cells (232).

PEDF triggers increased phosphorylation of the Inhibitor of NF- κ B (I κ B)- α , decreased levels of I κ B proteins, activation of NF- κ B, nuclear translocation of p65 (RelA) and increased NF- κ B DNA binding activity as part of its mechanism to protect immature cerebellar granule cells against apoptosis induced by low K⁺ (232). PEDF induces an increase in the anti-apoptotic proteins Bcl2 and Bcl-x, and in superoxide dismutase only in immature cerebellar granule cells, whereas it induces increased expression of NGF, BDNF and GDNF in both immature and mature cerebellar granule cells (232).

An important pathway that can lead to apoptotic cell death is initiated by the interaction between the Fas Ligand (FasL) and its receptor, Fas/CD95 (Figure 9). It was recently shown that PEDF increases the expression of FasL and activates a transduction cascade that promotes endothelial cell death (233). Fas/CD95 is a member of the TNF super family of receptors and is activated by FasL to transmit apoptotic signals. Neutralizing antibodies to Fas and FasL, and application of the caspase inhibitors zVAD-fmk (N-benzylocarbonyl-Val-Ala-Asp-fluoromethylketone) and DEVD-CHO (N-acetyl-Asp-Glu-Val-Asp-aldehyde) abrogated the apoptotic effects of PEDF on cultured endothelial cells in the presence of the proangiogenic stimulator bFGF.

Specifically, interfering with the activation of caspase 8 and 3, two essential transducers of the Fas/FasL death cascade, restricted the effects of PEDF on endothelial cells and halted their progression toward apoptosis. It was also shown that PEDF eliminated the VEGF induced up regulation of Flip1, a factor that interferes with caspase 8 activation and increases resistance to the apoptotic effects of FasL. It is interesting that NF- κ B also upregulates Flip1, and that Flip1 in turn promotes the activation of NF- κ B and the ERK signalling cascades (234, 235).



Mn-SOD; manganese-superoxide dismutase, NGF; nerve growth factor, BDNF; brain derived neurotrophic factor, GDNF; glial derived nerve factor, Ins(1, 4, 5)P₃; inositol-tri-phosphate, IKK; IκB Kinase, MEK; mitogen activated protein kinase kinase, ERK; extra-cellular signal regulated kinase, MEKK; mitogen ERK kinase kinase, JNKK; c-Jun N-terminal kinase kinase, SAPK; stress activated protein kinase.

Figure 9. Transduction pathways activated by pigment epithelium derived factor. Adapted from reference (175).

Although activation of NF- κ B is primarily associated with the prevention of neuronal cell death, it might also lead to apoptosis, possibly through the induction of FasL, the gene of which contains NF- κ B binding sites in its promoter (236, 237).

1.7.3.3. TROPHIC PROPERTIES OF PEDF.

The first studies of PEDF noted that it promoted the transformation of dividing retinoblastoma cells into differentiated neurons (219). Labelling of cerebellar granule cell cultures with 5-bromodeoxyUridine (BrdU) showed that PEDF did not affect proliferation of these neurons (238). So, unlike other growth factors, PEDF does not seem to be mitogenic but promotes cell differentiation. In chick spinal cord cultures, PEDF exerts a strong neurotrophic effect, enhancing both cell survival and length of neurites at concentrations as low as 0.1 nM (239). On the other hand, although similarly low concentrations of PEDF enhance the survival of cerebellar granule cells in culture, they did not have any effects on neurite out growth (240).

1.7.3.4. NEUROPROTECTIVE PROPERTIES OF PEDF.

PEDF at low nanomolar concentrations significantly prevents glutamate-induced apoptotic cell death in cultures of cerebellar granule cells, hippocampal neurons and spinal motor neurons (238-241). Whether PEDF alters the sensitivity of glutamate receptors, the intracellular movements of calcium or the downstream response of mitochondria to glutamate is still not known. In addition to experiments in culture, there is evidence that PEDF provides substantial protection to neurons in vivo. In neonatal mice, sciatic nerve section leads to death of about 50% of motor neurons and atrophy of many of the surviving

cells. Application of PEDF at the axotomy site reduces motor neuron death by 57% and completely prevents atrophy of the surviving neurons (239).

Similar results have been obtained in an organotypic rat spinal cord culture model of chronic glutamate toxicity. In this case, nanomolar concentrations of PEDF were effective in decreasing motor neuron degeneration as measured morphologically or by the expression of the enzyme choline acetyltransferase which is expressed by motor neurons (175). In this model, motor neuron processes are also remarkably well preserved by PEDF in the presence of the glutamate transport inhibitor D, L-threo- β -hydroxyaspartate. It is worth noting that the potency of PEDF is comparable to that of gabapentin, riluzole and IGF1, all of which have been tested for neuroprotective efficacy in this model and have been proposed to be clinically useful to treat chronic motor neuron diseases.

PEDF has also demonstrated the protection of rat rod photoreceptors from degenerating after exposure to constant light (242). The effect is as potent as that reported for BDNF and CNTF, two well-characterized NTFs that are active in the retina (243). In a different model in which cells were exposed to the oxidative damage of hydrogen peroxide, cell death was significantly reduced in dissociated cell cultures treated with PEDF (244). PEDF has also been shown to protect retinal neurons from damage caused by increased intraocular pressure from transient ischemic reperfusion (245). Together, the culture and animal studies support the neuroprotective role of PEDF in both acute and chronic forms of neurodegeneration. Increased pressure within the eye is a main risk factor for glaucoma and its associated ganglion cell death. Experimental pressure-induced ischaemia and subsequent reperfusion leads to extensive retinal cell death in the absence of PEDF.

1.7.3.5. PEDF AS A POTENT ANTI-ANGIOGENIC FACTOR.

Another facet of the activity of PEDF, one that involves the control of angiogenesis by activating a death pathway, has been the subject of recent intense investigation. An anti-angiogenic role for PEDF in the retina emerged when an earlier study showed that PEDF inhibited angiogenic processes and was more effective than the well-studied angiogenesis inhibitor angiostatin (246). PEDF inhibited endothelial cell migration even in the presence of pro-angiogenic factors such as FGF1, FGF2, VEGF, interleukin-8 and lysophosphatic acid. As PEDF is present in high concentrations in avascular regions of the eye, and RPE cells secrete inhibitors of angiogenesis in culture, this finding is not entirely surprising.

Hypoxia is a strong stimulus for angiogenesis. Under hypoxic conditions in culture, secretion of PEDF is decreased and expression of VEGF, one of the most potent mitogens in angiogenesis, is increased (246). Similar results have been obtained in vivo, showing a decrease in the vitreous level of PEDF in the eyes of patients with proliferative diabetic retinopathy and macular degeneration, conditions in which there is a significant increase in the vascularization of the eye (247, 248). These studies point to a direct correlation between PEDF and the extent of neovascularization in the eye. They also show a shift in the equilibrium between PEDF and VEGF in the uncontrolled growth of blood vessels in the eye. The mechanisms by which PEDF reduces the growth of new blood vessels seem to involve endothelial cell death through the activation of the Fas / FasL death pathway, which is particularly sensitive in endothelial cells that line newly, formed vessels (233).

Proliferating endothelial cells are the only targets identified so far in which PEDF promotes cell death. This might be due to a unique type of receptor on endothelial cells or to the regulation of different signal transduction pathways by PEDF. The effects of PEDF on angiogenesis in the retina have significant consequences to the survival and function of

retinal neurons, which would otherwise degenerate in an environment that is permissive to the growth of leaky blood vessels. Whether, PEDF has a similar role in other areas of the nervous system is worthy of further investigation.

2.0. Introduction. Part II.

2.1. ELEMENTARY CONCEPTS OF NUCLEAR MAGNETIC RESONANCE IMAGING.

2.1.1. ESTABLISHMENT OF A NET MAGNETIZATION.

Magnetic Resonance (MR) is based upon the interaction between an applied external magnetic field and a nucleus that possesses a spin. Nuclear spin is an intrinsic property of an atom and is characteristic of the precise atomic composition. Every element in the periodic table except argon and cerium has at least one naturally occurring isotope that possesses spin. In principle, nearly every element (except argon and cerium) has a naturally occurring isotope that possesses a spin and can be examined using MR. The basic idea of resonance absorption and relaxation are common to all of these elements even though the precise details will vary from nucleus to nucleus and from system to system.

Atoms consist of three fundamental particles: protons, possessing a positive charge; neutrons, with no charge; and electrons with a negative charge. The protons and neutrons are located in the nucleus of an atom, whereas the electrons are confined in shells or orbitals surrounding the nucleus. The properties most commonly used to categorize elements are their atomic number and weight. Atomic number represents the number of protons in the nucleus, whereas, the atomic weight is the sum of the number of protons and the number of neutrons. Atoms with the same atomic number but different atomic weights constitute the isotopes. A third property of the nucleus is its spin or in other words its intrinsic spin angular momentum. The nucleus can be considered to be constantly rotating

about an axis at a constant velocity. This self-rotation axis is perpendicular to the direction of rotation (Figure 10).

In nature, the spin (I), is quantized to certain discrete values. These values depend on the atomic number and weight of the particular nucleus. There can be three sets of values for I : zero, half-integral, and integral values. A nucleus will not have a spin ($I = 0$) if it possesses an even atomic weight and atomic number. Such a nucleus will remain unaffected by an external magnetic field and cannot be studied using the principle of MR.

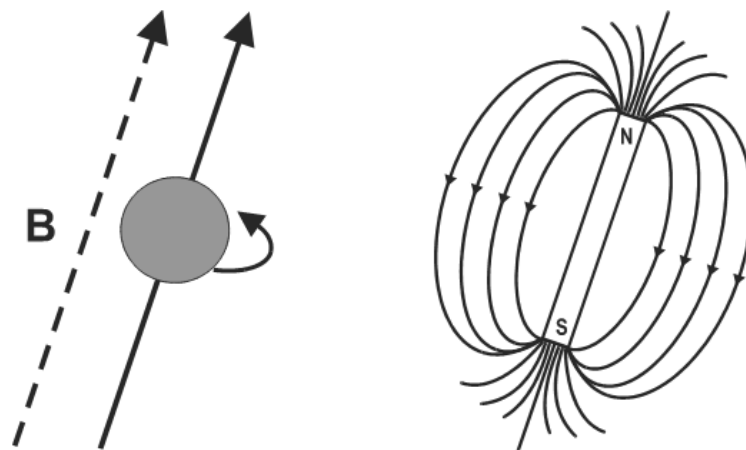


Figure 10. A rotating nucleus with a positive charge produces a magnetic field known as the magnetic moment B oriented parallel to the axis of rotation (left side of figure). This arrangement is analogous to that of a bar magnet in which the magnetic field is considered to be oriented from the south to the north pole (right side).

A nucleus will have an integral value for I (e.g., 1, 2, 3) if it has an even atomic weight and an odd atomic number. A nucleus has a half-integral value for I (e.g., $1/2$, $3/2$, $5/2$) if it has an odd atomic weight. Table 3 summarizes the spin and isotopic composition of some elements commonly found in biological systems. The ^1H nucleus, consisting of a single proton, is a natural choice for probing the body using MR techniques for a number of reasons. It possesses a spin of $1/2$ and is the most abundant isotope for hydrogen. Its response to an applied external magnetic field is one of the largest found among elements.

Finally, the human body is composed of tissues that contain plentiful of water and fat which in turn contain hydrogen.

Element	Protons	Neutrons	Nuclear Spin I	Gyromagnetic ratio (β) Mhz T ⁻¹	Natural abundance (%)	ω at 1.5 T (MHz)
¹ H, protium	1	0	1/2	42.57	99.99	63.86
² H, Deuterium	1	1	1	6.54	0.015	9.8
³ He	2	1	1/2	32.44	0.000138	48.7
⁶ Li	3	3	1	6.3	7.5	9.399
⁷ Li	3	4	3/2	16.54	92.5	24.82
¹² C	6	6	0	0	98.9	0
¹³ C	6	7	1/2	10.71	1.10	16.06
¹⁴ N	7	7	1	3.08	99.63	4.62
¹⁵ N	7	8	1/2	4.32	0.37	6.5
¹⁶ O	8	8	0	0	99.63	4.62
¹⁷ O	8	9	5/2	5.77	0.038	8.66
¹⁹ F	9	10	1/2	40.08	100	60.11
²³ Na	11	12	3/2	11.27	100	16.9
³¹ P	15	16	1/2	17.25	100	25.88
¹²⁹ Xe	54	75	1/2	11.86	26.4	17.8

Table 3. Constants for selected nuclei of biological interest.

In addition to spin, the positively charged nucleus also generates a local magnetic field or magnetic moment. This inherent magnetic moment is fundamental to MR. A nucleus with spin has an axis of rotation that can be viewed as a vector with a definite orientation and magnitude (Figure 10). The magnetic moment of the nucleus is oriented parallel to the axis of rotation. This orientation of the nuclear spin and the changes induced in it due to the experimental manipulations that the nucleus undergoes provide the basis for the MR signal.

As an example, consider an arbitrary volume of tissue containing hydrogen atoms (protons). Each proton has a spin vector of equal magnitude. However, since the spin vectors of the entire collection of protons within the tissue are randomly oriented in all directions, performing a vector addition of these vectors produces only a zero sum. That is, no net magnetization is observed in the tissue (Figure 11). If the tissue is placed inside a magnetic field \mathbf{B}_0 (vector quantity with both direction and magnitude), the individual protons begin to rotate perpendicular to, or to precess about, the magnetic field.

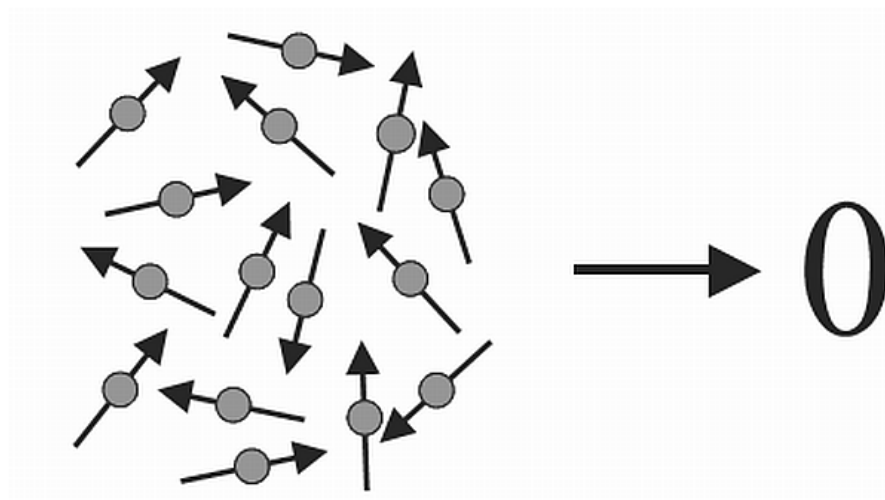


Figure 11. A collection of protons in the absence of an external magnetic field. The protons have their spin vectors oriented randomly and the vector sum of these spin vectors is zero.

The protons are tilted slightly away from the axis of the magnetic field, but the axis of rotation still remains parallel to \mathbf{B}_0 . This precession is at a constant rate and occurs due to the interaction of the magnetic field with the spinning positive charge of the nucleus. By convention, \mathbf{B}_0 and the axis of precession are defined to be oriented along the z direction of a Cartesian coordinate system. The motion of each proton can be described by a unique set of coordinates perpendicular (x and y) and parallel (z) to \mathbf{B}_0 . The perpendicular or transverse, coordinates (x and y) are non-zero and vary with time as the proton precesses, but the z coordinate is constant with respect to time (Figure 12). The rate or frequency of precession is proportional to the strength of the externally applied magnetic field and is expressed with the Larmor equation as follows: $\omega_0 = \gamma B_0 / 2\pi$.

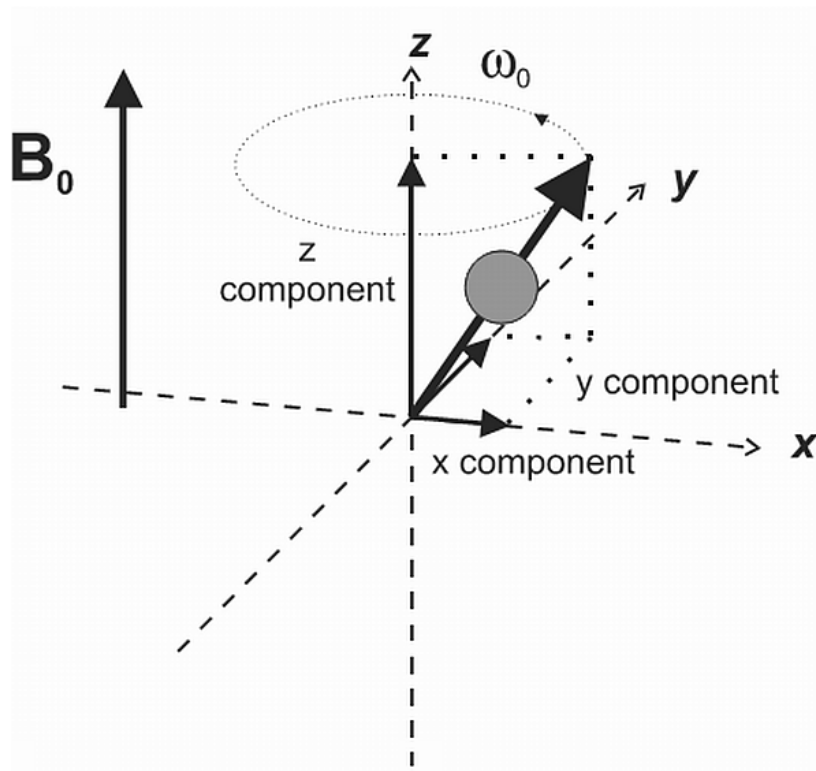


Figure 12. Inside a magnetic field, a proton precesses or revolves about the magnetic field. The precessional axis is parallel to the main magnetic field \mathbf{B}_0 . The z component of the spin vector (projection of the spin onto the z axis) is the component of interest because it does not change in magnitude or direction as the proton precesses.

where ω_0 is the Larmor frequency in megahertz (MHz), \mathbf{B}_0 is the magnetic field strength in Tesla (T) which the proton experiences, and γ is a constant for each nucleus in $\text{s}^{-1}\text{T}^{-1}$, known as the gyromagnetic ratio. Values for γ and ω at 1.5 T for several nuclei are tabulated in Table 3. If a vector addition is performed for the spin vectors inside the magnetic field, the results will be slightly different than for the sum outside the field. In the direction perpendicular to \mathbf{B}_0 , the spin orientations are still randomly distributed just as they were outside the magnetic field. In spite of the time-varying nature of each transverse component there is still no net magnetization perpendicular to \mathbf{B}_0 . However, in the direction parallel to the magnetic field, results are different. Since, there is an orientation to the precessional axis of the proton that is constant with time; there is a constant, nonzero interaction or coupling between the proton and \mathbf{B}_0 known as the Zeeman interaction. This coupling causes a difference in energy between protons aligned parallel to or along \mathbf{B}_0 and protons aligned anti-parallel to or against \mathbf{B}_0 . This energy difference ΔE is proportional to \mathbf{B}_0 (Figure 13).

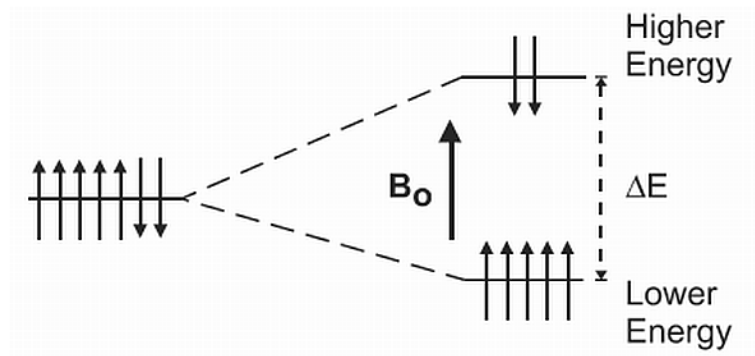


Figure 13. Zeeman diagram. In the absence of a magnetic field (left side of figure), a collection of protons will have the configurations of z components equal in energy so that there is no preferential alignment between the spin up and spin down orientations. In the presence of a magnetic field (right side), the spin up orientation (parallel to \mathbf{B}_0) is of lower energy and its configuration contains more protons than the higher energy, spin down configuration. The difference in energy ΔE between the two levels is proportional to \mathbf{B}_0 .

The result of Zeeman interaction is that spins in the two principal orientations, parallel (also known as spin up) and antiparallel (spin down), have different energies. The orientation that is parallel to \mathbf{B}_0 is of lower energy than the antiparallel orientation. For a collection of protons, more will be oriented parallel to \mathbf{B}_0 than will be oriented antiparallel; that is, there is an induced polarization of the spin orientation by the magnetic field (Figure 14a). The exact number of protons in each energy level is governed by a distribution known as the Boltzmann distribution:

$$N_{\text{upper}} / N_{\text{lower}} = e^{-\Delta\epsilon/kT}$$

where, N_{upper} and N_{lower} are the number of protons in the upper and lower energy levels, respectively, and k is Boltzmann's constant, $1.381 \times 10^{-23} \text{ J K}^{-1}$.

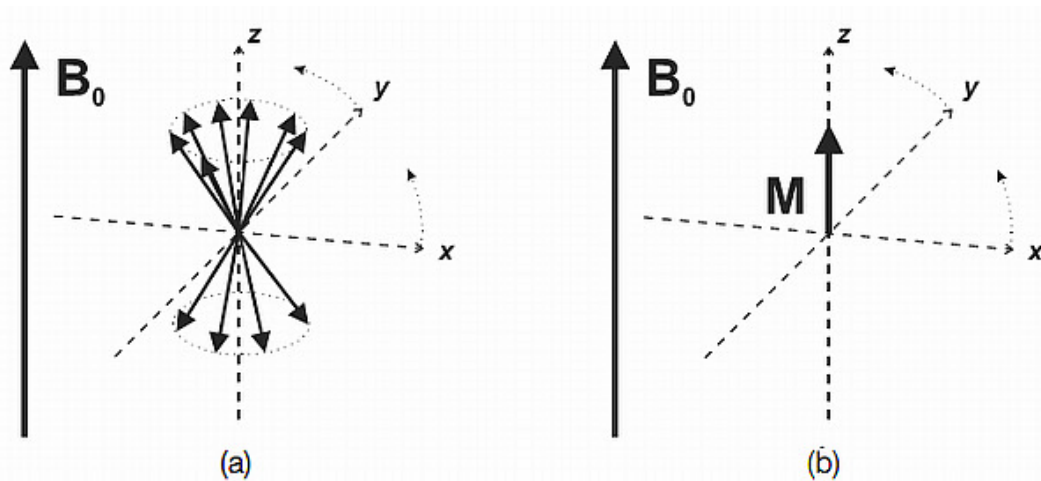


Figure 14. Microscopic (a) and macroscopic (b) pictures of a collection of protons in the presence of an external magnetic field. Each proton precesses about the magnetic field. If a rotating frame of reference is used with a rotation rate of ω_0 , then the collection of protons appears stationary. The z components are one of two values (one positive and one negative), but the x and y components can be any value, positive or negative. The protons will appear to track along two “cones,” one with a positive z component and one with a negative z component. Because there are more protons in the upper cone, there will be a nonzero vector sum M_0 , the net magnetization. It will be of constant magnitude and parallel to \mathbf{B}_0 .

Since the separation between the energy levels ΔE depends on the field strength \mathbf{B}_0 , the exact number of spins at each level will also be dependent upon \mathbf{B}_0 and increases with increasing \mathbf{B}_0 . For a collection of protons at body temperature (310 K) at 1.5 T, there will typically be an excess of $\sim 1:10^6$ protons in the lower level out of the approximately 10^{25} protons within the tissue. This unequal number of protons in each energy level also means that the vector sum of spins will be nonzero and will point parallel to the magnetic field. The tissue can be said to be polarized or magnetized in the presence of \mathbf{B}_0 with a value M_0 , known as the net magnetization. The orientation of this net magnetization will be along the same direction as \mathbf{B}_0 and will remain a constant with respect to time (Figure 14 b). For tissues in the body, the magnitude of M_0 is proportional to \mathbf{B}_0 :

$$M_0 = \chi B_0$$

where χ is known as the bulk magnetic susceptibility or simply magnetic susceptibility. Such a pattern with M_0 aligned along the magnetic field with no transverse component is the normal, or equilibrium, configuration for the protons. This configuration of spins assumes the lowest energy and is the arrangement to which the protons will try to return following any perturbations resulting from energy absorption. This induced magnetization, M_0 , is the source of signal for all of the MR experiments. Consequently, all other things being equal, the greater the applied field strength, the greater the value of M_0 and greater the potential MR signal.

2.1.2. FUNDAMENTAL PRINCIPLES OF NUCLEAR MAGNETIC RESONANCE.

The whole field of MR is based on the manipulation of this net magnetization M_0 , which has been formed as described before. The MR experiment, at its very basis, can be

analyzed in terms of energy transfer. During measurement, the subject or sample is exposed to energy irradiation at the correct frequency that will be absorbed. A short time later, this energy is re-emitted, at which time it can be detected and processed. The simplest and basic manipulation involves application of a short burst, or pulse, of Radio Frequency (RF) energy. This pulse, termed as an excitation pulse, contains many frequencies spread over a narrow range or BandWidth (BW). During the pulse, the protons absorb a portion of this energy at a particular frequency. Following the pulse, the protons reemit the energy at the same frequency.

The particular frequency absorbed is proportional to the magnetic field \mathbf{B}_0 ; the equation relating the two is the Larmor equation, as described previously. The frequency of energy absorbed by an individual proton is defined very precisely by the magnetic field that the proton experiences due to its quantized nature of the spin. When a proton is irradiated with energy of the correct frequency (ω_0), it will be excited from the lower energy (spin up) orientation to the higher energy (spin down) orientation (Figure 15). At the same time, a proton at the higher energy level will be stimulated to release its energy and will go to the lower energy level. The energy difference (ΔE) between the two levels will be exactly proportional to the frequency ω_0 and thus the magnetic field \mathbf{B}_0 :

$$\Delta E = h\gamma B_0 / 2\pi$$

where, h is Planck's constant, 6.626×10^{-34} J s. Only energy at this frequency stimulates transitions between the spin up and spin down energy levels. This quantized energy absorption is known as resonance absorption and the frequency of energy is known as the resonant frequency.

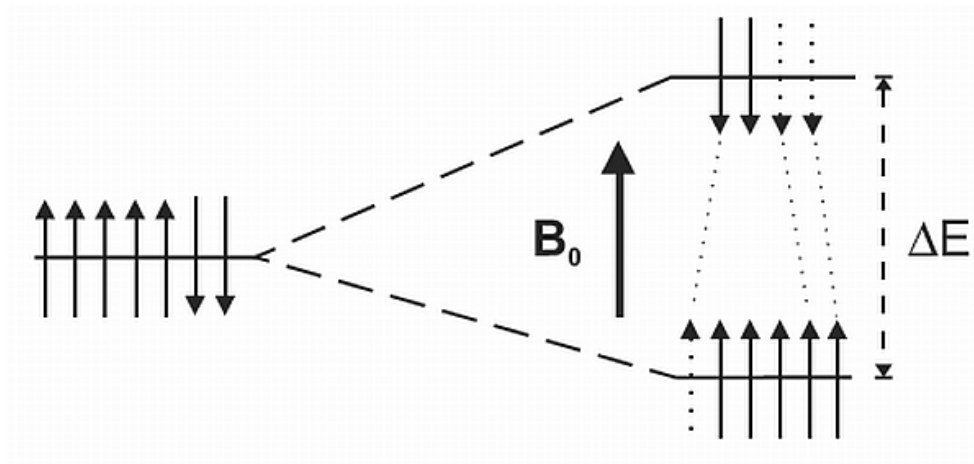


Figure 15. The difference in energy ΔE between the two configurations (spin up and spin down) is proportional to the magnetic field strength \mathbf{B}_0 and the corresponding precessional frequency ω_0 . When energy at this frequency is applied, a spin from the lower energy state is excited to the upper energy state. Also, a spin from the upper energy state is stimulated to give up its energy and relax to the lower energy state. Because there are more spins in the lower energy state, there is a net absorption of energy by the spins in the sample.

For the large number of protons as in a volume of tissue, there is a significant amount of both absorption and emission occurring during the RF pulse. Since, there are more protons at the lower energy level (Figure 15) there will be a net absorption of energy by the tissue. The energy is applied in the form of an RF pulse with a central frequency ω_0 and in an orientation perpendicular to \mathbf{B}_0 , as indicated by the effective field \mathbf{B}_1 (Figure 16). This orientation difference allows the coupling between the RF pulse and \mathbf{M}_0 so that a net energy transfer to the protons takes place. Absorption of RF energy of frequency ω_0 causes \mathbf{M}_0 to rotate away from its equilibrium orientation. The direction of rotation of \mathbf{M}_0 will be perpendicular to both \mathbf{B}_0 and \mathbf{B}_1 . If the transmitter is left on long enough and at a high enough amplitude, the absorbed energy causes \mathbf{M}_0 to rotate entirely into the transverse plane, a result of a 90° pulse.

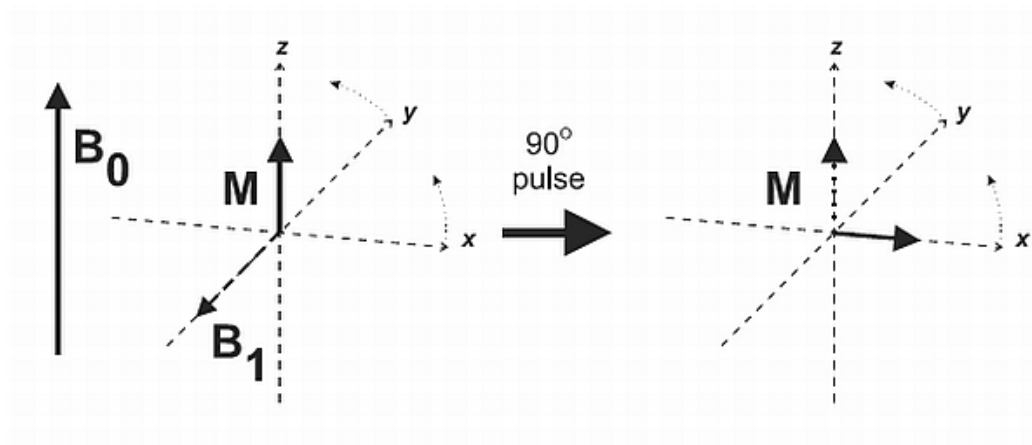


Figure 16. In a rotating frame of reference, the RF pulse broadcast at the resonant frequency ω_0 can be treated as an additional magnetic field \mathbf{B}_1 oriented perpendicular to \mathbf{B}_0 . When energy is applied at the appropriate frequency, the protons absorb it and M rotates into the transverse plane. The direction of rotation is perpendicular to both \mathbf{B}_0 and \mathbf{B}_1 . The amount of resulting rotation of M is known as the pulse flip angle.

When the transmitter is turned off, the protons immediately begin to realign themselves and return to their original equilibrium orientation by emitting energy at the frequency ω_0 . In addition, the net magnetization will begin to precess about \mathbf{B}_0 , similar to the behavior of a gyroscope when tilted away from a vertical axis. If a loop of wire (a receiver coil) is placed perpendicular to the transverse plane, the protons induce a voltage in the wire during their precession. This induced voltage, the MR signal, is known as the FID or Free Induction Decay (Figure 17a). The initial magnitude of the FID signal depends on the value of M_0 immediately prior to the 90° pulse. The FID decays with time as more and more protons give up their absorbed energy through a relaxation process and the coherence of the proton motion is lost. In general, three aspects of an MR signal are of interest: its magnitude or amplitude, its frequency, and its phase relative to the RF transmitter phase (Figure 18). As mentioned previously, the signal magnitude is related to the value of M_0 immediately prior to the RF pulse.

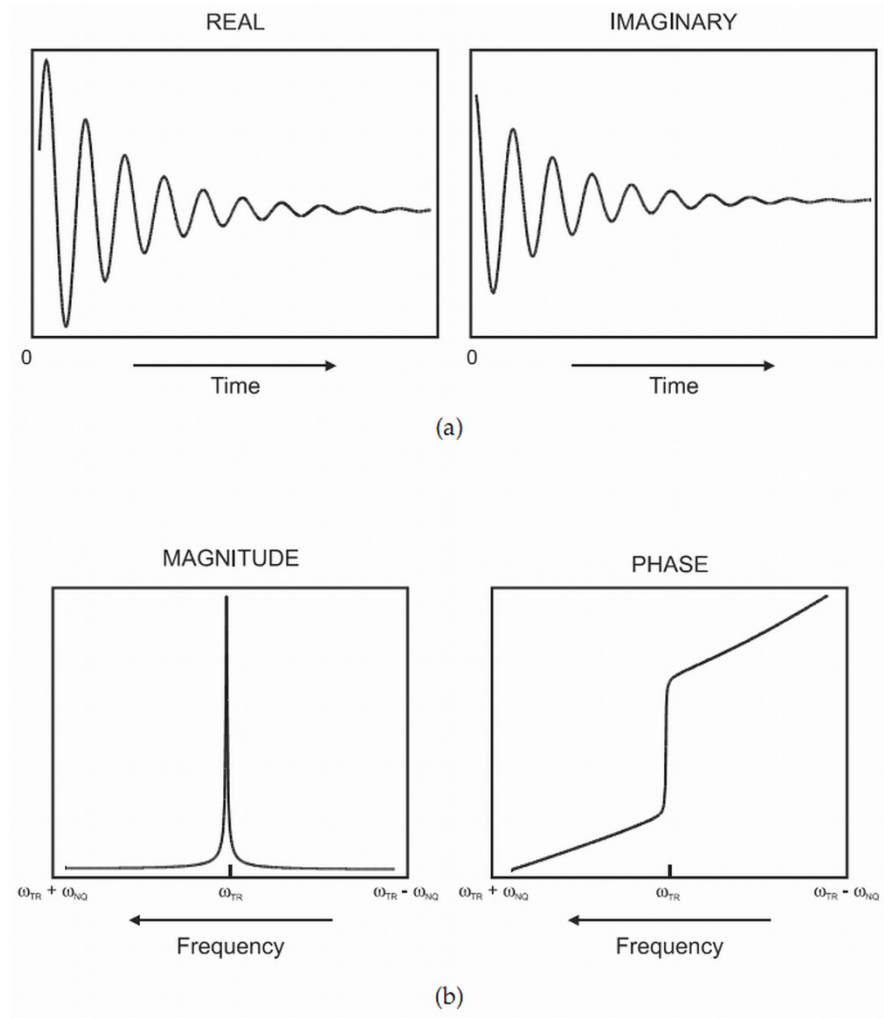


Figure 17 (a) Free induction decay, real and imaginary. The response of the net magnetization M to an RF pulse as a function of time is known as the free induction decay or FID. It is proportional to the amount of transverse magnetization generated by the pulse. The FID is maximized when using a 90° excitation pulse. (b) Fourier transformation of (a), magnitude and phase. The Fourier transformation is used to convert the digital version of the MR signal (FID) from a function of time to a function of frequency. Signals measured with a quadrature detector are displayed with the transmitter (reference) frequency TR in the middle of the display. The Nyquist frequency (NQ) below and above TR are the minimum and maximum frequencies of the frequency display, respectively. For historical reasons, frequencies are plotted with lower frequencies on the right side and higher frequencies on the left side of the display.

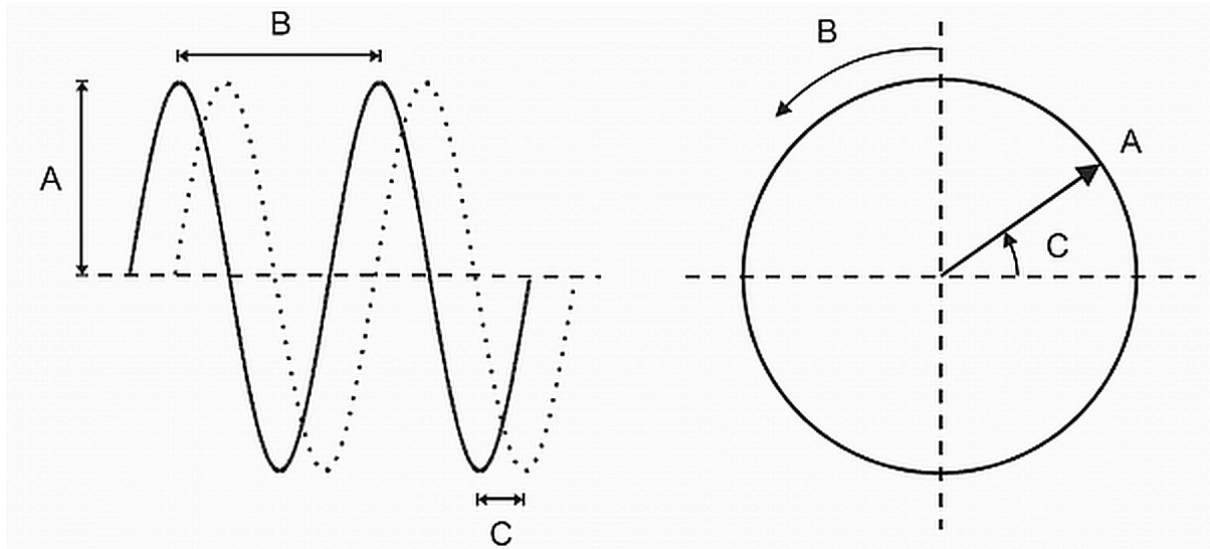


Figure 18. Planar and circular representations of a time-varying wave. The amplitude (A) is the maximum deviation of the wave from its mean value. The period (B) is the time required for completion of one complete cycle of the wave. The frequency of the wave is the reciprocal of the period. The phase or phase angle of the wave (C) describes the shift in the wave relative to a reference (a second wave for the planar representation, horizontal axis for circular representation). The two plane waves displayed have the same amplitude and period (frequency), but have a phase difference of $\pi/4$ or 90° .

The signal frequency is related to the externally applied magnetic field influencing the protons. If all the protons experience the same magnetic field \mathbf{B}_0 , then only one frequency would be present within the FID. In reality, there are many magnetic fields throughout the magnet, and thus many MR signals at many frequencies following the RF pulse. These signals are superimposed so that the FID contains many frequencies varying as a function of time. It is easier to examine such a multicomponent signal in terms of frequency rather than of time. The conversion of the signal amplitudes from a function of time to a function of frequency is accomplished using a mathematical operation called the Fourier transformation.

2.1.3. RELAXATION CHARACTERISTICS.

As mentioned before, the MR measurement can be analyzed in terms of energy transfer. Relaxation is the process by which protons release the energy that they absorbed from the RF pulse. Relaxation is a fundamental process in MR, as indispensable as energy absorption, and in turn provides the primary mechanism for image contrast. In resonance absorption, RF energy can be absorbed by the protons only when it is broadcast at the correct frequency. The additional energy simply disturbs the equilibrium arrangement of spins parallel and anti-parallel to \mathbf{B} . Following excitation, relaxation occurs when the protons release this absorbed energy and return to their original configuration through naturally occurring processes. Although individual protons absorb the energy, relaxation times are measured for the entire sample and are statistical or average measurements. Two relaxation times namely T_1 and T_2 can be measured and is of principal interest. Both times measure the spontaneous energy transfer by an excited proton, but they differ in the final disposition of the energy.

2.1.3.1. T_1 RELAXATION.

The T_1 relaxation time is the time required for the z component of \mathbf{M} to return to 63% of its original value following an excitation pulse. It is also known as the spin-lattice relaxation time or longitudinal relaxation time.

It has been mentioned earlier, that \mathbf{M}_0 is parallel to \mathbf{B}_0 at equilibrium and that energy absorption result in the rotation of \mathbf{M}_0 into the transverse plane. T_1 relaxation provides a mechanism by which the protons give up their energy to return to their original orientation. If a 90° pulse is applied to a sample, \mathbf{M}_0 will rotate as illustrated in Figure 16, and there

will be no longitudinal magnetization present following the pulse. As time goes on, a return of the longitudinal magnetization will be observed as the protons release their energy (Figure 19).

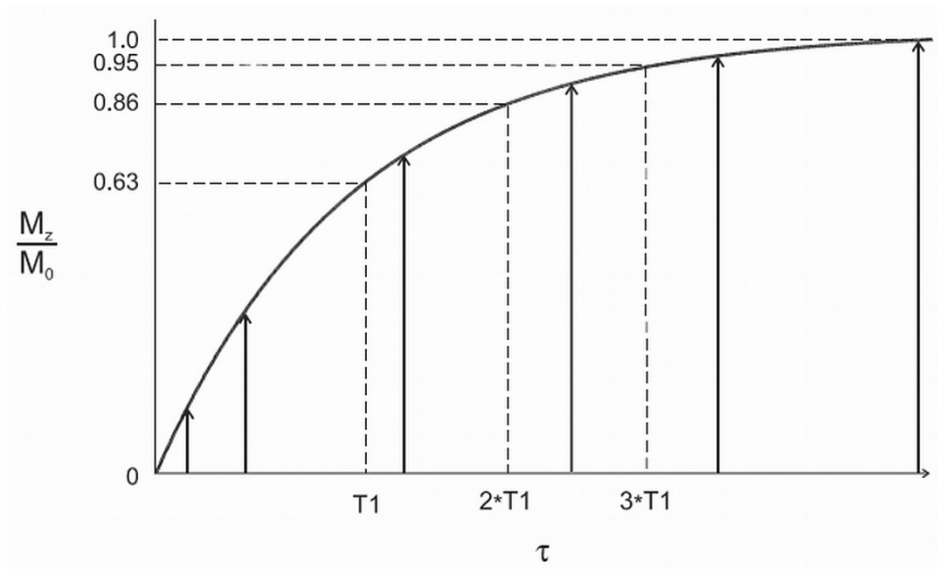


Figure 19. T_1 relaxation curve. Following a 90° RF pulse, there is no longitudinal magnetization. A short time later, longitudinal magnetization will be observed as the protons release their energy through T_1 relaxation. Gradually, as more protons release their energy, a larger fraction of M_z is reestablished. Eventually, M_0 will be restored completely. The change of M_z/M_0 with time follows an exponential growth process. The time constant for this process is T_1 , the spin-lattice relaxation time, and is the time when M_z has returned to 63% of its original value.

This return of magnetization follows an exponential growth process, with T_1 being the time constant describing the rate of growth:

$$M(\tau) = M_0(1 - e^{-\tau/T_1})$$

where τ is the time following the RF pulse. After three T_1 time periods, M will have returned to 95% of its value prior to the excitation pulse, M_0 . The term spin lattice refers to the fact that the excited proton (“spin”) transfers its energy to its surroundings (“lattice”)

rather than to another spin. Such a transfer of energy no longer contributes to spin excitation.

In a modern MR experiment, pulsed RF energy is applied to the protons repeatedly with a certain delay time between the excitation pulses. This time between pulses allows the excited protons to give up the absorbed energy (T_1 relaxation). As the protons give up this energy to their surroundings, the population difference (spin up versus spin down) is re-established so that net absorption can reoccur after the next pulse. In the macroscopic picture, \mathbf{M} returns toward its initial value \mathbf{M}_0 as more energy is dissipated. Since \mathbf{M} is the ultimate source of the MR signal, the more energy that is dissipated, the more signal that will be generated following the next RF pulse. In practice, the time between successive RF pulses is usually insufficient for complete T_1 relaxation so that \mathbf{M} will never be completely restored to \mathbf{M}_0 . Application of a second RF pulse prior to complete relaxation will rotate \mathbf{M} into the transverse plane, but with a smaller magnitude than following the first RF pulse. The following sketch describes the situation (Figure 20):

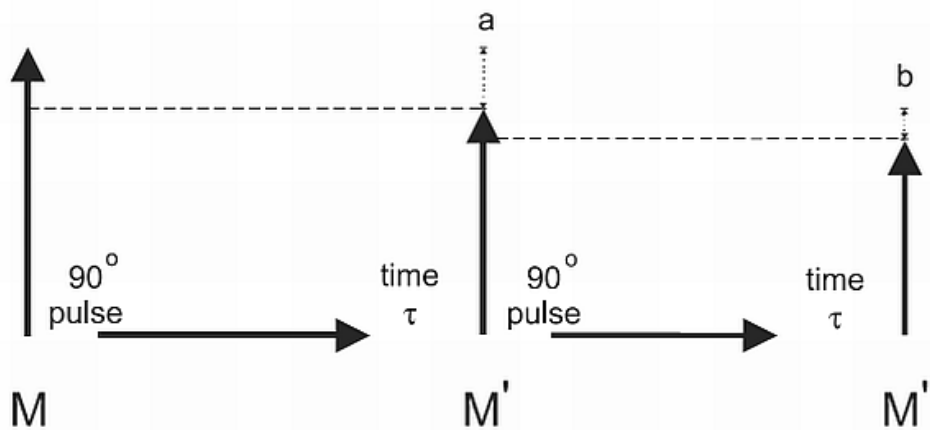


Figure 20. Following a 90° RF pulse, longitudinal magnetization is regenerated via T_1 relaxation. If the time between successive RF pulses τ is insufficient for complete recovery of \mathbf{M} , then only \mathbf{M}' will be present at the time of the next RF pulse (a). If time τ elapses again, then only \mathbf{M}'' will be present (b). \mathbf{M}'' will be smaller than \mathbf{M}' , but the difference will be less than the difference between \mathbf{M} and \mathbf{M}' .

1. A 90° RF pulse is applied. \mathbf{M} is rotated into the transverse plane.
2. A time τ elapses, insufficient for complete T_1 relaxation. The longitudinal magnetization at the end of τ , \mathbf{M}' , is less than in step 1.
3. A second 90° RF pulse is applied. \mathbf{M}' is rotated into the transverse plane.
4. After a second time τ elapses, \mathbf{M}'' is produced. It is smaller in magnitude than \mathbf{M}' , but the difference is less than the difference between \mathbf{M} and \mathbf{M}' .

Following few repetitions, \mathbf{M} returns to the same magnitude prior to each RF pulse; i.e., \mathbf{M} achieves a steady-state value. In general, this steady-state value depends on five parameters:

1. The main magnetic field \mathbf{B}_0 . The larger the value for \mathbf{B}_0 , larger will be the \mathbf{M} .
2. The number of protons producing \mathbf{M} (per unit volume of tissue, known as the proton density).
3. The amount of energy absorbed by the protons (the pulse angle or flip angle).
4. The rate of RF pulse application (time τ).
5. The efficiency of the protons in giving up their energy (T_1 relaxation time).

For many MRI experiments such as standard spin-echo and gradient-echo imaging, a steady state of \mathbf{M} is present because multiple RF pulses are applied and the repetition time (TR) between the pulses is nearly always less than sufficient for complete relaxation. To produce this steady state prior to data collection, additional RF pulses are applied to the tissue immediately prior to the main imaging pulses. These extra RF pulses are known as preparatory pulses or dummy pulses because the generated signals are usually ignored.

These preparatory pulses ensure that \mathbf{M} has the same magnitude prior to every measurement during the scan.

2.1.3.2. T_2 AND T_2^* RELAXATION AND FORMATION OF SPIN ECHOES.

The relaxation time T_2 is defined as the time required for the transverse component of \mathbf{M} to decay to 37% of its initial value via irreversible processes. It is also known as the spin-spin relaxation time or transverse relaxation time. At equilibrium \mathbf{M}_0 is oriented only along the z (\mathbf{B}_0) axis and that no portion of \mathbf{M}_0 is in the xy plane. The coherence is entirely longitudinal. The energy transmitted through a 90° RF pulse, as in Figure 16, causes \mathbf{M}_0 to rotate entirely into xy plane, so that the coherence is at the transverse plane at the end of the pulse. As time elapses, this coherence disappears, while at the same time the protons release their energy and reorient themselves along \mathbf{B}_0 . This disappearing coherence produces the FID described earlier. As this coherence disappears the value of \mathbf{M} in the xy plane decreases toward 0. T_2 or T_2^* relaxation is the principal process by which this transverse magnetization is lost.

A comparison of the microscopic and macroscopic pictures provides additional insight. At the end of the 90° RF pulse, when the protons have absorbed energy and are oriented in the transverse plane, each proton precesses at the same frequency ω_0 and is synchronized at the same point or phase of its precessional cycle. Since a nearby proton of the same type will have the same molecular environment and the same ω_0 , it can readily absorb the energy that is being released by its neighbour. Spin-spin relaxation refers to this energy transfer from an excited proton to another nearby proton (Figure 21).

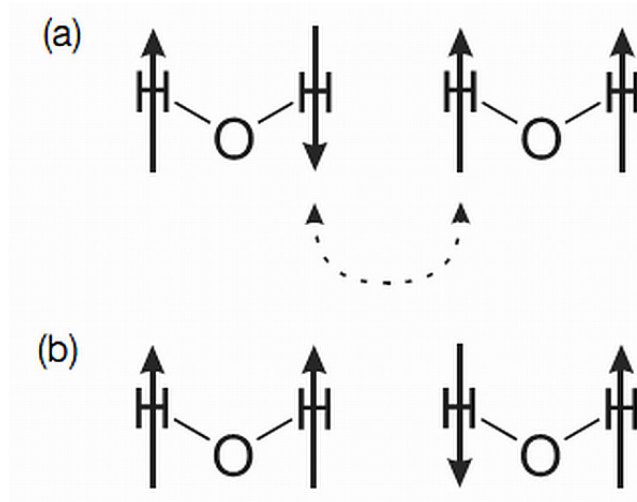


Figure 21. Spin-spin relaxation. (a) Two water molecules; one spin on one molecule has absorbed RF energy and is excited (spin down). (b) If the spins are in close proximity, the energy can be transferred from the first molecule to a spin on the second molecule.

The absorbed energy remains as spin excitation rather than being transferred to the surroundings as in T_1 relaxation. This proton-proton energy transfer can occur many times as long as the protons are in close proximity and remain at the same ω_0 . Intermolecular and intramolecular interactions such as vibrations or rotations cause ω_0 to fluctuate. This fluctuation produces a gradual, irreversible loss of phase coherence to the spins as they exchange energy and reduce the magnitude of the transverse magnetization and the generated signal (Figure 22). T_2 is the time when the transverse magnetization is 37% of its value immediately after the 90° pulse when this irreversible process is the only cause for the loss of coherence. As more time elapses, this transverse coherence completely disappears, only to reform in the longitudinal direction as T_1 relaxation occurs.

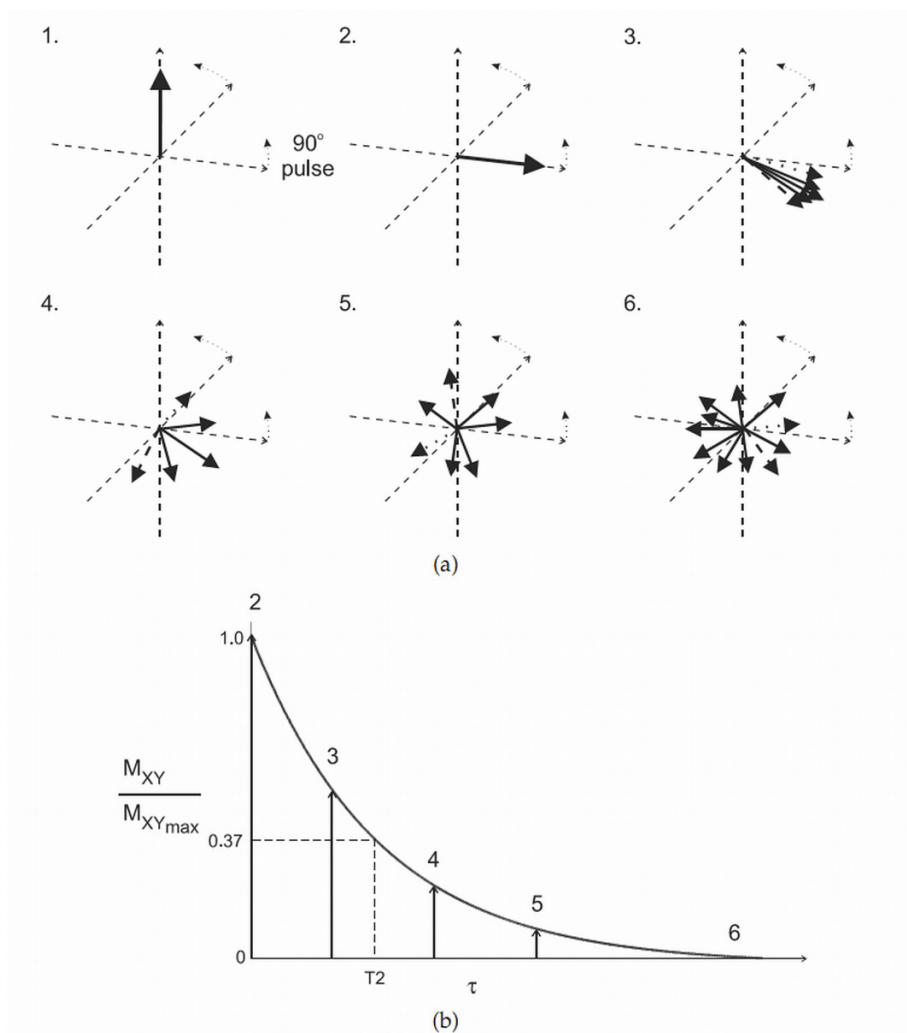


Figure 22. (a) A rotating frame slower than ω_0 is assumed for this figure. Net magnetization M (arrow) is oriented parallel to \mathbf{B}_0 (not shown) prior to pulse (1). Following a 90° RF pulse, the protons initially precess in phase in the transverse plane (2). Due to inter- and intramolecular interactions, the protons begin to precess at different frequencies (dashed arrow-faster; dotted arrow-slower) and become asynchronous with each other (3). As more time elapses (4, 5), the transverse coherence becomes smaller until there is complete randomness of the transverse components and no coherence (6). (b) Plot of the relative M_{XY} component as a function of time. The numbers correspond to the expected M_{XY} component from Figure 21a. The change in $M_{XY} / M_{XY \max}$ with time follows an exponential decay process. The time constant for this process is the spin-spin relaxation time T_2 and is the time when M_{XY} has decayed to 37% of its original value.

This dephasing time T_2 will always be less than or equal to T_1 . There are several potential causes for a loss of transverse coherence to M . One is the movement of the adjacent spins due to molecular vibrations or rotations. This movement is responsible for spin-spin relaxation or the true T_2 . Another cause arises from the fact that a proton never

experiences a magnetic field that is homogeneous. As the proton precesses, it experiences a fluctuating local magnetic field, causing a change in ω_0 and a loss in transverse phase coherence. This nonuniformity in \mathbf{B}_0 comes from three sources:

1. Main field inhomogeneity. There is always some degree of nonuniformity in \mathbf{B}_0 due to imperfections in magnet manufacturing, composition of nearby building walls, or other sources of metal. This field distortion is constant during the measurement time.

2. Sample-induced inhomogeneity. Differences in the magnetic susceptibility or degree of magnetic polarization of adjacent tissues (e.g., bone, air) will distort the local magnetic field near the interface between the different tissues. This inhomogeneity is of constant magnitude and is present as long as the patient is present within the magnet.

3. Imaging gradients. The technique used for spatial localization of signals generates a magnetic field inhomogeneity that induces proton dephasing.

Proper design of the pulse sequence eliminates the imaging gradients as a source of dephasing. The other sources contribute to the total transverse relaxation time, T_2^* :

$$1/T_2^* = 1/T_2 + 1/T_{2M} + 1/T_{2MS}$$

where T_{2M} is the dephasing time due to the main field inhomogeneity and T_{2MS} is the dephasing time due to the magnetic susceptibility differences. The decay of the transverse magnetization following a 90° RF pulse, the FID, follows an exponential process with the time constant of T_2^* rather than just T_2 :

$$\mathbf{M}_{XY}(t) = \mathbf{M}_{XY\max} e^{(-t/T_2^*)}$$

where M_{XYmax} is the transverse magnetization M_{XY} immediately following the excitation pulse. For most tissues or liquids, T_{2M} is the major factor in determining T_2^* , whereas for tissues with significant iron deposits or air-filled cavities, T_{2MS} predominates T_2^* . Some sources of proton dephasing can be reversed by the application of a 180° RF pulse, which is described by the following sequence of events (Figure 23) 1. A 90° RF pulse. 2. A short delay of time t . 3. A 180° RF pulse. 4. A second time delay t .

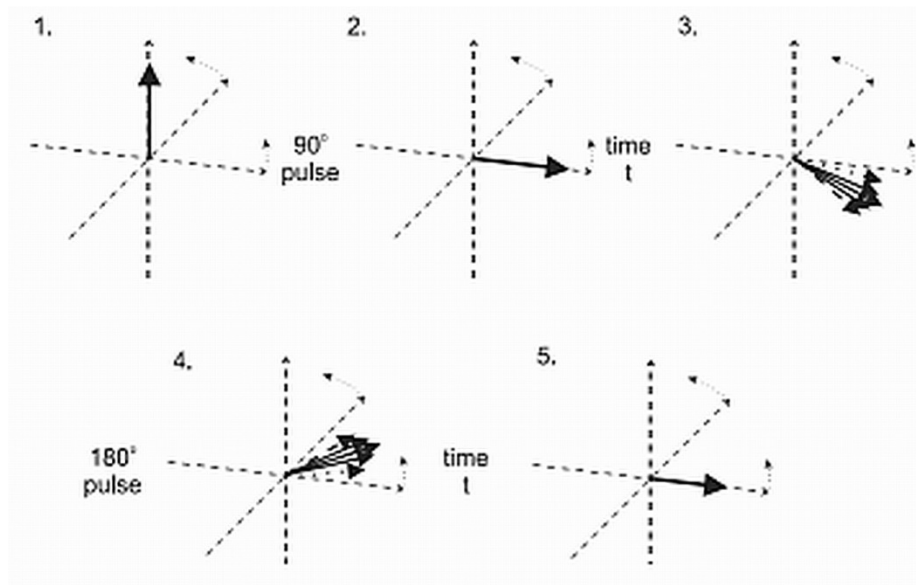


Figure 23. A rotation frame slower than ω_0 is assumed for this figure. Net magnetization M (arrow) is oriented parallel to B_0 (not shown) prior to pulse (1). Application of a 90° RF pulse rotates M into the transverse plane (2). Due to T_2^* relaxation processes, the protons become asynchronous with each other during time t (3). Application of a 180° RF pulse causes the protons to reverse their phase relative to the transmitter phase. The protons that precessed most rapidly are farthest behind (dashed arrow), whereas the slowest protons are in front (dotted arrow) (4). Allowing time t to elapse again allows the protons to regain their phase coherence in the transverse plane (5), generating a signal in the receiver coil known as a spin echo. The loss in magnitude of the reformed coherence relative to the original coherence (2) is due to irreversible processes (i.e., true spin-spin or T_2 relaxation).

The initial 90° RF pulse rotates M_0 into the transverse plane. During the time t , proton dephasing will occur through T_2^* relaxation processes and the transverse coherence will start to diminish. Application of a second 180° RF pulse causes the protons to reverse their

phases relative to the resonant frequency. The rates and directions of precession for the protons do not change, only their relative phase. If time t elapses again, then the protons will regain their transverse coherence. This reformation of phase coherence induces another signal in the receiver coil, termed as spin echo. Sources of dephasing that do not change during the two time periods, the main field inhomogeneity and magnetic susceptibility differences are eliminated because the protons experience exactly the same interactions prior to and following the 180° pulse.

This means that, contributions to T_2^* relaxation from these static sources will disappear. Only the irreversible spin-spin relaxation is unaffected by the 180° RF pulse so that the loss of phase coherence and signal amplitude for a spin echo is due only to true T_2 relaxation. Following the echo formation, the protons continue to precess and de-phase a second time as the sources of dephasing continue to affect them. Application of a second 180° RF pulse again reverses the proton phases and generates coherence to the protons, producing another spin echo. This second echo differs from the first echo by the increased amount of T_2 relaxation contributing to the signal loss. This process of spin echo formation by 180° RF pulses can be repeated as many times as desired, until T_2 relaxation completely dephases the protons. The use of multiple 180° pulses maintains phase coherence to the protons longer than the use of a single 180° RF pulse because of the significant dephasing that the field inhomogeneity induces over very short time periods. One important difference between T_1 and T_2 relaxation is in the influence of B_0 .

Good magnetic field uniformity is more difficult to generate at high magnetic fields, so that T_{2M} will be shorter. Greater B_0 will also cause greater differences in M_0 between two tissues with different magnetic susceptibilities, producing shorter T_{2MS} . The result is that

T₂-weighted techniques will see little sensitivity to B₀, whereas T₂^{*}-weighted techniques will show greater signal differences at higher B₀.

2.1.3.3. SPATIAL ALLOCATION OF RESONANT FREQUENCIES.

MRI uses the concept of field dependence to localize proton frequencies to different regions of space. In MRI, the magnetic field is made spatially dependent through the application of magnetic field gradients. These gradients are nothing but small perturbations superimposed on the main magnetic field **B**₀, with a typical imaging gradient producing a total field variation of less than 1%. They are also linear perturbations to **B**₀, so that the exact magnetic field is linearly dependent on the location inside the magnet:

$$\mathbf{B}_i = \mathbf{B}_0 + \mathbf{G}_T * \mathbf{r}_i$$

where B_i is the magnetic field at the location r_i and G_T is the total gradient amplitude, mathematically represented as a tensor. Gradients are also applied for short periods of time during a scan and are referred to as gradient pulses. In clinical MRI, the magnetic field gradients produce linear variations primarily in one direction only, so that the tensor product can be reduced to a vector representation. Three physical gradients are used, one in each of the x, y, and z directions. Each one is assigned, through the operating software, to one or more of the three “logical” or functional gradients required to obtain an image like: slice selection, readout or frequency encoding, and phase encoding. The particular pairing of physical and logical gradients is more or less arbitrary and depends on the

acquisition parameters and patient positioning as well as the particular manufacturer's choice of physical directions. The combination of gradient pulses, RF pulses, data sampling periods, and the timing between each of them which are used to acquire an image constitutes the pulse sequence. The presence of magnetic field gradients requires an additional expanded version of the original Larmor equation:

$$\omega_i = \gamma(B_0 + G \cdot r_i)$$

where ω_i is the frequency of the proton at position r_i and G is a vector representing the total gradient amplitude and direction. The dimensions of G are usually expressed in milli tesla per meter (mT m^{-1}) or gauss per centimetre (G cm^{-1}), where $1 \text{ G cm}^{-1} = 10 \text{ mT m}^{-1}$

The above equation states that, in the presence of a gradient field, each proton will resonate at a unique frequency that depends on its exact position within that gradient field. The MR image is nothing but simply a frequency and phase map of the protons generated by unique magnetic fields at each point throughout the image. The displayed image consists of digital picture elements (pixels) that represent volume elements (voxels) of tissue. The pixel intensity is proportional to the number of protons contained within the voxel weighted by the T_1 and T_2 relaxation times for the tissues within the voxel.

Slice Selection: The initial step in MRI is the localization of the RF excitation to a region of space, which is accomplished through the use of frequency-selective excitation in conjunction with a gradient known as the slice selection gradient, G_{SS} . The gradient direction (x, y, or z) determines the slice orientation, whereas the gradient amplitude together with certain RF pulse characteristics determines both the slice thickness and slice position. A frequency selective RF pulse has two parts associated with it: a central frequency and a narrow range or BW of frequencies (typically 1–2 kHz). When such a pulse is broadcast in the presence of the slice selection gradient, a narrow region of tissue

achieves the resonance condition and absorbs the RF energy. The duration of the RF pulse and its amplitude determines the amount of resulting proton rotation (e.g., 90°, 180°). The central frequency of the pulse determines the particular location excited by the pulse when the slice selection gradient is present. Different slice positions are achieved by changing the central frequency. The slice thickness is determined by the gradient amplitude G_{SS} and the BW of frequencies $\Delta\omega_{SS}$ incorporated into the RF pulse:

$$\Delta\omega = \gamma\Delta(G_{SS} * \text{Thickness})$$

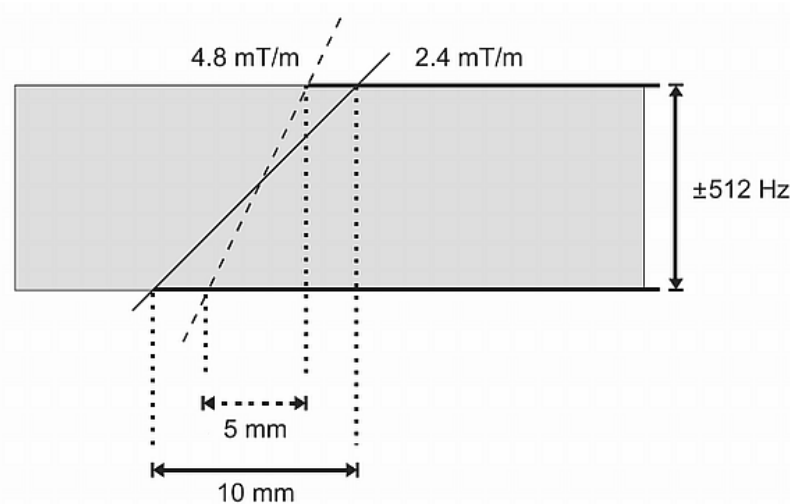


Figure 24. For a given range (bandwidth) of frequencies included in the RF pulse, the desired slice thickness is determined by the slice selection gradient amplitude. The user interface typically allows variation of slice thickness, which is achieved by increasing or decreasing the slice selection gradient amplitude, as appropriate.

Typically, $\Delta\omega$ is fixed so that the slice thickness is changed by modifying the amplitude of G_{SS} (Figure 24). Thinner slices require larger G_{SS} . Multislice imaging, the most commonly used approach for MRI, uses the same G_{SS} but a unique RF pulse during excitation for each slice. Each RF pulse has the same BW but a different central frequency, thereby exciting a different region of tissue.

Readout or frequency encoding: The signal detection portion of the MRI measurement is known as the readout or frequency encoding. The readout process differentiates MRI from MR spectroscopy. In an imaging pulse sequence, the MR signal is always detected in the presence of a gradient known as the readout gradient G_{RO} , which produces one of the two visual dimensions of the image. A typical pulse sequence uses some form of excitation, such as a 90° slice-selective pulse, to excite a particular region of tissue. Following excitation, the net magnetization within the slice is oriented transverse to \mathbf{B}_0 and will precess with frequency ω_0 . T_2^* processes induce dephasing of this transverse magnetization. This dephasing can be partially reversed to form an echo by the application of a 180° RF pulse, a gradient pulse, or both. As the echo is forming, the readout gradient is applied perpendicular to the slice direction. Under the influence of this new gradient field, the protons begin to precess at different frequencies depending on their position within it. Each of these frequencies is superimposed into the echo. At the desired time, the echo signal is measured by the receiver coil and digitized for later Fourier transformation.

The magnitude of the G_{RO} and the frequency that is detected enable the corresponding position of the proton to be determined. The magnitude of G_{RO} is determined by two user-definable parameters: the Field Of View in the readout direction, FOV_{RO} , and the Nyquist frequency, NQ , for the image, often referred to as the receiver BW.

This relationship can be expressed as:

$$\Delta\omega_{RO} = 2 \times \omega_{NQ} = \gamma\Delta(G_{RO} * FOV_{RO})$$

where $\Delta\omega_{RO}$ is the total range of frequencies in the image. G_{RO} is chosen so that protons located at the edge of FOV_{RO} precess at the Nyquist frequency for the image.

Smaller FOV_{ROs} are achieved by increasing G_{RO} , keeping the Nyquist frequency and thus the total frequency BW constant (Figure 25).

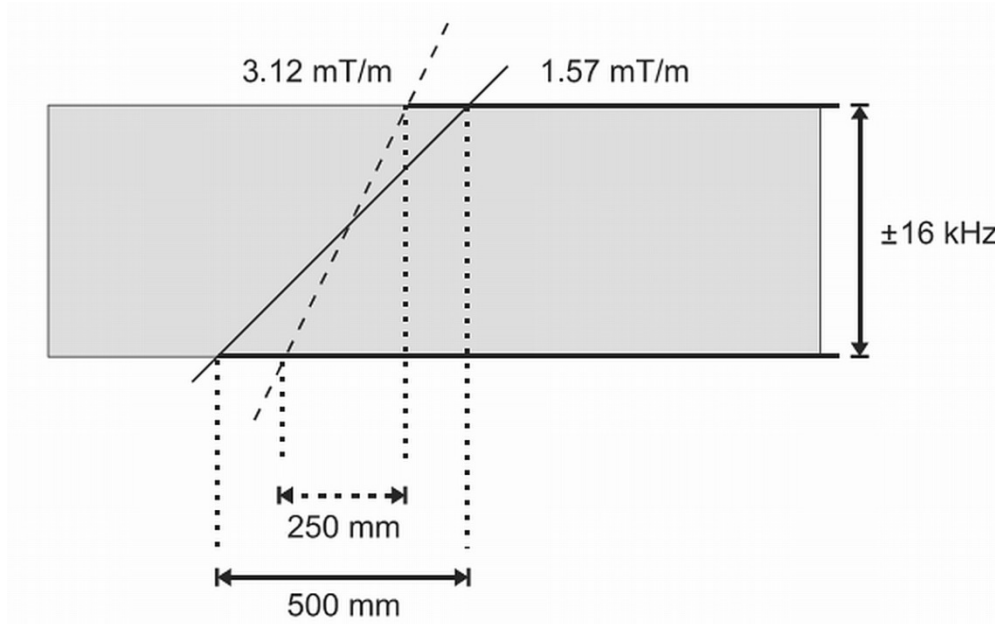


Figure 25. For a given range (bandwidth) of frequencies that are measured in the signal, the desired FOV is determined by the readout gradient amplitude. The user interface typically allows variation of the FOV, which is achieved by increasing or decreasing the readout gradient amplitude, as appropriate.

In an MR image, the resolution may be expressed in one of two ways: spatial resolution or frequency resolution. The spatial resolution, expressed as the voxel size with units of mm/pixel, is derived from two user parameters: FOV_{RO} and the number of readout sample points in the acquisition matrix, N_{RO} :

$$VOX_{RO} = FOV_{RO} / N_{RO}$$

The frequency resolution, with units of Hz/pixel, is based on N_{RO} and the total BW $\Delta\omega_{RO}$ for the image:

$$\text{Pixel BW} = \Delta\omega_{RO} / N_{RO} = 2 * \omega_{NQ} / N_{RO}$$

It is possible to improve the frequency resolution for the measurement independent of the spatial resolution by increasing the total sampling time used to measure the signal. This reduces the Nyquist frequency for the image and the background noise contributing to the measurement. In order to maintain the correct spatial resolution within the image, G_{RO} is reduced.

Phase Encoding: The third direction in an MR image is the phase encoding direction. The phase encoding gradient, G_{PE} , is perpendicular to both G_{SS} and G_{RO} and is the only gradient whose amplitude changes during the data acquisition loop of a standard two-dimensional (2D) imaging sequence. Any signal amplitude variation detected from one acquisition to the next is assumed to be caused by the influence of G_{PE} during the measurement. The principle of phase encoding is based on the fact that the proton precession is periodic in nature. Prior to the application of G_{PE} , a proton within a slice precesses at the base frequency ω_0 . In the presence of G_{PE} , its precessional frequency could either increase or decrease. Once G_{PE} is turned off, the proton precession returns to its original frequency, but is ahead or behind in phase relative to its previous state. The amount of induced phase shift depends on the magnitude and duration of G_{PE} that the proton experienced and the proton location. Protons located at different positions in the phase encoding direction experience different amounts of phase shift for the same G_{PE} pulse. A proton located at the edge of the chosen FOV experiences the maximum amount of phase shift from each phase encoding step. The MR image information is obtained by repeating the slice excitation and signal detection multiple times, each with a different amplitude of G_{PE} . The second Fourier transformation in the image converts signal amplitude at each readout frequency from a function of G_{PE} to a function of phase. The spatial resolution in the phase-encoding direction depends on two user-selectable parameters: the FOV in the phase encoding direction FOV_{PE} , and the number of phase

encoding steps in the acquisition matrix, N_{PE} . The FOV_{PE} is determined by the change in G_{PE} from one step to the next. For a proton located at the chosen FOV_{PE} , each phase-encoding step induces one-half cycle (180°) of phase change relative to the previous phase encoding step, assuming a constant pulse duration (Figure 26).

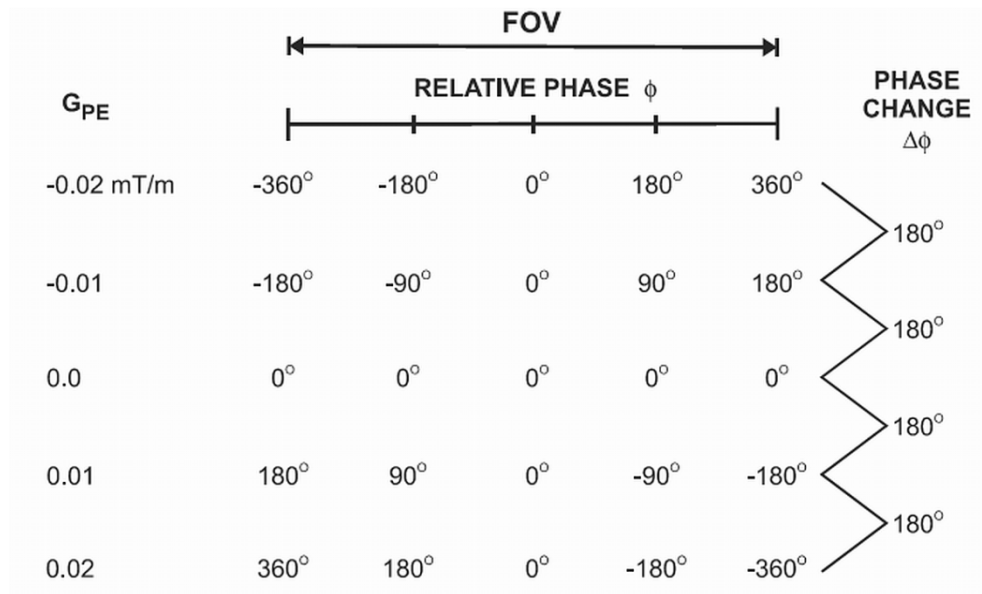


Figure 26. Phase-encoding process. A proton at the edge of the FOV in the phase-encoding direction undergoes 90° of phase change $\Delta\Phi$ from one phase encoding step to the next. Each point within the FOV undergoes progressively less phase change for the same gradient amplitude. A proton at the isocenter never experiences any phase change. The change in gradient amplitude (0.01 mT/m in this example) from one phase-encoding step to the next depends on the particular FOV chosen.

N_{PE} determines the total number of cycles of phase change ($N_{PE}/2$) produced at the edge of the FOV and thus the maximum frequency (ω_{NQ}) in the phase encoding direction for the given pulse duration. The spatial resolution in the phase-encoding direction is expressed as the voxel size and is measured in mm/pixel:

$$VOX_{PE} = FOV_{PE}/N_{PE}$$

Increased resolution is obtained by reducing the FOV_{PE} or by increasing N_{PE} . The FOV reduction is accomplished by increasing the gradient amplitude change from one G_{PE} to the next. Because of the two different physical processes involved, the FOV in the phase-

encoding direction is not required to be the same as the FOV in the readout direction, nor is the voxel size. The ratio of VOX_{RO} to VOX_{PE} is known as the aspect ratio between the two dimensions. An aspect ratio of 1.0 (100%) means that the voxel size is the same in both directions, a situation referred to as isotropic resolution. An aspect ratio less than 1.0 (<100%) is referred to as anisotropic resolution, with VOX_{PE} typically larger than VOX_{RO} .

Excerpts adapted from the book: - MRI: Basic Principles and Applications, Third Edition, by M. A. Brown and R. C. Semelka ISBN 0-471-43310-1 © 2003 John Wiley & Sons, Inc.

3.0. Aim and objectives.

3.1. AIM.

The aim of the present study was to non-invasively evaluate the selected indices of neurotrophic / neuroprotective properties of trophic factors, namely, epidermal growth factor and pigment epithelium derived factor on ischemia-reperfusion injury in a rat model of transient cerebral ischemia employing magnetic resonance imaging.

3.2. OBJECTIVES.

3.2.1. Establishment of small animal magnetic resonance imaging strategies on a 3 tesla clinical dedicated head magnetic resonance scanner.

- MRI protocols for rodent models ischemic and haemorrhagic stroke.
- MRI protocols for rodent models of spinal cord injuries.
- MRI protocols for murine model of Glioblastoma.
- Determination of quantitative tissue parameters like transverse relaxation time (T_2), longitudinal relaxation time (T_1) and susceptibility weighted transverse relaxation time (T_2^*).
- Qualitative imaging paradigms like, T_2 -, T_1 -, T_2^* -weighted, diffusion and perfusion weighted image acquisitions.
- Semi-quantitative parameters like, estimation of relative cerebral blood flow and blood volume from acquired perfusion weighted images.

3.2.2. Serial magnetic resonance imaging to determine the blood brain barrier permeability changes and the dynamic fluxes in vasogenic oedema formation following ischemia-reperfusion injury in rats.

3.2.3. Trophic properties of epidermal growth factor and pigment epithelium derived factor on selected indices of neurovascular injury following ischemia-reperfusion injury in rats.

- The infarct volume.
- The oedema formation.
- The blood brain barrier permeability.
- Metabolic status.
- Ischemic stroke induced diaschisis.

4.0. Materials and methods.

4.1. ESTABLISHMENT OF SMALL ANIMAL MAGNETIC RESONANCE IMAGING STRATEGIES ON A 3 TESLA CLINICAL DEDICATED HEAD MAGNETIC RESONANCE SCANNER.

Ethics Statement: All animal experiments were carried out in accordance with European communities council directive (86/609/EEC) and institutional guidelines for animal care after local ethics committee approval (Ethics committee for animal laboratories, Medical Faculty, University of Regensburg, 93042, Regensburg, Germany). The Human Cancer Stem Cell (HCSC) induced orthotopic xenograft mouse model of Glioblastoma (GBM) was developed after approval by the local authorities governing health care (Regierung der Oberpfalz, Emmeransplatz 8, 93047, Regensburg, Germany, www.ropf.de; AZ: 54-2531.2-22/08).

4.1.1. THE MR SYSTEM.

The employed clinical MR system is the US-FDA approved, high field, 2.895 Tesla dedicated head MR scanner (Siemens Magnetom Allegra, Siemens Healthcare Sector, Erlangen, Germany). The incorporated gradient sub-system achieves a peak amplitude of 40 mT/m with a slew rate of 400 mT/m/ms. The RF system comprises of a fully digital transmit-receive compact solid state RF amplifier at 123.2 MHz with a receiver BW of 1MHz.

4.1.2. THE PHASED ARRAY RADIOFREQUENCY COIL SYSTEM.

To facilitate small animal imaging, MR system hardware was complemented by a 4-channel rat brain and spine phased array coil assemblies. The RF assembly was complete with an animal handling system with provisions for inhalational anaesthetic supply and a feedback regulated heating pad (RAPID Biomedical, Rimpar, Germany). In order to ensure uniform excitation across the Region of Interest (RoI), these receive-only coils were combined to a volume resonator (RAPID Biomedical, Rimpar, Germany) with an inner diameter of 69mm.

The rat head receive-only RF coil array is fixed tuned to the operating frequency of 123.2 MHz. The four rectangular coil elements were aligned along the X-axis covering an area of 46 mm (Length) x 31 mm (Width) placed in a half-cylindrical design to accommodate the rat head (Figure 27A). The overall size of the array is chosen to cover the entire rat brain. The coil elements have a 'Q' value of 110, which means a 'Q' drop by a factor of 1.15, when compared to the unloaded coil. The impedance of all elements is fixed tuned and matched to 50 Ω when loaded with a rat head. Active decoupling of the coil elements during RF transmission is achieved with trap circuits switched by PIN diodes, found to be better than 30dB. Mutual coupling of neighbouring elements is compensated by a shared inductor design. Preamplifier decoupling (better than 20dB, where applicable, added up to the decoupling of next neighbours) ensures decoupling of all the other element pairs.

The rat spine receive-only RF coil array is again fixed tuned, matched and is combined with the same volume transmit coil. Here the four array elements are aligned along the Z-

axis to form a rectangle of dimensions 80mm (Length) x 30mm (Width) (Figure 27B). The unloaded 'Q' of each coil element was 144, dropping by a factor of 2, when loaded. In the spine array, neighbouring elements are decoupled by an overlap design. Again, active decoupling by trap circuits (better than 35 dB) and preamplifier decoupling are used for achieving decoupling from the transmit coil and between pairs of coil elements.

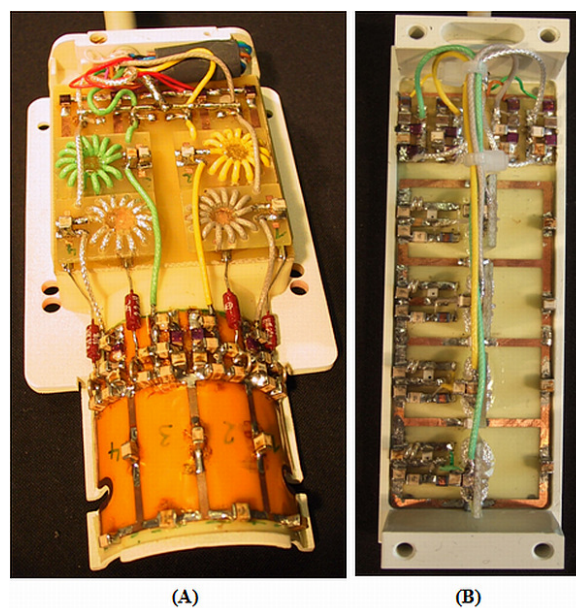


Figure 27. Geometry of the 4-channel phased array radio frequency coil system. (A) Rat head coil array where the 4 coil elements are placed in a half-cylindrical design along the X-axis of the scanner. (B) Rat spine coil array where the 4 coil elements are placed along the length of the Z-axis of the scanner.

4.1.3. IN-VIVO MRI.

4.1.3.1. CONFIGURATION AND OPTIMIZATION OF SEQUENCE PARAMETERS.

All implemented sequence parameters are modified from the pre-loaded standard Siemens product sequences. A number of modifications pertaining to Spin-Echo (SE),

Turbo Spin-Echo (TSE), Gradient Recalled Echo (GRE), Diffusion Weighted and Perfusion Echo Planar Imaging (DW- & PE-EPI) sequences have been addressed. All modifications are aimed to ensure maximum signal with enough in-plane resolution for sensitive detection and spatial allocation of lesions by eliminating artefacts. In our approach, Acquisition Times (AT) was given the least priority and was traded against factors contributing to enhanced image quality.

In the 2-dimensional mode, all acquisitions, irrespective of the sequence type has been performed in multi-slice interleaved fashion to enhance signal by eliminating slice crosstalk. Slice Thickness (ST) of the rodent brain was maintained at 1 mm in the case of SE, TSE and EPI sequences, primarily to facilitate cross comparison with histological tissue sections prepared by the rodent brain matrix (ASI Instruments, Inc. USA) where the minimum ST is limited to 1mm. However, due to gradient strength limitations, the minimum achievable ST with GRE sequences was 1.5 mm. The same ST (1.5mm) was considered for the rodent spine primarily to enhance the available signal due to the small size of the object of interest. Gradient performance also imposed limits on minimizing the FOV which, was confined to 50 mm in the case of EPI and GRE sequences, which, could be further reduced to 25 mm in the case of SE and TSE sequences. However, in the case of rodents a 25 mm FOV, resulted in anatomical regions extending beyond the ROI causing aliasing artefacts along the phase encode direction and were countered by employing phase oversampling.

Further, the phase encoding direction was always kept maintained in the right-left direction (X-axis of the scanner) as the phase encoding along the anterior-posterior direction (Y-axis of the scanner) demonstrated motion related artefacts. The only

exception to this case was that with DW-EPI sequence, because, such a scheme resulted in relatively higher geometric distortions along the phase encode direction. In order to maximize the available signal and to reduce noise, minimal receiver BW had been resorted to wherever possible as in the case with SE and GRE sequences. However, the BW selection for T₂- and PD-TSE sequences was guided by the tissue T₂ value and the corresponding echo-spacing resulting from the selected echo train length (Turbo factor).

EPI, particularly at higher field strengths are prone to geometric distortions, signal loss and image blurring caused by frequency shifts and T₂^{*} relaxation distortion of the MR signal along the k-space trajectory due to magnetic field inhomogeneities (249). A two-tier strategy has been adopted to minimize such distortions involving, 1) manual shimming of the magnet has been carried out following an auto-shimming routine to achieve a proton BW ≤ 35 Hz at full width half maximum with an accompanying T₂^{*} value ≥ 30. 2) Due to the availability of multiple receiver channels, Parallel Imaging (PI) has been implemented for all EPI sequences (250). The k-space based Reconstruction Algorithm (RA) allowed by GeneRalized Auto-calibrating Partially Parallel Acquisition (GRAPPA) at an Acceleration Factor (AF) of 3 was considered for DW-EPI and PE-EPI was performed at an AF of 4. Further, for EPI sequences the FOV in the phase encoding direction was maintained at or less than 50% of the FOV in read direction as this reduces the acquisition time in case of DW-EPI and contributes to enhanced temporal resolution of the PE-EPI sequence.

In our lab, GRE sequences are primarily considered to detect haemorrhage, haemorrhagic streaks and haemosiderin deposits in the brain with maximum possible sensitivity. However, susceptibility artefacts arising out of magnetic field inhomogeneities

were minimized by employing 1) manual magnet shimming, 2) low Time-to-Echo (TE) value, and 3) a higher acquisition matrix (251).

Optimization of sequence parameters can never be considered adequate without determining the tissue relaxation characteristics, which in turn decides the Time-to-Repeat (TR) and TE values. Currently, there are no quantitative reports on the basic MR properties of the rat brain, spine and mouse brain at 3 T in the literature. Knowledge of these properties are essential for determining the mechanisms that are responsible for the endogenous MRI contrast between the Gray and White matter (GM & WM) of the spinal cord, establishing sensitivity and specificity of the MR parameters to pathological changes seen in normal and injured tissues, and describing the signal enhancement features achieved with the use of exogenous contrast agents.

Therefore, the first aim of this work was to perform baseline measurements of the spin-lattice (T_1), spin-spin (T_2), relaxation times at 3 T for the rat and mouse brains along with determination of the relative Proton Density (rel-PD) values of the GM & WM of the rat spine. Further, T_2^* relaxation due to magnetic susceptibility effects has also been derived for the rat and mouse brains. Moreover, since two Parallel Imaging Reconstruction Algorithms (PI RAs) like modified SENSitivity Encoding (mSENSE) and GRAPPA were available to choose from for DW- and PE-EPI sequences, these strategies has been compared and contrasted against each other primarily for the available Signal-to-Noise Ratio (SNR) and also for any gross geometric distortions and reconstruction related artefacts.

4.1.3.2. DETERMINATION OF TISSUE RELAXATION CHARACTERISTICS.

Male Wistar rats (N = 8) (Charles River Laboratories, Sulzfeld, Germany) weighing 250-300 g and male in-house bred NMRI^(nu/nu) mice (N = 8) weighing 20-25 g were used for the determination of the brain cortical and striatal T_1 , T_2 and T_2^* relaxation characteristics. Anaesthesia was induced using 5% Isoflurane for rats and mice and the anaesthetic state was maintained with 1.5 and 0.5 % Isoflurane respectively. Animals were mounted in prone position within the scanner and the body temperature was kept maintained with feedback regulated heating pad. Normal spine gray and white matter has been characterized on female Fischer 344 rats (N = 8) (Charles River Laboratories, Sulzfeld, Germany) weighing 160-180 g. Following anaesthesia animals were mounted in supine position over the rectangular spine coil array housing and the parameters determined also include rel-PD values along with T_1 and T_2 profile. The parameter dataset for characterizing these tissue relaxation values are detailed in Table 4.

T ₁ -Relaxation (IR)			T ₂ -Relaxation (SE)		T ₂ [*] -Relaxation (GRE)	
TR(ms)	TE(ms)	IT(ms)	TR(ms)	TE(ms)	TR(ms)	TE(ms)
10,000	74	500	4000	29	700	20
		800		58		30
		1000		88		40
		1500		117		50
		2000		146		60
		4000		204		
		6000				
		8000				

IR, inversion recovery; SE, spin-echo; GRE, gradient recalled echo; TR, repetition time; TE, echo time; IT, inversion time.

Table 4. Parameter dataset employed for calculating tissue relaxation characteristics.

4.1.3.3. DETERMINATION OF THE OPTIMAL PARALLEL IMAGING RECONSTRUCTION ALGORITHM: GRAPPA OR mSENSE?

The criteria chosen for the selection of the optimal PI strategy was based on the available SNR and also on the absence of any gross geometric distortions. SNR calculations were carried out by the ``difference method`` referred hereafter as SNR_{diff} based on the evaluation of a difference image from two repeated but identical acquisitions as described previously (252). Two separate, but, identical datasets for each of the DW- and PE-EPI were acquired from an anesthetized male Wistar rat weighing 250-300 g employing both GRAPPA and mSENSE. In the case of DW-EPI, acquisitions were performed at all the possible AFs (from 2-4) and an image set without PI was also acquired for the sake of comparison. PE-EPI acquisitions were carried out without any contrast agent administration and were performed at AFs of 3 and 4 as the AF of 2 and acquisition without PI prolonged the TR value and affected the temporal resolution of the PE-EPI sequence. All the other EPI sequence parameters employed are as described in Table 5.

4.1.3.4. ANATOMICAL CHARACTERIZATION OF A RAT BRAIN.

As a prelude to pathological rat brain imaging, an attempt has been made for phenotypic characterization of the rat brain using a 3-Dimensional T_1 -weighted Magnetization Prepared Rapid Acquisition Gradient Echo (3D-MPRAGE) sequence. This was performed on a healthy male Wistar rat weighing 250-300 g. The animal was anaesthetized and positioned within the scanner as mentioned before. After acquiring localizer images, 3D-MPRAGE acquisition was performed with TR = 1070 ms, TE = 4.95 ms, Inversion Time (TI) = 900 ms, FOV = 50 mm, Image Matrix (IM) = 256 x 256 and

BW=130 Hz/Px.

4.1.3.5. MR IMAGING OF A RAT MODEL OF ISCHEMIC STROKE.

Three male Wistar rats weighing 250-300 g were considered for this study. Transient MCAO (tMCAO) was performed for inducing cerebral ischemia as described by Longa et al. with modifications of employing a silicon coated suture to occlude the MCA as described by Spratt et al. (253, 254).

Polyethylene tubing (Portex, UK) with a nominal internal diameter of 0.35 mm was cut into 1.5 cm segments. Three centimetre lengths of 4/0 polyamide monofilament suture (Ethicon, USA) was introduced up to 5 mm within one end of the tubing and silicone (President, Germany) was slowly injected from the other end using a needle and syringe, enveloping the distal 5mm of the suture. Care was taken throughout the procedure to ensure that air bubbles did not form within the silicone. After 24 hours the tubing and encased silicone was cut using a razor blade at a point 0.5 mm beyond the tip of the suture. Immediately prior to surgery the suture was removed from the tubing, leaving a uniform coating of silicone bonded to the distal 5mm.

Anaesthesia was induced, using 5% Isoflurane in a mixture of 30% oxygen and 70% nitrous oxide. Following this, animals were endotracheally intubated and mechanically ventilated (RS Biomed ventilator, Sinzing, Germany). The anaesthetic concentration was then lowered and maintained at 1.5% throughout the period of surgery. The animal was then placed in supine position over a heating blanket (Harvard Apparatus, USA) and the thermistor probe of the heating blanket was gently inserted into the rectum providing a feedback system to maintain the body temperature at 37-37.5° C. The femoral vein was then exposed and cannulated for contrast agent injection.

Pathology	Ischemic stroke				ICH	Spine Injury	GBM	
Animal	Rat						Mouse	
Sequence	DW -EPI	PE-EPI	T ₂ -TSE	T ₁ -SE	T ₂ *-GRE	PD + T ₂ -TSE	T ₂ -TSE	T ₁ -SE
TR (ms)	3000	900	3000	900	500	5000~7000*	4000	1000
TE (ms)	90	27	70	10	20	13, 80	68	18
FOV (Read,cm)	5.7	5.7	2.5	2.5	5.0	2.5	2.5	2.5
FOV (Phase, %)	46.9	50	100	100	100	100	100	68.8
IM	128x60	64x128	128x128	128x128	256x256	128x128	128x128	88x128
ISG (%)	0	0	0	0	0	0	0	0
FA(°)	-NA-	130	180	130	20	180	180	90
BW(Hz/Pixel)	752	752	94	158	30	150	40	90
PED	A-P	R-L	R-L	R-L	R-L	R-L	R-L	R-L
POS (%)	0	50	50	50	0	100	0	0
TF/EPI factor	60	64	7	-	-	5	5	-
ES(ms)	1.52	1.54	23.2	-	-	13.3	34.2	-
MSM	IL	IL	IL	IL	IL	IL	IL	IL
Series	IL	IL	IL	IL	IL	IL	IL	IL
NoA	4	2	4	3	2	4	4	4
PI(GRAPPA)	Yes	Yes	No	No	No	No	No	No
AF	3	4	-	-	-	-	-	-
NoM	-	50	-	-	-	-	-	-
DD	3	-	-	-	-	-	-	-
'b'	0	-	-	-	-	-	-	-
values(s/mm ²)	500	-	-	-	-	-	-	-
	1000	-	-	-	-	-	-	-
	1500	-	-	-	-	-	-	-
	2000	-	-	-	-	-	-	-
	2500	-	-	-	-	-	-	-

ICH, intra-cerebral haemorrhage; GBM, glioblastoma; DW-EPI, diffusion weighted echo planar imaging; PE-EPI, perfusion echo planar imaging; T₂-TSE, T₂-weighted turbo spin echo; T₁-SE, T₁-weighted spin echo; T₂*-GRE, susceptibility weighted gradient recalled echo; PD-TSE, proton density weighted turbo spin echo; TR, repetition time; TE, echo time; FOV, field of view; IM, image matrix; ISG, inter slice gap; FA, flip angle; BW, band width; PED, phase encoding direction; POS, phase over-sampling; TF, turbo factor; ES, echo spacing; MSM, multi-slice mode; NoA, number of averages; PI, parallel imaging; GRAPPA, generalized auto-calibrating partially parallel acquisition; AF, acceleration factor; NoM, number of measurements; DD, diffusion direction; A-P, anterior-posterior; R-L, right-left; IL, interleaved. *Depending upon the respiration rate of the animal.

Table 5. Modified sequence parameters employed for facilitating small animal imaging.

The neck region of the animal was then cleared of all hairs employing an electric razor and then disinfected using hydrogen peroxide solution. Under the operating microscope, the left Common Carotid Artery (CCA) was exposed through a midline incision; a self retaining retractor was positioned between the digastric and sternomastoid muscles, and the omohyoid muscle was divided. The occipital artery branches of the External Carotid Artery (ECA) were then isolated and coagulated. Next, the superior thyroid and ascending pharyngeal arteries were dissected and coagulated. The ECA was dissected further distally

and coagulated along with the terminal lingual and maxillary artery branches, which were then divided. The Internal Carotid Artery (ICA) was isolated and carefully separated from the adjacent vagus nerve. Further dissection identified the ansa of the glossopharyngeal nerve at the origin of the pterygopalatine artery; this posteriorly directed extracranial branch of the ICA was ligated with 6-0 polyamide suture close to its origin. At this point, the ICA is the only remaining extracranial branch of the CCA.

Next, a 3-0 silk suture was tied loosely around the mobilized ECA stump, and a curved microvascular clip was placed across both the CCA and the ICA adjacent to the ECA origin. A 3-cm length of 4-0 monofilament nylon silicone coated suture, prepared as mentioned above, was introduced into the ECA lumen through a puncture or through one of the terminal branches of the ECA. The silk suture around the ECA stump was tightened around the intraluminal nylon suture to prevent bleeding, and the microvascular clip was removed. The nylon suture was then gently advanced from the ECA to the ICA lumen; the position of the suture within the ICA lumen could be seen as it reached the base of the skull. After a variable length of the polyamide suture had been inserted into the ECA stump, resistance was felt and a slight curving of the suture or stretching of the ICA was observed, indicating that the silicon tip of the suture had passed the MCA origin and reached the proximal segment of the Anterior Cerebral Artery (ACA), which has a smaller diameter.

At this point, the intraluminal suture has blocked the origin of the MCA, occluding all sources of blood flow from the ICA, ACA and Posterior Cerebral Artery (PCA). The incision was closed, leaving 1 cm of the nylon suture protruding so it could be withdrawn to allow reperfusion. Following 90 minutes of occlusion, restoration of MCA blood flow

was performed under the same anaesthetic mixture administered through a nose cone. The incision was reopened and the suture was pulled back until resistance was felt, indicating that the tip had cleared the ACA-ICA lumen and was in the ECA stump, and then trimmed. The incision is again closed by applying sutures.

Neurologic examinations were performed after almost 10-20 minutes following occlusion of the MCAO. Successful occlusion was confirmed with neurologic findings scored on a five-point scale: a score of 0 indicated no neurologic deficit, a score of 1 (failure to extend right forepaw fully) a mild focal neurologic deficit, a score of 2 (circling to the right) a moderate focal neurologic deficit, and a score of 3 (falling to the right) a severe focal deficit; rats with a score of 4 did not walk spontaneously and had a depressed level of consciousness.

One hour following tMCAO, animals were anaesthetized as mentioned before, mounted on the animal holder of the scanner and the body temperature was kept maintained. After acquiring localizer images, DW-EPI acquisitions with trace weighted Apparent Diffusion Co-efficient (ADC) maps were generated to confirm ischemic injury followed by T₂-weighted Turbo Spin-Echo (T₂-TSE) acquisition. Cerebral blood perfusion characteristics were determined with PE-EPI sequences. Two PE-EPI acquisitions were attempted employing both mSENSE and GRAPPA at an AF of 4 in a time interval of 25~30 minutes. PE-EPI with mSENSE was performed first and after 25 minutes another PE-EPI acquisition was carried out with GRAPPA at the same AF. For both PE-EPI acquisitions, first 3 measurements were ignored and following another five baseline measurements, Gadolinium DiethyleneTriamine-Penta-acetic Acid (Gd-DTPA, 0.2 mmol/kg, Magnevist[®], Shering, Germany) was injected through the femoral vein within a sub-second time duration without saline flush. Relative Cerebral blood perfusion

characteristics like Blood Flow (rel-CBF) and Blood Volume (rel-CBV) maps were also derived from the acquired perfusion images. In another animal, following 90 minutes of tMCAO, the animal was reperfused for four hours. After acquiring all the parameters except that of PE-EPI as in the above mentioned case, the integrity of the BBB was evaluated by a post-contrast T_1 -SE sequence following 25 minutes of Gd-DTPA administration. Modified sequence parameters employed are as detailed in Table 5.

4.1.3.6. MR IMAGING OF A RAT MODEL OF INTRA-CEREBRAL HAEMORRHAGE.

The rat model of Intra-Cerebral Haemorrhage (ICH) was prepared as described previously (255). Male Wistar rats (N = 2) weighing 250-300 g were subjected to the same anaesthetizing regimen and the body temperature was kept maintained as in the case of ischemic stroke. The right femoral artery was then catheterized for blood sampling. After this, rats were positioned in a stereotaxic frame (Kopf Instruments, Tujunga, USA) and a cranial burr hole was drilled near the right coronal suture 3.5 mm lateral to the midline. A 26 gauge needle was inserted stereotaxically into the right basal ganglia (Coordinates: 0.2 mm anterior, 5.5 mm ventral and 3.5 mm lateral to the bregma). Autologous whole blood withdrawn from the femoral artery was infused at a rate of 10 μ l / min employing a microinfusion pump (Harvard Apparatus Inc, Holliston, USA). The needle was then slowly removed over a time period of 10 minutes and the skin incision was closed with a suture. Within an hour of surgery, the animals were again anesthetized and positioned within the scanner as mentioned before. T_2 -TSE and T_2^* -GRE images were acquired following localizer scans. T_2 -TSE sequence parameters were identical to those used for cerebral ischemia whereas, modified parameters for T_2^* -GRE acquisition were

used as in Table 5. The present study was conducted longitudinally with multiple imaging time points at < 1, 72 hours, 1 week and 1 month post injury.

4.1.3.7. MR IMAGING OF RAT SPINAL CORD INJURY MODELS.

MR imaging of rodent spine was first attempted at the thoracic (T10) level on a normal healthy adult female Fischer rat weighing 160-180 g. Anaesthesia was induced using 5% Isoflurane - air mixture, following which, the animal was placed supine, over the rectangular surface of the rodent spine array coil housing. Anaesthesia was then continued with 1.5% Isoflurane and the animal was carefully observed for a variable time period (10-15 minutes) to ensure rhythmic and automatic breathing, before, the MR scanner was synchronized to the respiratory cycle (ECG Trigger Unit, HR V02, RAPID Biomedical, Rimpar, Germany) by placing the button sized air-cushion sensor below the diaphragm. A trigger delay of varying time interval (200-300 ms) was introduced to obtain motion-artefact free images.

Following satisfactory results, spine imaging was further extended to two models of spinal cord injuries. The first model was based on a Tungsten wire knife induced cut at the rostral-cervical (C3) spinal cord as described earlier (256). Three female Fischer rats were considered for the study. Animals underwent anaesthesia made up of a mixture of ketamine (62.5mg/kg bodyweight; WDT, Garbsen, Germany.), xylazine (3.175mg/kg bodyweight; WDT), and acepromazine (0.625 mg/kg body weight, Sanofi-Ceva, Düsseldorf, Germany.) in 0.9% sterile saline solution. Rats underwent laminectomy at C3, and a tungsten wire knife (Kopf Instruments, Tujunga, USA.) was stereotaxically positioned at the spinal dorsal midline and lowered to a depth of 1.1 mm ventral to the

dorsal surface, 0.6 mm to the left of midline. The tip of the knife was extruded, forming a 2.25-mm-wide wire arc that was raised 2 mm to lesion the corticospinal tract bilaterally. A large proportion of the overlying dorsal funicular dorsal sensory ascending projection was also lesioned by this procedure. The wire arc was retracted back into the wire knife device and removed.

The second model was based on spine contusion injury induced at the thoracic (T10) level in adult female Fischer rats as described (257). Five animals were considered for this model. After administering the same anaesthetic cocktail mixture, a laminectomy was performed at T10 to expose the dorsal portion of the spinal cord. The animals were suspended by attaching Adson forceps to the rostral T9 and caudal T11 vertebral bodies. Particular care was taken to align the exposed spinal cord perpendicular to the axis of the impactor (Infinite Horizon Impactor, Precision Systems & Instrumentation, USA.). The 2.5-mm stainless steel impounder tip was lowered to approximately 3-4 mm above the surface of the exposed spinal cord. The contusion injury was finally induced by applying an impact force of 2 Newton (equal to 200 kilodyne) to the exposed spinal cord at a velocity of 130 mm/s. Overlying muscle layers were sutured and the skin was closed. Postoperatively, animals were kept warm, placed on beds of sawdust, and given manual bladder evacuation twice a day for a period of 10 days as necessary and received intramuscular injections of 10 mg Cotrimoxazol (Ratiopharm, Ulm, Germany) once daily for a period of 10 days. Animals regained automatic neurogenic bladder function after 5-10 days.

MR imaging was performed at 30 days post-injury with the aim of studying long-term MR signatures of spinal injury except for one animal with the cervical cut studied at 24

hours post injury. Animals with cervical and contusion injuries were mounted in prone and supine positions respectively, and all the other settings were as in the case of normal spine image acquisition as mentioned above. Cervical and thoracic spine was characterized using modified T₂- and PD-TSE sequences, the details of which are as provided in Table 5. Following this procedure, animals were immediately sacrificed and spine tissue was processed for Nissl and Prussian blue staining as described (257). Animals were transcardially perfused with 0.9% saline followed by 4% paraformaldehyde in Phosphate Buffered Saline (PBS) following the last imaging session. The spinal cords were removed, post-fixed overnight in 4% paraformaldehyde in PBS and left for 1 day in PBS containing 30% sucrose.

The injured region of the spinal cord from the two models were cut into 40- µm thick coronal sections with a cryostat and processed for further histochemical analysis. Nissl staining was performed to assess the overall neuropathological changes (tissue loss, hemorrhage, cyst formation). Prussian blue staining was employed to identify haemosiderin deposits. This was followed by bright field microscopy using Leica digital module R microscope equipped with a Spot CCD (Charge-Coupled Device) camera model 2.2.1 (Diagnostic Instruments, Sterling Heights, USA.).

4.1.3.8. MR IMAGING OF A MOUSE MODEL OF GLIOBLASTOMA.

The HCSC induced orthotopic xenograft mouse model of GBM was developed as described (258). Native tumour tissue samples from GBM resections were provided by the local department of neurosurgery. All tumours were histologically classified according to the WHO classification of CNS tumours (259). Samples were stored in sterile saline at 4°C

and processed within 24 hours after resection. They were washed and dissociated by mechanical and enzymatic means (1% trypsin, which does not alter CD133 cell surface expression). Erythrocytes were lysed using ammonium chloride. Trypan blue staining confirmed > 80% viability after the procedure. Tumor cells were then grown in stem cell permissive DMEM-F12 medium supplemented with 20 ng / mL of each human recombinant EGF, human recombinant bFGF (R & D Systems, Inc. USA) and human LIF and 2% B27 (Life technologies, USA). These culture conditions enable tumour cells to retain the molecular characteristics of the primary tumour with only minor changes in differentiation, expression pattern, and genetic mutation profile (258). 50% of the medium was substituted twice weekly. Metabolic activity was measured using 10% Alamar Blue that was added to the cell culture medium. The absorbance was determined after 16 h at 590 and 540 nm.

A total of 1×10^6 cells suspended in 2 μ l PBS was stereotaxically injected into subcortical region of T-lymphocyte deficient NMRI^(nu/nu) mice. Three months after HCSC injection, animals (N = 15) were anesthetized with 0.5% Isoflurane and T₂-TSE and an identical T₂*-GRE sequence as in the case of the rat model of ICH were primarily considered to characterize the evolving tumour and haemorrhage, if any, respectively. To assess BBB and/or Blood Tumour Barrier (BTB) permeability characteristics, Gd-DTPA (0.2 mmol/kg) was administered by cardiac puncture. Post-contrast T₁-SE images were acquired after 25 minutes. All sequence parameters are as detailed in Table 5. The brains were immediately removed; frozen and 10-micrometer sections were stained with Hematoxylin and Eosin. The degree of correlation between the tumour volumes obtained from the T₂-weighted sequence has also been compared to those obtained by histological studies.

4.1.4. DATA ANALYSIS.

Mono-exponential non-linear curve fitting for performing quantitative relaxometry and two-tailed unpaired ‘t’ tests for comparing the relaxometric values of the cortex and striatum of the rat and mouse brains and comparisons of the gray and white matter of the spinal cord along with the determination of Pearson correlation co-efficient between the mouse tumour volumes obtained from T₂-TSE images and histological studies were performed using Graphpad Prism Version 5.00 for Windows (Graphpad Software, San Diego, California, USA).

For calculating SNR_{diff} with DW-EPI images, identical RoIs were defined over the sub-cortical regions over a 0.7 sq.cm circular area on a pair of 1 mm thick slices (acquired as two identical separate set of images) located 6mm posterior to the frontal cortex employing the built-in image analysis tools of the Siemens *SyngoMR* 2004A platform (Siemens Healthcare Sector, Erlangen, Germany). In the case of PE-EPI images, RoIs were defined on the cortical region for the same area and slice position as in the case of DW-EPI images. The resultant values of signal intensity and their differences in Standard Deviation (SD_{diff}) are substituted in the following equation to obtain the SNR as described elsewhere (252).

$$SNR_{diff(k_1, k_2)} = \frac{\frac{1}{2} \text{mean}(S_N(r, k_1 + r, k_2))}{\frac{1}{\sqrt{2}} \text{stddev}(S_N(r, k_1 - r, k_2))}$$

Where, ‘k₁’ and ‘k₂’ represent the two identical image acquisitions at identical RoIs represented by ‘r’.

Cerebral blood perfusion parameters including rel-CBV and -CBF maps were derived by defining an ROI at the contralateral hemisphere covering the origin of the right MCA to allow measurement of the arterial input function, from which pixels representative of the right MCA branch were selected. Following this, perfusion maps were derived automatically with the built-in *SyngoMR 2004A* software. Regions of altered BBB permeability to Gd-DTPA were located by generating subtraction maps from pre- and post-contrast T₁-SE images using the same built-in software tools.

4.2. SERIAL MAGNETIC RESONANCE IMAGING TO DETERMINE THE BLOOD BRAIN BARRIER PERMEABILITY CHANGES AND THE DYNAMIC FLUXES IN VASOGENIC OEDEMA FORMATION FOLLOWING ISCHEMIA-REPERFUSION INJURY IN RATS.

4.2.1. EXPERIMENTAL DESIGN.

Male Wistar rats (Charles River Laboratories, Sulzfeld, Germany) weighing between 250 - 300 g, were either subjected to 90 minutes of tMCAO followed by 48 hours of reperfusion (Experimental group, N = 11) or were sham operated (Sham group, N = 8). Serial MRI was performed at the following time points: Pre-ischemic (Control), 1 hour after ischemia or 30 minutes Before Reperfusion (BR), immediately After Reperfusion (AR), 4 hours Post-Reperfusion (04PR), 24 hours Post-Reperfusion (24PR) and 48 hours Post-Reperfusion (48PR). Experimental animals were scanned at six time points (Control, BR, AR, 04PR, 24PR and 48PR), and sham animals at the last three time points (04PR, 24PR and 48PR).

4.2.2. SURGICAL PROCEDURE.

tMCAO was performed for a time period of 90 minutes as previously described with suggested modifications (253, 254). The femoral vein was also cannulated for contrast agent administration. Sham surgery was performed in the same manner, except for MCA occlusion. The animals were then allowed to recover. One hour post occlusion, the animals were re-anesthetized with 1.5% Isoflurane and MRI was performed for the time point BR. Following this, animals were subjected to reperfusion by gently pulling back the filament.

4.2.3. MAGNETIC RESONANCE IMAGING.

The animals were anesthetized and mounted on the scanner as per the procedures mentioned before. To detect ischemic changes especially at the early time points (BR and AR), DW-EPI images were acquired first and trace weighted ADC maps were generated. This was performed at time points (BR, AR, 04PR, 24PR & 48PR). T₂-TSE images were then acquired at time points (BR, AR, 04PR, 24PR & 48PR) to detect and locate vasogenic oedema formation. T₂-relaxometric estimations to quantify oedema formation were performed at all the time points (Control, BR, AR, 04PR, 24PR and 48PR). To determine BBB permeability changes following Ischemia-Reperfusion (I/R) injury, post-contrast T₁-SE imaging was performed at the last three time points (04PR, 24PR & 48PR) as per the procedure detailed before. The dataset employed for T₂-relaxometry is as provided in Table 4. The sequence parameters employed for performing DW-EPI, T₂-TSE and T₁-SE are as detailed in Table 5.

4.2.4. DATA ANALYSIS.

All the required parameters were acquired from a single coronal slice (1 mm thick) located at 7 mm posterior to the anterior tip of the frontal cortex. Quantitative T₂-relaxometry was performed at three ROIs; the ipsi- and contralateral striatum and on the ipsilateral cortex. In the striatal region, circular ROIs have been defined over the entire striatal region excluding the ventricles irrespective of whether the selected region encloses healthy looking or infarcted tissue.

Mono-exponential non-linear curve fitting was performed using Graphpad Prism Version 5.00 for Windows to determine T₂ relaxation parameters. Volumetric estimations

of the cerebral hemispheres were again performed on T₂-weighted images using the available built-in tools of Siemens *SyngoMR 2004A* software.

Analysis of BBB permeability changes was conducted on subtracted maps from the pre- and post-contrast T₁-SE images to highlight regions of Gd-DTPA extravasation. Gd-DTPA Permeable BBB Volume (PBV) in cubic centimeters (cm³) representing brain tissue with leaky BBB and the average pixel intensity (T₁SI_{diff}) of the hyper-intense enhanced regions derived from the subtraction maps were calculated using the built-in tools. The obtained values of the mean pixel intensity for the subtracted images (T₁SI_{diff}) are software generated (Siemens *syngoMR 2004A*). A product of T₁SI_{diff} and PBV (T₁SI_{diff} x PBV) has been considered to account for the observed temporal and spatial changes in the average pixel intensity of the enhanced regions (T₁SI_{diff}) and the brain volume with leaky BBB (PBV). The T₁SI_{diff} x PBV product serves as an indicator to quantify the overall entry of contrast agent into the brain over time. For sham analysis, the average PBV from the experimental group was projected onto the subtracted images of the sham animals, and T₁SI_{diff} was determined within this region.

Throughout the study, values are treated as mean ± Standard Error of Mean (SEM). Repeated measures Analysis Of VAriance ANOVA followed by Tukey-Kramer post-hoc tests have been considered for within-group comparisons. For between-group comparisons (experimental v/s sham group) at different time points, unpaired 't' tests with Welch correction were applied. A P value < 0.05 was considered significant. All statistical analyses were performed using the same Graphpad Prism software.

4.3. TROPHIC PROPERTIES OF EPIDERMAL GROWTH FACTOR AND PIGMENT EPITHELIUM DERIVED FACTOR ON SELECTED INDICES OF NEUROVASCULAR INJURY FOLLOWING ISCHEMIA-REPERFUSION INJURY IN RATS.

4.3.1. EVALUATION OF BLOOD BRAIN BARRIER PERMEABILITY FOR MACROMOLECULES.

Prior to the initiation of any treatment regimen with macromolecular peptides like EGF (Molecular Mass (MM): 6222 Da) and PEDF (MM: 50kDa), it's mandatory to map the BBB permeability changes that follows I/R injury in order to ensure that these NTFs are able to traverse the BBB and reach the brain parenchyma in adequate amounts so as to exert their protective effects at the selected time points. Evan's Blue (EB), due to its property of binding to serum albumin with the relatively large MM of 67kDa serves as a reliable marker to assess the BBB permeability characteristics. The extravasation of EB-albumin complex into the brain parenchyma is identified by the bluish coloration indicative of compromised BBB permeability due to I/R injury (260, 261).

4.3.1.1. EXPERIMENTAL DESIGN.

Male Sprague-Dawley (SD) rats weighing 250-300 g were divided into three groups with three animals in each group. The three groups were 3 hours Reperfusion group (3R), 6 hours Reperfusion group (6R) and 8 hours Reperfusion (8R) group. Animals were subjected to 60 minutes tMCAO with modifications as mentioned before (253, 254). The femoral vein was also kept cannulated for EB administration. In the 3R group, following

reperfusion for 3 hours EB was administered (2% EB in 0.9% saline, 4 ml/kg) through the femoral vein and was allowed to circulate for one hour. The same procedure was repeated at 6 hours and at 8 hours for animals belonging to the other two groups.

Following 1 hour circulation with EB, animals were deeply anesthetized with Pentobarbital (40 mg/kg i.p.) and the chest cavity was opened. Normal saline was perfused through the left ventricle at 110 mmHg, until a colourless perfusate was obtained from the right atrium.

The skull was immediately opened and the whole brain was taken out and was deep frozen at -80°C for 30 minutes. Following this, the frozen brain was cut into 1mm thick sections with a rodent brain matrix (ASI Instruments, USA). The sections were then gently placed on a transparent plastic film and subsequently scanned at 1200 dpi using an office document scanner (Scanjet 7650, Hewlett-Packard Company, USA) to obtain a digital image.

4.3.2. TREATMENT REGIMEN WITH EGF AND PEDF.

EGF and PEDF dosing regimens were prepared to achieve an equimolar dose of BDNF (MM: 28kDa) which at a dose of 50 µg / 300g rat was considered for its neuroprotective effect in a previous study (262). Dilutions of human recombinant PEDF (Creative Biomart, USA) and EGF (BIOTREND Chemikalien GmbH, Germany) were prepared in cold sterile water for injection (< 4°C) to achieve a final concentration of 89.28 µg / 1000 µl and 11.16 µg / 1000 µl respectively for a 300 g rat. These dilutions were prepared from previously constituted stock solutions, which was randomized and blinded from the experimenter. The dosing regimen, consisted of a bolus IV injection of 10 % of the dose

(100 μ l) followed by continuous infusion of the remaining 90% of the dose (900 μ l) at a rate of 225 μ l / hour for four hours employing a microinfusion pump (Harvard Apparatus Inc. Holliston, USA).

4.3.2.1. EXPERIMENTAL DESIGN.

Since, the animal strain had to be changed from Wistar to SD, tissue relaxation characteristics like T_2 , T_2^* and T_1 were estimated at the cortex and striatum following the same procedures as mentioned beforehand. Relaxation characteristics were estimated on this strain of healthy intact animals (N = 8) employing the same parameter dataset as provided in Table 1. In the subsequent text this group will be referred to as the ``Healthy`` group.

Three treatment groups consisting of EGF (N = 16), PEDF (N = 14) and saline treated control (N = 17) were considered. Male Sprague-dawley rats weighing 250-300 g were subjected to 60 minutes of tMCAO with modifications as mentioned before (253, 254). The femoral vein was also cannulated for EGF or PEDF / saline / contrast agent administration. Following three hours of reperfusion, the growth factor or saline was infused for 4 hours after a bolus loading dose (10% of the total dose).

During infusion, $\frac{3}{4}$ th of the syringe barrel was kept immersed in ice cold water ($< 3^\circ\text{C}$) for the entire duration of the infusion. The animal was then subjected to MR imaging at 24, 48, 96 hours and also at 1 week. Following the last imaging session at 1 week, the animal was anesthetized with Pentobarbital (40 mg/kg i.p.) and was transcardially perfused with ice cold PBS followed by 4% paraformaldehyde solution. The brain was immediately

removed, post fixed with 4% paraformaldehyde in PBS overnight and stored in PBS containing 30% sucrose for later immunohistochemical studies.

4.3.2.2. MAGNETIC RESONANCE IMAGING.

Serial MR imaging was performed at the pre-designated time points of 24, 48, 96 hours and 1 week post-reperfusion. T₂-TSE sequences were employed to visualise the temporal and spatial changes in vasogenic oedema formation. T₂-relaxometry was implemented to quantify the oedema water content. T₂^{*}-relaxometry was also performed to verify the hypothesis that, being sensitive to susceptibility effects caused by oxygenation level changes, the estimated T₂^{*}-values could provide vital clues towards the metabolic status of tissues under consideration (263).

Post-contrast T₁-SE sequences were also considered as described previously to determine the BBB permeability status to Gd-DTPA into the brain parenchyma resulting from compromised barrier characteristics. The dataset for estimating relaxometric parameters are as detailed in Table 4. The details of the employed sequence parameters are similar to that provided in Table 5, except that the slice thickness of T₂-TSE and T₁-SE has been increased to 1.5mm to match those images obtained with T₂^{*}-GRE.

4.3.2.3. DATA ANALYSIS.

The T₂-lesion volumes in cubic centimetres (cc/cm³) were determined by manually outlining the lesion employing the same built in tools of the Siemens SyngoMR 2004A software. The outlined area from each slice is multiplied by its ST to obtain the lesion

volume which was then added together and represented as a percentage of the total brain volume.

The required parameters for both (T_2 and T_2^*) relaxometric estimations in milliseconds (ms) and BBB permeability characteristics were acquired from a single coronal slice (1.5 mm thick) located at 6 mm posterior to the anterior tip of the frontal cortex, which possessed the largest infarct volume at 48 hours. Quantitative relaxometry was performed at three ROIs; The ROI at the ipsilateral striatum was placed carefully over the hyperintense region depicted by the T_2 -TSE image. The same region was copied and superimposed over an identical region at the contralateral side. Care was taken not to include any of the cerebral ventricles. A ROI was also defined at the healthy ipsilateral cortex well outside any region of infarction, if present.

Since the T_2 -lesion volume maximizes at the time point of 48 hours, the area of the ROI placed for this area has been kept constant for all the subsequent time points (i.e. the outlined area remains same for 48 hours, 96 hours and 1week). Such a procedure was adopted for both T_2 - and T_2^* - relaxometric estimations.

Since the T_2 -lesion volume continues to expand through the 24 hour time point until 48 hours the T_2 value obtained at 24 and 48 hours is strictly confined to the hyperintense T_2 -lesion site. Further, since the T_2 -value is averaged across the whole lesion volume and since this does not consider the expansion and thereby the change in volume of the lesions as such, one more calculation involving a multiplication of the T_2 -value (ms) to that of the lesion volume (cc) has also been performed to further appreciate the ``total`` oedema content. This calculation employs arbitrary units and is represented as `` T_{2vol} ``. Since the area of the ROI for T_2 relaxometric calculations from 48 hour time point is kept constant

for subsequent time points, which do not consider the existing infarct volume, no calculations of this kind was possible for 96 hours and 1 week time points.

To analyse the BBB permeability changes, digital subtraction maps from the pre- and post-contrast T₁-SE images were derived to highlight regions of Gd-DTPA extravasation. A ROI was defined on the subtraction map to encompass the whole of striatal region. The returned average pixel intensities (T₁SI_{diff}) were considered to represent the extent of Gd-DTPA extravasation.

Throughout the study, values are treated as mean ± SEM. Mono-exponential non-linear curve fitting to determine relaxation parameters and statistical data analysis was performed using Graphpad Prism Version 5.00 for Windows. One way-ANOVA with Tukey-Kramer post-hoc tests have been considered for comparisons between all pairs of groups and Dunnett's multiple comparisons test has been performed to compare healthy values to treated groups.

5.0. Results.

5.1. ESTABLISHMENT OF SMALL ANIMAL MAGNETIC RESONANCE IMAGING STRATEGIES ON A 3 TESLA CLINICAL DEDICATED HEAD MAGNETIC RESONANCE SCANNER.

5.1.1. CONFIGURATION AND OPTIMIZATION OF SEQUENCE PARAMETERS.

The T_1 , T_2 and T_2^* values determined at the cortical and striatal regions of the rat and mouse brains are given in Table 6. All these values exhibited negligible inter-hemispherical differences. Rat spinal relaxation values (T_1 and T_2) along with rel-PD values at the gray and white matter of the thoracic (T10) region are also detailed. Statistically significant differences were found only between T_2^* values of cortex and striatum of the rat and mouse brains and rel-PD values of gray and white matter of the rat spine.

Animal Brain/Spine	Rat				Mouse	
	Brain (Mean \pm SEM)		Spine (Mean \pm SEM)		Brain (Mean \pm SEM)	
Region	Cortex	Striatum	Gray matter	White matter	Cortex	Striatum
T_2 -value (ms)	76.69 \pm 3.9	69.995 \pm 3.9	79.92 \pm 4.97	87.65 \pm 9.32	77.8 \pm 13.1	69.29 \pm 6.74
T_1 -value (ms)	1064.76 \pm 18.45	968.64 \pm 31.9	730.8 \pm 70.62	871.65 \pm 91.22	1201.5 \pm 70.1	1081.5 \pm 56.73
T_2^* -value (ms)*	67.71 \pm 4.169	53.17 \pm 4.4	-	-	32.13 \pm 5.97	20.39 \pm 2.92
rel-PD (%)*	-	-	56.02 \pm 0.96	43.98 \pm 0.96	-	-

T_2 -value, transverse relaxation time; T_1 -value, longitudinal relaxation time; rel-PD, relative proton density, * $P < 0.0001$., considered extremely significant. T_2^* -value, susceptibility weighted transverse relaxation time, * $P = 0.0254$ (Rat), 0.0185 (Mouse), considered significant.

Table 6. Tissue relaxation characteristics at the considered anatomical regions of the rodent brain, spinal cord and mouse brain.

The PI RAs, GRAPPA and mSENSE demonstrated distinctly different properties in relation to mean signal, their SD_{diff} and reconstruction related artefacts for the employed

EPI sequences. Irrespective of DW- or PE-EPI sequences, implementation of PI consistently shortened the TE value and thereby demonstrated an increase in mean signal. In the case of DW-EPI, GRAPPA reconstruction at an AF of 3 demonstrated peak SNR accompanied by minimal SD_{diff} , whereas, parallel acquisition with the maximum allowed AF of 4 resulted in reconstruction related artefacts. DW-EPI with mSENSE RA at an AF of 4 could not be completed as the image reconstruction programme raised exceptions.

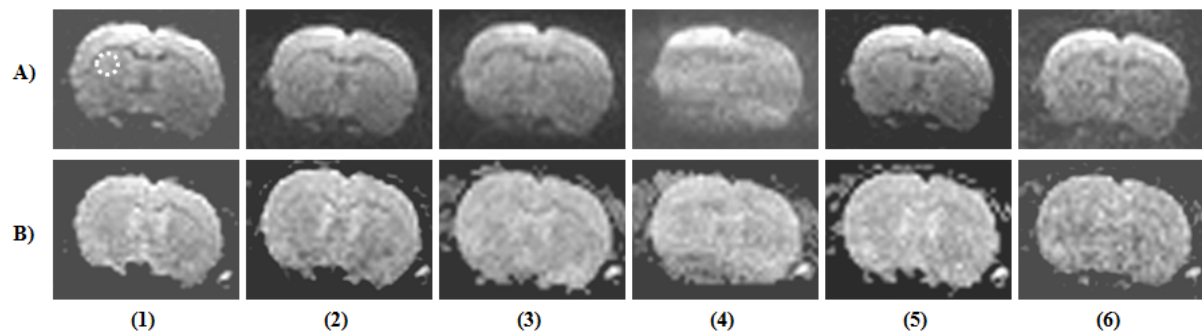


Figure 28. DW-EPI of a rat brain with and without parallel imaging. Row (A) DW-EPI images ($b = 1000 \text{ s/mm}^2$) and row (B) their corresponding ADC maps. First column contains images acquired without implementing PI. Columns (2-4) contains image sets acquired with the RA, GRAPPA employing AFs from 2-4. Columns (5-6) represent images acquired with the RA, mSENSE at AFs 2 & 3. The white dotted circle represents the area considered for calculating the signal-to-noise ratio.

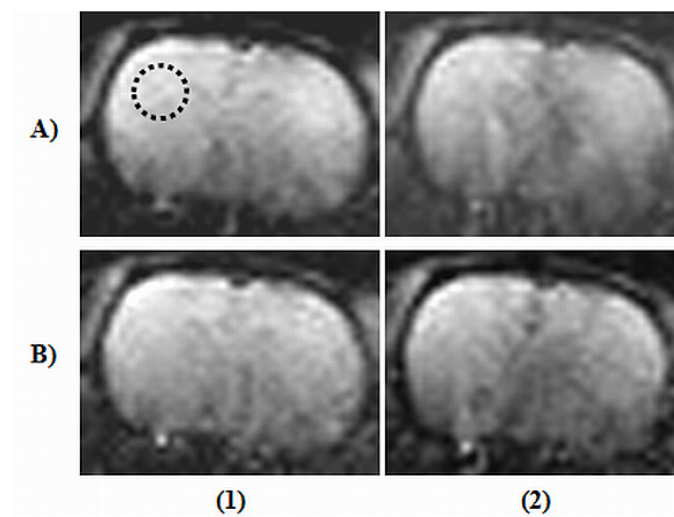


Figure 29. PE-EPI of a rat brain with parallel imaging. Two reconstruction algorithms namely, GRAPPA and mSENSE at AFs 3 & 4 has been considered. Image sets (A1) and (A2) represents PE-EPI images acquired with GRAPPA at AFs 3 & 4 respectively and images (B1) and (B2) includes acquisitions with mSENSE at the same AFs. The black dotted circle represents the area considered for calculating signal-to-noise ratio.

RA	PI features			Image set-01		Image set-02		MI	SD _{diff}	SNR
	AF	TE	ACS	SI	SD	SI	SD			
GRAPPA	4	87	45	130.2	15.7	129	19.1	129.6	3.4	26.95
mSENSE	4	87	45	Image reconstruction failed!						
GRAPPA	3	90	39	116.4	11.1	114.6	10.8	115.5	0.3	272.24
mSENSE	3	90	39	113.3	15.1	112	18.2	112.65	3.1	25.7
GRAPPA	2	99	30	93.8	14.9	93.1	14	93.45	0.9	73.42
mSENSE	2	99	30	90.8	16.9	97.6	15.8	94.2	1.1	60.55
No RA	--	128	--	64.6	11.4	65.4	10.8	65	0.6	76.6

RA, reconstruction algorithm; PI, parallel imaging; AF, acceleration factor; TE, echo time; ACS, auto-calibration scanning lines; SI, signal intensity; SD, standard deviation; MI, mean intensity; SD_{diff}, standard deviation difference; SNR, signal-to-noise ratio, GRAPPA, generalized auto-calibrating partially parallel acquisition; mSENSE, modified sensitivity encoding.

Table 7. Effect of two reconstruction algorithms on the SNR of DW-EPI images.

RA	PI features			Image set-01		Image set-02		MI	SD _{diff}	SNR
	AF	TE	ACS	SI	SD	SI	SD			
GRAPPA	4	27	70	416.7	42.4	430.8	39.5	423.75	2.9	103.3
mSENSE	4	27	70	498.4	52.5	492	53.3	495.2	0.8	437.7
GRAPPA	3	32	63	387.9	21.5	375.1	18	381.5	3.5	77.07
mSENSE	3	32	63	411.6	34.7	397.9	33	404.75	1.7	168.3

RA, reconstruction algorithm; PI, parallel imaging; AF, acceleration factor; TE, echo time; ACS, auto-calibration scanning lines; SI, signal intensity; SD, standard deviation; MI, mean intensity; SD_{diff}, standard deviation difference; SNR, signal-to-noise ratio, GRAPPA, generalized auto-calibrating partially parallel acquisition; mSENSE, modified sensitivity encoding.

Table 8. Effect of two reconstruction algorithms on the SNR of PE-EPI images.

Further, mSENSE RA provided lower mean signal intensity and increased SD_{diff} compared to that of GRAPPA with AFs of 2 & 3. In the case of PE-EPI, mSENSE acquisitions demonstrated higher mean signal intensity and lower variations in SD_{diff} at the AFs of 3 and 4 compared to that of GRAPPA based RA. The change in mean signal intensity, SD_{diff} , and the calculated SNR for both GRAPPA and mSENSE at the considered AFs are detailed in Table 7 & 8 for DW- and PE-EPI respectively. Representative DW-EPI images ($b = 1000 \text{ s/mm}^2$) acquired with both GRAPPA and mSENSE along with their corresponding ADC maps are shown in Figure 28. Further, PE-EPI acquisitions with both RAs acquired with the two AFs are shown in Figure 29. The acquired image characteristics are as detailed in Table 9.

Pathology	Ischemic stroke				ICH	Spine Injury	GBM	
Animal	Rat						Mouse	
Sequence	DW-EPI	PE-EPI	T ₂ -TSE	T ₁ -SE	T ₂ [*] -GRE	T ₂ + PD TSE	T ₂ -TSE	T ₁ -SE
IPR(mm)	0.4 x 0.4	0.4 x 0.4	0.2 x 0.2	0.2 x 0.2	0.2 x 0.2	0.2 x 0.2	0.2 x 0.2	0.2 x 0.2
ST(mm)	1	1	1	1	1.5	1.5	1	1
NoS	15	15	15	15	10	20	9	9
AT(min:sec)	3:36	1:40	5:39	11:34	4:18	20:00~25:00*	10:28	11:48

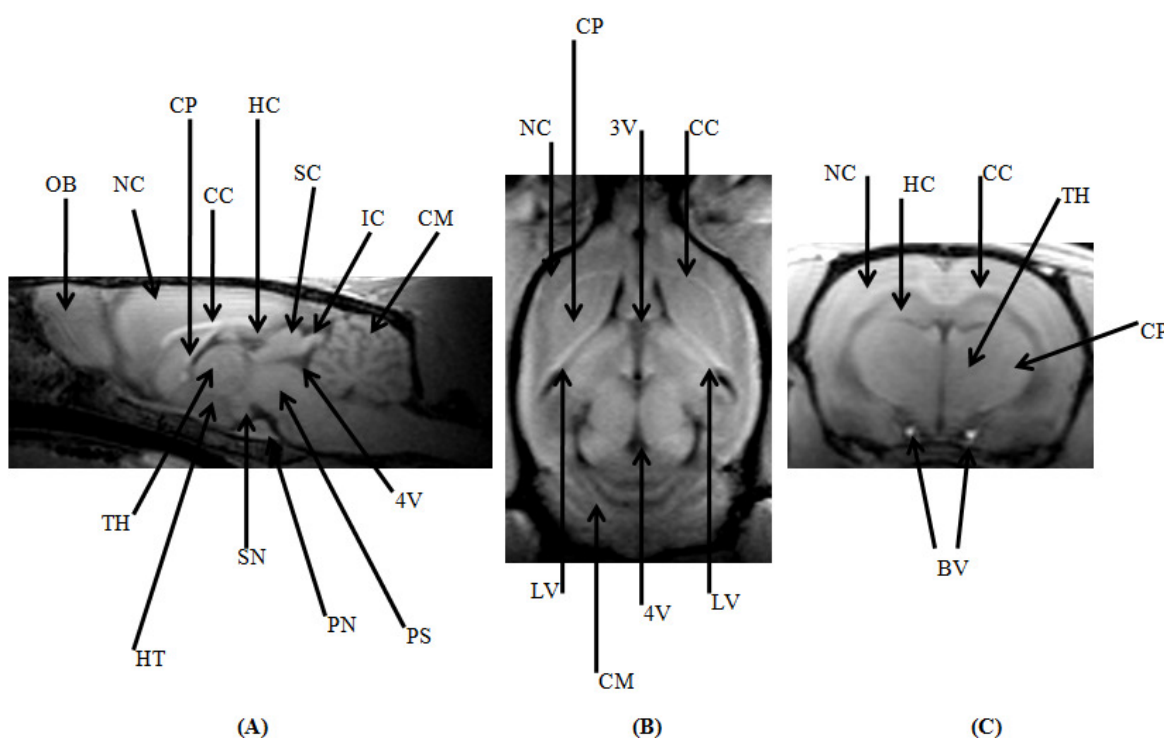
ICH, intra-cerebral haemorrhage; GBM, glioblastoma; DW-EPI, diffusion weighted echo planar imaging; PE-EPI, perfusion echo planar imaging; T₂-TSE, T₂-weighted turbo spin echo; T₁-SE, T₁-weighted spin echo; T₂^{*}-GRE, susceptibility weighted gradient recalled echo; PD-TSE, proton density weighted turbo spin echo; IPR, in-plane resolution; ST, slice thickness; NoS, number of Slices; AT, acquisition time.

Table 9. Image acquisition characteristics achieved with the different sequence types.

5.1.2. 3D-MPRAGE CHARACTERIZATION OF RAT BRAIN ANATOMY.

Representative images of an intact rat brain in mid-sagittal plane (Figure 30A), axial plane at the level of eyes (Figure 30B) and in the coronal plane (Figure 30C) are provided. The acquired images had an in-plane resolution of 200 μm with an ST of 1 mm. The 3D acquisition with 15 contiguous slices acquired with 4 averages consumed 18 minutes and 16 seconds. The T₁-weighted MPRAGE sequence clearly represented the cerebrospinal

fluid filled spaces as hypo-intense regions, the corpus callosum as a hyper-intense band separating the cortical and sub-cortical structures. The mid-sagittal section could clearly characterize a number of different anatomical regions like, the olfactory bulb, neocortex, caudate putamen, corpus callosum, cerebellum, 4th ventricle, hippocampus, superior and inferior colliculus, pons, pontine nuclei, substantia nigra, hypothalamus and thalamic regions.



OB, olfactory bulb; NC, neocortex; CP, caudate putamen; CC, corpus callosum; HC, hippocampus; SC, superior colliculus; IC, inferior colliculus; CM, cerebellum; 4V, 4th ventricle; PS, pons; PN, pontine nuclei; SN, substantia nigra; HT, hypothalamus; TH, thalamus; 3V, 3rd ventricle; LV, lateral ventricle; BV, blood vessels (internal carotid arteries)

Figure 30. 3D-MPRAGE data sets of a rat brain in three orthogonal planes. (A) Mid-sagittal plane, (B) Axial plane at the level of the eyes and, (C) Coronal plane.

The axial plane again portrayed the neocortex, corpus callosum, caudate putamen, cerebellum along with lateral, 3rd and 4th ventricles. The coronal section adequately represented many of the previously mentioned regions like the neocortex, corpus callosum,

thalamus, caudate putamen along with the hippocampi. Two bright spots indicative of intact internal carotid arteries could also be clearly distinguished.

5.1.3. THE RAT MODEL OF CEREBRAL ISCHEMIA.

One hour post-tMCAO, sequels of diffusion and perfusion deficits, as confirmed by DW- and PE-EPI images along with a T₂-weighted image is provided in Figure 31. Representative DW-EPI image ($b = 1000 \text{ s/mm}^2$) (Figure 31-A1) acquired with the PI RA GRAPPA and the corresponding ADC map (Figure 31-A2) clearly depict the ischemic area.

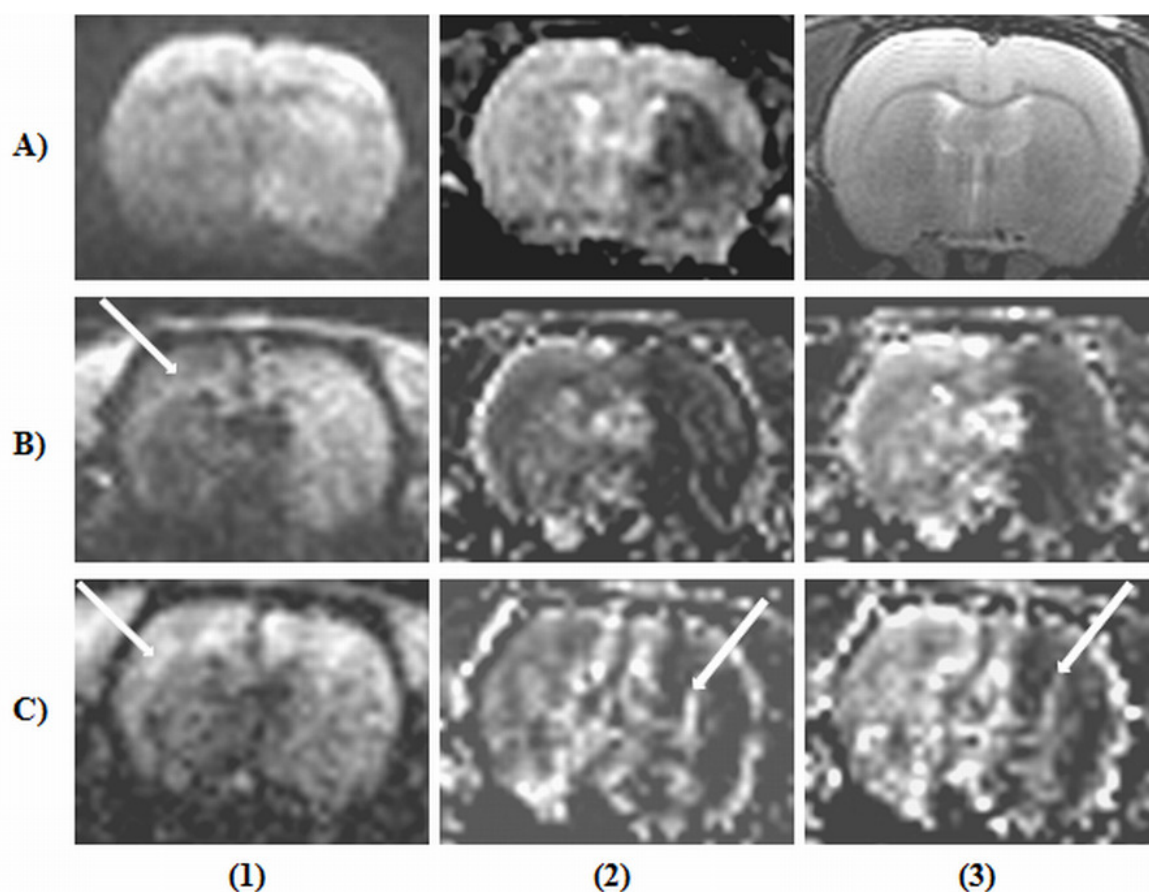


Figure 31. Representative images depicting diffusion and perfusion characteristics of an ischemic rat brain. Data sets acquired at 1 hour post-tMCAO includes, (A1) DW-EPI image ($b = 1000 \text{ s/mm}^2$), (A2) Corresponding ADC map, and (A3) T₂-TSE image. Row (B) represents PE-EPI images acquired with the RA, GRAPPA at AF of 4. (B1) PE-EPI acquisition demonstrating altered perfusion characteristics following tMCAO, (B2) derived rel-CBV map and (B3) rel-CBF map. Row (C) represents PE-EPI images acquired with the RA, mSENSE at AF 4. (C1) PE-EPI acquisition, (C2) rel-CBV map and (C3) rel-CBF map. Arrow marks on images (B1) and (C1) indicates differential sensitivity to first-pass Gd-DTPA and the arrows on (C2) and (C3) may probably indicate reconstruction related artefacts.

The PE-EPI image (Figure 31-B1) acquired with GRAPPA demonstrates well defined regions of perfusion deficit. Derived perfusion parameters like, rel-CBV (Figure 31-B2), rel-CBF (Figure 31-B3), maps are in good agreement with the obtained DW-EPI and ADC images indicating compromised blood flow characteristics typical of this pathology.

However, PE-EPI images (Figure 31-C1) acquired with mSENSE demonstrated reduced sensitivity to the first-pass of Gd-DTPA which can be clearly discerned, at the cortical region by a reduction in signal attenuation due to the passage of Gd-DTPA. The derived perfusion maps including rel-CBV (Figure 31-C2) and rel-CBF (Figure 31-C3) demonstrated altered rel-CBV and rel-CBF characteristics at the ischemic region which are not in total agreement with the GRAPPA derived maps. The acquired T₂-TSE image without any noticeable changes is also provided (Figure 31-A3).

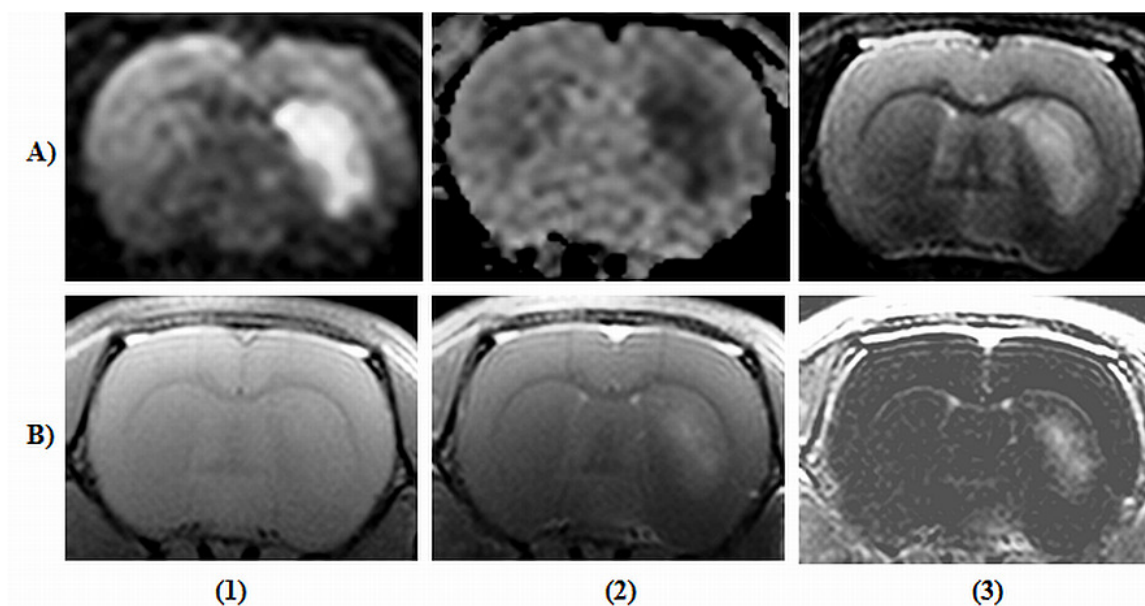


Figure 32. Representative images of a rat brain at 4 hours post-reperfusion. Following 90 minutes of transient middle cerebral artery occlusion, animal was allowed to reperfuse for 4 hours before the following acquisitions were made. A1) DW-EPI image, A2) ADC map, A3) T₂-TSE image, B1) Pre-contrast T₁-SE image, B2) Post-contrast T₁-SE image, B3) Subtraction image.

Representative images from another rat at 4 hours post-reperfusion are shown in Figure 32. Hyper intense ischemic lesions could be clearly delineated on DW-EPI and T₂-TSE

images (Figure 32-A1 & -A3), which co-localized with regions of reduced ADC (Figure 32-A2). Subtraction image (Figure 32-B3) derived from pre-and post-contrast T_1 -SE images (Figure 32-B1 & -B2) clearly depict regions of altered BBB permeability following ischemia-reperfusion injury. The acquired image characteristics are detailed in Table 9.

5.1.4. THE RAT MODEL OF INTRA-CEREBRAL HAEMORRHAGE.

The longitudinal study performed at multiple time points with T_2 -TSE and T_2^* -GRE sequences duly detected blood and/or degraded blood products like haemosiderin during these time points (Figure 33). T_2 -TSE image within 1 hour of the injury portrayed the characteristic hyper-intense border along with hypo-intense representation of the location and extent of hematoma (Figure 33-A1). Susceptibility (T_2^*)-weighted images also spatially localized the hematoma throughout the intended duration of the study. The acquired image characteristics are as detailed in Table 9.

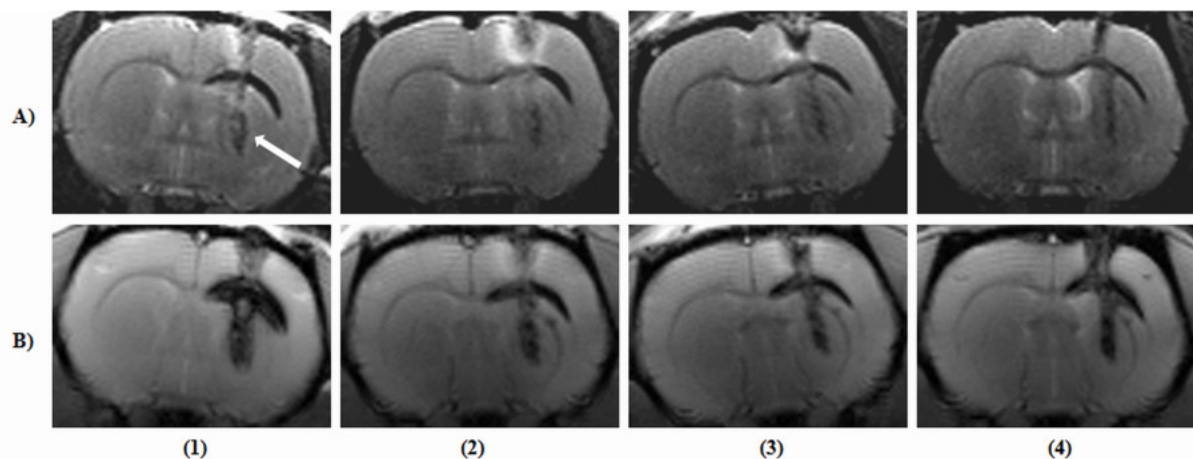


Figure 33. Image datasets obtained from a rodent brain following intra-cerebral haemorrhage. The study monitored up to one month includes, Row (A), T_2 -TSE images. Row (B), T_2^* -GRE images. Column (1), images acquired within an hour of injury ; (2) at 72 hours; (3) at 1 week; (4) at 1 month post-injury. The arrow indicates the bright rim surrounding the hematoma due to oedema formation and/or extruded serum from the injected blood.

5.1.5. THE RAT MODEL OF CERVICAL AND THORACIC SPINAL CORD INJURIES.

The images obtained from the healthy intact rodent spine at the thoracic (T10) region characterized with T₂- and PD- TSE sequences in both the sagittal and coronal planes are provided (Figure 34). No motion related artefacts were discernible with the images acquired in both planes. The T₂-TSE coronal section (Figure 34C) could clearly delineate the spinal tissue from the bright encircling CSF, whereas, the PD-TSE image depicted the 'H' shaped gray matter (Figure 34D) from the surrounding white matter tissue.

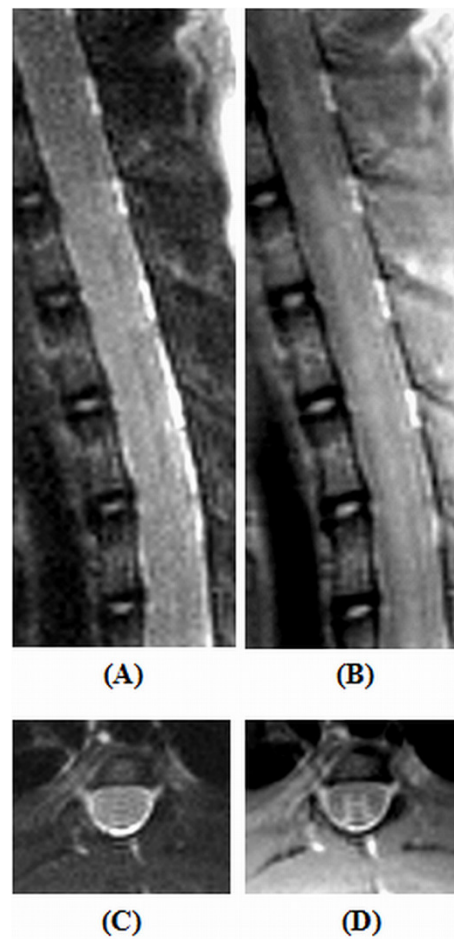


Figure 34. Images acquired from normal healthy rodent spine at the thoracic T(10) level. (A) and (C), T₂-TSE images in sagittal and coronal planes. (B) and (D), PD-TSE images in sagittal and coronal planes.

Representative T₂- and PD-TSE images in both coronal and sagittal planes of cervical lesion post 24 hours are provided (Figure 35). T₂-TSE images clearly depicted the hyper-intense band attributed to oedema/serum formation with hypo-intense spots due to hematoma (Figure 35-A & C). PD-TSE images also portrayed the same sequels albeit lower sensitivity but with added gray-white matter contrast (Figure 35-B & D).

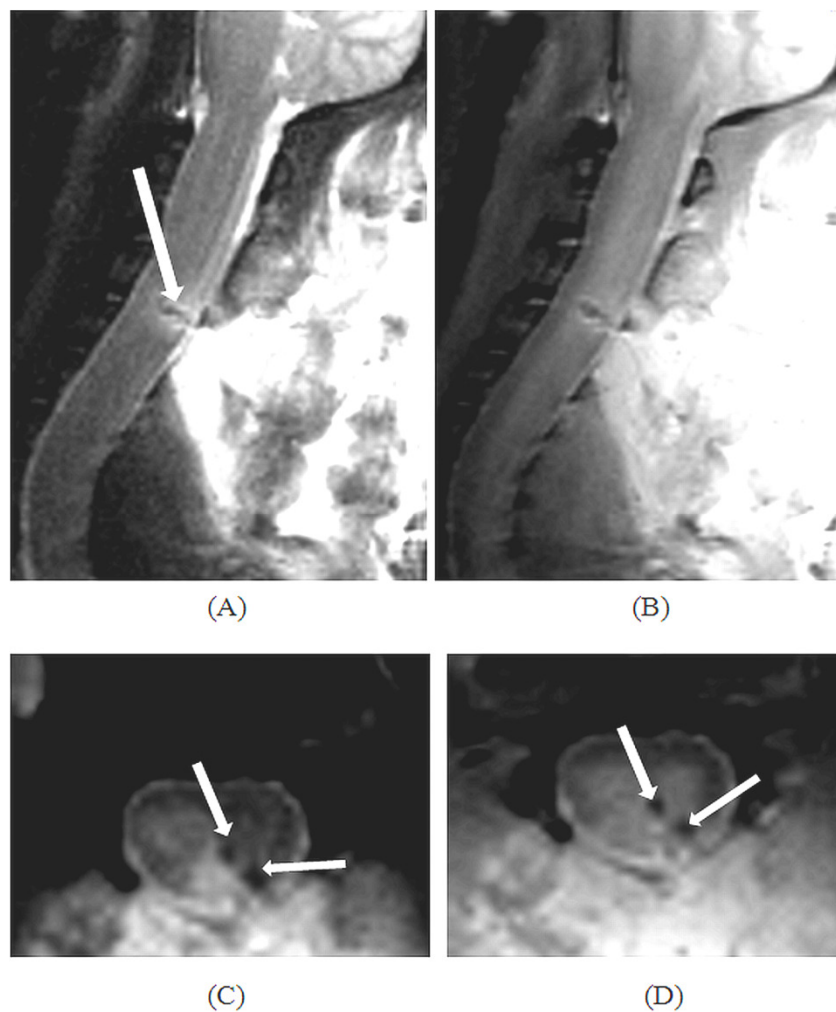


Figure 35. Tungsten wire knife induced cervical spinal lesion at 24-hours post-injury. (A) Sagittal T₂-TSE image. Arrow indicates the surrounding oedema and/or serum (bright band) extruded from the blood ; (B) Sagittal PD-TSE image ; (C & D) Coronal T₂-TSE and PD-TSE images. Arrow marks indicate localized hematoma formation.

T₂- and PD-TSE images in both coronal and sagittal planes from another animal 30 days post cervical injury along with their histology are provided (Figure 36). T₂-TSE images clearly characterized cyst formation as confirmed by histological sections (Figure 36- A, C ,E & F) whereas PD-TSE images portrayed injury along with a clear delineation of the gray-white matter structure confirmed by Nissl stained histology section (Figure 36- B, D & F).

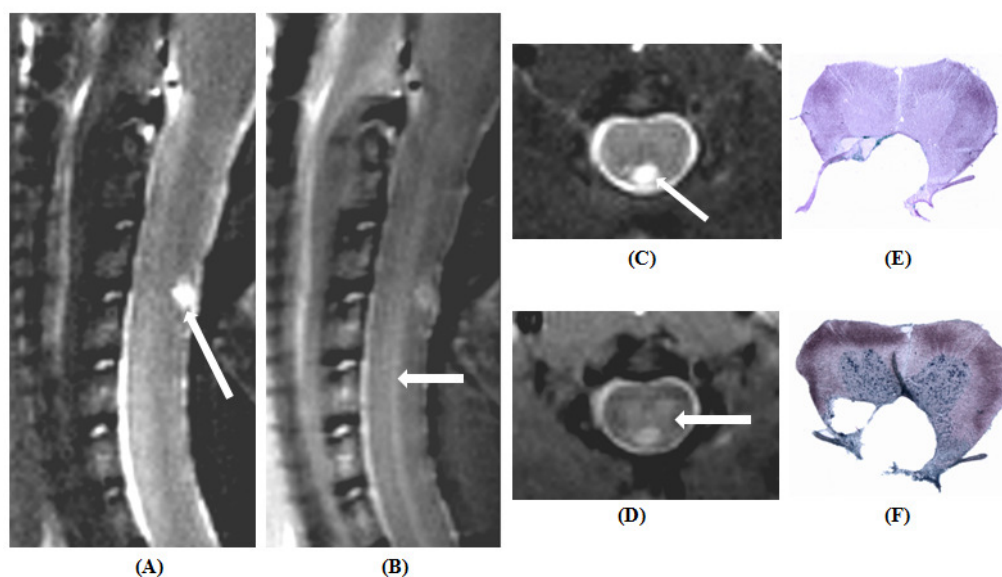


Figure 36. Tungsten wire knife induced cervical spinal lesion at 30-days post-injury. (A & C) Sagittal and coronal T₂-TSE images. Arrows indicate fluid filled cyst as confirmed by Prussian blue and Nissl stained histological sections (E & F). (B & D) Sagittal and coronal PD-TSE images. Arrows indicates the visible gray matter tracts.

Images in multiple planes (sagittal, axial and coronal) from 30-day post-contusion lesion along with histological correlates are provided (Figure 37). T₂-TSE images, irrespective of the acquisition planes sensitively captured haemosiderin and cyst formation as confirmed by Prussian blue staining (Figure 37-A, B, E & G). PD-TSE images demonstrated a complete loss of gray-white matter contrast at the site of injury as confirmed by Nissl stained histology and by the existed lower body paralysis of the animals (Figure 37-C, D, F & H). Image acquisition characteristics are as provided in Table 9.

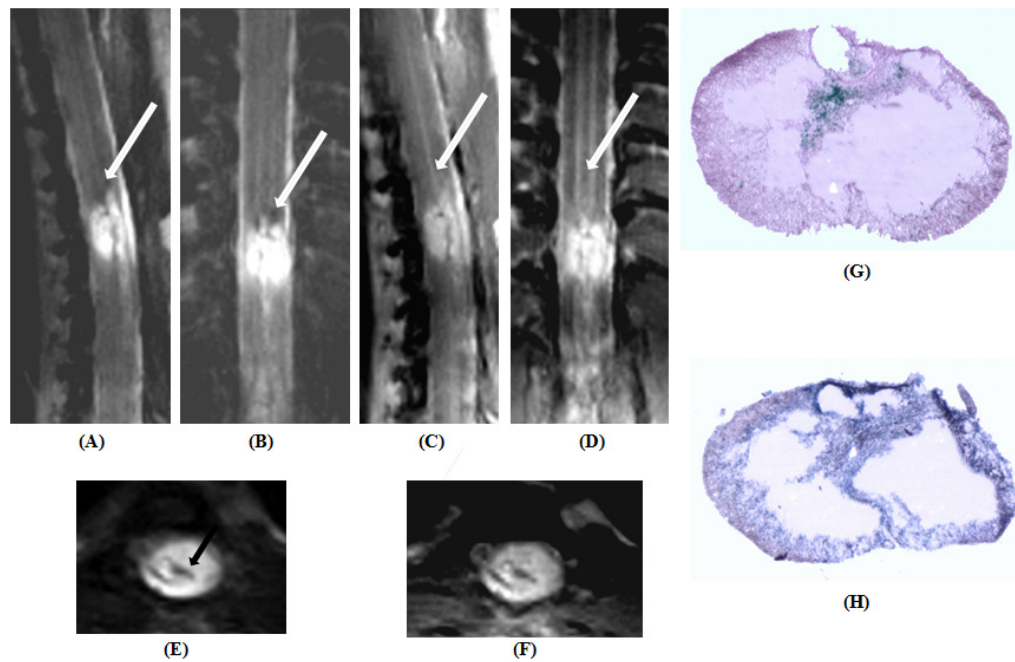


Figure 37. Representative images depicting spine contusion injury at the thoracic (T10) level post 30 days. (A, B & E) Sagittal, axial and coronal T₂-TSE images. Arrow marks point to haemosiderin deposits, presence of which is confirmed by Prussian blue staining (G). (C, D & F) Sagittal, axial and coronal PD-TSE images. Arrow marks point to gray matter tracts, contrast of which is completely lost at the site of injury. (H) Nissl stained histological section confirms the complete loss gray matter tissue.

5.1.6. THE MOUSE MODEL OF GLIOBLASTOMA.

The MR signatures of HCSC induced murine xenograft GBM are given (Figure 38). T₂-TSE image captured the fluid filled necrotic core of the tumour with surrounding hyperintense regions indicative of invading tumour cells and these features closely correlates with the provided Hematoxyllin and Eosin (H & E) stained histological section (Figure38-A1,3). Meanwhile, T₂^{*}-GRE image and the histology did not detect any haemorrhage which may co-exist with tumour (Figure 38-A2,3).As expected, post-contrast T₁-SE image (Figure38-B2) clearly localizes Gd-DTPA extravasation to the necrotic core detected by T₂-TSE image but not to the invading brain parenchyma. Image acquisition details are as provided in Table 9. The tumour volumes determined from T₂-TSE images and from the histological study are detailed in Table 10. The Pearson correlation coefficient (r) was 0.9214 with significant correlation ($P < 0.0001$).

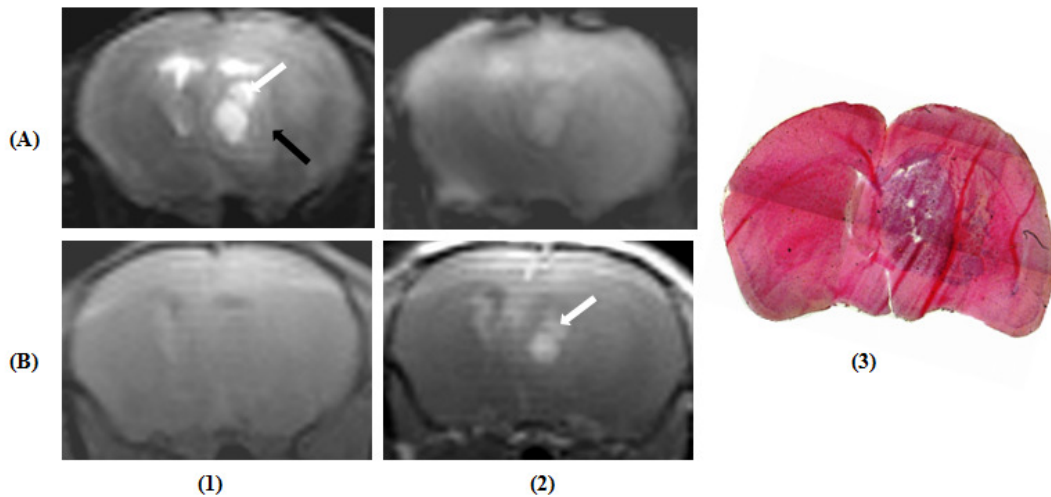


Figure 38. Representative images of a mouse brain with glioblastoma. (A1) T₂-TSE image. Bright arrow points to fluid filled necrotic core and dark arrow points to hyperintense regions attributed to invading tumour cells; (A2) Corresponding T₂^{*}-GRE image, (B1) Pre-contrast T₁-SE image, (B2) Post-contrast T₁-SE image. Arrow indicate region of Gd-DTPA extravasation, (3) Hematoxyllin and Eosin stained tissue sections depicting the purple coloured tumourous tissue.

Animal ID	MRI tumour volume (mm³)	Histological tumour volume (mm³)
1	3.72	1.2
2	4.4	0.35
3	5.28	1.16
4	0.57	0.49
5	2.64	0.396
6	1.0	0.39
7	0.45	0.0
8	1.34	0.0
9	10.4	6.3
10	17	8.7
11	4.3	2.08
12	1.04	0.44
13	2.75	2.87
14	2.3	2.5
15	1.2	1.2

Table 10. Comparison of tumour volumes determined by MRI and the histological study.

5.2. SERIAL MAGNETIC RESONANCE IMAGING TO DETERMINE THE BLOOD BRAIN BARRIER PERMEABILITY CHANGES AND THE DYNAMIC FLUXES IN VASOGENIC OEDEMA FORMATION FOLLOWING ISCHEMIA-REPERFUSION INJURY IN RATS.

Three out of 11 animals did not survive the duration of this study, making for an effective $N = 8$ for the experimental group. Representative images for T_2 -TSE, acquired ADC maps and T_1SI_{diff} are shown in Figure 39 for 04PR, 24PR, and 48PR time points.

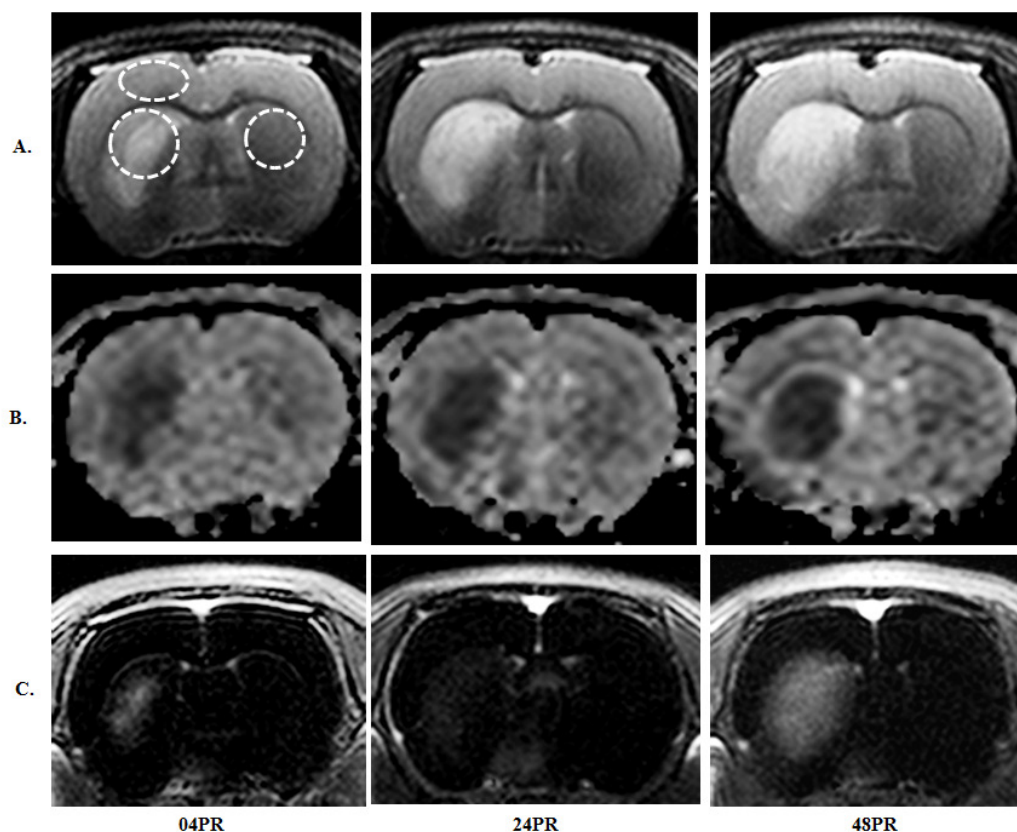


Figure 39. Representative T_2 -TSE images (Row A), T_1 -SE subtraction maps (T_1SI_{diff}) (Row C) and the corresponding ADC maps (Row B) at 04, 24 and 48 hours post-reperfusion. Highlighted areas (as in upper left image) have been considered for T_2 -relaxometric estimations.

5.2.1. BI-PHASIC BBB OPENING AND PROGRESSION OF BRAIN VOLUME WITH LEAKY BBB FOLLOWING ISCHEMIA-REPERFUSION INJURY AS INVESTIGATED BY POST-CONTRAST T₁-SEQUENCES.

The temporal profiles of BBB leakage (post-contrast T₁SI_{diff}) and the overall extravasated contrast agent (T₁SI_{diff} x PBV product) for the ipsilateral hemisphere are compared to sham (Figure 40A and B). Post-contrast T₁SI_{diff} profiles of the contralateral striatum are again compared to that of sham (Figure 40C).

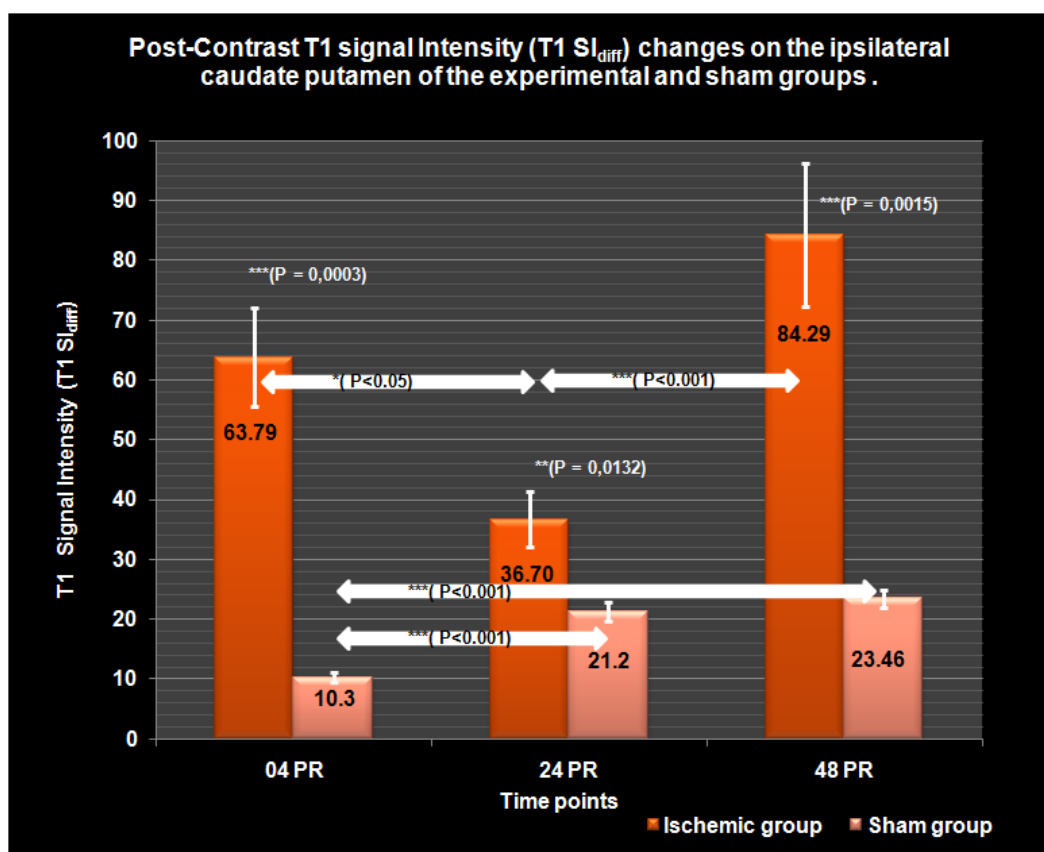


Figure 40A. Post-contrast T₁ signal intensity (T₁SI_{diff}) changes on the ipsilateral caudate putamen of the experimental and sham groups.

At 04PR, the post-contrast T₁SI_{diff} value at the ipsilateral striatum of the experimental group was found to be significantly elevated (63.79 ± 8.2) compared to sham group (10.3 ± 0.79 , $P = 0.0003$). The brain volume with leaky BBB (PBV) at the ipsilateral hemisphere

of the experimental group was $0.13 \pm 0.02 \text{ cm}^3$ and the $T_1SI_{\text{diff}} \times \text{PBV}$ value was also significantly higher (8.67 ± 1.77) to that of sham (1.34 ± 0.23 , $P = 0.0002$). In contrast, there was a non-significant drop in the post-contrast T_1SI_{diff} intensity at the contralateral hemisphere (10.95 ± 1.28) when compared to sham (12.5 ± 1.8).

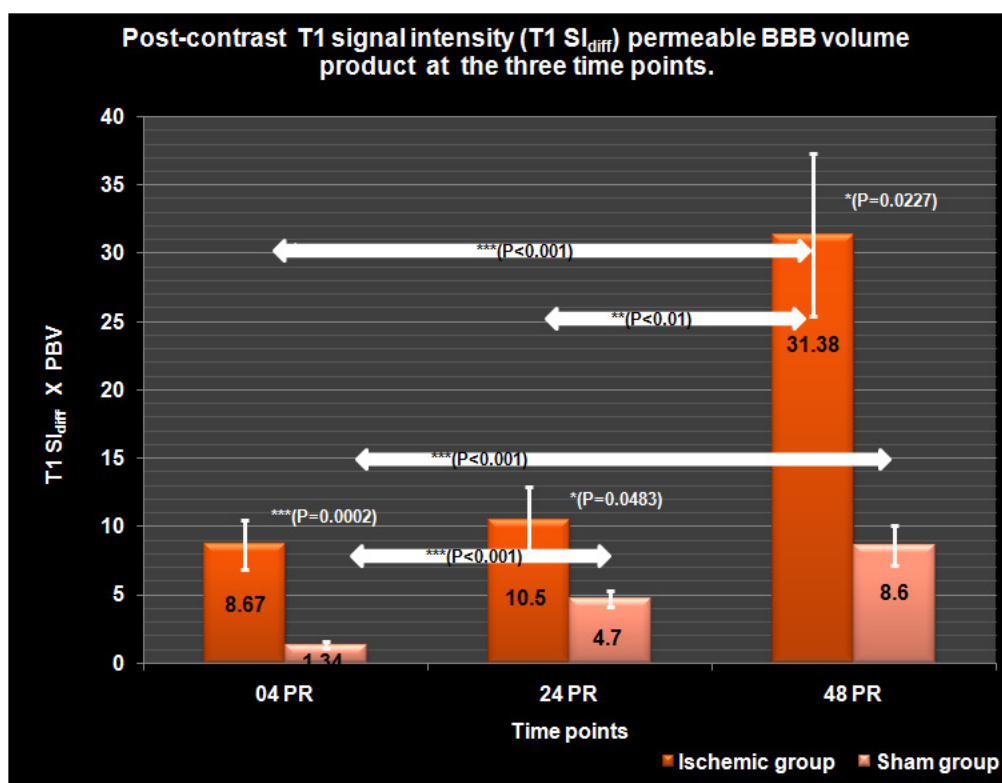


Figure 40B. Post-contrast T_1 signal intensity (T_1SI_{diff}) permeable BBB volume (PBV) product changes on the ipsilateral caudate putamen of the experimental and sham groups.

By 24PR, post-contrast T_1SI_{diff} (36.70 ± 4.61) declined significantly to that at 04 PR ($P < 0.05$). However, the observed value was still significantly higher than sham control (21.2 ± 1.623 , $P = 0.0132$). The PBV doubled in volume ($0.265 \pm 0.032 \text{ cm}^3$) and was significantly more widespread compared to 04PR ($P < 0.05$). The $T_1SI_{\text{diff}} \times \text{PBV}$ demonstrated a non significant increase (10.50 ± 2.43) compared to 04PR, but was

significantly higher than sham (4.7 ± 0.60 , $P = 0.0483$). On the contralateral side, the post-contrast T_1SI_{diff} intensity (12.11 ± 1.61) was not significantly increased in comparison to 04PR, while being significantly lower than sham values (19.9 ± 0.85 , $P = 0.0004$).

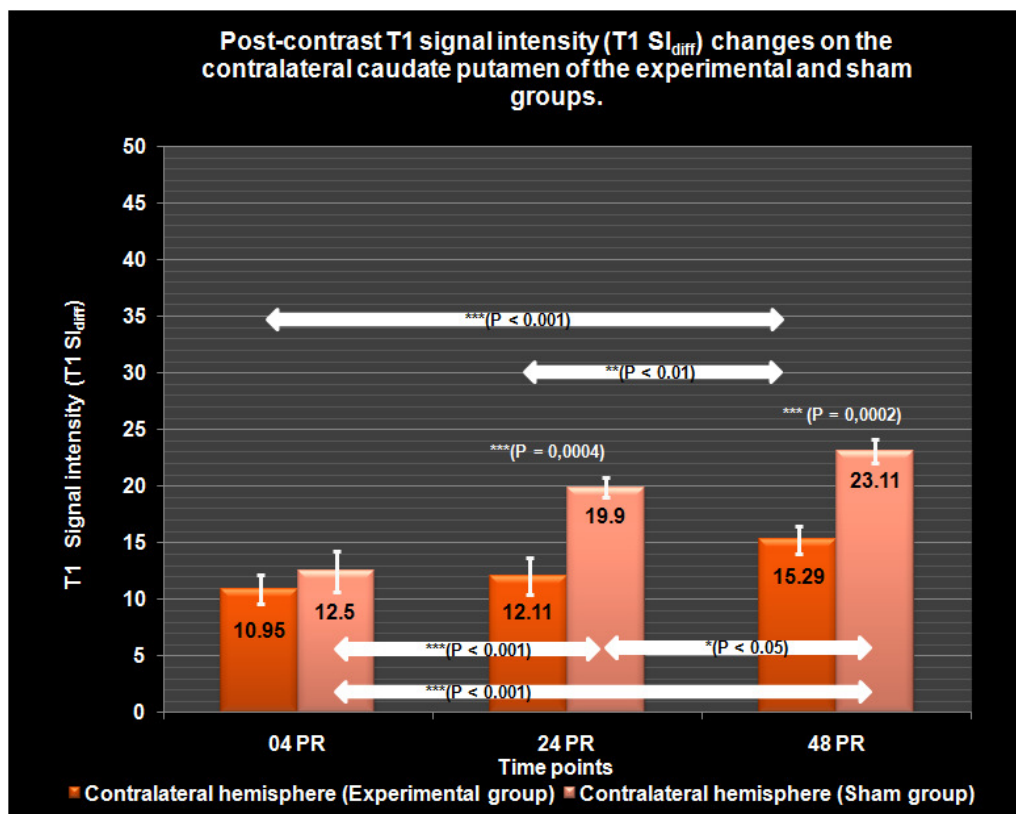


Figure 40C. Post-contrast T_1 signal intensity (T_1SI_{diff}) changes on the contralateral caudate putamen of the experimental and sham groups.

The 48PR post-contrast T_1SI_{diff} value (84.29 ± 11.99) was significantly higher than 24PR ($P < 0.001$) and sham (23.46 ± 1.52 ; $P = 0.0015$). The increase in the ipsilateral PBV ($0.36 \pm 0.055 \text{ cm}^3$) was non-significant, but the $T_1SI_{diff} \times \text{PBV}$ product (31.38 ± 5.98) was significantly higher compared to 24PR ($P < 0.01$) and also to that of sham (8.6 ± 1.44 , $P = 0.0227$). On the contralateral side, the post-contrast intensity (15.29 ± 1.19) was significantly higher compared to 24PR ($P < 0.01$), while being significantly lower than sham (23.11 ± 1.088 , $P = 0.0002$).

5.2.2. IPSILATERAL AND REMOTE OEDEMA FORMATION AS INVESTIGATED BY THE TEMPORAL PROFILE OF TRANSVERSE RELAXATION TIMES.

Transverse relaxation times from healthy, ischemic, and reperfused tissues are shown for the ipsi- and contralateral striatum along with the cortical region on the ipsilateral side (Figure 41 A-C). The control T_2 values indicative of increased water content obtained at the cortex was 73.04 ± 2.313 ms with negligible inter-hemispherical difference while the striatal values were 68.56 ± 3.58 ms and 66.68 ± 1.38 ms at the ipsi- and contralateral hemispheres, respectively.

During tMCAO (BR) the T_2 values dropped at the ipsilateral cortex (63.59 ± 2.52 ms) and striatum (57.64 ± 2.625 ms), while the contralateral striatal T_2 value was slightly elevated (72.75 ± 5.617 ms). However, none of these changes were statistically significant. Following reperfusion (AR), the T_2 value at the ipsilateral striatum showed a significant increase to 72.05 ± 3.4 ms ($P < 0.05$), whereas the cortical value incremented insignificantly (71.62 ± 3.7 ms) compared to BR. Again, the contralateral striatal T_2 values declined (70.54 ± 4.6 ms) insignificantly to that of BR. By 04PR, the T_2 values at the ipsilateral (86.31 ± 3.71 ms; $P < 0.01$) and contralateral striatum (84.55 ± 3.36 ms, $P < 0.05$) were significantly elevated compared to the corresponding control values. However, the cortical T_2 values showed only a marginal increase (74.7 ± 3.59 ms) to that of the control. The corresponding ipsilateral hemispherical volume was 0.60 ± 0.01 cm³.

At 24PR, the ipsilateral striatal T_2 value (98.68 ± 3.12 ms) increased significantly compared to both 04PR ($P < 0.05$) and control ($P < 0.001$) associated with significant increase in the ipsilateral hemispheric volume (0.62 ± 0.02 cm³, $P < 0.05$). The corresponding cortical T_2 value (72.84 ± 2.41 ms) was non-significantly reduced to that at

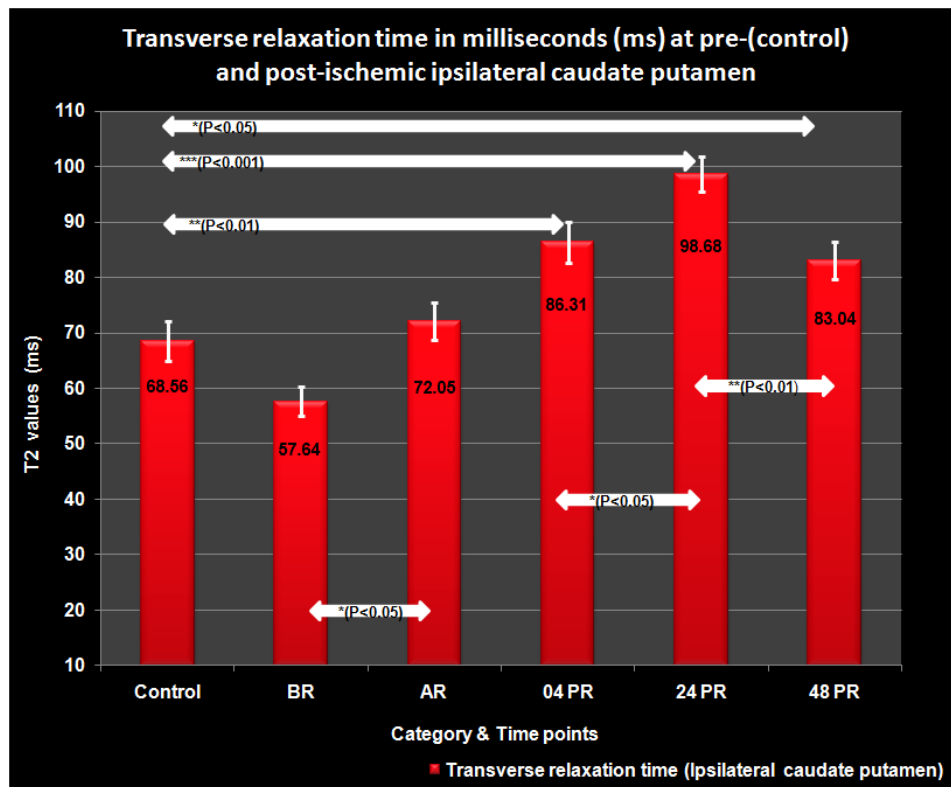


Figure 41A. Temporal changes in T_2 -values at the pre- and post-ischemic ipsilateral caudate putamen up to 48 hours.

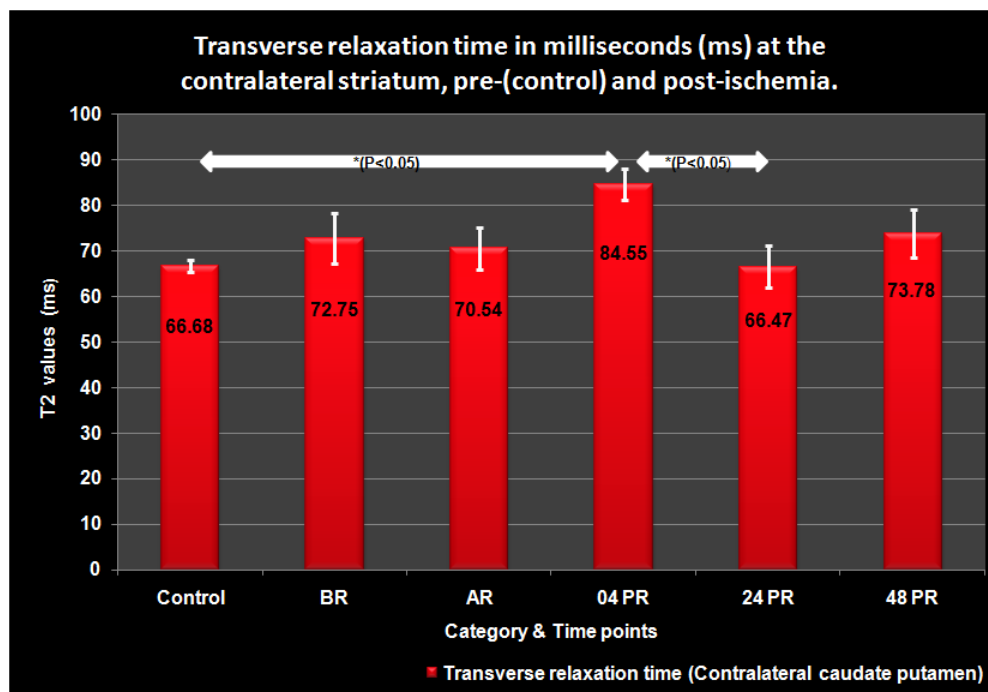


Figure 41B. Temporal profile of T_2 -values at the pre- and post-ischemic contralateral caudate putamen up to 48 hours.

04PR. The contralateral striatal T_2 value (66.47 ± 4.56 ms) was also significantly ($P < 0.05$) lower to that at 04PR.

By 48PR, T_2 value at the ipsilateral striatum (83.04 ± 3.4 ms) showed significant ($P < 0.01$) decline compared to 24PR, but was still significantly ($P < 0.05$) higher when compared to that of control and is accompanied by a significant fall in hemispheric volume (0.59 ± 0.02 cm³, $P < 0.01$). The corresponding cortical values (70.18 ± 3.3 ms) declined insignificantly from that at 24PR and the T_2 value at the contralateral striatum (73.78 ± 5.17 ms) showed a marginal rise compared to that of 24PR.

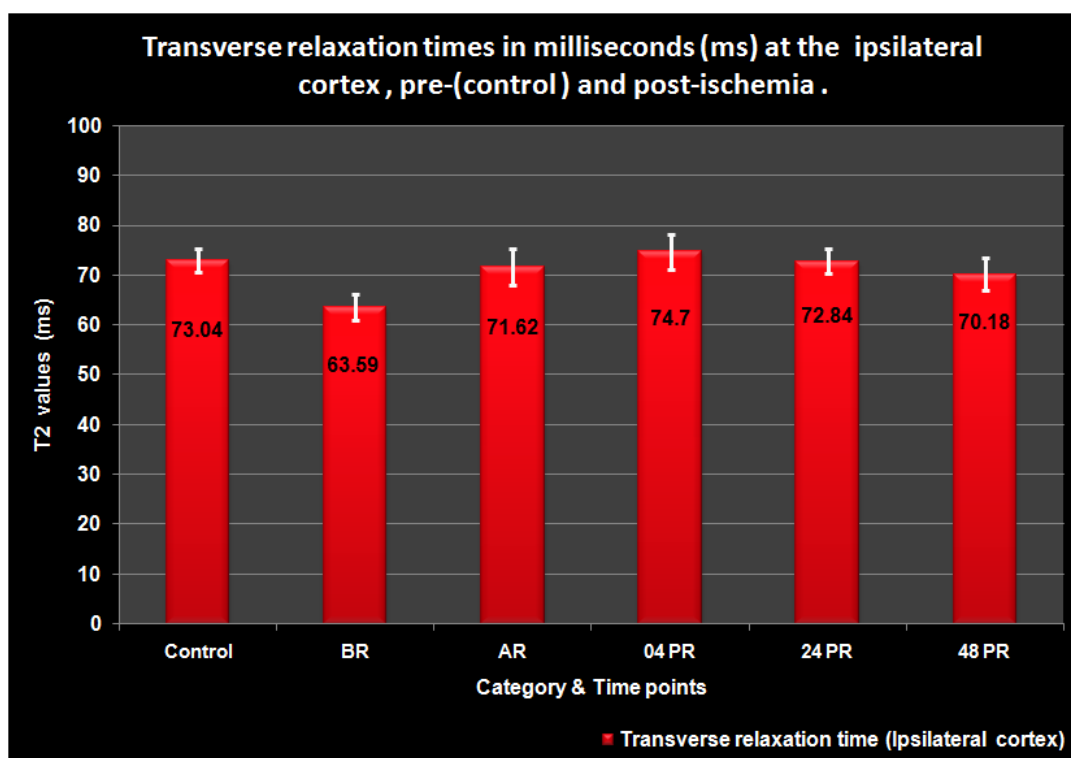


Figure 41C. Changes in T_2 -values at the pre- and post-ischemic ipsilateral cortex up to 48 hours.

5.3. TROPHIC PROPERTIES OF EPIDERMAL GROWTH FACTOR AND PIGMENT EPITHELIUM DERIVED FACTOR ON SELECTED INDICES OF NEUROVASCULAR INJURY FOLLOWING ISCHEMIA-REPERFUSION INJURY IN RATS.

5.3.1. EVALUATION OF BLOOD BRAIN BARRIER PERMEABILITY FOR MACROMOLECULES.

All the three animal groups (3, 6 and 8 hours) post-reperfusion demonstrated EB extravasation into the ipsilateral brain parenchyma as indicated by the bluish discoloration following one hour of exposure to circulating EB. Representative images for 3, 6 and 8 hours are provided in Figure 42.

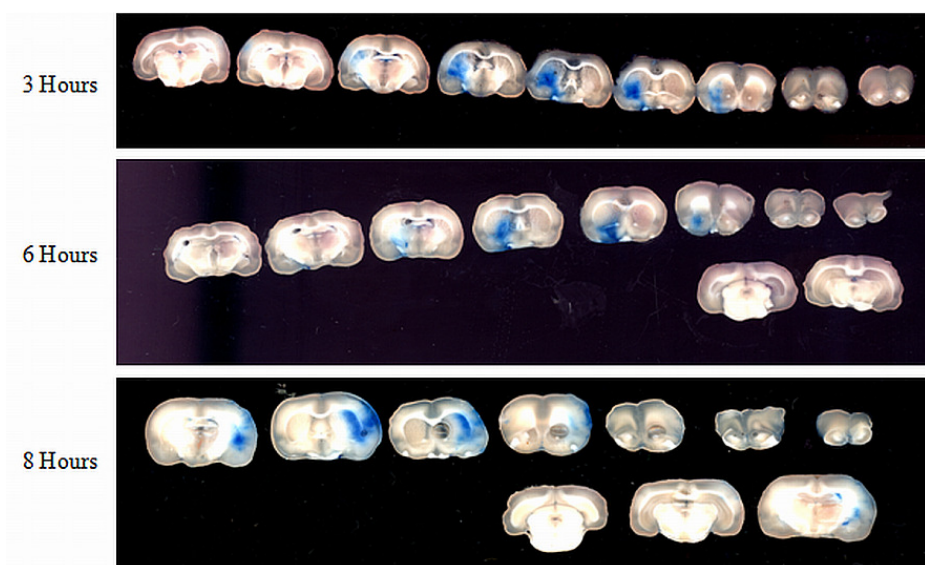


Figure 42. Representative images depicting bluish discoloration resulting from EB extravasation obtained at different time points post-reperfusion.

5.3.2. TROPHIC PROPERTIES OF EGF AND PEDF ON ISCHEMIA-REPERFUSION INJURY.

All the three treatment groups had strength of 10 animals each following the loss of 7, 6 and 4 animals in the saline (Control), EGF and PEDF groups respectively. These deaths

included experimental errors, due to vasogenic oedema and also from anaesthesia. There was no clear pattern of mortality that could be readily attributable to the subjected mode of treatment.

5.3.2.1. EFFECT OF EGF AND PEDF ON THE INFARCT VOLUME.

At 24 hours post-reperfusion, the infarct volumes defined by the hyperintense regions on T₂-TSE images of the EGF treatment group resulted in statistically significant reduction in infarct volumes ($5.69 \pm 0.36 \text{ cm}^3$, $P < 0.0001$) compared to that of control (Saline treated group) ($7.79 \pm 0.37 \text{ cm}^3$). The PEDF group demonstrated further reduction in infarct volume ($4.46 \pm 0.21 \text{ cm}^3$) which was significantly smaller compared to that of saline ($P < 0.0001$) and also to that of EGF ($P < 0.05$). Representative T₂-TSE images from the three treatment groups at all the four time points are provided below (Figure 43).

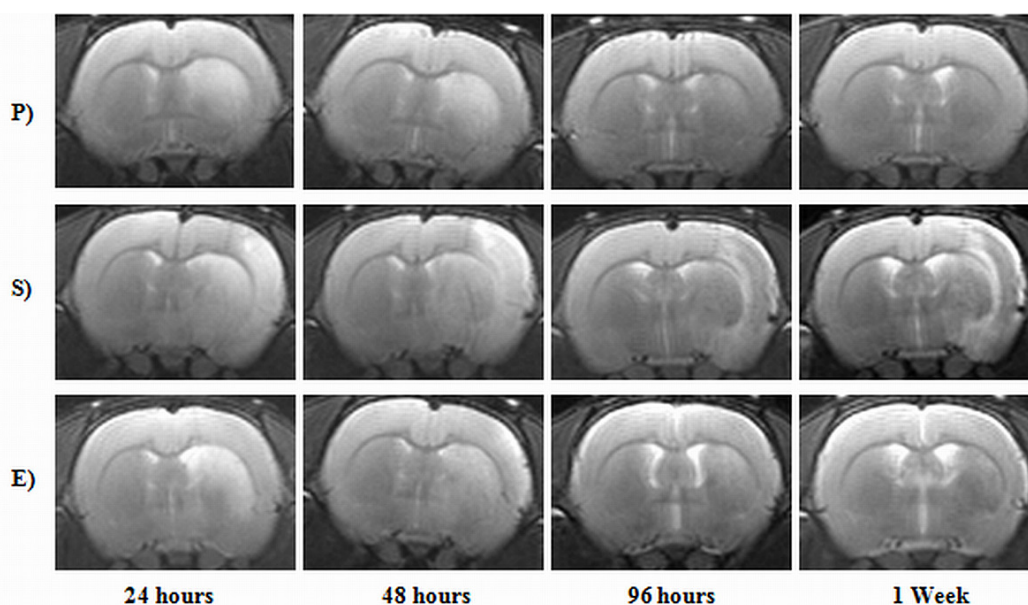


Figure 43. Representative T₂-TSE images from the three treatment groups namely PEDF (P), Saline (S) and EGF (E) studied up to 1 week.

By 48 hours the control group infarct volume increased significantly ($11.62 \pm 1.67 \text{ cm}^3$, $P < 0.001$) compared to that at 24 hours, whereas the EGF value at 48 hours increased non-significantly ($7.45 \pm 0.76 \text{ cm}^3$) compared to that at 24 hours. However, the EGF group

had a significantly ($P < 0.05$) lower infarct volume when compared to that of saline group at 48 hours. The PEDF group infarct volume decreased non-significantly ($4.06 \pm 0.21 \text{ cm}^3$) compared to that at 24 hours, but was significantly ($P < 0.0001$) lower compared to that of saline group volume at 48 hours. All the three groups demonstrated statistically significant reductions in infarct volumes at 96 hours, when compared to that at 48 hours. The infarct volumes for control, EGF and PEDF were $6.8 \pm 0.9 \text{ cm}^3$ ($P < 0.0001$), $4.60 \pm 0.98 \text{ cm}^3$ ($P < 0.0001$) and $2.38 \pm 0.27 \text{ cm}^3$ ($P < 0.0001$). At this time, only PEDF demonstrated statistically significant ($P < 0.001$) reduction in infarct volume, when compared to that of control group.

At one week, the infarct volumes continued to decline for saline ($5.5 \pm 0.99 \text{ cm}^3$) and EGF ($3.5 \pm 0.75 \text{ cm}^3$), while statistically significant reduction has been observed with PEDF ($1.7 \pm 0.18 \text{ cm}^3$, $P < 0.05$) only. Further, only PEDF group demonstrated statistically significant ($P < 0.001$) reduction in infarct volume when compared to saline group. All the results have been summarized in Figure 44.

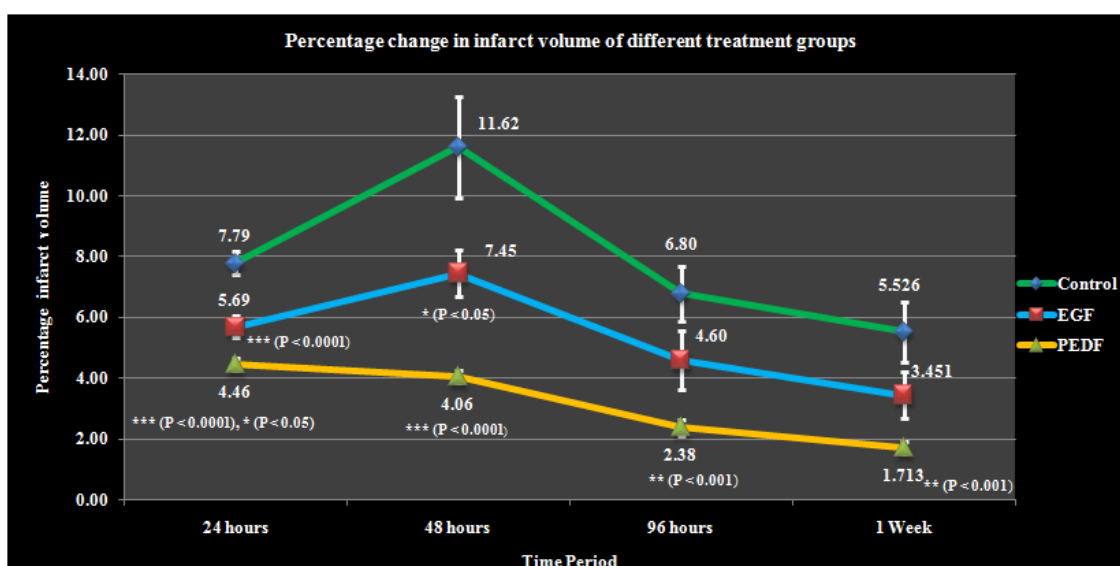


Figure 44. Percentage change in infarct volume of Control, EGF and PEDF groups at extended time points up to 1 week.

5.3.2.2. EFFECT OF EGF AND PEDF ON THE T₂-VALUES WITHIN THE INFARCT REGION.

At 24 hours post-reperfusion, statistically significant elevation in T₂-values in milliseconds (ms) was observed for control (122.2 ± 9.01 ms, P < 0.0001), EGF (130.7 ± 3.5 ms, P < 0.0001) and PEDF (116.5 ± 2.9 ms, P < 0.0001) treated groups in comparison to that of healthy animals (83.21 ± 1.5 ms). These results are graphically presented in Figure 45.

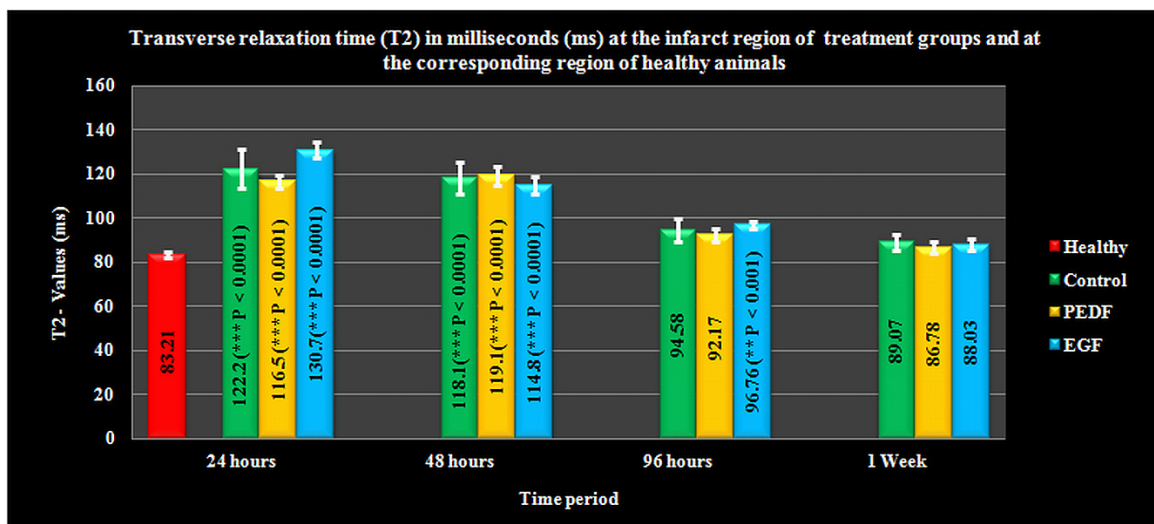


Figure 45. Temporal profile of T₂-values from different treatment groups in comparison to that of the healthy group obtained at time points up to 1 week.

By 48 hours post-reperfusion the control and PEDF T₂-values decreased non-significantly to 118.1 ± 6.9 ms and 119.1 ± 4.3 ms respectively when compared to the value at 24 hours. However, the EGF group demonstrated statistically significant reduction in T₂ values (114.8 ± 3.97 ms, P < 0.001) compared to 24 hour value. Again, at this time point all the groups demonstrated significantly (P < 0.0001) higher T₂ values when compared to that of the healthy group. At 96 hours post-reperfusion, the control values decreased non-significantly to 94.58 ± 5.4 ms, compared to the value at 24 hours, whereas,

statistically significant reduction in T_2 values has been demonstrated by both EGF (96.76 ± 1.8 ms, $P < 0.0001$) and PEDF (92.17 ± 2.95 ms, $P < 0.0001$) groups. Only the T_2 -value of the EGF (96.76 ± 1.8 ms, $P < 0.001$) group demonstrated significantly higher T_2 -values compared to that of healthy group. By 1 week, the control (89.1 ± 3.6 ms), EGF (88.03 ± 2.5 ms) and PEDF (86.78 ± 2.6 ms) treatment groups had non-significant T_2 -value reduction compared to that at the previous time point. None of these values were significantly different than the healthy group.

5.3.2.3. EFFECT OF EGF AND PEDF ON THE T_2 -VALUE X INFARCT VOLUME PRODUCT (T_{2vol}) UP TO 48 HOURS.

The following results represent the changes in T_{2vol} values of the different treatment groups (Control, EGF and PEDF) up to 48 hours. A schematic representation is provided below (Figure 46).

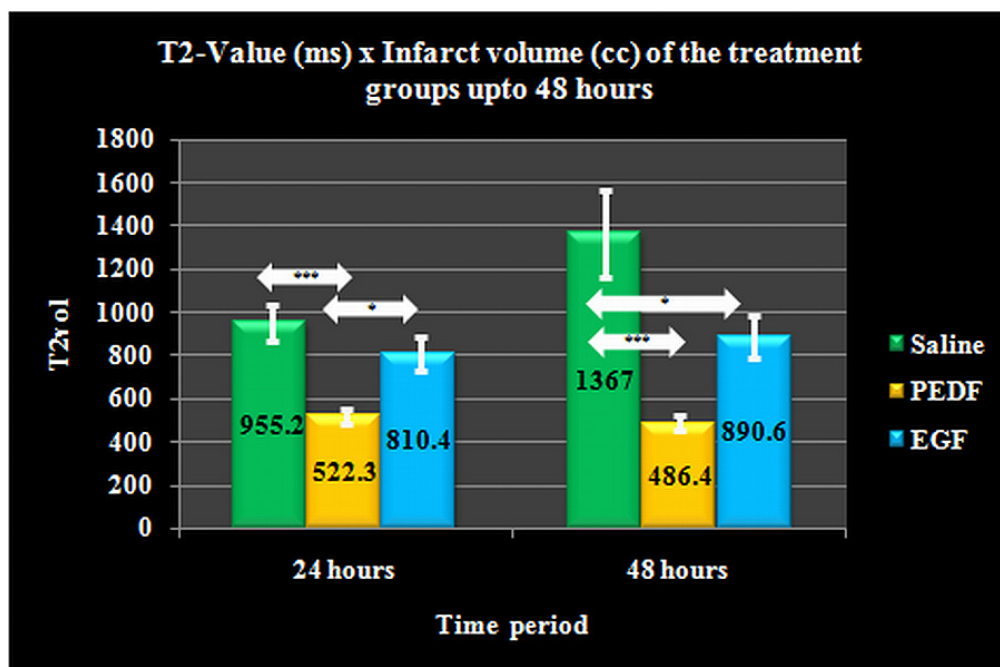


Figure 46. Temporal changes in T_{2vol} of the different treatment groups up to 48 hours.

At 24 hours, the PEDF group (522.3 ± 33.13) demonstrated significantly lower $T_{2\text{vol}}$ values in comparison to both control (955.2 ± 82.56 , $P < 0.0001$) and EGF (810.4 ± 78.25 , $P < 0.05$) groups. By 48 hours the control group (1367 ± 203.5 , $P < 0.05$) demonstrated significant increase in $T_{2\text{vol}}$ compared to the earlier 24 hour time point. The PEDF $T_{2\text{vol}}$ (486.4 ± 35.28) and EGF $T_{2\text{vol}}$ (890.6 ± 100.2) demonstrated a marginal decrease and increase, respectively, compared to their 24 hour time point values. Moreover both the PEDF ($P < 0.0001$) and EGF ($P < 0.05$) values were significantly lower than the control values.

5.3.2.4. EFFECT OF EGF AND PEDF ON THE T_2 -VALUES AT THE IPSILATERAL CORTEX.

At 24 hours, the T_2 -value of the control group was 85.16 ± 4.7 ms, whereas the T_2 -values of PEDF (91.4 ± 1.9 ms, $P < 0.05$) and EGF (91.7 ± 2.1 ms, $P < 0.05$) groups were significantly higher than the cortical T_2 -values values of healthy animals (83.87 ± 1.6 ms). By 48 hours, the T_2 -value of the control (91.31 ± 0.96 ms) and EGF (87.75 ± 1.9 ms) groups increased and decreased non-significantly from 24 hour time point. The T_2 -value of the PEDF (97.59 ± 2.5 ms, $P < 0.05$) group demonstrated a significant increase from the earlier time point. Further, this value was significantly higher than healthy ($P = 0.0001$), EGF ($P < 0.05$) and PEDF ($P < 0.05$) groups.

At 96 hours the control group T_2 -value (87 ± 3.9 ms) decreased non-significantly and the T_2 -value (88.13 ± 1.6 ms) of the EGF group was almost similar to that of the earlier time point. The PEDF T_2 -value (91.01 ± 1.5 ms) decreased significantly compared to the earlier time point but still remained significantly ($P < 0.05$) higher than the healthy group. By 1 week, the T_2 -values of control (87.49 ± 3.3 ms), EGF (88.83 ± 2.1 ms) and PEDF (91.39 ± 1.46 ms) were almost similar to that of the earlier time point. Nevertheless, the

T₂-value of PEDF (P < 0.05) was still significantly higher than the healthy group. These data are graphically represented with Figure 47.

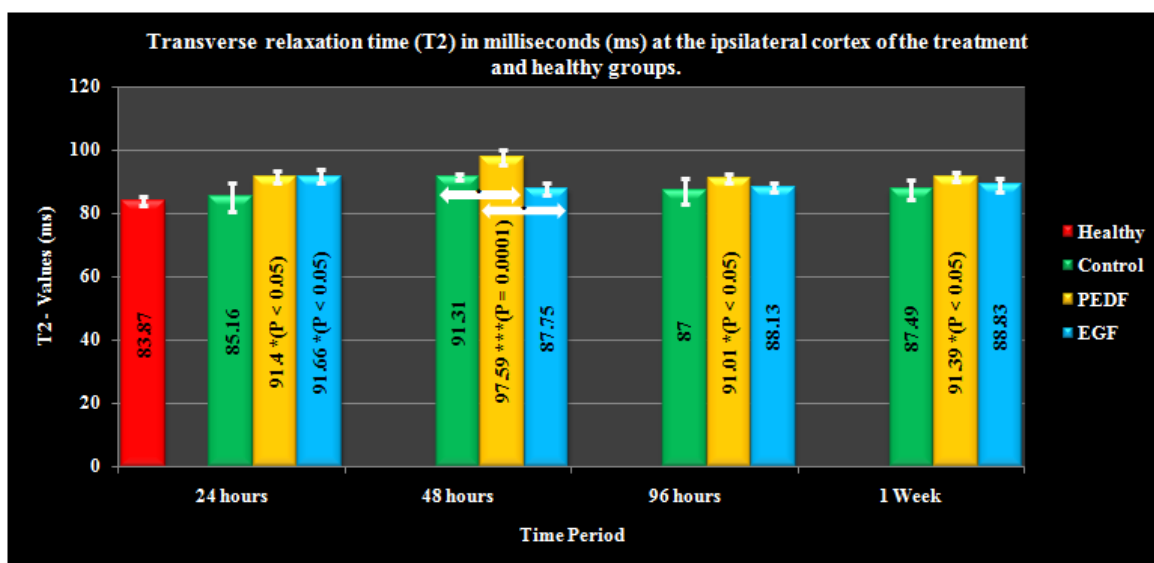


Figure 47. Temporal profile of T₂-values of the three different treatment groups at the ipsilateral cortex along with their comparison to that of the healthy group.

5.3.2.5. EFFECT OF EGF AND PEDF ON THE T₂-VALUES AT THE CONTRALATERAL STRIATUM.

At 24 hours, the control (77.66 ± 4.04 ms) and PEDF (81.65 ± 1.6 ms) T₂-values were non-significantly lower than the healthy group (83.21 ± 1.5 ms), whereas, the value for the EGF (89.41 ± 1.8 ms, P < 0.05) was found to be significantly higher than that of healthy group. Further, the EGF (89.41 ± 1.8 ms, P < 0.05) T₂-value was also found to be significantly higher than that of control. By 48 hours, the control (80.53 ± 2.8 ms) and EGF (88.27 ± 2.3 ms) T₂-value increased and decreased non-significantly compared to the earlier time points whereas the PEDF (88.44 ± 1.7 ms, P < 0.001) T₂-value increased significantly compared to the earlier time point. Further, the EGF and PEDF values were

significantly ($P < 0.05$) higher than that of healthy group and was also significantly higher ($P < 0.05$) than that of the control group.

At 96 hours, the control T_2 -values (82.88 ± 3.6 ms) increased marginally compared to the earlier time point, whereas the PEDF (85.14 ± 2 ms) T_2 -values decreased non-significantly. The EGF (78.84 ± 1.4 ms, $P < 0.001$) T_2 -values decreased significantly compared to the previous time point. By 1 week, the control (80.99 ± 3 ms) T_2 -values decreased non-significantly compared to that at 96 hours. The EGF (83.74 ± 1.3 ms) and PEDF (88.59 ± 1.4 ms) T_2 -value increased non-significantly compared to the earlier time point, whereas the PEDF (88.59 ± 1.4 ms, $P < 0.05$) T_2 -value was significantly higher than the healthy as well as the control T_2 -value. A schematic representation of the data is provided below (Figure 48).

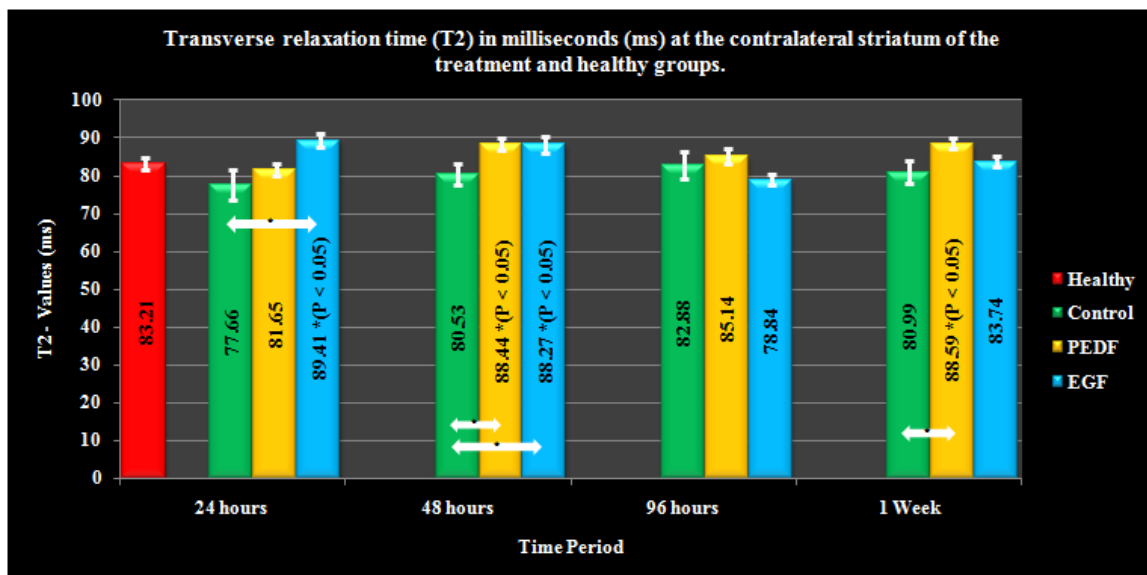


Figure 48. Temporal profile of T_2 -values of the three different treatment groups at the contralateral striatum along with their comparison to the healthy group.

5.3.2.6. EFFECT OF EGF AND PEDF ON THE SUSCEPTIBILITY WEIGHTED T_2^* -VALUES AT THE INFARCT REGION.

At 24 hours post-reperfusion, all the three treatment groups including the control (120.2 ± 7.5 ms), EGF (112.2 ± 11 ms) and PEDF (112.1 ± 15.51 ms) T_2^* -values were significantly ($P < 0.0001$) higher than the healthy group (41.83 ± 2.83 ms) T_2^* -value. By 48 hours, the PEDF (71.61 ± 6.5 ms, $P < 0.001$) T_2^* -value was significantly reduced compared to the earlier time point. Further, this value was significantly ($P < 0.05$) lower than that of the T_2^* -values of both EGF (127.6 ± 12.79 ms) and control groups (117.11 ± 16.14 ms). At this time, the control group T_2^* -value was non-significantly reduced compared to the earlier time point, but, remained significantly ($P < 0.0001$) elevated compared to that of the healthy group. The EGF group T_2^* -value was increased non-significantly compared to the earlier time point, and, remained significantly ($P < 0.0001$) higher than the healthy group.

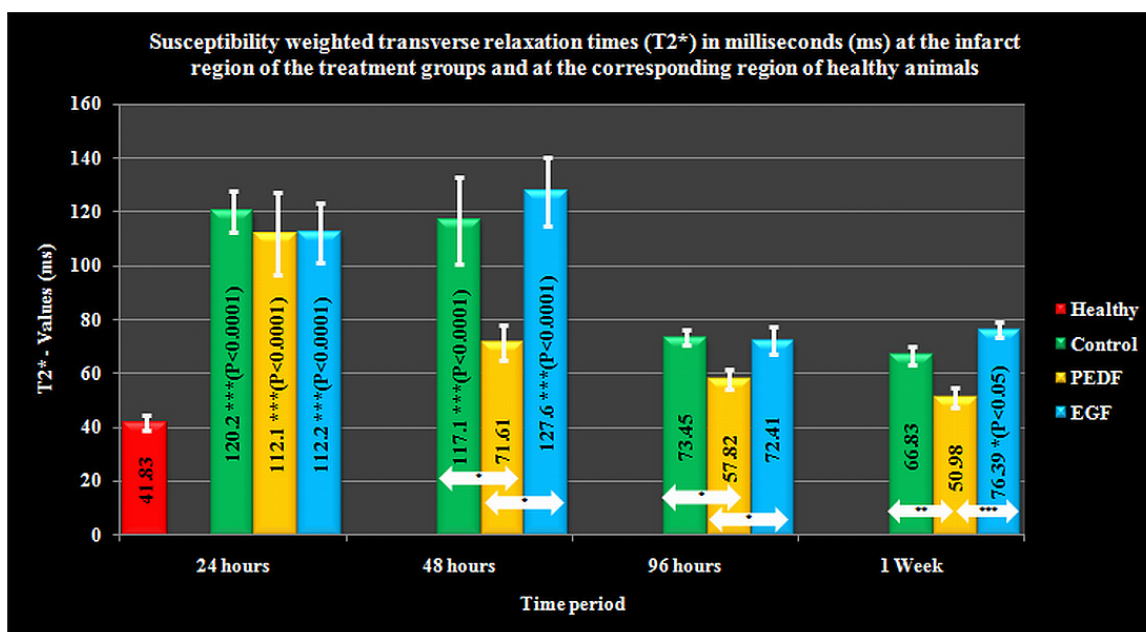


Figure 49. Susceptibility weighted T_2^* relaxation characteristics of the different treatment groups along with their comparison to that of the healthy group.

At 96 hours, the control (73.45 ± 2.73 ms, $P < 0.05$) and EGF (72.41 ± 5.2 ms, $P < 0.001$) group T_2^* -value was significantly reduced compared to their corresponding earlier time points. The PEDF (57.82 ± 3.8 ms) group T_2^* -value also reduced non-significantly compared to its early time point. Further, the T_2^* -value of the PEDF group was found to be significantly ($P < 0.05$) lower than both of EGF and control.

By 1 week, both the control (66.83 ± 3.4 ms) and PEDF (50.98 ± 3.8 ms) groups demonstrated a non-significant decrease in T_2^* -values from their earlier time point. None of these values were significantly higher than that of the healthy group value. The EGF group (76.39 ± 2.9 ms) T_2^* -value was non-significantly elevated compared to the earlier time point, but remained significantly ($P < 0.05$) higher than that of the healthy group. At this time the PEDF T_2^* -value was found to be significantly lower than either of the control and EGF groups. A graphical representation of the temporal changes in T_2^* -relaxation profile of the various treatment groups and also in comparison to the corresponding region of the healthy group at the infarct region is provided with Figure 49.

5.3.2.7. EFFECT OF EGF AND PEDF ON THE SUSCEPTIBILITY WEIGHTED T_2^* -VALUES AT THE CONTRALATERAL REGION.

At 24 hours, the control (60.13 ± 3.1 ms, $P < 0.001$) and EGF (63.53 ± 3.4 ms, $P < 0.001$) group T_2^* -values were significantly elevated when compared to that of the healthy group value (41.83 ± 2.83 ms). The PEDF (54.81 ± 2.6 ms) T_2^* -value was elevated non-significantly compared to that of the healthy group. By 48 hours, the control (62.83 ± 3.9 ms), PEDF (58.7 ± 3.9 ms) and EGF (60.94 ± 2.4 ms) T_2^* -values increased non-significantly compared to their early time points. However all the treatment groups

demonstrated different degrees of statistical significance like control ($P < 0.001$), PEDF ($P < 0.05$) and EGF ($P < 0.001$) when compared to the T_2^* -values of the healthy group (41.83 ± 2.83 ms).

At 96 hours, all the groups demonstrated a non-significant marginal increase in their T_2^* -values compared to their early time point. Still, the control (65.27 ± 5.2 ms, $P < 0.0001$), PEDF (60.33 ± 4.3 ms, $P < 0.001$) and EGF (65.64 ± 5.1 ms, $P < 0.0001$) T_2^* -values were significantly elevated than that of the healthy group. By 1 week, all the groups demonstrated a non-significant increase in T_2^* -values compared to the early time point. However, the control (70.78 ± 3.8 ms, $P < 0.0001$), PEDF (61.88 ± 5.6 ms, $P < 0.001$) and EGF (66.16 ± 4.9 ms, $P < 0.0001$) T_2^* -values remained significantly higher than the healthy values. These data are schematically represented in Figure 50.

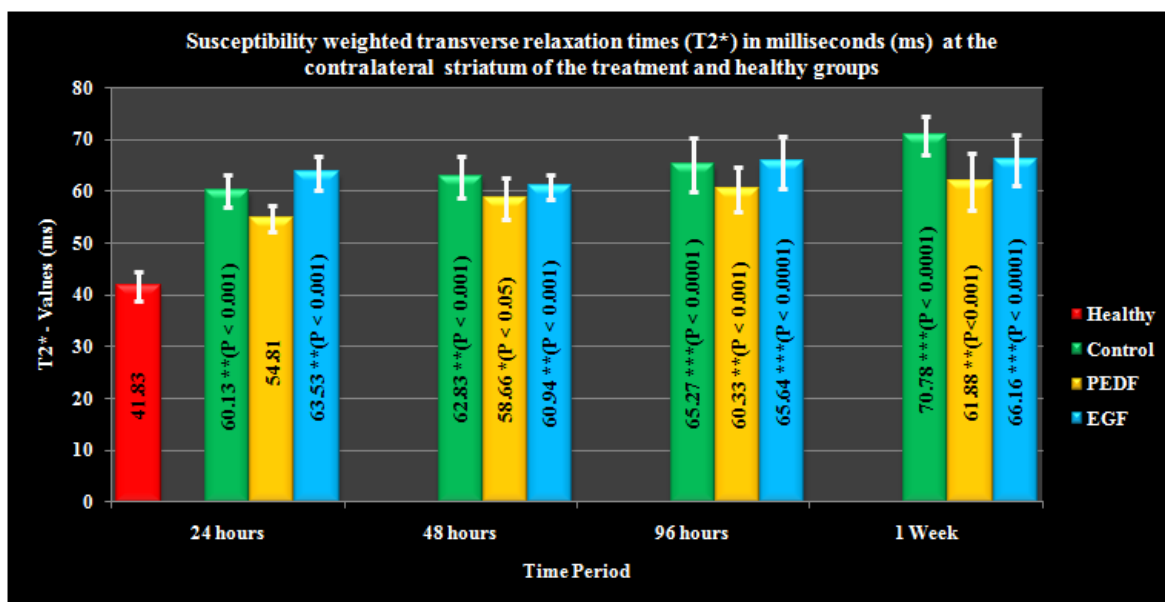


Figure 50. Susceptibility weighted T_2^* relaxation characteristics of the different treatment groups along with their comparison to that of the healthy group.

5.3.2.8. EFFECT OF EGF AND PEDF ON THE T_1SI_{DIFF} VALUE AT THE IPSILATERAL STRIATUM.

At 24 hours post- reperfusion the T_1SI_{diff} at the ipsilateral striatum of the control, EGF and PEDF groups were 22.58 ± 1.9 , 18.91 ± 1.7 and 12.16 ± 1 respectively. The PEDF value was significantly lower than that of control group ($P < 0.0001$) and also to that of the EGF group ($P < 0.05$). By 48 hours, the T_1SI_{diff} of the control (52.66 ± 4.8 , $P < 0.05$), EGF (57.6 ± 9.2 , $P < 0.0001$) and PEDF (23.43 ± 2.4 , $P < 0.001$) increased significantly compared to their earlier time points. Moreover, at this time the PEDF (23.43 ± 2.4 , $P < 0.001$) value was found to be significantly lower than that of control and EGF groups.

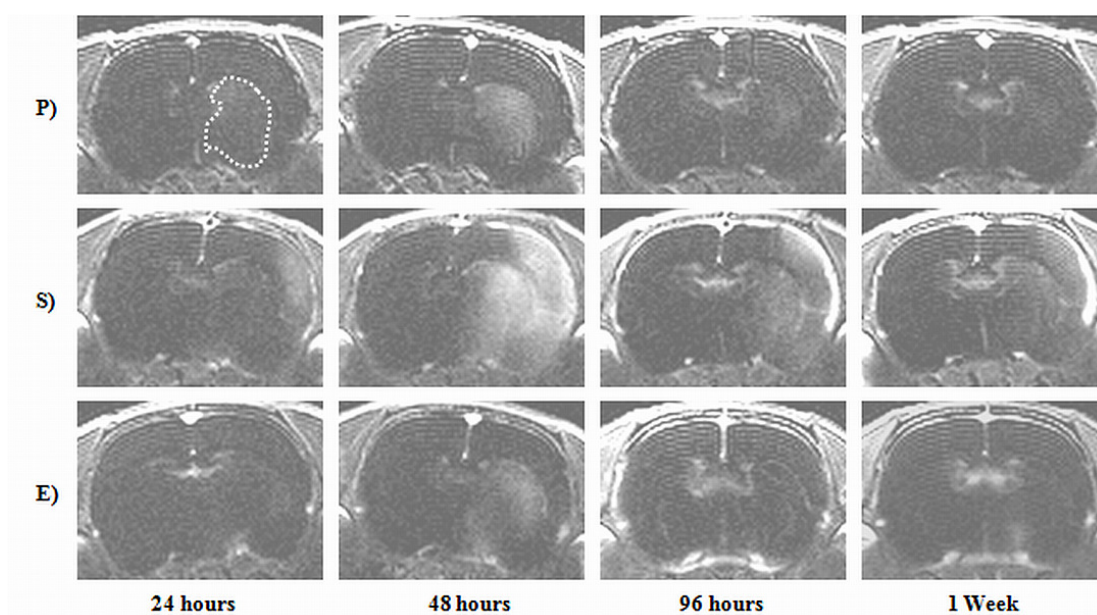


Figure 51. Subtraction T_1 -SE images of the three different treatment groups at the studied time points up to 1 week. The highlighted region (Upper left image) was considered to obtain the T_1SI_{diff} values. The same region was considered at the contralateral side to obtain the corresponding values.

By 96 hours, the T_1SI_{diff} value of control (45.98 ± 9.6) and PEDF (16.98 ± 2) decreased non-significantly compared to their respective earlier time points. Meanwhile, the EGF T_1SI_{diff} value (31.03 ± 2.1 , $P < 0.05$) decreased significantly compared to its early time

point. At the same time, the T_1SI_{diff} value of PEDF (16.98 ± 2 , $P < 0.001$) was significantly lower than the control value. At 1 week, the T_1SI_{diff} value of control (31.96 ± 1.9) and PEDF (15.35 ± 2.4) decreased non-significantly, whereas, the EGF T_1SI_{diff} (36.36 ± 4.4) value showed a marginal increase compared to the earlier time point. However, the T_1SI_{diff} value of PEDF still remained significantly lower than the T_1SI_{diff} value of both control ($P < 0.001$) and EGF ($P < 0.0001$). Subtraction images from pre- and post-contrast T_1 -SE images of the three different treatment groups at time points up to 1 week are provided (Figure 51). These data are schematically represented in Figure 52.

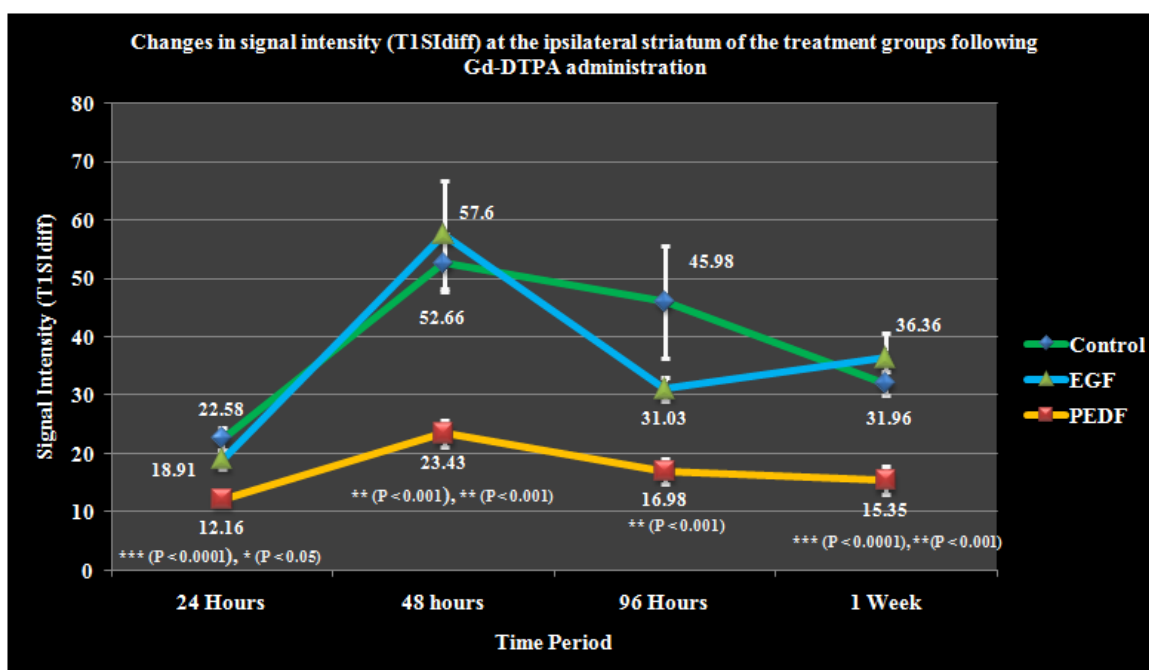


Figure 52. Temporal profile of signal intensity (T_1SI_{diff}) changes at the ipsilateral striatum of three different treatment groups at multiple time points up to 1 week.

5.3.2.9. EFFECT OF EGF AND PEDF ON THE T_1SI_{DIFF} VALUE AT THE CONTRALATERAL STRIATUM.

At 24 hours post-reperfusion, the T_1SI_{diff} values at the contralateral striatum of the control, EGF and PEDF were 12.92 ± 1.0 , 12.53 ± 0.94 and 8.9 ± 1 respectively. The

PEDF T_1SI_{diff} value was significantly lower than both the control ($P < 0.05$) and EGF ($P < 0.05$). By 48 hours, the control (12.8 ± 1.3) T_1SI_{diff} value was almost similar to that at 24 hours whereas the EGF (10.7 ± 0.97) T_1SI_{diff} value was only marginally reduced. At this time, the PEDF (11.11 ± 1.1 , $P < 0.05$) T_1SI_{diff} value increased significantly compared to 24 hour time point.

At 96 hours, the control (12.3 ± 1.1) T_1SI_{diff} value was almost similar to that at 48 hours, whereas the EGF (15.59 ± 1.8 , $P < 0.05$) and PEDF (8.9 ± 0.8 , $P < 0.05$) T_1SI_{diff} value significantly increased and decreased respectively compared to the earlier time point. Further, the PEDF T_1SI_{diff} value was significantly ($P < 0.001$) lower than that of EGF. By 1 week, the control (12.96 ± 1.6) and PEDF (8.9 ± 1.1) T_1SI_{diff} values remained more and less similar to that at 96 hours. The EGF (19.31 ± 2.2) T_1SI_{diff} value increased non-significantly compared to the earlier time point. However, the EGF T_1SI_{diff} value is significantly higher than both control ($P < 0.05$) and PEDF ($P < 0.0001$). These results are summarized in Figure 53.

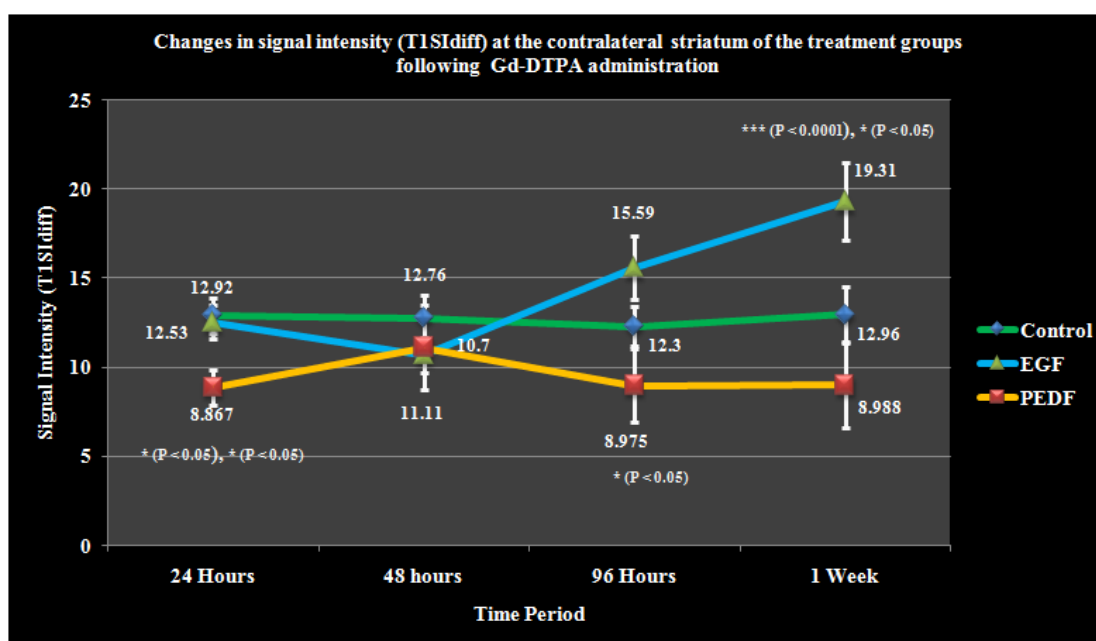


Figure 53. Temporal profile of signal intensity (T_1SI_{diff}) changes at the contralateral striatum of the three different treatment groups at multiple time points up to 1 week.

6.0. Discussion.

6.1. ESTABLISHMENT OF SMALL ANIMAL MAGNETIC RESONANCE IMAGING STRATEGIES ON A 3 TESLA CLINICAL DEDICATED HEAD MAGNETIC RESONANCE SCANNER.

In this study, a series of high-resolution MR images of small animal models with a variety of CNS pathologies has been acquired and characterized. Quantitative relaxometry was performed not only to optimize MR sequence parameters, but also to gain an understanding of these paradigms which is of paramount importance in research applications for at least two reasons: - A) Tissue relaxation characteristics are extremely sensitive to subtle changes like blood flow, tissue oxygenation and oedema formation within minutes of the ictus (264). B) Efficacy of therapeutic interventions could be better appreciated with the quantitative nature of such estimations. Since, no data is available with scanners of comparable field strength; these values may serve as a reference standard.

In our study, we have observed a significant difference between the T_2^* values at the cortex and striatum in the brains of both rats and mice. Since T_2^* values are influenced by a number of factors like field inhomogeneity, tissue oxygenation, blood flow and tissue distribution of paramagnetic substances like iron, a much more detailed study needs to be conducted to ascertain the causative factors behind this observation (265). Studies have shown that a number of sub-cortical structures like the globus pallidus, ventral tegmentum and substantia nigra preferentially stores iron in rats which is particularly pronounced in elderly and female animals (266, 267). Furthermore, studies in young mice have also demonstrated selective iron accumulation in the white matter tracts (268). Even though

such regional variations are a strong contender for the observed results especially in mice, we are not particularly ascertaining to this cause with the employed rats as they were relatively young at 6-8 weeks of age. Another factor that may be responsible is the very nature of the T_2^* -weighted GRE sequences. The T_2^* value of the tissue has been determined by employing a range of TE values from 20-60 ms with a relatively low image acquisition matrix of 128 x 128 and the resultant in-plane resolution was 400 μ which is two times lower than the one employed for detecting cerebral haemorrhage. The acquisition of T_2^* images at the relatively longer TE values of 50 and 60 coupled to the lower matrix size could have rendered the sequence too susceptible to field inhomogeneities rendering such a disparity between the two anatomic regions.

The employed MRI system, with a relatively smaller Diameter of a Spherical Volume (DSV) at 220 mm had more magnetic field homogeneity (< 0.1 Parts Per Million (PPM) Volume Root Mean Square (VRMS)) compared to whole-body scanners which usually have a DSV of 400 mm and results in elevated (< 0.35 ppm) Vrms. Such a small DSV also contributed to improved gradient performance with a doubled slew rate up to 400 mT/m/ms compared to 200mT/m/ms of whole body scanners. The employed system also possessed a short magnet length of 1.25m which was helpful particularly with small animal imaging with an easy access to the anesthetized animal for contrast/drug administration and animal monitoring. All the above-mentioned comparisons were performed against the whole body scanner, Siemens magnetom Trio (Siemens Health care Sector, Erlangen, Germany). To the best of our knowledge, this is the first small animal study performed on such a dedicated head scanner with customized phased array coils at 3 T.

Considering the implementation of PI strategies for DW- & PE-EPI sequences, DW-EPI image set without implementing any PI did not demonstrate gross geometric distortions and was readily comparable to those obtained with PI. This relative freedom from distortions probably arises from the adoption of a rectangular FOV and the resultant reduction of TE, from 197 (for a square FOV) to 128 (data not shown). The additional benefit of employing GRAPPA seems to stem out of two factors, namely, a concomitant increase in signal intensity as a result of a much shorter TE coupled to a reduced SD_{diff} which, in turn contributed to maximal resultant SNR when implemented at an AF of 3. Even though we could not directly compare our results with similar studies, the obtained data seems to be in good agreement with human studies carried out at identical field strength (269). Even though, both GRAPPA and mSENSE demonstrated an increase in mean signal intensity with increase in AFs, GRAPPA provided a minimal SD_{diff} with an AF of 3 whereas SD_{diff} with mSENSE increased with higher AFs to the point where the image reconstruction program quit abruptly raising exceptions at the AF of 4, probably from unacceptable noise amplifications. Such distinct behaviour of both RAs could be due to factors like, the reconstruction methodologies followed, and the spatially varying geometry factor (g-factor), which in turn is again dependent on a plethora of factors like coil geometry, phase encoding direction and acceleration factor (252).

In addition, a comparison of both GRAPPA and mSENSE with PE-EPI sequence, in the absence of injected Gd-DTPA demonstrated identical results as in the case with DW-EPI by showing an increase in mean signal intensity which could be reasonably expected with a concomitant reduction in TE. However, the fact that mSENSE demonstrated consistently low SD_{diff} values is in contrast to its behaviour observed with DW-EPI sequences. Again, with an increase in AF from 3 to 4 both the RAs showed a reduction in the observed SD_{diff} values, which is also not in agreement with its early behaviour. We

could not find similar studies either in animals or in humans where these RAs were compared in PE-EPI sequences making this a rather singular observation. Since, DW-EPI sequence happens to be a spin-echo EPI sequence with diffusion sensitizing gradients, and, PE-EPI sequence being a GRE-EPI sequence presenting two different environments might hold the key, amongst others as mentioned above, to the different behaviour of these two RAs with respect to variations in SD_{diff} .

Even though, the present work does not attempt to perform MR phenotyping of rodent brains, the employed 3D-MPRAGE sequence delineated a number of anatomical regions. The employed inversion time of 900 ms was that of the striatum, since, we did not go for extensive relaxometric characterization of other anatomical regions. The obtained contrast, primarily between brain parenchyma and the cerebrospinal fluid may be due to the greater T_1 -contrast available with the short echo time, and the preparatory 180° pulse yielding an inversion recovery type of contrast. To the best of our knowledge, we could not find similar data at this field strength, except for one study employing spin-echo sequences for structural characterization of the rodent brain and was therefore unable to perform a cross comparison of results (270). A number of works at 1.5 T has attempted to perform such anatomical characterizations and the added quality of the presented MPRAGE images can extend the scope of applications involving brain lesion detections, tissue grafting and enables morphometric studies (271-273).

6.1.1. IMAGING OF THE RODENT MODEL OF CEREBRAL ISCHEMIA.

PE- and DW-EPI detected regions of perfusion deficits and accompanying ischemia at an early time point. DW-EPI images are acquired using relatively high 'b' values to

'desensitize' the sequence to fast moving protons such as those within blood vessels while sensitizing them to less mobile protons in the extra- and intra-cellular spaces (274). Further, performing DW-EPI with more than three 'b' values also helped to minimize noise in the generated ADC maps (275). Implementation of an adapted parallel imaging method has contributed enormously in improving the image quality of EPI sequences. The k-space based reconstruction, GRAPPA, generated alias free full FOV images without significant artefacts (250). Gd-DTPA, the widely used paramagnetic lanthanide chelate, preferentially alters T_1 and T_2^* relaxation characteristics (276). To accurately assess perfusion characteristics it is necessary to measure the drop in signal during passage of the bolus with high sensitivity to susceptibility changes at high temporal resolution. EPI sequences are primarily preferred due to their very short ATs. However, in EPI the whole MR signal during the read-out duration decays due to T_2^* relaxation, which makes EPI sequences inherently sensitive to T_2^* effects (277). As a readout technique EPI could be combined with a number of excitation schemes and the GRE-EPI is superior to other EPI sequences with regards to the available SNR and maximum signal reduction (277). Since, they are susceptible to field inhomogeneities particularly at high fields; the enhanced field homogeneity offered by this dedicated head scanner has been complementary to the quality of the obtained perfusion images.

Even though mSENSE, provided superior results in terms of the obtained SNR and SD_{diff} with a normal healthy brain and in the absence of first pass Gd-DTPA, GRAPPA proved more sensitive to Gd-DTPA bolus passage and the reconstructed images were free from any artefacts. Once again, we could not directly compare our results to any previous studies either in animals or in humans. The most probable reason for the observed results with mSENSE could possibly be attributed to differences between distortions in EPI images and the obtained coil sensitivity maps (278). Further, such differences could

probably be augmented by the additional T_2^* relaxation perturbations resulting from the first pass Gd-DTPA.

Following 3-4 hours of reperfusion, BBB permeability characteristics are altered resulting in increased water shift from the intra- to extra-vascular compartment accompanied by prolonged T_1 and T_2 relaxation effects (261, 279). The fact that Gd-DTPA is of low molecular weight and its T_1 interactions are only pronounced for short distances qualify it as a marker for assessing BBB integrity (280). Since the T_1 -relaxivity (R_1) shortens with field strength, contrast-enhanced imaging at higher field strengths could contribute to enhanced delineation of tissue volumes with compromised BBB permeability (281).

6.1.2. IMAGING OF THE RODENT MODEL OF INTRACEREBRAL HAEMORRHAGE.

In the rodent model of hyper-acute ICH (≤ 1 hour), the extravasated blood should undergo de-oxygenation so that the heme iron in ferrous (Fe^{2+}) form turns paramagnetic by virtue of its four unpaired electrons (282). Oxygen extraction from blood is facilitated by the hypo-perfused, oxygen deprived surrounding tissue accompanied by rapid acidification causing the 'Bohr effect' to promote local oxygen dissociation from hemoglobin (283). The observed band of high signal intensity on the T_2 -TSE images around the periphery of the hematoma portrays the distribution of extravasated serum from the clot or oedema in adjacent brain parenchyma (283, 284).

T_2^* -GRE images may lead to a certain overestimation of the hematoma volume as they are also highly sensitive to magnetic field inhomogeneities induced by inherent susceptibility differences at the hematoma/tissue interface. Since high field strength and

GRE techniques increase the sensitivity to magnetic susceptibility effects through different mechanisms, they are additive and produce marked signal loss when applied together (285).

6.1.3. IMAGING OF THE RODENT MODEL OF SPINAL CORD INJURIES.

In-vivo MR studies of the rodent central nervous system comprising the spinal cord is particularly challenging owing to the relative small size of the cord which varies between 1-3 mm in diameter. Such small internal structures of rodents can easily overwhelm the limits of conventional clinical scanners. Such undertakings usually demand higher field strengths (up to 17.6 T) and implanted surface coils to maximize SNR while maintaining a smaller FOV (257, 286-288). Even though impressive in terms of the obtained image quality, the 17.6 T system also had its drawbacks arising from a narrow bore, limiting air circulation resulting in anaesthetic vapour accumulation leading to death of animals (257). Implanted surface coils also gives rise to unique problems, which, not only involve an invasive procedure, but also, such coils suffer from resonance frequency drifts over time, which is irreversible, resulting in loss of SNR and thereby rendering longitudinal studies almost impossible. Furthermore, since the cervical spinal cord is located relatively deep from the surface, the implantation procedure could cause widespread tissue damage (289).

Considering the rather harsh magnetic environment surrounding the cord, the commonly employed field strength for studying rodent spine happens to be at 7 T even though a number of workers have performed rodent spine imaging at the relatively lower field strength of 2.0 T allowing distinction of gray and white matter, estimating relaxation times and diffusion characteristics (290-293). Almost all of these studies have been

exclusively carried out with dedicated animal scanners using either external or implanted coils. Recently, a couple of studies have been performed with customized rat spine phased array coils, as they offer extended coverage, high SNR and PI capabilities (289, 294). To the best of our knowledge, this is the only work that has been performed on a clinical scanner, with a 4-channel phased array coil, designed primarily to image the thoracic spine, was employed to image a wire knife cut injury at the cervical (C3) level. The employed sequence clearly detected oedema and haemorrhage from the surrounding spinal cord parenchyma at the acute phase and de-lineated cyst formation at the extended time point of 30 days. The obtained IPR of 200 μ with an AT of 20-25 minutes is comparable to the only MRI study involving cervical spine obtained with a 7 T scanner employing a 3-channel phased array coil where the IPR was 175 μ at an AT of 15 minutes and 21 seconds (289).

MR imaging studies on spine contusion injury models have been carried out previously (257, 286, 295, 296). Even though the present study is distinct by employing a clinical scanner and a phased array coil system, we were able to clearly detect gray-white matter differentiation and de-lineation of cyst formation and haemosiderin deposits at the extended time point following 30 days from the injury. Consistent with previous studies, MR images consistently depicted hypo intensities rostral to the contusion injury at the thoracic level, which was confirmed as haemosiderin deposits due to trauma induced haemorrhage by Prussian blue staining (286). From our results, most of the hypo intense signals arise from the gray matter, which was also observed by another study where the haemorrhage was mainly confined to the gray matter at the acute time point (297). However, at least one study at the higher field strength of 17.6 T demonstrated signal changes even in the white matter (257). Such high field strength and its dependent changes in relaxation times and spatial resolution could have enabled the visualization of relatively

discrete haemosiderin deposits in white matter tracts (298). Another aspect is that, this study was conducted 58 days post injury and that is almost double the time allowed for our study which was restricted to 30 days. It remains to be determined whether, an extended time period allows for such an appearance.

The loss of gray-white matter contrast is the hallmark of spinal contusion injuries, which is invariably associated with lower body paralysis. An early study had noted a return of the gray matter, indicated by added contrast between the gray and white matter at late time points from 3-8 weeks post trauma and the authors attribute this to neuronal recovery (286). PD-TSE sequences are of paramount importance in spinal cord injury as it is the only one that can clearly delineate the gray and white matter tracts. The return of gray-white matter contrast in images acquired by PD-TSE sequences therefore serves as a surrogate marker for clinical improvement.

6.1.4. IMAGING OF THE MOUSE GLIOBLASTOMA MODEL.

The employed phased array coil assembly has been originally designed to image rodent brains with volumes of $600 \pm 10.6 \text{ mm}^3$ (299). The mouse brain ($269.16 \pm 2.2 \text{ mm}^3$) being much smaller has been preferentially studied at higher field strengths even though murine GBM have also been characterized using clinical scanners (258, 300-302). GBM is characterized by high angiogenic activity accompanied by loss of permeability characteristics at BTB and/or BBB structures leading to lethal oedema formation (303). The TE value of the T₂-TSE sequence, determined by tissue relaxometry was instrumental to the sensitive representation of tissue hyper-intensity surrounding the necrotic core indicative of tumour proliferation and helped to differentiate between tumour necrosis and

brain parenchyma invaded by tumour cells. In addition, the scans obtained showed a remarkably high correlation to the histological findings underscoring the quality of the established sequence parameters.

Taken together, it could be concluded that the lack of a dedicated high-field scanner shouldn't be a deterrent to carry out small animal imaging studies. This study demonstrates the importance of a certain degree of user-end customisations, including the dedicated RF coil system along with careful optimization of sequence protocols which can dramatically improve the quality of images. Further work would extend the prospects of such an endeavour and will broaden the required armamentarium for neuroscience research.

6.2. SERIAL MAGNETIC RESONANCE IMAGING TO DETERMINE THE BLOOD BRAIN BARRIER PERMEABILITY CHANGES AND THE DYNAMIC FLUXES IN VASOGENIC OEDEMA FORMATION FOLLOWING ISCHEMIA-REPERFUSION INJURY IN RATS.

Employing serial MRI at 3T we detected the phasic nature of BBB opening following I/R injury. The injured BBB demonstrated dynamic temporal changes in permeability characteristics and might mediate local and remote vasogenic oedema. Further, the first phase of differential permeability characteristics at the BBB lasting up to 24 hours led to progressive oedema accumulation whereas the second phase did not contribute to oedema formation and may mediate oedema resorption. Upon reperfusion, three distinct phases of increased BBB permeability changes attributed to endothelial paracellular / TJ opening have been documented (261, 304, 305). Increased BBB permeability (also termed BBB opening, BBB disruption, BBB leakage) is commonly characterized by the extravasation of blood-pool agents that under normal physiological conditions do not cross the BBB to enter the brain parenchyma. Such blood-pool agents include the EB dye-albumin complex (MM 65961 Da), ³H-sucrose (MM 342 Da) for histological studies and Gd-DTPA (MM 590 Dalton) for in vivo MRI, amongst others (261, 280, 304, 305).

It is conceivable, given the differences in molecular weight, charge and protein binding characteristics of the tracer and detection methods, sensitivity of these methods for altered BBB permeability may differ considerably. Following reperfusion, the initial change in BBB permeability is attributed to acute elevations in regional Cerebral Blood Flow

(rCBF), which is then followed by the characteristic “biphasic” permeability response. Since, this is short lasting and is of hemodynamic in origin; we focused our attention on the subsequent pathologic ‘biphasic’ opening. In principle, at least three components of I/R injury are likely to contribute and act in sequential, but, overlapping time courses: 1. Direct injury to the neurovascular unit. 2. Resultant inflammation and repair. 3. Regenerative strategies such as angiogenesis.

6.2.1. MR IMAGING OF BBB PERMEABILITY CHARACTERISTICS.

Following 4 hours of reperfusion and consistent with studies using EB, we observed the first significant increase in BBB permeability as indicated by an increase of T_1SI_{diff} . This observation denotes the first phase of the biphasic permeability changes and may be attributed to increased inflammatory and oxidative stress at the BBB, in conjunction with enzymatic degradation of the extracellular matrix (119, 306). Inflammatory mediators, such as thrombin, histamine and bradykinin cause BBB permeability changes by actin polymerization-dependent Endothelial Cell (EC) rounding and formation of inter endothelial gaps (307). Proteolytic enzymes like MMPs mediate the degradation of TJ Proteins (TJPs) at such an early time point (308). The deleterious role of oxidative stress has also been demonstrated by the reversible disruptive effect of hydrogen peroxide on the physiological, biochemical, and immunocytochemical parameters of TJP integrity (309).

RNA levels of VEGF and Angiopoetin-2 (Ang-2) has been described to increase as early as 1–3 hours following ischemia, while proteins peak later during severe vasogenic oedema. Since, the angiogenic and endothelial cell destabilizing effects has been shown to lag behind their peak levels, their contributory roles in this initial opening seem to be

minimal (310). A correlation has been demonstrated between neutrophil infiltration into the brain parenchyma and the overlying time-frame of the biphasic permeability responses (311). Peak neutrophil infiltration may however not be the cause but may be facilitated by the disassembly of TJPs as a result of MMP activation and / or due to oxidative stress following I / R injury. Since, the observed enhancement being a characteristic feature of tMCAO and is not demonstrated by permanent MCAO models, it is reasonable to speculate that the increased oxidative stress, resulting from reperfusion may be the principal factor contributing to the reversible TJP disruption and thereby bringing about the observed Gd-DTPA extravasation.

The first phase of the biphasic BBB permeability was followed by a significant drop in BBB permeability measured by T_1SI_{diff} at 24 hours; however, complete recovery of BBB integrity did not occur as T_1SI_{diff} were still higher than that of sham. In fact, brain tissue with leaky BBB (as measured by PBV) doubled in volume compared to that at 4 hours post-reperfusion and the net amount of extravasated Gd-DTPA as measured as $T_1SI_{diff} \times PBV$ product remained almost similar to that of the 4 hour post-reperfusion. Even though the precise mechanisms of this partial recovery in barrier function found at this time are not well understood, two independent mechanisms might contribute. ROS mediated disassembly of TJPs has been shown to reverse within a period of 6 hours, while ongoing effects of inflammatory mediators maintain the EC rounding resulting in an endothelial gap so large that even fully functional TJPs cannot form functional tight junctions limiting paracellular diffusion (309). Such a situation at the BBB may still allow the extravasation of water while the free flow of Gd-DTPA molecules is partially hindered by the re-assembled TJPs causing the observed drop in post-contrast T_1SI_{diff} .

Following these observations at 24PR, we observed an increase in BBB permeability and brain tissue with leaky BBB as indicated by both, T_1SI_{diff} and PBV, at 48PR. The angiogenic and endothelial cell destabilizing effect of VEGF and Ang2 levels are known to peak at 48PR and may contribute to the observed BBB permeability changes (310). MCP-1 secretion by both astrocytes and brain endothelial cells also coincide well with the time course of events described and directly alter the BBB permeability characteristics associated with redistribution of occludin, ZO-1, ZO-2, and claudin-5. This also facilitates the entry of neutrophils to the site of the lesion (312). Infiltrating neutrophils, being a rich source of MMP-9, have also been demonstrated to mediate vasogenic oedema and hemorrhagic transformation in a transient ischemic model of stroke (313).

We observed a consistent increase of brain tissue with leaky BBB (PBV) up to 48 PR, with the most dramatic increase observed at the 24PR. Interestingly, the entire PBV presented rather homogeneously at the time points of 24 and 48 PR in- and outside the initial ischemic core. Throughout the experiment, the BBB permeability as measured by T_1SI_{diff} at the contralateral side of the experimental group has been consistently lower than that of sham controls probably due to compression of cerebral vessels due to raised intracranial pressure by cerebral oedema. Also, we observed an increase in post-contrast T_1SI_{diff} values in the sham group as well as at the contralateral hemisphere of the experimental group, which can, most likely be attributed to Isoflurane anaesthesia.

Although not thoroughly investigated, Isoflurane has shown to induce cerebrovascular dilation mediated through endothelial Nitric Oxide Synthase (eNOS) and the formed nitric oxide (NO) in humans and animals in a dose-dependent manner (314). The confounding effects of Isoflurane on the observed ipsilateral T_1SI_{diff} may not be as direct as this region also possesses the infarct core along with profound oedema. Low basal cerebrovascular

tone results in a decreased capacity to vasodilate whereas high cerebrovascular tone expands the auto-regulatory range (314) . Persistent oedema observed at the ipsilateral hemisphere with increased Intra Cranial Pressure (ICP) results in low cerebrovascular tone in order to maintain adequate CBF. Any additional effect of Isoflurane to cause further vasodilatation is rather doubtful.

6.2.2. OEDEMA DEVELOPMENT IN RELATION TO BBB PERMEABILITY.

Quantification of oedema formation in both hemispheres using MRI was performed by T₂-relaxometry over time and correlated to BBB permeability in parallel. At the early time point of 04PR, we could detect increased brain water content / oedema as indicated by an elevated T₂ value not only at the ipsi- but also at the contralateral striatum. Such remote effects at the non-ischemic contralateral hemisphere have thus far been demonstrated in permanent MCAO and cold brain injury models only (315). In permanent MCAO peak oedema at the contralateral regions was only apparent at 24-48 hours post occlusion. However, in the cold brain injury model, oedema mediated by leaked protein was observed at the lesion site and periphery after one hour and by 24–48 hours the leaked protein was strongly stained at both the hemispheres (315). The authors attribute this to ‘routed protein migration’ and consider such ‘remote’ effects within the realm of ‘Diaschisis’.

A similar assumption may also be valid in the case tMCAO for two reasons. First, the initial BBB permeability change would have resulted in the extravasation of serum proteins, which, along with the cellular debris following necrosis could proliferate through the white matter tracts. Second, with an intact BBB at the contralateral striatum, net transport of water need to be driven by osmotic forces due to solute movements as there are no primary active, ATP-driven, water pumps (316).

By 24 hours, the observation of a constant amount of extravasated contrast agent into the brain as observed by a constant $T_1SI_{diff} \times PBV$ product to that at 04PR accompanied by a peak oedema observed by T_2 values and volumetric swelling of the ipsilateral hemisphere may indicate an ongoing unperturbed water shift from the vascular to the brain compartment. Contrary to the earlier time point, the observed oedema is unlikely to be caused by significant BBB leakage for proteins as indicated by the partial recovery of BBB function at this time point. Potential candidates mediating oedema accumulation may include members of the non-selective cationic Transient Receptor Potential (TRP) channels, which serve as redox sensors at the vascular endothelium (317). TRPs may form the molecular basis of oxidant-activated cation channels and are increasingly recognized for their role in regulating barrier function (307, 318). Some members of the TRP family, especially the canonical TRPs (TRPCs) are well recognized for their lack of cation specificity and the ability to generate substantial monovalent conductances that govern membrane potential and cationic gradients.

According to the biophysical properties reported so far, inward currents through most TRPC channels are carried by both Na^+ and Ca^{2+} ions in physiological conditions (319). However, the entry of Na^+ has been implicated in physiological Ca^{2+} signalling phenomena such as Ca^{2+} oscillations and also in pathophysiological Ca^{2+} overload (320, 321). Such a mechanism would explain the observation that BBB permeability to sodium occurs at 12-48 hours following MCA occlusion, which, together with an antecedent intracellular shift to sodium, cause a massive water and sodium influx (322). Again, continued oxidative stress resulting from reperfusion, entry of neutrophils and the generation of superoxide by microglia activated by extravasated albumin and other serum components may continuously drive the up-regulation and proliferation of such ion

channels and therefore would be responsible for the massive oedema observed at these times (323).

At 24 hours post reperfusion, we also observe a significant drop in the T_2 value at the contralateral striatum compared to the T_2 value at 04 PR when remote oedema has been consistently demonstrated attributed to extravasated protein migration through the white matter tracts. In the immediate absence of any scavenging mechanisms to remove those protein and / or their degradation products, we expected a further increases of vascular oedema at this time point especially in the presence of the up regulation of ion channels as discussed before. The unexpected significant fall in the T_2 value at 24 hours, however, may possibly be due to the reduction in the oxy-hemoglobin content resulting from vessel compression by the existing bilateral oedema and the increased cerebral oxygen extraction and / or decreased volume of oxygenated blood volume. In this scenario the resultant T_2 value being a function of both water content and the blood oxygenation effects happens to be tilted downwards.

Consistent with previous studies we found a decrease in brain water content/oedema as indicated by the fall in T_2 values and a reduction in ipsilateral hemispherical volume at 48hours despite an increase of BBB permeability and BBB disrupted area as indicated by both, T_1SI_{diff} and PBV (261, 305, 306). This indicates resorption of vasogenic oedema possibly brought about by a variety of mechanisms including the uptake of extravasated proteins by glial cells and the resulting reduction in oncotic force, migration of oedema into the cerebrospinal fluid spaces and also due to effects from proliferating endothelium.(324-326).

Off late, selective water channels at the astrocytic end feet, the AQuaPorins (AQPs), especially aquaporin-4 (AQP-4), have also been proposed to play an important role in the

pathophysiology of brain oedema both in rodents and humans with a peak at 48PR (327). Further, the T_2 values at the contralateral striatum demonstrated a non-significant but a rebound increase in values. Since this value being higher than that of the control, possibly indicate the persistent presence of remote oedema at these times which was duly masked at the 24 hour time point due to the increased ICP.

T_2 -relaxometry is also influenced by flow effects, alteration in the amounts of oxy- and deoxyhemoglobin, tissue oxygenation and the exchange of nuclear spin magnetization between the “free” and “bound” proton pools (264). We observed this ‘Blood Oxygenation Level Dependant’ (BOLD) effect in the very early phase of ischemia by a consistent fall in the T_2 values which affected the whole ischemic hemisphere even in regions that did not demonstrate pannecrosis (253, 328). As expected, following reperfusion, the increased inflow of oxygenated blood resulting from reactive hyperemia which invariably develops after the release of arterial occlusion elevated the transverse relaxation time at the ipsilateral striatum.

6.2.3. BIPHASIC BBB PERMEABILITY; A SURROGATE MARKER FOR THE ‘NEW PENUMBRA’?

In a recent editorial, Eng Lo coined the term ‘new penumbra’ to define the transition of most targets of ischemic stroke therapy (VEGF, MMPs, NO, glutamate release, JNK pathway, amongst others) from mediators of injury to be the effectors of repair following acute stroke (58). Indeed, the lack of understanding of this ‘Janus-faced’ nature of many targets of neuroprotection in stroke research might represent the increasing frustration with a number of the proposed neuroprotectants (329). The observed phasic permeability

characteristics of the BBB and the resultant shifts in oedema may possibly be orchestrated by a variety of mediators, from growth factors (i.e. VEGF, EGF, BDNF), MMPs, NO to inflammatory cytokines (i.e. IL-6, IL-1 β , C-reactive protein, TNF- α). Such, intricate and highly complex interactions resulting in dynamic shifts in the BBB permeability characteristics cannot be solely considered to mediate oedema alone. The proposed role of the expression of ion channels might also have a larger role in mediating the adaptive mechanisms of the injured brain by exerting its plastic behaviour. Pharmacotherapy for neuroprotection and / or oedema prevention in stroke therapy may be carefully characterized as the same drug moiety may cause beneficial and detrimental effects on BBB function, functional improvement and ultimately stroke outcome when given early, late or throughout the phase of ischemic injury.

Overall, MRI may provide a translational read-out of BBB function reflecting the transition from injury and repair. However, confirming similar characterization of BBB changes in humans being a pre-requisite for such timely pharmacotherapy, demands great efforts from acute stroke patients and neuroradiologists in the early hours following thrombolysis. In addition, due to the inherent variability in human stroke, the biphasic BBB behaviour may not occur as uniform as in experimental settings but in overlapping time intervals, which may complicate analysis of MRI data. Using a human 3T MR scanner with identical sequences to the application in human stroke allows us to employ identical analysis as used in this study.

6.2.4. SUMMARY.

In the present MRI study conducted on a relatively low field clinical scanner we were able to define the timely correlation between the biphasic opening of the BBB and the dynamics of brain water content during the first 48 hours after focal cerebral ischemia. The

phasic phenomena of altered BBB permeability might not only contribute to local but also possibly mediate widespread oedematous changes including resorption at late time points. MRI equivalents of BBB permeability characteristics and oedema formation are exceedingly complex and continuously influenced by raised ICP, altered CBF, BOLD effects and effects of inhalational anesthetics. The biphasic BBB opening and oedema formation as demonstrated here may reflect injury and repair following ischemia and reperfusion at the neurovascular unit and needs to be confirmed in acute stroke patients employing similar MRI sequences. Stroke therapy aimed at the vasogenic oedema and neuroprotection strategies may be guided according to the functional status of the BBB.

6.3. TROPHIC PROPERTIES OF EPIDERMAL GROWTH FACTOR AND PIGMENT EPITHELIUM DERIVED FACTOR ON SELECTED INDICES OF NEUROVASCULAR INJURY FOLLOWING ISCHEMIA-REPERFUSION INJURY IN RATS.

The studies performed with the selected neurotrophic growth factors were primarily aimed at studying the rather sub-acute effects of these factors on I/R injury. The slow IV infusion of the trophic factors extending over a period of 4 hours was performed to mimic the clinical situation, where there is a time delay of several hours from stroke onset and therapy initiation. Such an approach of IV trophic factor administration is relatively rare except for a couple of studies performed in this manner (330, 331). In this regard, this study differs from the majority of other studies, where, the trophic factors are administered directly into the cerebral ventricles where they are primarily considered for proliferation and differentiation of neural progenitor cells rather than their neuroprotective effects (332, 333). Moreover, this is the first study performed to evaluate the trophic properties of PEDF administered post reperfusion through IV route in a rodent model of I/R injury. To the best of our knowledge there is only one related study where neuroprotective effects have been observed following PEDF gene transfection seven days prior to tMCAO.

6.3.1. EFFECT OF EGF AND PEDF ON THE INFARCT VOLUME.

Intravenous infusion of the considered NTFs significantly attenuated the T₂ lesion volume (i.e. Infarct volume) at the first time point of 24 hours. A number of trophic factors have demonstrated such protective effects when studied with transient and permanent occlusion models of ischemic stroke (330, 334, 335). Even though the underlying

mechanisms responsible for such neuroprotection are not very clear, it is highly likely that multiple mechanisms are involved.

After transient MCA occlusion, EGFR is highly induced in reactive astrocytes and microglia / macrophages by 3 to 4 days after ischemia (336). Therefore, exogenous EGF administered in this study probably acts on neuronal membrane-anchored EGFR because neuronal protection must take place during the first hours after MCA occlusion before marked glial reactivity is apparent. Neurons within the MCA territory, i.e. lateral cortex and striatum, are rich in EGFR and are thus susceptible to the action of exogenously administered EGF.

A multitude of pathways already exists that could be proposed to explain the observed neuroprotection at the relatively early time point of 24 hours. Transient ischemic models represent a phase of ischemia and reperfusion, which, in fact is conducive to the overproduction of free radicals and lipid peroxides which then mediate neuronal damage and oedema formation (337, 338). EGF successfully prevented neuronal death and lipid peroxidation induced by ferrous sulphate (FeSO_4) which has been used to generate hydroxyl radicals in culture (339, 340) . However, simultaneous addition of EGF and FeSO_4 into the culture medium did not attenuate FeSO_4 neurotoxicity, which demonstrates EGF itself does not appear to act as a free radical scavenger (214).

bFGF, NGF, and BDNF, which are all well-known NTFs, reduce lipid peroxidation induced by glutamate exposure. It has been demonstrated that the three NTFs enhance more or less the activities of antioxidant enzymes such as superoxide dismutase, glutathione peroxidase, and catalase (341). Because receptors for EGF, bFGF, BDNF, and NGF use similar transduction pathways via tyrosine phosphorylation, EGF may rescue ischemic neurons by enhancing the activities of the antioxidant enzymes (203). On the

other hand, it's been reported that EGF rescued neurons from anoxic injury in vitro. Under the anoxic environment, the enhancement of antioxidant enzymes by EGF may not be responsible for the neuroprotective effect (211). The antianoxic action of EGF may play a significant role in rescuing ischemic neurons together with the antioxidant activity.

Even though it's been demonstrated that the neuroprotection offered by EGF is mediated partly through the induction of antioxidant enzymes, we remain sceptical about this as the EGF group had the highest T_2 -value indicative of oedema formation at the 24 hour time point. The failure of EGF to attenuate oedema formation does not seem to go in hand with its proposed mechanism of antioxidant enzyme up regulation despite a significant reduction in infarct volume.

It's considered that, EGF could mediate two principal types of signalling mechanisms, where a transient activation of EGF signal could mediate cell proliferation and a sustained activation of EGF signal could exert distinct mitogenic, survival, differentiative and neuromodulatory effects (201). The attributed mechanisms include a change in protein tyrosine phosphatase (PTP) activity that dephosphorylates EGFR and MAPK allowing for sustained signalling or a decreased rate of EGFR down-regulation through internalization and lysosomal degradation.

PEDF demonstrated significant reduction in T_2 - lesion volume at the 24 hour time point, when compared to that of EGF and the control group demonstrating its neuroprotective properties. Even though this data being first of its kind demonstrating neuroprotection in ischemic stroke, a number of previous studies have noted such an effect in a variety of experimental settings. PEDF originally was shown to induce a neuronal phenotype in retinoblastoma Y-79 cell line cultures and, later, to promote the survival of primary cultures of rat cerebellar granule neurons (238). In addition, PEDF has

been shown to protect cerebellar granule neurons from acute glutamate toxicity and from apoptosis occurring naturally in culture or as a result of serum withdrawal (240, 342). PEDF also has been reported to affect the metabolism of glial cells in cultures and to protect postnatal rat motor neurons against chronic glutamate-induced excitotoxicity in cultured spinal cord explants (343). Another, interesting aspect of PEDF enabled neuroprotection particularly with reference to the employed transient ischemic model in our work could be due to their antioxidant properties.

Studies have demonstrated that PEDF exerts significant protection to cultured retinal pericytes from oxidative injury and has also shown to suppress ROS formation within microvascular endothelial cells (344, 345). Even though the underlying mechanisms behind the observed neuroprotection by reduction of the T₂-lesion volume are far from being elucidated, we assume that PEDF exerts its neuroprotective effect principally by countering the excitotoxic effects of glutamate and through its proposed antioxidant properties.

Both the control and EGF groups demonstrated an increase in the T₂-lesion volume by 48 hours whereas the PEDF group demonstrated almost similar volume as that at 24 hours. Even though the lesion volume of EGF was still significantly smaller than that of control, this observation indicates that the lesion volume expansion could not be completely arrested by EGF administration. Since the T₂-values indicative of oedema content was found to be decreased, the observed increase in T₂-lesion volume cannot be due to oedema accumulation. At all later time points the T₂-lesion volumes continue to decrease in a rather uniform manner where no specificities could be attributed to the mode of treatment.

Nevertheless it's worth noting that only the PEDF group could maintain statistically significant reduction in T₂-lesion volume after 48 hour time point up to 1 week.

6.3.2. EFFECT OF EGF AND PEDF ON OEDEMA FORMATION AND RESORPTION AT THE INFARCT REGION.

Consistent with the earlier works, tMCAO resulted in significant T₂-value elevation at the infarct site indicative of vasogenic oedema formation which was found to be maximal at 24 hours post reperfusion (346, 347). In fact, neither EGF nor PEDF was able to significantly reduce the water content within the infarct region. However, since the infarct volume itself being significantly different between the treatment groups, it can be considered that average T₂ values estimated from within the lesion site will not give the complete picture. A product of the T₂-value and infarct volume (T_{2vol}) unmasked the potency of both PEDF and EGF (at 48 hours) by its ability to act on both parameters of oedema and infarct volume.

This reduction in oedema formation by PEDF was also confirmed by two earlier studies. One of the studies, wherein the human PEDF was over expressed in a rat model of tMCAO has demonstrated that PEDF blocks increased expression of AQP4 mRNA and attributes this to the reduced oedema (348). Moreover the same work proposes that the anti-inflammatory properties of PEDF have been shown to down regulate the pro-inflammatory cytokine IL-1 β which in turn inhibits AQP4 expression.

Another study on a mice model of cold brain injury demonstrated the significant oedema attenuation following exogenous PEDF administration (349). The mechanism

proposed was that PEDF inhibited the brain oedema by suppression of Rac-1 activation in the cold-injured brain, which is essential for NADPH oxidase activation (97). A number of properties of PEDF can act together to bring out the observed reduction in T₂-lesion volume coupled to low oedema accumulation at the early time point of 24 hours. The antioxidant property may also prevent the up regulation of non-selective cationic TRP channels which was considered to contribute oedema formation. The role of such channels in oedema formation has been described in adequate detail before (347). Further, PEDF has been proposed to be acting as an endogenous anti-inflammatory agent. In the eyes of oxygen induced retinopathy and diabetic rat models, injection of PEDF significantly inhibited the expression of MCP-1, TNF- α and ICAM-1 (350). The same study also demonstrated that PEDF reversed the permeability enhancing effect of VEGF in retinal capillary endothelial cells. Retinal levels of VEGF along with its receptor, (Receptor 2, KDR) has also been found to be drastically reduced by PEDF treatment. Moreover, PEDF has also shown to stabilize actin, maintain normal membrane occludin, and N-cadherin structure and preserve the barrier function of retinal pigment epithelial cells against oxidative stress (351). All these properties could possibly be acting in concert to reduce the deleterious effects of I/R injury reflected by a reduction in infarct volume and accompanying oedema.

At 48 hours, both the control and EGF groups demonstrated reduced T₂-values where the reduction for the EGF group was statistically significant. Even though the precise mechanisms behind oedema resorption are still unclear, it could involve many of the same mechanisms as detailed in the earlier study (347). However, the fact that the PEDF group demonstrated a marginal increase in the T₂-value was rather unexpected. However, it seems that such behaviour may be adequately explained by the effects of PEDF on

inflammation. Neuronal death following cerebral ischemia activates innate immunity and triggers an inflammatory response (352). This response is necessary to remove cell debris and to start regenerative processes. Blood derived leukocytes along with resident microglia are the more activated inflammatory cells, accumulating in the brain tissue after cerebral ischemia, leading to inflammatory injury. Microglia, the major source of cytokines and other immune molecules of the CNS, are the first non-neuronal cells that respond to CNS injury becoming phagocytic when fully activated by neuronal death.

In-vitro studies have demonstrated that PEDF is an inhibitor of microglial and astrocyte proliferation even though it is found to increase the metabolism of microglia (343). However, available data do not provide any clue as to the effect of PEDF on glial cells in the presence of ischemic stroke. PEDF also being an inhibitor of inflammation is found to reduce the expression of ICAM-1 (350). Therefore, it may be possible that the blood borne leukocytes and monocyte migration into the necrotic region are interrupted and thereby hampering tissue clearance from the necrotic region. The uncleared cellular debris by virtue of its osmolality can continue to draw water out of the vasculature and causes its retention demonstrating an increase in the T_2 value compared to the earlier time point of 24 hours. However, oedema continued to decrease up to the 1 week time point, with no demonstrable differences between different treatment groups.

6.3.3. EFFECT OF EGF AND PEDF ON OEDEMA FORMATION AND RESORPTION AT DISTANT SITES REMOTE FROM INFARCTED REGION.

It's of interest to note that treatment with the macromolecular peptides (EGF and PEDF) has demonstrated increased T_2 -values at remote regions distant from the site of

injury. In our earlier study, we had demonstrated remote oedema formation for the first time with tMCAO models of I/R injury (347). The proposed mechanism was attributed to ``routed protein migration`` and seems to be consistent with the nature of I/R injury. Adding further credibility to such an observation, EGF and PEDF treated groups preferentially demonstrated significant increase in T_2 -values at the ipsilateral cortex. The pattern of the course of these T_2 -values seems to go in hand with their differences in molecular weight. Elevated T_2 -values for the EGF group was observed only at the relatively early time point of 24 hours, whereas, the T_2 - value elevation persisted throughout the duration of the study in the case with PEDF group when compared to that of the control group.

Routed protein migration of these macromolecules may be considered to be the causative factor behind these observed elevations in T_2 -values. PEDF molecule is at least 8 times heavier than that of the EGF. Even though, we employed equimolar doses of both EGF and PEDF, the PEDF molecule being the heavier one may disintegrate into much more number of smaller peptide fragments and by means of their collective colligative properties could have retained more water content. Once again, the same properties of both EGF and PEDF at the ipsilateral cortex have more or less been reproduced at the contralateral striatum. However, at the 24 hour time point, only EGF demonstrated significant elevation in T_2 -values compared to both the healthy group and the control ones. It has been described that EGF possesses a low tortuosity (λ), a parameter representing the hindrance imposed on molecules by the convoluted brain extracellular space which was found to be 1.8 (353). This low resistance to migration, which, when accompanied by a probable degradation might be the factor responsible for the elevated T_2 -value demonstrated by EGF at the relatively early time point of 24 hours. Following this both PEDF and EGF demonstrated elevated T_2 -values at the 48 hour time point. The relatively

late demonstration of elevated T_2 -values by PEDF can probably be attributed to the bulk of the molecule in comparison to that of EGF. Further, only the PEDF group has shown the persistent presence of oedema until one week time point.

All the results seems to be mutually supportive of the original hypotheses that ``routed protein migration`` might well serve as one of the explanation behind such remote oedema formation. To the best our knowledge, this is the first time that the ``bulk`` nature of the therapeutic agent has shown to be directly involved in mediating such remote effects which are well within the realm of ischemic ``Diashisis``.

6.3.4. ALTERED METABOLIC STATE AT THE INFARCT SITE AS MAPPED BY SUSCEPTIBILITY WEIGHTED (T_2^*) SEQUENCES.

The principal reason for considering susceptibility (T_2^*) weighted relaxometry at the site of infarction at extended time periods is to monitor the degree of blood oxygenation that might in turn provide an insight into neuroprotection / neurogenesis and altered metabolic states at the sites of interest. Deoxyhemoglobin is paramagnetic and oxyhemoglobin is diamagnetic in nature, changes in haemoglobin oxygenation levels affect magnetic resonance signal intensities (354). Susceptibility weighted GRE sequences are particularly sensitive to T_2^* decay which in fact, is the combined effect of spin-spin dephasing (T_2) and dephasing owing to magnetic field inhomogeneities.

At 24 hours, all the three groups demonstrated more or less similar values which were significantly higher than those of the healthy group. This is precisely what that is to be expected at a necrotic region (T_2 -lesion volume), where there is hardly any deoxyhaemoglobin formation to shorten the T_2^* -value. At 48 hours the PEDF group

demonstrated a significant decline in the T_2^* -values, whereas the other two groups demonstrated more or less similar values as that at 24 hours.

PEDF is not a mitogen like EGF and in fact shifts the balance between proliferation and differentiation favouring the latter. PEDF has been effective against neurodegenerative cascades promoted by a variety of insults like axotomy, glutamate excitotoxicity and oxidative stress and is an NTF promoting neurite outgrowth (355). Considering these aspects, it's highly unlikely that the observed decrease in T_2^* -value may be attributed to spontaneous metabolic enhancement brought about by cell proliferation especially at such an early time point. The observation is rather intriguing one and is in need of further clarification. It's been demonstrated that, the microglial infiltration into the infarct core peaks at 48 hours and this infiltration is considered to be the cause of infarct expansion observed until this time (146, 356). Moreover, it has also been shown that activated resident microglia pre-dominates the total macrophage count within the infarct region (T_2 -lesion volume) at this early time point (357). An in-vitro study has demonstrated that PEDF increases the microglial metabolism and suppresses its proliferation (343).

As stated before, there is a lack of information concerning the effect of PEDF on resident microglia in the presence of necrosis. We speculate that the increased metabolism of microglia or microglia derived macrophages at the infarct site may be the most probable reason for increasing the local deoxyhaemoglobin content responsible for the reduction in the observed T_2^* -value. In the subsequent time points (96 hours and 1week) the value remained significantly lower than both the control and EGF groups demonstrating the maintained metabolic enhancement. Even though, the saline and EGF group values started to decline from this time point onwards, no difference owing to EGF treatment could be discerned even though EGF demonstrated a significant reduction in infarct volume.

6.3.5. ALTERED METABOLIC STATE AT THE CONTRALATERAL STRIATUM AS MAPPED BY SUSCEPTIBILITY WEIGHTED (T_2^*) SEQUENCES.

Another, rather unexpected observation was the persistently elevated and almost similar T_2^* -values at the contralateral striatum of all the treatment groups. It's of interest to note that the neuroprotective role of both the trophic factors (as evident by reduced infarct volume and oedema) did not exert any meaningful effect on this presumed metabolic suppression.

Metabolic depression has been reported to occur after a variety of lesions such as concussive head injury, freezing lesions and ischemia (358-360). In models of chronic bilateral carotid artery occlusion or fluid percussion injury, the metabolic depression days after the lesion could be induced irrespective of overt cell damage (361, 362). Another study demonstrated depression in local cerebral glucose utilization in areas devoid of histologically verifiable chronic cell damage and was found to be independent of local cerebral blood flow (363).

Oxidative metabolism, as measured by cytochrome oxidase histochemistry and protein synthesis, may still be depressed 5 to 10 days after the head injury with values still below control levels (359). The mechanism underlying these derangements remains to be clarified. However, one may presume that long-lasting perturbations of membrane potential due to shifts in ionic balance after the lesion lead to an altered metabolic state, a view that is corroborated by the finding that these alterations can be prevented at least in part by antagonists of excitatory amino acids (364). At this point, we can only speculate that similar phenomena may also be determining the postischemic hypometabolism observed in the present study, and it would be useful to determine whether this metabolic alteration is accessible to therapeutic intervention.

6.3.6. TEMPORAL PROFILE OF BLOOD BRAIN BARRIER PERMEABILITY CHARACTERISTICS AT THE IPSILATERAL STRIATUM AS DETECTED BY POST-CONTRAST T_1 IMAGING.

The PEDF group demonstrated significant attenuation of T_1SI_{diff} at the ipsilateral striatum at all the considered time points. However, considering a variety of protective mechanisms exhibited by PEDF it's highly likely that multiple mechanisms may be involved in suppressing the barrier permeability. According to the previous study, the 24 hour time point represents a phase where the barrier permeability is found to be minimal for Gd-DTPA even though it's the period of peak oedema formation (347). Even at this time point, PEDF has demonstrated significant suppression of barrier permeability in comparison to both the control and EGF groups. It has been described that transcripts of VEGF and Ang2 were found to be increased consistently within hours of ischemia and peaks at 24-48 hours accompanying peak oedema (310). VEGF receptors along with VEGF also appears to be up regulated after ischemia and peak levels are observed at about the same time as that in the case of VEGF. Moreover, it should be noted that peak angiogenesis is found to lag behind the peak increase of VEGF, Ang2 and its receptors (310).

Taken together, it appears to be highly unlikely that VEGF plays a central role in mediating the barrier permeability at this early time point of 24 hours. The significant reduction in barrier permeability as a result of PEDF treatment could be attributed to its three distinct properties; 1) as an antioxidant, 2) anti-inflammatory and 3) direct protective effects on tight junction proteins like occludin and cadherin (344, 345, 350). The effect of ROS and its effect on TJPs have been described in sufficient detail before (347). Therefore, it may not be surprising that an agent with anti-oxidant properties demonstrates

significant reduction in barrier permeability characteristics. Further, inflammatory mediators, such as thrombin, histamine and bradykinin can cause BBB permeability changes by actin polymerization dependent EC rounding and results in formation of inter endothelial gaps and altered BBB permeability (307). Since PEDF has shown to stabilize actin, it's likely that EC rounding brought about by inflammatory mediators may be inhibited by PEDF resulting in reduced barrier permeability. Since PEDF also happens to be an inhibitor of inflammatory processes as such, these mechanisms can be additive and act in a synergistic way to minimize the barrier permeability.

Even though all the three groups demonstrated the same pattern of increased permeability at 48 hours, PEDF group demonstrated the least increase in the T_1SI_{diff} values and moreover the PEDF group had significantly lower T_1SI_{diff} values, when compared to both the EGF and control groups. The rather dramatic increase in BBB permeability following I/R injury at 48 hours seems to correspond with the time course of the angiogenic action mediated by VEGF (365, 366). Moreover, in almost every other case that has been investigated, vascular hyperpermeability has been intricately associated and is inherent to progressive angiogenesis (367, 368). Wealth of existing data demonstrates that PEDF is an inhibitor of angiogenesis. PEDF inhibited endothelial cell migration toward a variety of angiogenic inducers including PDGF, VEGF, IL-8, acidic FGF and lysophosphatidic acid (246). PEDF has demonstrated to act through a variety of mechanisms to arrest angiogenesis. The addition of PEDF to micro-vascular endothelium has been shown to increase the γ -secretase activity, which in turn cleaves the 80-kDa C-terminal unit of VEGFR-1 in the presence of VEGF. The same study also demonstrated that PEDF inhibits the phosphorylation of VEGFR-1 adding another route to suppress angiogenesis brought about by VEGF signalling (369).

Silencing of the PEDF gene by siRNA resulted in significant upregulation of VEGF expression at both the RNA and protein levels suggesting PEDF to be an endogenous negative regulator of VEGF. PEDF also inhibited the hypoxia induced increases in VEGF promoter activity, Hypoxia Inducible Factor (HIF) -1 nuclear translocation and MAP kinase phosphorylation (370). In-vitro receptor binding assay experiments demonstrated that PEDF competed with VEGF for binding to VEGF receptor 2, which may represent yet another mechanism for PEDF mediated angiogenesis inhibition.

Induction of apoptosis on proliferating endothelial cells is an important PEDF anti-angiogenic activity. Moreover, apoptosis induced by PEDF has been found to be mediated by a number of players. Endothelial cells within mature vessels are protected from apoptosis by cell-cell and cell-matrix contacts (371). Such cells are also less susceptible to VEGF stimulated sprouting. In response to increased levels of the angiogenic inducer, followed by rising Ang2, the cells are released from contacts and activated to digest matrix, migrate, divide and eventually form new vessels. Such activated endothelial cells also upregulate surface Fas, and thereby become sensitive to apoptosis when FasL is induced by inhibitors such as PEDF (233). PEDF has demonstrated to increase FasL mRNA and protein possibly through activation of JNK-1 and when the angiogenic inducers were not in excess, interactions of inhibitor-induced FasL with inducer-stimulated Fas resulted in apoptosis (233). Fas-mediated signalling mainly induces procaspase-8 auto-proteolytic cleavage, although it may subsequently cause activation of procaspase-9 (372).

Another study demonstrated that PEDF increase the expression and transcriptional activity of the Peroxisome Proliferator Activated Receptor gamma (PPAR γ) in human umbilical vein endothelial cells. Further, PEDF action on PPAR γ resulted in apoptosis of endothelial cells which is thought to be mediated through p53. They also demonstrated that

an inhibitor to p38 MAPK extensively blocks PPAR γ mRNA and protein expression (372). Our data on PEDF and its robust inhibition of angiogenesis following tMCAO is the first of its kind that was subjected to study so far in a rat model of I/R injury. Considering the multitude of mechanisms, as described above, it's highly likely that multiple pathways may converge together in bringing out the obtained results. Much more intriguing is the potent angiogenic inhibitory action of PEDF at extended time points following a single exposure to PEDF.

6.3.7. TEMPORAL PROFILE OF T_1SI_{DIFF} CHANGES AT THE CONTRALATERAL STRIATUM.

In this region, we could not discern any evidence for Gd-DTPA extravasation, as demonstrated by gross hyperintense regions. Therefore, the intensity differences observed between the groups is a reflection of the amount of Gd-DTPA circulating within the cerebral vessels. It's rather remarkable to note that, the T_1SI_{diff} values at the contralateral striatum of the control group remained similar if not identical throughout the duration of the study. This is an important factor demonstrating the stability of the scanner and the RF coil array system without which such a serial imaging study would have been rendered completely meaningless. Exactly the same could be said about the characteristics of the PEDF, which has also demonstrated similar values except at the time point of 48 hours.

The fact that PEDF T_1SI_{diff} values being lower than the EGF group, especially at the later time points, when EGF values were increasing significantly, presents an interesting insight into their persistent effects, long after the inducers have been withdrawn.

It has been mentioned earlier that PEDF might reduce oedema by interfering with the VEGF-NADPH oxidase pathway (349). It has been considered that ROS may serve as important signalling molecules in cerebral circulation. In contrast to systemic arteries, major products of superoxide metabolism, including hydrogen peroxide, are powerful cerebral vasodilators, raising the possibility that ROS represent important molecules for increasing local cerebral blood flow (373). In cerebral arteries, it's considered that NADPH-oxidases along with cyclooxygenases and lipoxygenases, are probably the primary sources of ROS formation. Further, in cerebral arteries, activation of NADPH-oxidase elicits both an increase in superoxide production and vasodilatation (373).

Since PEDF happens to demonstrate antioxidant properties coupled to the inhibition of the VEGF-NADPH oxidase pathway it could effectively suppress the vasodilatory mechanism. Such suppression may adequately explain the observed values of PEDF.

Another, interesting aspect observed is the consistent increase in the T_1SI_{diff} value of the EGF group from 48 hour onwards until the entire duration of the study. EGF being a mitogen, acting through the MAPK signalling cascade has demonstrated a dose and time dependant increase of eNOS protein levels (374). This assumes further significance especially when considering the mode of our anaesthesia administration during the imaging session at the MR scanner. In our earlier work, we have categorically demonstrated the effect of Isoflurane induced vasodilatation as a result of the concerned anaesthetic to induce eNOS (347). So, a treatment with EGF and Isoflurane should have demonstrated additive properties in the induction of eNOS resulting in the observed T_1SI_{diff} increase attributed to cerebral vasodilatation.

6.3.8 .CONCLUDING REMARKS AND FUTURE DIRECTIVES.

The presented work performed by giving emphasis to non-invasive serial MR imaging of cerebral I/R injury yielded considerable insights into its pathology and its response to therapeutic interventions at extended time periods. The information provided is unique in its own way as the study was performed non-invasively on identical animals with multiple monitoring time points and without any kind of histological interventions like organ collection, sectioning and staining procedures.

Such studies are relatively rare as repeated MR characterization of severely ill animals is both a challenging and laborious task to the experimenter. Moreover, repeated handling and anaesthetic procedures especially during MR imaging procedures can be extremely stressful to the subjected animals especially during the sub-acute stage of I/R injury. However, considering the wealth of information that has been derived from a fraction of the number of animals which will otherwise be required if histological studies were to be performed, the entire effort seems to be rather worthwhile.

As is always the case, MR imaging yields vast amounts of data in relatively short time periods which is indeed overwhelming and is time consuming to analyze and interpret. Moreover, this study also had its share of drawbacks and limitations of which the most important ones are as follows.,

- 1) The above mentioned study has been performed with a single dose of EGF and PEDF. By all means this is not an ideal situation and will not provide considerable insight into the existence of a probable dose-response relationship in the protective effects of these NTFs in the context of ischemic stroke.

- 2) Any treatment, aimed at neuroprotection in stroke will always be incomplete without being subjected to behavioural assessment of the animals. All the improvements in any of the parameters considered here will be at a loss if it's not accompanied by functional improvement. Such a work has not been performed in our study and needs to be performed to confirm any/all of the observed benefits/effects.

- 3) MRI indices like estimation of T_2 -relaxation time for characterizing oedema has been well validated a number of times with different studies and were not repeated here again. The same can be said about post-contrast T_1 characterization of BBB leakage. However, the presumed metabolic suppression which we propose as the underlying reason behind prolonged T_2^* -relaxation times has not been validated as such. A correlative study is proposed to estimate oxygen-glucose uptake and their relation to T_2^* -values in the injured brain following I/R injury. This might provide invaluable insights into the remote effects of brain injuries and endogenous repair mechanisms.

- 4) As an attempt to elucidate possible neuroprotective pathways, an immunohistochemical study is considered to profile the expression patterns of selected protein molecules. This work is presently underway at our laboratory to characterize and confirm the probable mechanisms behind these observed effects as put forward in the work presented here. We hope to present these data in the subsequent publications as and when they are completed.

References

1. Sarti C, Rastenyte D, Cepaitis Z, Tuomilehto J. International trends in mortality from stroke, 1968 to 1994. *Stroke*. 2000 Jul;31(7):1588-601.
2. Murray CJ, Lopez AD. Mortality by cause for eight regions of the world: Global Burden of Disease Study. *Lancet*. 1997 May 3;349(9061):1269-76.
3. Feigin VL, Lawes CM, Bennett DA, Anderson CS. Stroke epidemiology: a review of population-based studies of incidence, prevalence, and case-fatality in the late 20th century. *Lancet Neurol*. 2003 Jan;2(1):43-53.
4. Foulkes MA, Wolf PA, Price TR, Mohr JP, Hier DB. The Stroke Data Bank: design, methods, and baseline characteristics. *Stroke*. 1988 May;19(5):547-54.
5. Caro JJ, Huybrechts KF, Duchesne I. Management patterns and costs of acute ischemic stroke : an international study. For the Stroke Economic Analysis Group. *Stroke*. 2000 Mar;31(3):582-90.
6. Lo EH, Dalkara T, Moskowitz MA. Mechanisms, challenges and opportunities in stroke. *Nat Rev Neurosci*. 2003 May;4(5):399-415.
7. Bejot Y, Benatru I, Rouaud O, Fromont A, Besancenot JP, Moreau T, et al. Epidemiology of stroke in Europe: geographic and environmental differences. *J Neurol Sci*. 2007 Nov 15;262(1-2):85-8.
8. Broderick JP, Brott T, Tomsick T, Miller R, Huster G. Intracerebral hemorrhage more than twice as common as subarachnoid hemorrhage. *J Neurosurg*. 1993 Feb;78(2):188-91.
9. Takebayashi S. Ultrastructural morphometry of hypertensive medial damage in lenticulostriate and other arteries. *Stroke*. 1985 May-Jun;16(3):449-53.
10. Cole FM, Yates PO. The occurrence and significance of intracerebral microaneurysms. *J Pathol Bacteriol*. 1967 Apr;93(2):393-411.
11. Broderick JP, Adams HP, Jr., Barsan W, Feinberg W, Feldmann E, Grotta J, et al. Guidelines for the management of spontaneous intracerebral hemorrhage: A statement for healthcare professionals from a special writing group of the Stroke Council, American Heart Association. *Stroke*. 1999 Apr;30(4):905-15.
12. Davalos A, Fisher M. Emerging therapies for cerebrovascular disorders. *Stroke*. 2005 Feb;36(2):208-10.
13. Richard Green A, Odergren T, Ashwood T. Animal models of stroke: do they have value for discovering neuroprotective agents? *Trends Pharmacol Sci*. 2003 Aug;24(8):402-8.

14. Ginsberg MD. Neuroprotection for ischemic stroke: past, present and future. *Neuropharmacology*. 2008 Sep;55(3):363-89.
15. Tissue plasminogen activator for acute ischemic stroke. The National Institute of Neurological Disorders and Stroke rt-PA Stroke Study Group. *N Engl J Med*. 1995 Dec 14;333(24):1581-7.
16. Furlan A, Higashida R, Wechsler L, Gent M, Rowley H, Kase C, et al. Intra-arterial prourokinase for acute ischemic stroke. The PROACT II study: a randomized controlled trial. *Prolyse in Acute Cerebral Thromboembolism*. *JAMA*. 1999 Dec 1;282(21):2003-11.
17. Sherman DG, Atkinson RP, Chippendale T, Levin KA, Ng K, Futrell N, et al. Intravenous ancrod for treatment of acute ischemic stroke: the STAT study: a randomized controlled trial. *Stroke Treatment with Ancrod Trial*. *JAMA*. 2000 May 10;283(18):2395-403.
18. Ginsberg MD. Current status of neuroprotection for cerebral ischemia: synoptic overview. *Stroke*. 2009 Mar;40(3 Suppl):S111-4.
19. Larrue V, von Kummer RR, Muller A, Bluhmki E. Risk factors for severe hemorrhagic transformation in ischemic stroke patients treated with recombinant tissue plasminogen activator: a secondary analysis of the European-Australasian Acute Stroke Study (ECASS II). *Stroke*. 2001 Feb;32(2):438-41.
20. Astrup J, Siesjo BK, Symon L. Thresholds in cerebral ischemia - the ischemic penumbra. *Stroke*. 1981 Nov-Dec;12(6):723-5.
21. Fisher M. The ischemic penumbra: identification, evolution and treatment concepts. *Cerebrovasc Dis*. 2004;17 Suppl 1:1-6.
22. Rothman SM, Olney JW. Glutamate and the pathophysiology of hypoxic-ischemic brain damage. *Ann Neurol*. 1986 Feb;19(2):105-11.
23. Dirnagl U, Iadecola C, Moskowitz MA. Pathobiology of ischaemic stroke: an integrated view. *Trends Neurosci*. 1999 Sep;22(9):391-7.
24. Wahlgren NG, Ahmed N. Neuroprotection in cerebral ischaemia: facts and fancies--the need for new approaches. *Cerebrovasc Dis*. 2004;17 Suppl 1:153-66.
25. Green AR, Shuaib A. Therapeutic strategies for the treatment of stroke. *Drug Discov Today*. 2006 Aug;11(15-16):681-93.
26. Endres M, Wang ZQ, Namura S, Waeber C, Moskowitz MA. Ischemic brain injury is mediated by the activation of poly(ADP-ribose)polymerase. *J Cereb Blood Flow Metab*. 1997 Nov;17(11):1143-51.

27. Pringle AK, Iannotti F, Wilde GJ, Chad JE, Seeley PJ, Sundstrom LE. Neuroprotection by both NMDA and non-NMDA receptor antagonists in in vitro ischemia. *Brain Res.* 1997 Apr 25;755(1):36-46.
28. Abdelkarim GE, Gertz K, Harms C, Katchanov J, Dirnagl U, Szabo C, et al. Protective effects of PJ34, a novel, potent inhibitor of poly(ADP-ribose) polymerase (PARP) in in vitro and in vivo models of stroke. *Int J Mol Med.* 2001 Mar;7(3):255-60.
29. Shibata M, Kumar SR, Amar A, Fernandez JA, Hofman F, Griffin JH, et al. Anti-inflammatory, antithrombotic, and neuroprotective effects of activated protein C in a murine model of focal ischemic stroke. *Circulation.* 2001 Apr 3;103(13):1799-805.
30. Liu R, Suzuki A, Guo Z, Mizuno Y, Urabe T. Intrinsic and extrinsic erythropoietin enhances neuroprotection against ischemia and reperfusion injury in vitro. *J Neurochem.* 2006 Feb;96(4):1101-10.
31. O'Collins VE, Macleod MR, Donnan GA, Horky LL, van der Worp BH, Howells DW. 1,026 experimental treatments in acute stroke. *Ann Neurol.* 2006 Mar;59(3):467-77.
32. Vornov JJ, Wozniak K, Lu M, Jackson P, Tsukamoto T, Wang E, et al. Blockade of NAALADase: a novel neuroprotective strategy based on limiting glutamate and elevating NAAG. *Ann N Y Acad Sci.* 1999;890:400-5.
33. Jensen BS. BMS-204352: a potassium channel opener developed for the treatment of stroke. *CNS Drug Rev.* 2002 Winter;8(4):353-60.
34. Taylor CP, Meldrum BS. Na⁺ channels as targets for neuroprotective drugs. *Trends Pharmacol Sci.* 1995 Sep;16(9):309-16.
35. Schabitz WR, Li F, Fisher M. The N-methyl-D-aspartate antagonist CNS 1102 protects cerebral gray and white matter from ischemic injury following temporary focal ischemia in rats. *Stroke.* 2000 Jul;31(7):1709-14.
36. Di X, Bullock R, Watson J, Fatouros P, Chenard B, White F, et al. Effect of CP101,606, a novel NR2B subunit antagonist of the N-methyl-D-aspartate receptor, on the volume of ischemic brain damage off cytotoxic brain edema after middle cerebral artery occlusion in the feline brain. *Stroke.* 1997 Nov;28(11):2244-51.
37. Suzuki M, Sasamata M, Miyata K. Neuroprotective effects of YM872 coadministered with t-PA in a rat embolic stroke model. *Brain Res.* 2003 Jan 3;959(1):169-72.
38. Zaleska MM, Mercado ML, Chavez J, Feuerstein GZ, Pangalos MN, Wood A. The development of stroke therapeutics: promising mechanisms and translational challenges. *Neuropharmacology.* 2009 Feb;56(2):329-41.
39. Cheng YD, Al-Khoury L, Zivin JA. Neuroprotection for ischemic stroke: two decades of success and failure. *NeuroRx.* 2004 Jan;1(1):36-45.

40. Gladstone DJ, Black SE, Hakim AM. Toward wisdom from failure: lessons from neuroprotective stroke trials and new therapeutic directions. *Stroke*. 2002 Aug;33(8):2123-36.
41. Grotta J. Neuroprotection is unlikely to be effective in humans using current trial designs. *Stroke*. 2002 Jan;33(1):306-7.
42. Muir KW, Teal PA. Why have neuro-protectants failed?: lessons learned from stroke trials. *J Neurol*. 2005 Sep;252(9):1011-20.
43. Green AR. Why do neuroprotective drugs that are so promising in animals fail in the clinic? An industry perspective. *Clin Exp Pharmacol Physiol*. 2002 Nov;29(11):1030-4.
44. Faden AI, Stoica B. Neuroprotection: challenges and opportunities. *Arch Neurol*. 2007 Jun;64(6):794-800.
45. Recommendations for clinical trial evaluation of acute stroke therapies. *Stroke*. 2001 Jul;32(7):1598-606.
46. Fisher M, Feuerstein G, Howells DW, Hum PD, Kent TA, Savitz SI, et al. Update of the stroke therapy academic industry roundtable preclinical recommendations. *Stroke*. 2009 Jun;40(6):2244-50.
47. Recommendations for standards regarding preclinical neuroprotective and restorative drug development. *Stroke*. 1999 Dec;30(12):2752-8.
48. Fisher M. Recommendations for advancing development of acute stroke therapies: Stroke Therapy Academic Industry Roundtable 3. *Stroke*. 2003 Jun;34(6):1539-46.
49. Fisher M, Hanley DF, Howard G, Jauch EC, Warach S. Recommendations from the STAIR V meeting on acute stroke trials, technology and outcomes. *Stroke*. 2007 Feb;38(2):245-8.
50. Fisher M, Albers GW, Donnan GA, Furlan AJ, Grotta JC, Kidwell CS, et al. Enhancing the development and approval of acute stroke therapies: Stroke Therapy Academic Industry roundtable. *Stroke*. 2005 Aug;36(8):1808-13.
51. Small DL, Buchan AM. Animal models. *Br Med Bull*. 2000;56(2):307-17.
52. Girouard H, Iadecola C. Neurovascular coupling in the normal brain and in hypertension, stroke, and Alzheimer disease. *J Appl Physiol*. 2006 Jan;100(1):328-35.
53. Fisher M. Stroke and TIA: epidemiology, risk factors, and the need for early intervention. *Am J Manag Care*. 2008 Jun;14(6 Suppl 2):S204-11.
54. Fornage M, Hinojos CA, Nurowska BW, Boerwinkle E, Hammock BD, Morisseau CH, et al. Polymorphism in soluble epoxide hydrolase and blood pressure in spontaneously hypertensive rats. *Hypertension*. 2002 Oct;40(4):485-90.

55. Martini SR, Kent TA. Hyperglycemia in acute ischemic stroke: a vascular perspective. *J Cereb Blood Flow Metab.* 2007 Mar;27(3):435-51.
56. Courtine G, Bunge MB, Fawcett JW, Grossman RG, Kaas JH, Lemon R, et al. Can experiments in nonhuman primates expedite the translation of treatments for spinal cord injury in humans? *Nat Med.* 2007 May;13(5):561-6.
57. Lok J, Gupta P, Guo S, Kim WJ, Whalen MJ, van Leyen K, et al. Cell-cell signaling in the neurovascular unit. *Neurochem Res.* 2007 Dec;32(12):2032-45.
58. Lo EH. A new penumbra: transitioning from injury into repair after stroke. *Nat Med.* 2008 May;14(5):497-500.
59. Carmichael ST. Rodent models of focal stroke: size, mechanism, and purpose. *NeuroRx.* 2005 Jul;2(3):396-409.
60. Jonas S, Tran AQ, Eisenberg E, Azam M, Viera D, Grumet S. Does effect of a neuroprotective agent on volume of experimental animal cerebral infarct predict effect of the agent on clinical outcome in human stroke? *Ann N Y Acad Sci.* 1997 Oct 15;825:281-7.
61. Grotta JC. Acute stroke therapy at the millennium: consummating the marriage between the laboratory and bedside. The Feinberg lecture. *Stroke.* 1999 Aug;30(8):1722-8.
62. Kidwell CS, Liebeskind DS, Starkman S, Saver JL. Trends in acute ischemic stroke trials through the 20th century. *Stroke.* 2001 Jun;32(6):1349-59.
63. Coimbra C, Drake M, Boris-Moller F, Wieloch T. Long-lasting neuroprotective effect of postischemic hypothermia and treatment with an anti-inflammatory/antipyretic drug. Evidence for chronic encephalopathic processes following ischemia. *Stroke.* 1996 Sep;27(9):1578-85.
64. Valtysson J, Hillered L, Andine P, Hagberg H, Persson L. Neuropathological endpoints in experimental stroke pharmacotherapy: the importance of both early and late evaluation. *Acta Neurochir (Wien).* 1994;129(1-2):58-63.
65. Corbett D, Nurse S. The problem of assessing effective neuroprotection in experimental cerebral ischemia. *Prog Neurobiol.* 1998 Apr;54(5):531-48.
66. Kawamata T, Alexis NE, Dietrich WD, Finklestein SP. Intracisternal basic fibroblast growth factor (bFGF) enhances behavioral recovery following focal cerebral infarction in the rat. *J Cereb Blood Flow Metab.* 1996 Jul;16(4):542-7.
67. Kawamata T, Dietrich WD, Schallert T, Gotts JE, Cocke RR, Benowitz LI, et al. Intracisternal basic fibroblast growth factor enhances functional recovery and up-regulates the expression of a molecular marker of neuronal sprouting following focal cerebral infarction. *Proc Natl Acad Sci U S A.* 1997 Jul 22;94(15):8179-84.

68. Johansson BB. Brain plasticity and stroke rehabilitation. The Willis lecture. *Stroke*. 2000 Jan;31(1):223-30.
69. Lee JM, Zipfel GJ, Choi DW. The changing landscape of ischaemic brain injury mechanisms. *Nature*. 1999 Jun 24;399(6738 Suppl):A7-14.
70. Kaste M. Thrombolysis in ischaemic stroke -- present and future: role of combined therapy. *Cerebrovasc Dis*. 2001;11 Suppl 1:55-9.
71. Dawson DA, Wadsworth G, Palmer AM. A comparative assessment of the efficacy and side-effect liability of neuroprotective compounds in experimental stroke. *Brain Res*. 2001 Feb 23;892(2):344-50.
72. Lekieffre D, Benavides J, Scatton B, Nowicki JP. Neuroprotection afforded by a combination of eliprodil and a thrombolytic agent, rt-PA, in a rat thromboembolic stroke model. *Brain Res*. 1997 Nov 21;776(1-2):88-95.
73. Andersen M, Overgaard K, Meden P, Boysen G, Choi SC. Effects of citicoline combined with thrombolytic therapy in a rat embolic stroke model. *Stroke*. 1999 Jul;30(7):1464-71.
74. Meden P, Overgaard K, Sereghy T, Boysen G. Enhancing the efficacy of thrombolysis by AMPA receptor blockade with NBQX in a rat embolic stroke model. *J Neurol Sci*. 1993 Nov;119(2):209-16.
75. Lyden P, Lonzo L, Nunez S. Combination chemotherapy extends the therapeutic window to 60 minutes after stroke. *J Neurotrauma*. 1995 Apr;12(2):223-30.
76. Barth A, Barth L, Newell DW. Combination therapy with MK-801 and alpha-phenyl-tert-butyl-nitron enhances protection against ischemic neuronal damage in organotypic hippocampal slice cultures. *Exp Neurol*. 1996 Oct;141(2):330-6.
77. Rod MR, Auer RN. Combination therapy with nimodipine and dizocilpine in a rat model of transient forebrain ischemia. *Stroke*. 1992 May;23(5):725-32.
78. Onal MZ, Li F, Tatlisumak T, Locke KW, Sandage BW, Jr., Fisher M. Synergistic effects of citicoline and MK-801 in temporary experimental focal ischemia in rats. *Stroke*. 1997 May;28(5):1060-5.
79. Gladstone DJ, Black SE. Enhancing recovery after stroke with noradrenergic pharmacotherapy: a new frontier? *Can J Neurol Sci*. 2000 May;27(2):97-105.
80. Hasbani MJ, Schlieff ML, Fisher DA, Goldberg MP. Dendritic spines lost during glutamate receptor activation reemerge at original sites of synaptic contact. *J Neurosci*. 2001 Apr 1;21(7):2393-403.
81. Cramer SC, Chopp M. Recovery recapitulates ontogeny. *Trends Neurosci*. 2000 Jun;23(6):265-71.

82. Johansson BB, Belichenko PV. Neuronal plasticity and dendritic spines: effect of environmental enrichment on intact and postischemic rat brain. *J Cereb Blood Flow Metab.* 2002 Jan;22(1):89-96.
83. Li Y, Chen J, Chopp M. Cell proliferation and differentiation from ependymal, subependymal and choroid plexus cells in response to stroke in rats. *J Neurol Sci.* 2002 Jan 15;193(2):137-46.
84. Morshead CM, Reynolds BA, Craig CG, McBurney MW, Staines WA, Morassutti D, et al. Neural stem cells in the adult mammalian forebrain: a relatively quiescent subpopulation of subependymal cells. *Neuron.* 1994 Nov;13(5):1071-82.
85. Ren J, Kaplan PL, Charette MF, Speller H, Finklestein SP. Time window of intracisternal osteogenic protein-1 in enhancing functional recovery after stroke. *Neuropharmacology.* 2000 Mar 3;39(5):860-5.
86. Fisher M, Finklestein S. Pharmacological approaches to stroke recovery. *Cerebrovasc Dis.* 1999;9 Suppl 5:29-32.
87. Young D, Lawlor PA, Leone P, Dragunow M, During MJ. Environmental enrichment inhibits spontaneous apoptosis, prevents seizures and is neuroprotective. *Nat Med.* 1999 Apr;5(4):448-53.
88. Arvidsson A, Kokaia Z, Lindvall O. N-methyl-D-aspartate receptor-mediated increase of neurogenesis in adult rat dentate gyrus following stroke. *Eur J Neurosci.* 2001 Jul;14(1):10-8.
89. Papadia S, Stevenson P, Hardingham NR, Bading H, Hardingham GE. Nuclear Ca²⁺ and the cAMP response element-binding protein family mediate a late phase of activity-dependent neuroprotection. *J Neurosci.* 2005 Apr 27;25(17):4279-87.
90. Ikonomidou C, Turski L. Why did NMDA receptor antagonists fail clinical trials for stroke and traumatic brain injury? *Lancet Neurol.* 2002 Oct;1(6):383-6.
91. Zhao BQ, Wang S, Kim HY, Storrie H, Rosen BR, Mooney DJ, et al. Role of matrix metalloproteinases in delayed cortical responses after stroke. *Nat Med.* 2006 Apr;12(4):441-5.
92. Lee SR, Kim HY, Rogowska J, Zhao BQ, Bhide P, Parent JM, et al. Involvement of matrix metalloproteinase in neuroblast cell migration from the subventricular zone after stroke. *J Neurosci.* 2006 Mar 29;26(13):3491-5.
93. Zhao BQ, Tejima E, Lo EH. Neurovascular proteases in brain injury, hemorrhage and remodeling after stroke. *Stroke.* 2007 Feb;38(2 Suppl):748-52.
94. Gao Y, Signore AP, Yin W, Cao G, Yin XM, Sun F, et al. Neuroprotection against focal ischemic brain injury by inhibition of c-Jun N-terminal kinase and attenuation of the mitochondrial apoptosis-signaling pathway. *J Cereb Blood Flow Metab.* 2005 Jun;25(6):694-712.

95. Waetzig V, Zhao Y, Herdegen T. The bright side of JNKs-Multitalented mediators in neuronal sprouting, brain development and nerve fiber regeneration. *Prog Neurobiol.* 2006 Oct;80(2):84-97.
96. Chen J, Cui X, Zacharek A, Jiang H, Roberts C, Zhang C, et al. Niaspan increases angiogenesis and improves functional recovery after stroke. *Ann Neurol.* 2007 Jul;62(1):49-58.
97. Ushio-Fukai M. Redox signaling in angiogenesis: role of NADPH oxidase. *Cardiovasc Res.* 2006 Jul 15;71(2):226-35.
98. Shin HK, Dunn AK, Jones PB, Boas DA, Moskowitz MA, Ayata C. Vasoconstrictive neurovascular coupling during focal ischemic depolarizations. *J Cereb Blood Flow Metab.* 2006 Aug;26(8):1018-30.
99. Bazan NG, Marcheselli VL, Cole-Edwards K. Brain response to injury and neurodegeneration: endogenous neuroprotective signaling. *Ann N Y Acad Sci.* 2005 Aug;1053:137-47.
100. Dirnagl U, Simon RP, Hallenbeck JM. Ischemic tolerance and endogenous neuroprotection. *Trends Neurosci.* 2003 May;26(5):248-54.
101. Stenzel-Poore MP, Stevens SL, King JS, Simon RP. Preconditioning reprograms the response to ischemic injury and primes the emergence of unique endogenous neuroprotective phenotypes: a speculative synthesis. *Stroke.* 2007 Feb;38(2 Suppl):680-5.
102. del Zoppo GJ. Stroke and neurovascular protection. *N Engl J Med.* 2006 Feb 9;354(6):553-5.
103. Mabuchi T, Lucero J, Feng A, Koziol JA, del Zoppo GJ. Focal cerebral ischemia preferentially affects neurons distant from their neighboring microvessels. *J Cereb Blood Flow Metab.* 2005 Feb;25(2):257-66.
104. del Zoppo GJ. Inflammation and the neurovascular unit in the setting of focal cerebral ischemia. *Neuroscience.* 2009 Feb 6;158(3):972-82.
105. Okada Y, Copeland BR, Mori E, Tung MM, Thomas WS, del Zoppo GJ. P-selectin and intercellular adhesion molecule-1 expression after focal brain ischemia and reperfusion. *Stroke.* 1994 Jan;25(1):202-11.
106. Haring HP, Berg EL, Tsurushita N, Tagaya M, del Zoppo GJ. E-selectin appears in nonischemic tissue during experimental focal cerebral ischemia. *Stroke.* 1996 Aug;27(8):1386-91; discussion 91-2.
107. Granger DN, Benoit JN, Suzuki M, Grisham MB. Leukocyte adherence to venular endothelium during ischemia-reperfusion. *Am J Physiol.* 1989 Nov;257(5 Pt 1):G683-8.

108. Bevilacqua MP, Stengelin S, Gimbrone MA, Jr., Seed B. Endothelial leukocyte adhesion molecule 1: an inducible receptor for neutrophils related to complement regulatory proteins and lectins. *Science*. 1989 Mar 3;243(4895):1160-5.
109. Defilippi P, Silengo L, Tarone G. Alpha 6.beta 1 integrin (laminin receptor) is down-regulated by tumor necrosis factor alpha and interleukin-1 beta in human endothelial cells. *J Biol Chem*. 1992 Sep 15;267(26):18303-7.
110. Tagaya M, Haring HP, Stuiver I, Wagner S, Abumiya T, Lucero J, et al. Rapid loss of microvascular integrin expression during focal brain ischemia reflects neuron injury. *J Cereb Blood Flow Metab*. 2001 Jul;21(7):835-46.
111. Milner R, Hung S, Wang X, Berg GI, Spatz M, del Zoppo GJ. Responses of endothelial cell and astrocyte matrix-integrin receptors to ischemia mimic those observed in the neurovascular unit. *Stroke*. 2008 Jan;39(1):191-7.
112. Del Zoppo GJ, Milner R, Mabuchi T, Hung S, Wang X, Koziol JA. Vascular matrix adhesion and the blood-brain barrier. *Biochem Soc Trans*. 2006 Dec;34(Pt 6):1261-6.
113. Stamatovic SM, Dimitrijevic OB, Keep RF, Andjelkovic AV. Inflammation and brain edema: new insights into the role of chemokines and their receptors. *Acta Neurochir Suppl*. 2006;96:444-50.
114. Reed RK, Rubin K, Wiig H, Rodt SA. Blockade of beta 1-integrins in skin causes edema through lowering of interstitial fluid pressure. *Circ Res*. 1992 Oct;71(4):978-83.
115. Hamann GF, Okada Y, Fitridge R, del Zoppo GJ. Microvascular basal lamina antigens disappear during cerebral ischemia and reperfusion. *Stroke*. 1995 Nov;26(11):2120-6.
116. Wagner S, Tagaya M, Koziol JA, Quaranta V, del Zoppo GJ. Rapid disruption of an astrocyte interaction with the extracellular matrix mediated by integrin alpha 6 beta 4 during focal cerebral ischemia/reperfusion. *Stroke*. 1997 Apr;28(4):858-65.
117. Milner R, Hung S, Wang X, Spatz M, del Zoppo GJ. The rapid decrease in astrocyte-associated dystroglycan expression by focal cerebral ischemia is protease-dependent. *J Cereb Blood Flow Metab*. 2008 Apr;28(4):812-23.
118. Neely JD, Amiry-Moghaddam M, Ottersen OP, Froehner SC, Agre P, Adams ME. Syntrophin-dependent expression and localization of Aquaporin-4 water channel protein. *Proc Natl Acad Sci U S A*. 2001 Nov 20;98(24):14108-13.
119. Heo JH, Han SW, Lee SK. Free radicals as triggers of brain edema formation after stroke. *Free Radic Biol Med*. 2005 Jul 1;39(1):51-70.
120. Fukuda S, Fini CA, Mabuchi T, Koziol JA, Eggleston LL, Jr., del Zoppo GJ. Focal cerebral ischemia induces active proteases that degrade microvascular matrix. *Stroke*. 2004 Apr;35(4):998-1004.

121. Mydel P, Shipley JM, Adair-Kirk TL, Kelley DG, Broekelmann TJ, Mecham RP, et al. Neutrophil elastase cleaves laminin-332 (laminin-5) generating peptides that are chemotactic for neutrophils. *J Biol Chem*. 2008 Apr 11;283(15):9513-22.
122. Lin M, Jackson P, Tester AM, Diaconu E, Overall CM, Blalock JE, et al. Matrix metalloproteinase-8 facilitates neutrophil migration through the corneal stromal matrix by collagen degradation and production of the chemotactic peptide Pro-Gly-Pro. *Am J Pathol*. 2008 Jul;173(1):144-53.
123. Benveniste EN. Cytokine actions in the central nervous system. *Cytokine Growth Factor Rev*. 1998 Sep-Dec;9(3-4):259-75.
124. Haydon PG. Neuroglial networks: neurons and glia talk to each other. *Curr Biol*. 2000 Oct 5;10(19):R712-4.
125. Sofroniew MV, Bush TG, Blumauer N, Lawrence K, Mucke L, Johnson MH. Genetically-targeted and conditionally-regulated ablation of astroglial cells in the central, enteric and peripheral nervous systems in adult transgenic mice. *Brain Res*. 1999 Jul 17;835(1):91-5.
126. Ullian EM, Sapperstein SK, Christopherson KS, Barres BA. Control of synapse number by glia. *Science*. 2001 Jan 26;291(5504):657-61.
127. Bush TG, Puvanachandra N, Horner CH, Polito A, Ostenfeld T, Svendsen CN, et al. Leukocyte infiltration, neuronal degeneration, and neurite outgrowth after ablation of scar-forming, reactive astrocytes in adult transgenic mice. *Neuron*. 1999 Jun;23(2):297-308.
128. Abbott NJ. Astrocyte-endothelial interactions and blood-brain barrier permeability. *J Anat*. 2002 Jun;200(6):629-38.
129. Brillault J, Berezowski V, Cecchelli R, Dehouck MP. Intercommunications between brain capillary endothelial cells and glial cells increase the transcellular permeability of the blood-brain barrier during ischaemia. *J Neurochem*. 2002 Nov;83(4):807-17.
130. Raub TJ. Signal transduction and glial cell modulation of cultured brain microvessel endothelial cell tight junctions. *Am J Physiol*. 1996 Aug;271(2 Pt 1):C495-503.
131. Arthur FE, Shivers RR, Bowman PD. Astrocyte-mediated induction of tight junctions in brain capillary endothelium: an efficient in vitro model. *Brain Res*. 1987 Nov;433(1):155-9.
132. Tontsch U, Bauer HC. Glial cells and neurons induce blood-brain barrier related enzymes in cultured cerebral endothelial cells. *Brain Res*. 1991 Jan 25;539(2):247-53.
133. Yagi T, Jikihara I, Fukumura M, Watabe K, Ohashi T, Eto Y, et al. Rescue of ischemic brain injury by adenoviral gene transfer of glial cell line-derived neurotrophic factor after transient global ischemia in gerbils. *Brain Res*. 2000 Dec 8;885(2):273-82.

134. Igarashi Y, Utsumi H, Chiba H, Yamada-Sasamori Y, Tobioka H, Kamimura Y, et al. Glial cell line-derived neurotrophic factor induces barrier function of endothelial cells forming the blood-brain barrier. *Biochem Biophys Res Commun*. 1999 Jul 22;261(1):108-12.
135. Didier N, Romero IA, Creminon C, Wijkhuisen A, Grassi J, Mabondzo A. Secretion of interleukin-1beta by astrocytes mediates endothelin-1 and tumour necrosis factor-alpha effects on human brain microvascular endothelial cell permeability. *J Neurochem*. 2003 Jul;86(1):246-54.
136. Mi H, Haeberle H, Barres BA. Induction of astrocyte differentiation by endothelial cells. *J Neurosci*. 2001 Mar 1;21(5):1538-47.
137. Lee SW, Kim WJ, Choi YK, Song HS, Son MJ, Gelman IH, et al. SSeCKS regulates angiogenesis and tight junction formation in blood-brain barrier. *Nat Med*. 2003 Jul;9(7):900-6.
138. Dong Y, Benveniste EN. Immune function of astrocytes. *Glia*. 2001 Nov;36(2):180-90.
139. Shaw SK, Owolabi SA, Bagley J, Morin N, Cheng E, LeBlanc BW, et al. Activated polymorphonuclear cells promote injury and excitability of dorsal root ganglia neurons. *Exp Neurol*. 2008 Apr;210(2):286-94.
140. Temporin K, Tanaka H, Kuroda Y, Okada K, Yachi K, Moritomo H, et al. IL-1beta promotes neurite outgrowth by deactivating RhoA via p38 MAPK pathway. *Biochem Biophys Res Commun*. 2008 Jan 11;365(2):375-80.
141. Thornton P, Pinteaux E, Allan SM, Rothwell NJ. Matrix metalloproteinase-9 and urokinase plasminogen activator mediate interleukin-1-induced neurotoxicity. *Mol Cell Neurosci*. 2008 Jan;37(1):135-42.
142. Heo JH, Lucero J, Abumiya T, Koziol JA, Copeland BR, del Zoppo GJ. Matrix metalloproteinases increase very early during experimental focal cerebral ischemia. *J Cereb Blood Flow Metab*. 1999 Jun;19(6):624-33.
143. Balabanov R, Washington R, Wagnerova J, Dore-Duffy P. CNS microvascular pericytes express macrophage-like function, cell surface integrin alpha M, and macrophage marker ED-2. *Microvasc Res*. 1996 Sep;52(2):127-42.
144. Hoogerbrugge PM, Suzuki K, Poorthuis BJ, Kobayashi T, Wagemaker G, van Bekkum DW. Donor-derived cells in the central nervous system of twitcher mice after bone marrow transplantation. *Science*. 1988 Feb 26;239(4843):1035-8.
145. Aloisi F. Immune function of microglia. *Glia*. 2001 Nov;36(2):165-79.
146. Mabuchi T, Kitagawa K, Ohtsuki T, Kuwabara K, Yagita Y, Yanagihara T, et al. Contribution of microglia/macrophages to expansion of infarction and response of oligodendrocytes after focal cerebral ischemia in rats. *Stroke*. 2000 Jul;31(7):1735-43.

147. Rolfe DF, Brown GC. Cellular energy utilization and molecular origin of standard metabolic rate in mammals. *Physiol Rev.* 1997 Jul;77(3):731-58.
148. Hawkins BT, Davis TP. The blood-brain barrier/neurovascular unit in health and disease. *Pharmacol Rev.* 2005 Jun;57(2):173-85.
149. Abbott NJ, Ronnback L, Hansson E. Astrocyte-endothelial interactions at the blood-brain barrier. *Nat Rev Neurosci.* 2006 Jan;7(1):41-53.
150. Wolburg H, Lippoldt A. Tight junctions of the blood-brain barrier: development, composition and regulation. *Vascul Pharmacol.* 2002 Jun;38(6):323-37.
151. Loscher W, Potschka H. Drug resistance in brain diseases and the role of drug efflux transporters. *Nat Rev Neurosci.* 2005 Aug;6(8):591-602.
152. Minn A, Ghersi-Egea JF, Perrin R, Leininger B, Siest G. Drug metabolizing enzymes in the brain and cerebral microvessels. *Brain Res Brain Res Rev.* 1991 Jan-Apr;16(1):65-82.
153. Pardridge WM. Blood-brain barrier drug targeting: the future of brain drug development. *Mol Interv.* 2003 Mar;3(2):90-105, 51.
154. Fenstermacher J, Gross P, Sposito N, Acuff V, Pettersen S, Gruber K. Structural and functional variations in capillary systems within the brain. *Ann N Y Acad Sci.* 1988;529:21-30.
155. Oldendorf WH, Cornford ME, Brown WJ. The large apparent work capability of the blood-brain barrier: a study of the mitochondrial content of capillary endothelial cells in brain and other tissues of the rat. *Ann Neurol.* 1977 May;1(5):409-17.
156. Kiesel U, Wolburg H. Tight junctions of the blood-brain barrier. *Cell Mol Neurobiol.* 2000 Feb;20(1):57-76.
157. Tagami M, Nara Y, Kubota A, Fujino H, Yamori Y. Ultrastructural changes in cerebral pericytes and astrocytes of stroke-prone spontaneously hypertensive rats. *Stroke.* 1990 Jul;21(7):1064-71.
158. Farkas E, Luiten PG. Cerebral microvascular pathology in aging and Alzheimer's disease. *Prog Neurobiol.* 2001 Aug;64(6):575-611.
159. Butt AM, Jones HC, Abbott NJ. Electrical resistance across the blood-brain barrier in anaesthetized rats: a developmental study. *J Physiol.* 1990 Oct;429:47-62.
160. Yu AS, McCarthy KM, Francis SA, McCormack JM, Lai J, Rogers RA, et al. Knockdown of occludin expression leads to diverse phenotypic alterations in epithelial cells. *Am J Physiol Cell Physiol.* 2005 Jun;288(6):C1231-41.
161. Schinkel AH. P-Glycoprotein, a gatekeeper in the blood-brain barrier. *Adv Drug Deliv Rev.* 1999 Apr 5;36(2-3):179-94.

162. Hawkins RA, Peterson DR, Vina JR. The complementary membranes forming the blood-brain barrier. *IUBMB Life*. 2002 Sep;54(3):101-7.
163. O'Kane RL, Hawkins RA. Na⁺-dependent transport of large neutral amino acids occurs at the abluminal membrane of the blood-brain barrier. *Am J Physiol Endocrinol Metab*. 2003 Dec;285(6):E1167-73.
164. Berninger B, Poo M. Fast actions of neurotrophic factors. *Curr Opin Neurobiol*. 1996 Jun;6(3):324-30.
165. Abe K. Therapeutic Potential of Neurotrophic Factors and Neural Stem Cells Against Ischemic Brain Injury. *Journal of Cerebral Blood Flow and Metabolism* 2000; 20: 1393–408.
166. Hefti F. Pharmacology of neurotrophic factors. *Annu Rev Pharmacol Toxicol*. 1997;37:239-67.
167. Abe K, Aoki M, Kawagoe J, Yoshida T, Hattori A, Kogure K, et al. Ischemic delayed neuronal death. A mitochondrial hypothesis. *Stroke*. 1995 Aug;26(8):1478-89.
168. Martin DP, Schmidt RE, DiStefano PS, Lowry OH, Carter JG, Johnson EM, Jr. Inhibitors of protein synthesis and RNA synthesis prevent neuronal death caused by nerve growth factor deprivation. *J Cell Biol*. 1988 Mar;106(3):829-44.
169. Abe K. Therapeutic potential of neurotrophic factors and neural stem cells against ischemic brain injury. *J Cereb Blood Flow Metab*. 2000 Oct;20(10):1393-408.
170. Barbacid M. Structural and functional properties of the TRK family of neurotrophin receptors. *Ann N Y Acad Sci*. 1995 Sep 7;766:442-58.
171. Fruman DA, Meyers RE, Cantley LC. Phosphoinositide kinases. *Annu Rev Biochem*. 1998;67:481-507.
172. Yuan J, Yankner BA. Apoptosis in the nervous system. *Nature*. 2000 Oct 12;407(6805):802-9.
173. Philpott KL, McCarthy MJ, Klippel A, Rubin LL. Activated phosphatidylinositol 3-kinase and Akt kinase promote survival of superior cervical neurons. *J Cell Biol*. 1997 Nov 3;139(3):809-15.
174. Datta SR, Brunet A, Greenberg ME. Cellular survival: a play in three Akts. *Genes Dev*. 1999 Nov 15;13(22):2905-27.
175. Tombran-Tink J, Barnstable CJ. PEDF: a multifaceted neurotrophic factor. *Nat Rev Neurosci*. 2003 Aug;4(8):628-36.
176. Yang E, Zha J, Jockel J, Boise LH, Thompson CB, Korsmeyer SJ. Bad, a heterodimeric partner for Bcl-XL and Bcl-2, displaces Bax and promotes cell death. *Cell*. 1995 Jan 27;80(2):285-91.

-
177. Datta SR, Dudek H, Tao X, Masters S, Fu H, Gotoh Y, et al. Akt phosphorylation of BAD couples survival signals to the cell-intrinsic death machinery. *Cell*. 1997 Oct 17;91(2):231-41.
178. Du K, Montminy M. CREB is a regulatory target for the protein kinase Akt/PKB. *J Biol Chem*. 1998 Dec 4;273(49):32377-9.
179. Brunet A, Bonni A, Zigmond MJ, Lin MZ, Juo P, Hu LS, et al. Akt promotes cell survival by phosphorylating and inhibiting a Forkhead transcription factor. *Cell*. 1999 Mar 19;96(6):857-68.
180. Riccio A, Ahn S, Davenport CM, Blendy JA, Ginty DD. Mediation by a CREB family transcription factor of NGF-dependent survival of sympathetic neurons. *Science*. 1999 Dec 17;286(5448):2358-61.
181. Kane LP, Shapiro VS, Stokoe D, Weiss A. Induction of NF-kappaB by the Akt/PKB kinase. *Curr Biol*. 1999 Jun 3;9(11):601-4.
182. Bonni A, Brunet A, West AE, Datta SR, Takasu MA, Greenberg ME. Cell survival promoted by the Ras-MAPK signaling pathway by transcription-dependent and -independent mechanisms. *Science*. 1999 Nov 12;286(5443):1358-62.
183. Lin LF, Doherty DH, Lile JD, Bektesh S, Collins F. GDNF: a glial cell line-derived neurotrophic factor for midbrain dopaminergic neurons. *Science*. 1993 May 21;260(5111):1130-2.
184. Wen TC, Matsuda S, Yoshimura H, Kawabe T, Sakanaka M. Ciliary neurotrophic factor prevents ischemia-induced learning disability and neuronal loss in gerbils. *Neurosci Lett*. 1995 May 19;191(1-2):55-8.
185. Schaar DG, Sieber BA, Dreyfus CF, Black IB. Regional and cell-specific expression of GDNF in rat brain. *Exp Neurol*. 1993 Dec;124(2):368-71.
186. Kitagawa H, Hayashi T, Mitsumoto Y, Koga N, Itoyama Y, Abe K. Reduction of ischemic brain injury by topical application of glial cell line-derived neurotrophic factor after permanent middle cerebral artery occlusion in rats. *Stroke*. 1998 Jul;29(7):1417-22.
187. Abe K, Hayashi T, Itoyama Y. Amelioration of brain edema by topical application of glial cell line-derived neurotrophic factor in reperfused rat brain. *Neurosci Lett*. 1997 Aug 1;231(1):37-40.
188. Hayashi T, Abe K, Itoyama Y. Reduction of ischemic damage by application of vascular endothelial growth factor in rat brain after transient ischemia. *J Cereb Blood Flow Metab*. 1998 Aug;18(8):887-95.
189. Zhang WR, Kitagawa H, Hayashi T, Sasaki C, Sakai K, Warita H, et al. Topical application of neurotrophin-3 attenuates ischemic brain injury after transient middle cerebral artery occlusion in rats. *Brain Res*. 1999 Sep 18;842(1):211-4.

190. Wang JM, Hayashi T, Zhang WR, Sakai K, Shiro Y, Abe K. Reduction of ischemic brain injury by topical application of insulin-like growth factor-I after transient middle cerebral artery occlusion in rats. *Brain Res.* 2000 Mar 24;859(2):381-5.
191. Yamashita K, Wiessner C, Lindholm D, Thoenen H, Hossmann KA. Post-occlusion treatment with BDNF reduces infarct size in a model of permanent occlusion of the middle cerebral artery in rat. *Metab Brain Dis.* 1997 Dec;12(4):271-80.
192. Kawakami N, Kashiwagi S, Kitahara T, Yamashita T, Ito H. Effect of local administration of basic fibroblast growth factor against neuronal damage caused by transient intracerebral mass lesion in rats. *Brain Res.* 1995 Oct 30;697(1-2):104-11.
193. MacMillan V, Judge D, Wiseman A, Settles D, Swain J, Davis J. Mice expressing a bovine basic fibroblast growth factor transgene in the brain show increased resistance to hypoxemic-ischemic cerebral damage. *Stroke.* 1993 Nov;24(11):1735-9.
194. Gluckman P, Klempt N, Guan J, Mallard C, Sirimanne E, Dragunow M, et al. A role for IGF-1 in the rescue of CNS neurons following hypoxic-ischemic injury. *Biochem Biophys Res Commun.* 1992 Jan 31;182(2):593-9.
195. Shigeno T, Mima T, Takakura K, Graham DI, Kato G, Hashimoto Y, et al. Amelioration of delayed neuronal death in the hippocampus by nerve growth factor. *J Neurosci.* 1991 Sep;11(9):2914-9.
196. Chan KM, Lam DT, Pong K, Widmer HR, Hefti F. Neurotrophin-4/5 treatment reduces infarct size in rats with middle cerebral artery occlusion. *Neurochem Res.* 1996 Jul;21(7):763-7.
197. Carpenter G, Stoscheck CM, Soderquist AM. Epidermal growth factor. *Ann N Y Acad Sci.* 1982 Dec 10;397:11-7.
198. Savage CR, Jr., Inagami T, Cohen S. The primary structure of epidermal growth factor. *J Biol Chem.* 1972 Dec 10;247(23):7612-21.
199. Savage CR, Jr., Hash JH, Cohen S. Epidermal growth factor. Location of disulfide bonds. *J Biol Chem.* 1973 Nov 25;248(22):7669-72.
200. Taylor JM, Mitchell WM, Cohen S. Epidermal growth factor. Physical and chemical properties. *J Biol Chem.* 1972 Sep 25;247(18):5928-34.
201. Yamada M, Ikeuchi T, Hatanaka H. The neurotrophic action and signalling of epidermal growth factor. *Prog Neurobiol.* 1997 Jan;51(1):19-37.
202. Yarden Y. The EGFR family and its ligands in human cancer. signalling mechanisms and therapeutic opportunities. *Eur J Cancer.* 2001 Sep;37 Suppl 4:S3-8.
203. Schlessinger J, Ullrich A. Growth factor signaling by receptor tyrosine kinases. *Neuron.* 1992 Sep;9(3):383-91.

-
204. Schlessinger J. SH2/SH3 signaling proteins. *Curr Opin Genet Dev.* 1994 Feb;4(1):25-30.
205. Pawson T. Protein modules and signalling networks. *Nature.* 1995 Feb 16;373(6515):573-80.
206. van der Geer P, Hunter T, Lindberg RA. Receptor protein-tyrosine kinases and their signal transduction pathways. *Annu Rev Cell Biol.* 1994;10:251-337.
207. Jorissen RN, Walker F, Pouliot N, Garrett TP, Ward CW, Burgess AW. Epidermal growth factor receptor: mechanisms of activation and signalling. *Exp Cell Res.* 2003 Mar 10;284(1):31-53.
208. Nishizuka Y. Intracellular signaling by hydrolysis of phospholipids and activation of protein kinase C. *Science.* 1992 Oct 23;258(5082):607-14.
209. Nishida E, Gotoh Y. The MAP kinase cascade is essential for diverse signal transduction pathways. *Trends Biochem Sci.* 1993 Apr;18(4):128-31.
210. Yamada M, Enokido Y, Ikeuchi T, Hatanaka H. Epidermal growth factor prevents oxygen-triggered apoptosis and induces sustained signalling in cultured rat cerebral cortical neurons. *Eur J Neurosci.* 1995 Oct 1;7(10):2130-8.
211. Kinoshita A, Yamada K, Hayakawa T, Kataoka K, Mushiroy T, Kohmura E, et al. Modification of anoxic neuronal injury by human recombinant epidermal growth factor and its possible mechanism. *J Neurosci Res.* 1990 Mar;25(3):324-30.
212. Pauwels PJ, van Assouw HP, Leysen JE. Attenuation of neurotoxicity following anoxia or glutamate receptor activation in EGF- and hippocampal extract-treated neuronal cultures. *Cell Signal.* 1989;1(1):45-54.
213. Maiese K, Boniece I, DeMeo D, Wagner JA. Peptide growth factors protect against ischemia in culture by preventing nitric oxide toxicity. *J Neurosci.* 1993 Jul;13(7):3034-40.
214. Peng H, Wen TC, Tanaka J, Maeda N, Matsuda S, Desaki J, et al. Epidermal growth factor protects neuronal cells in vivo and in vitro against transient forebrain ischemia- and free radical-induced injuries. *J Cereb Blood Flow Metab.* 1998 Apr;18(4):349-60.
215. Law RH, Zhang Q, McGowan S, Buckle AM, Silverman GA, Wong W, et al. An overview of the serpin superfamily. *Genome Biol.* 2006;7(5):216.
216. van Gent D, Sharp P, Morgan K, Kalsheker N. Serpins: structure, function and molecular evolution. *Int J Biochem Cell Biol.* 2003 Nov;35(11):1536-47.
217. Silverman GA, Bird PI, Carrell RW, Church FC, Coughlin PB, Gettins PG, et al. The serpins are an expanding superfamily of structurally similar but functionally diverse proteins. Evolution, mechanism of inhibition, novel functions, and a revised nomenclature. *J Biol Chem.* 2001 Sep 7;276(36):33293-6.

-
218. Becerra SP, Sagasti A, Spinella P, Notario V. Pigment epithelium-derived factor behaves like a noninhibitory serpin. Neurotrophic activity does not require the serpin reactive loop. *J Biol Chem*. 1995 Oct 27;270(43):25992-9.
219. Tombran-Tink J, Johnson LV. Neuronal differentiation of retinoblastoma cells induced by medium conditioned by human RPE cells. *Invest Ophthalmol Vis Sci*. 1989 Aug;30(8):1700-7.
220. Tombran-Tink J, Shivaram SM, Chader GJ, Johnson LV, Bok D. Expression, secretion, and age-related downregulation of pigment epithelium-derived factor, a serpin with neurotrophic activity. *J Neurosci*. 1995 Jul;15(7 Pt 1):4992-5003.
221. Perez-Mediavilla LA, Chew C, Campochiaro PA, Nickells RW, Notario V, Zack DJ, et al. Sequence and expression analysis of bovine pigment epithelium-derived factor. *Biochim Biophys Acta*. 1998 Jun 16;1398(2):203-14.
222. Wu YQ, Notario V, Chader GJ, Becerra SP. Identification of pigment epithelium-derived factor in the interphotoreceptor matrix of bovine eyes. *Protein Expr Purif*. 1995 Aug;6(4):447-56.
223. Bilak MM, Becerra SP, Vincent AM, Moss BH, Aymerich MS, Kuncel RW. Identification of the neuroprotective molecular region of pigment epithelium-derived factor and its binding sites on motor neurons. *J Neurosci*. 2002 Nov 1;22(21):9378-86.
224. Tombran-Tink J, Mazuruk K, Rodriguez IR, Chung D, Linker T, Englander E, et al. Organization, evolutionary conservation, expression and unusual Alu density of the human gene for pigment epithelium-derived factor, a unique neurotrophic serpin. *Mol Vis*. 1996 Nov 4;2:11.
225. Sariola H. The neurotrophic factors in non-neuronal tissues. *Cell Mol Life Sci*. 2001 Jul;58(8):1061-6.
226. Tombran-Tink J, Pawar H, Swaroop A, Rodriguez I, Chader GJ. Localization of the gene for pigment epithelium-derived factor (PEDF) to chromosome 17p13.1 and expression in cultured human retinoblastoma cells. *Genomics*. 1994 Jan 15;19(2):266-72.
227. Goliath R, Shugart Y, Janssens P, Weissenbach J, Beighton P, Ramasar R, et al. Fine localization of the locus for autosomal dominant retinitis pigmentosa on chromosome 17p. *Am J Hum Genet*. 1995 Oct;57(4):962-4.
228. Steele FR, Chader GJ, Johnson LV, Tombran-Tink J. Pigment epithelium-derived factor: neurotrophic activity and identification as a member of the serine protease inhibitor gene family. *Proc Natl Acad Sci U S A*. 1993 Feb 15;90(4):1526-30.
229. Simonovic M, Gettins PG, Volz K. Crystal structure of human PEDF, a potent anti-angiogenic and neurite growth-promoting factor. *Proc Natl Acad Sci U S A*. 2001 Sep 25;98(20):11131-5.

230. Alberdi E, Aymerich MS, Becerra SP. Binding of pigment epithelium-derived factor (PEDF) to retinoblastoma cells and cerebellar granule neurons. Evidence for a PEDF receptor. *J Biol Chem*. 1999 Oct 29;274(44):31605-12.
231. Aymerich MS, Alberdi EM, Martinez A, Becerra SP. Evidence for pigment epithelium-derived factor receptors in the neural retina. *Invest Ophthalmol Vis Sci*. 2001 Dec;42(13):3287-93.
232. Yabe T, Wilson D, Schwartz JP. NF-kappaB activation is required for the neuroprotective effects of pigment epithelium-derived factor (PEDF) on cerebellar granule neurons. *J Biol Chem*. 2001 Nov 16;276(46):43313-9.
233. Volpert OV, Zaichuk T, Zhou W, Reiher F, Ferguson TA, Stuart PM, et al. Inducer-stimulated Fas targets activated endothelium for destruction by anti-angiogenic thrombospondin-1 and pigment epithelium-derived factor. *Nat Med*. 2002 Apr;8(4):349-57.
234. Micheau O, Lens S, Gaide O, Alevizopoulos K, Tschopp J. NF-kappaB signals induce the expression of c-FLIP. *Mol Cell Biol*. 2001 Aug;21(16):5299-305.
235. Kataoka T, Budd RC, Holler N, Thome M, Martinon F, Irmeler M, et al. The caspase-8 inhibitor FLIP promotes activation of NF-kappaB and Erk signaling pathways. *Curr Biol*. 2000 Jun 1;10(11):640-8.
236. Mattson MP, Goodman Y, Luo H, Fu W, Furukawa K. Activation of NF-kappaB protects hippocampal neurons against oxidative stress-induced apoptosis: evidence for induction of manganese superoxide dismutase and suppression of peroxynitrite production and protein tyrosine nitration. *J Neurosci Res*. 1997 Sep 15;49(6):681-97.
237. Post A, Holsboer F, Behl C. Induction of NF-kappaB activity during haloperidol-induced oxidative toxicity in clonal hippocampal cells: suppression of NF-kappaB and neuroprotection by antioxidants. *J Neurosci*. 1998 Oct 15;18(20):8236-46.
238. Taniwaki T, Becerra SP, Chader GJ, Schwartz JP. Pigment epithelium-derived factor is a survival factor for cerebellar granule cells in culture. *J Neurochem*. 1995 Jun;64(6):2509-17.
239. Houenou LJ, D'Costa AP, Li L, Turgeon VL, Enyadike C, Alberdi E, et al. Pigment epithelium-derived factor promotes the survival and differentiation of developing spinal motor neurons. *J Comp Neurol*. 1999 Sep 27;412(3):506-14.
240. Araki T, Taniwaki T, Becerra SP, Chader GJ, Schwartz JP. Pigment epithelium-derived factor (PEDF) differentially protects immature but not mature cerebellar granule cells against apoptotic cell death. *J Neurosci Res*. 1998 Jul 1;53(1):7-15.
241. DeCoster MA, Schabelman E, Tombran-Tink J, Bazan NG. Neuroprotection by pigment epithelial-derived factor against glutamate toxicity in developing primary hippocampal neurons. *J Neurosci Res*. 1999 Jun 15;56(6):604-10.

-
242. Cao W, Tombran-Tink J, Elias R, Sezate S, Mrazek D, McGinnis JF. In vivo protection of photoreceptors from light damage by pigment epithelium-derived factor. *Invest Ophthalmol Vis Sci.* 2001 Jun;42(7):1646-52.
243. LaVail MM, Unoki K, Yasumura D, Matthes MT, Yancopoulos GD, Steinberg RH. Multiple growth factors, cytokines, and neurotrophins rescue photoreceptors from the damaging effects of constant light. *Proc Natl Acad Sci U S A.* 1992 Dec 1;89(23):11249-53.
244. Cao W, Tombran-Tink J, Chen W, Mrazek D, Elias R, McGinnis JF. Pigment epithelium-derived factor protects cultured retinal neurons against hydrogen peroxide-induced cell death. *J Neurosci Res.* 1999 Sep 15;57(6):789-800.
245. Ogata N, Wang L, Jo N, Tombran-Tink J, Takahashi K, Mrazek D, et al. Pigment epithelium derived factor as a neuroprotective agent against ischemic retinal injury. *Curr Eye Res.* 2001 Apr;22(4):245-52.
246. Dawson DW, Volpert OV, Gillis P, Crawford SE, Xu H, Benedict W, et al. Pigment epithelium-derived factor: a potent inhibitor of angiogenesis. *Science.* 1999 Jul 9;285(5425):245-8.
247. Spranger J, Osterhoff M, Reimann M, Mohlig M, Ristow M, Francis MK, et al. Loss of the antiangiogenic pigment epithelium-derived factor in patients with angiogenic eye disease. *Diabetes.* 2001 Dec;50(12):2641-5.
248. Ogata N, Nishikawa M, Nishimura T, Mitsuma Y, Matsumura M. Inverse levels of pigment epithelium-derived factor and vascular endothelial growth factor in the vitreous of eyes with rhegmatogenous retinal detachment and proliferative vitreoretinopathy. *Am J Ophthalmol.* 2002 Jun;133(6):851-2.
249. Yang QX, Wang J, Smith MB, Meadowcroft M, Sun X, Eslinger PJ, et al. Reduction of magnetic field inhomogeneity artifacts in echo planar imaging with SENSE and GESEPI at high field. *Magn Reson Med.* 2004 Dec;52(6):1418-23.
250. Griswold MA, Jakob PM, Heidemann RM, Nittka M, Jellus V, Wang J, et al. Generalized autocalibrating partially parallel acquisitions (GRAPPA). *Magn Reson Med.* 2002 Jun;47(6):1202-10.
251. Zhuo J, Gullapalli RP. AAPM/RSNA physics tutorial for residents: MR artifacts, safety, and quality control. *Radiographics.* 2006 Jan-Feb;26(1):275-97.
252. Dietrich O, Raya JG, Reeder SB, Reiser MF, Schoenberg SO. Measurement of signal-to-noise ratios in MR images: influence of multichannel coils, parallel imaging, and reconstruction filters. *J Magn Reson Imaging.* 2007 Aug;26(2):375-85.
253. Longa EZ, Weinstein PR, Carlson S, Cummins R. Reversible middle cerebral artery occlusion without craniectomy in rats. *Stroke.* 1989 Jan;20(1):84-91.
254. Spratt NJ, Fernandez J, Chen M, Rewell S, Cox S, van Raay L, et al. Modification of the method of thread manufacture improves stroke induction rate and reduces

- mortality after thread-occlusion of the middle cerebral artery in young or aged rats. *J Neurosci Methods*. 2006 Sep 15;155(2):285-90.
255. Nakamura T, Xi G, Hua Y, Hoff JT, Keep RF. Nestin expression after experimental intracerebral hemorrhage. *Brain Res*. 2003 Aug 15;981(1-2):108-17.
256. Weidner N, Ner A, Salimi N, Tuszynski MH. Spontaneous corticospinal axonal plasticity and functional recovery after adult central nervous system injury. *Proc Natl Acad Sci U S A*. 2001 Mar 13;98(6):3513-8.
257. Weber T, Vroemen M, Behr V, Neuberger T, Jakob P, Haase A, et al. In Vivo High-Resolution MR Imaging of Neuropathologic Changes in the Injured Rat Spinal Cord. *AJNR*. 2006; 27:598-604.
258. Beier D, Rohrl S, Pillai DR, Schwarz S, Kunz-Schughart LA, Leukel P, et al. Temozolomide preferentially depletes cancer stem cells in glioblastoma. *Cancer Res*. 2008 Jul 15;68(14):5706-15.
259. Louis DN, Ohgaki H, Wiestler OD, Cavenee WK, Burger PC, Jouvet A, et al. The 2007 WHO classification of tumours of the central nervous system. *Acta Neuropathol*. 2007 Aug;114(2):97-109.
260. Bhakoo KK, Crockard HA, Lascelles PC, Avery SF. Prostaglandin synthesis and oedema formation during reperfusion following experimental brain ischaemia in the gerbil. *Stroke*. 1984 Sep-Oct;15(5):891-5.
261. Belayev L, Busto R, Zhao W, Ginsberg MD. Quantitative evaluation of blood-brain barrier permeability following middle cerebral artery occlusion in rats. *Brain Res*. 1996 Nov 11;739(1-2):88-96.
262. Zhang Y, Pardridge WM. Neuroprotection in transient focal brain ischemia after delayed intravenous administration of brain-derived neurotrophic factor conjugated to a blood-brain barrier drug targeting system. *Stroke*. 2001 Jun;32(6):1378-84.
263. Ogawa S, Lee TM, Kay AR, Tank DW. Brain magnetic resonance imaging with contrast dependent on blood oxygenation. *Proc Natl Acad Sci U S A*. 1990 Dec;87(24):9868-72.
264. Calamante F, Lythgoe MF, Pell GS, Thomas DL, King MD, Busza AL, et al. Early changes in water diffusion, perfusion, T1, and T2 during focal cerebral ischemia in the rat studied at 8.5 T. *Magn Reson Med*. 1999 Mar;41(3):479-85.
265. Bandettini PA, Wong EC, Jesmanowicz A, Hinks RS, Hyde JS. Spin-echo and gradient-echo EPI of human brain activation using BOLD contrast: a comparative study at 1.5 T. *NMR Biomed*. 1994 Mar;7(1-2):12-20.
266. Hill JM, Switzer RC, 3rd. The regional distribution and cellular localization of iron in the rat brain. *Neuroscience*. 1984 Mar;11(3):595-603.

-
267. Zaleska MM, Floyd RA. Regional lipid peroxidation in rat brain in vitro: possible role of endogenous iron. *Neurochem Res.* 1985 Mar;10(3):397-410.
268. Hulet SW, Hess EJ, Debinski W, Arosio P, Bruce K, Powers S, et al. Characterization and distribution of ferritin binding sites in the adult mouse brain. *J Neurochem.* 1999 Feb;72(2):868-74.
269. Bhagat YA, Emery DJ, Naik S, Yeo T, Beaulieu C. Comparison of generalized autocalibrating partially parallel acquisitions and modified sensitivity encoding for diffusion tensor imaging. *AJNR Am J Neuroradiol.* 2007 Feb;28(2):293-8.
270. Pfefferbaum A, Adalsteinsson E, Sullivan EV. In vivo structural imaging of the rat brain with a 3-T clinical human scanner. *J Magn Reson Imaging.* 2004 Nov;20(5):779-85.
271. Guzman R, Lovblad KO, Meyer M, Spenger C, Schroth G, Widmer HR. Imaging the rat brain on a 1.5 T clinical MR-scanner. *J Neurosci Methods.* 2000 Apr 1;97(1):77-85.
272. Whitwell JL. Voxel-based morphometry: an automated technique for assessing structural changes in the brain. *J Neurosci.* 2009 Aug 5;29(31):9661-4.
273. Linn J, Schwarz F, Schichor C, Wiesmann M. Cranial MRI of small rodents using a clinical MR scanner. *Methods.* 2007 Sep;43(1):2-11.
274. Le Bihan D, Breton E, Lallemand D, Aubin ML, Vignaud J, Laval-Jeantet M. Separation of diffusion and perfusion in intravoxel incoherent motion MR imaging. *Radiology.* 1988 Aug;168(2):497-505.
275. Chen F, De Keyser F, Wang H, Vandecaveye V, Landuyt W, Bosmans H, et al. Diffusion weighted imaging in small rodents using clinical MRI scanners. *Methods.* 2007 Sep;43(1):12-20.
276. Villringer A, Rosen BR, Belliveau JW, Ackerman JL, Lauffer RB, Buxton RB, et al. Dynamic imaging with lanthanide chelates in normal brain: contrast due to magnetic susceptibility effects. *Magn Reson Med.* 1988 Feb;6(2):164-74.
277. Heiland S, Kreibich W, Reith W, Benner T, Dorfler A, Forsting M, et al. Comparison of echo-planar sequences for perfusion-weighted MRI: which is best? *Neuroradiology.* 1998 Apr;40(4):216-21.
278. Blaimer M, Breuer F, Mueller M, Heidemann RM, Griswold MA, Jakob PM. SMASH, SENSE, PILS, GRAPPA: how to choose the optimal method. *Top Magn Reson Imaging.* 2004 Aug;15(4):223-36.
279. Brant-Zawadzki M, Norman D, Newton TH, Kelly WM, Kjos B, Mills CM, et al. Magnetic resonance of the brain: the optimal screening technique. *Radiology.* 1984 Jul;152(1):71-7.

280. Stoll G, Kleinschnitz C, Meuth SG, Braeuninger S, Ip CW, Wessig C, et al. Transient widespread blood-brain barrier alterations after cerebral photothrombosis as revealed by gadofluorine M-enhanced magnetic resonance imaging. *J Cereb Blood Flow Metab.* 2009 Feb;29(2):331-41.
281. Essig M. Protocol design for high relaxivity contrast agents in MR imaging of the CNS. *Eur Radiol.* 2006 Nov;16 Suppl 7:M3-7.
282. Bradley WG, Jr. MR appearance of hemorrhage in the brain. *Radiology.* 1993 Oct;189(1):15-26.
283. Atlas SW, Thulborn KR. MR detection of hyperacute parenchymal hemorrhage of the brain. *AJNR Am J Neuroradiol.* 1998 Sep;19(8):1471-7.
284. Del Bigio MR, Yan HJ, Buist R, Peeling J. Experimental intracerebral hemorrhage in rats. Magnetic resonance imaging and histopathological correlates. *Stroke.* 1996 Dec;27(12):2312-9; discussion 9-20.
285. Atlas SW, Mark AS, Grossman RI, Gomori JM. Intracranial hemorrhage: gradient-echo MR imaging at 1.5 T. Comparison with spin-echo imaging and clinical applications. *Radiology.* 1988 Sep;168(3):803-7.
286. Narayana PA, Grill RJ, Chacko T, Vang R. Endogenous recovery of injured spinal cord: longitudinal in vivo magnetic resonance imaging. *J Neurosci Res.* 2004 Dec 1;78(5):749-59.
287. Bilgen M, Elshafiey I, Narayana PA. In vivo magnetic resonance microscopy of rat spinal cord at 7 T using implantable RF coils. *Magn Reson Med.* 2001 Dec;46(6):1250-3.
288. Behr VC, Weber T, Neuberger T, Vroemen M, Weidner N, Bogdahn U, et al. High-resolution MR imaging of the rat spinal cord in vivo in a wide-bore magnet at 17.6 Tesla. *MAGMA.* 2004 Dec;17(3-6):353-8.
289. Mogatadakala KV, Bankson JA, Narayana PA. Three-element phased-array coil for imaging of rat spinal cord at 7T. *Magn Reson Med.* 2008 Dec;60(6):1498-505.
290. Fenyés DA, Narayana PA. In vivo echo-planar imaging of rat spinal cord. *Magn Reson Imaging.* 1998 Dec;16(10):1249-55.
291. Fenyés DA, Narayana PA. In vivo diffusion characteristics of rat spinal cord. *Magn Reson Imaging.* 1999 Jun;17(5):717-22.
292. Fenyés DA, Narayana PA. In vivo diffusion tensor imaging of rat spinal cord with echo planar imaging. *Magn Reson Med.* 1999 Aug;42(2):300-6.
293. Narayana P, Fenyés D, Zacharopoulos N. In vivo relaxation times of gray matter and white matter in spinal cord. *Magn Reson Imaging.* 1999 May;17(4):623-6.

-
294. Yung AC, Kozlowski P. Signal-to-noise ratio comparison of phased-array vs. implantable coil for rat spinal cord MRI. *Magn Reson Imaging*. 2007 Oct;25(8):1215-21.
295. Ford JC, Hackney DB, Joseph PM, Phelan M, Alsop DC, Tabor SL, et al. A method for in vivo high resolution MRI of rat spinal cord injury. *Magn Reson Med*. 1994 Feb;31(2):218-23.
296. Narayana P, Abbe R, Liu SJ, Johnston D. Does loss of gray- and white-matter contrast in injured spinal cord signify secondary injury? In vivo longitudinal MRI studies. *Magn Reson Med*. 1999 Feb;41(2):315-20.
297. Bilgen M, Abbe R, Liu SJ, Narayana PA. Spatial and temporal evolution of hemorrhage in the hyperacute phase of experimental spinal cord injury: in vivo magnetic resonance imaging. *Magn Reson Med*. 2000 Apr;43(4):594-600.
298. Schenck JF, Zimmerman EA. High-field magnetic resonance imaging of brain iron: birth of a biomarker? *NMR Biomed*. 2004 Nov;17(7):433-45.
299. Sahin B AH, Unal B, Canan S, Bilgic S, Kaplan S and Tumkaya L. Brain volumes of the lamb, rat and bird do not show hemispheric asymmetry: A stereological study. *Image Anal Stereol*. 2001;20:9-13.
300. Koshibu K, Levitt P, Ahrens ET. Sex-specific, postpuberty changes in mouse brain structures revealed by three-dimensional magnetic resonance microscopy. *Neuroimage*. 2004 Aug;22(4):1636-45.
301. Brockmann MA, Ulmer S, Leppert J, Nadrowitz R, Wuestenberg R, Nolte I, et al. Analysis of mouse brain using a clinical 1.5 T scanner and a standard small loop surface coil. *Brain Res*. 2006 Jan 12;1068(1):138-42.
302. Christoforidis GA, Kangarlu A, Abduljalil AM, Schmalbrock P, Chaudhry A, Yates A, et al. Susceptibility-based imaging of glioblastoma microvasculature at 8 T: correlation of MR imaging and postmortem pathology. *AJNR Am J Neuroradiol*. 2004 May;25(5):756-60.
303. Rascher G, Fischmann A, Kroger S, Duffner F, Grote EH, Wolburg H. Extracellular matrix and the blood-brain barrier in glioblastoma multiforme: spatial segregation of tenascin and agrin. *Acta Neuropathol*. 2002 Jul;104(1):85-91.
304. Huang ZG, Xue D, Preston E, Karbalai H, Buchan AM. Biphasic opening of the blood-brain barrier following transient focal ischemia: effects of hypothermia. *Can J Neurol Sci*. 1999 Nov;26(4):298-304.
305. Kuroiwa T, Ting P, Martinez H, Klatzo I. The biphasic opening of the blood-brain barrier to proteins following temporary middle cerebral artery occlusion. *Acta Neuropathol*. 1985;68(2):122-9.
306. Wang CX, Shuaib A. Critical role of microvasculature basal lamina in ischemic brain injury. *Prog Neurobiol*. 2007 Oct;83(3):140-8.

-
307. Ahmmed GU, Malik AB. Functional role of TRPC channels in the regulation of endothelial permeability. *Pflugers Arch*. 2005 Oct;451(1):131-42.
308. Yang Y, Estrada EY, Thompson JF, Liu W, Rosenberg GA. Matrix metalloproteinase-mediated disruption of tight junction proteins in cerebral vessels is reversed by synthetic matrix metalloproteinase inhibitor in focal ischemia in rat. *J Cereb Blood Flow Metab*. 2007 Apr;27(4):697-709.
309. Meyer TN, Schwesinger C, Ye J, Denker BM, Nigam SK. Reassembly of the tight junction after oxidative stress depends on tyrosine kinase activity. *J Biol Chem*. 2001 Jun 22;276(25):22048-55.
310. Croll SD, Wiegand SJ. Vascular growth factors in cerebral ischemia. *Mol Neurobiol*. 2001 Apr-Jun;23(2-3):121-35.
311. Sandoval KE, Witt KA. Blood-brain barrier tight junction permeability and ischemic stroke. *Neurobiol Dis*. 2008 Nov;32(2):200-19.
312. Stamatovic SM, Shakui P, Keep RF, Moore BB, Kunkel SL, Van Rooijen N, et al. Monocyte chemoattractant protein-1 regulation of blood-brain barrier permeability. *J Cereb Blood Flow Metab*. 2005 May;25(5):593-606.
313. Gidday JM, Gasche YG, Copin JC, Shah AR, Perez RS, Shapiro SD, et al. Leukocyte-derived matrix metalloproteinase-9 mediates blood-brain barrier breakdown and is proinflammatory after transient focal cerebral ischemia. *Am J Physiol Heart Circ Physiol*. 2005 Aug;289(2):H558-68.
314. Werner C, Lu H, Engelhard K, Unbehauen N, Kochs E. Sevoflurane impairs cerebral blood flow autoregulation in rats: reversal by nonselective nitric oxide synthase inhibition. *Anesth Analg*. 2005 Aug;101(2):509-16, table of contents.
315. Izumi Y, Haida M, Hata T, Isozumi K, Kurita D, Shinohara Y. Distribution of brain oedema in the contralateral hemisphere after cerebral infarction: repeated MRI measurement in the rat. *J Clin Neurosci*. 2002 May;9(3):289-93.
316. Kimelberg HK. Water homeostasis in the brain: basic concepts. *Neuroscience*. 2004;129(4):851-60.
317. Kwan HY, Huang Y, Yao X. TRP channels in endothelial function and dysfunction. *Biochim Biophys Acta*. 2007 Aug;1772(8):907-14.
318. Simard JM, Kent TA, Chen M, Tarasov KV, Gerzanich V. Brain oedema in focal ischaemia: molecular pathophysiology and theoretical implications. *Lancet Neurol*. 2007 Mar;6(3):258-68.
319. Eder P, Poteser M, Romanin C, Groschner K. Na(+) entry and modulation of Na(+)/Ca(2+) exchange as a key mechanism of TRPC signaling. *Pflugers Arch*. 2005 Oct;451(1):99-104.

-
- 320.Craner MJ, Hains BC, Lo AC, Black JA, Waxman SG. Co-localization of sodium channel Nav1.6 and the sodium-calcium exchanger at sites of axonal injury in the spinal cord in EAE. *Brain*. 2004 Feb;127(Pt 2):294-303.
- 321.Paltauf-Doburzynska J, Frieden M, Spitaler M, Graier WF. Histamine-induced Ca²⁺ oscillations in a human endothelial cell line depend on transmembrane ion flux, ryanodine receptors and endoplasmic reticulum Ca²⁺-ATPase. *J Physiol*. 2000 May 1;524 Pt 3:701-13.
- 322.Gotoh O, Asano T, Koide T, Takakura K. Ischemic brain edema following occlusion of the middle cerebral artery in the rat. I: The time courses of the brain water, sodium and potassium contents and blood-brain barrier permeability to 125I-albumin. *Stroke*. 1985 Jan-Feb;16(1):101-9.
- 323.Abraham CS, Harada N, Deli MA, Niwa M. Transient forebrain ischemia increases the blood-brain barrier permeability for albumin in stroke-prone spontaneously hypertensive rats. *Cell Mol Neurobiol*. 2002 Aug;22(4):455-62.
- 324.Hatashita S, Hoff JT. Biomechanics of brain edema in acute cerebral ischemia in cats. *Stroke*. 1988 Jan;19(1):91-7.
- 325.Hatashita S, Hoff JT. Brain edema and cerebrovascular permeability during cerebral ischemia in rats. *Stroke*. 1990 Apr;21(4):582-8.
- 326.Klatzo I. Brain oedema following brain ischaemia and the influence of therapy. *Br J Anaesth*. 1985 Jan;57(1):18-22.
- 327.Saadoun S, Papadopoulos MC. Aquaporin-4 in brain and spinal cord oedema. *Neuroscience*. Jul 28;168(4):1036-46.
- 328.Young AR, Sette G, Touzani O, Rioux P, Derlon JM, MacKenzie ET, et al. Relationships between high oxygen extraction fraction in the acute stage and final infarction in reversible middle cerebral artery occlusion: an investigation in anesthetized baboons with positron emission tomography. *J Cereb Blood Flow Metab*. 1996 Nov;16(6):1176-88.
- 329.Endres M, Engelhardt B, Koistinaho J, Lindvall O, Meairs S, Mohr JP, et al. Improving outcome after stroke: overcoming the translational roadblock. *Cerebrovasc Dis*. 2008;25(3):268-78.
- 330.Li Q, Stephenson D. Postischemic administration of basic fibroblast growth factor improves sensorimotor function and reduces infarct size following permanent focal cerebral ischemia in the rat. *Exp Neurol*. 2002 Oct;177(2):531-7.
- 331.Sugimori H, Speller H, Finklestein SP. Intravenous basic fibroblast growth factor produces a persistent reduction in infarct volume following permanent focal ischemia in rats. *Neurosci Lett*. 2001 Mar 2;300(1):13-6.

-
332. Teramoto T, Qiu J, Plumier JC, Moskowitz MA. EGF amplifies the replacement of parvalbumin-expressing striatal interneurons after ischemia. *J Clin Invest.* 2003 Apr;111(8):1125-32.
333. Jin K, Mao XO, Sun Y, Xie L, Jin L, Nishi E, et al. Heparin-binding epidermal growth factor-like growth factor: hypoxia-inducible expression in vitro and stimulation of neurogenesis in vitro and in vivo. *J Neurosci.* 2002 Jul 1;22(13):5365-73.
334. Jin K, Sun Y, Xie L, Childs J, Mao XO, Greenberg DA. Post-ischemic administration of heparin-binding epidermal growth factor-like growth factor (HB-EGF) reduces infarct size and modifies neurogenesis after focal cerebral ischemia in the rat. *J Cereb Blood Flow Metab.* 2004 Apr;24(4):399-408.
335. Gibson CL, Bath PM, Murphy SP. G-CSF reduces infarct volume and improves functional outcome after transient focal cerebral ischemia in mice. *J Cereb Blood Flow Metab.* 2005 Apr;25(4):431-9.
336. Planas AM, Justicia C, Soriano MA, Ferrer I. Epidermal growth factor receptor in proliferating reactive glia following transient focal ischemia in the rat brain. *Glia.* 1998 Jun;23(2):120-9.
337. Iadecola C. Bright and dark sides of nitric oxide in ischemic brain injury. *Trends Neurosci.* 1997 Mar;20(3):132-9.
338. Hara H, Kato H, Kogure K. Protective effect of alpha-tocopherol on ischemic neuronal damage in the gerbil hippocampus. *Brain Res.* 1990 Mar 5;510(2):335-8.
339. Zhang Y, Tatsuno T, Carney JM, Mattson MP. Basic FGF, NGF, and IGFs protect hippocampal and cortical neurons against iron-induced degeneration. *J Cereb Blood Flow Metab.* 1993 May;13(3):378-88.
340. Cheng B, Mattson MP. PDGFs protect hippocampal neurons against energy deprivation and oxidative injury: evidence for induction of antioxidant pathways. *J Neurosci.* 1995 Nov;15(11):7095-104.
341. Mattson MP, Lovell MA, Furukawa K, Markesbery WR. Neurotrophic factors attenuate glutamate-induced accumulation of peroxides, elevation of intracellular Ca²⁺ concentration, and neurotoxicity and increase antioxidant enzyme activities in hippocampal neurons. *J Neurochem.* 1995 Oct;65(4):1740-51.
342. Taniwaki T, Hirashima N, Becerra SP, Chader GJ, Etcheberrigaray R, Schwartz JP. Pigment epithelium-derived factor protects cultured cerebellar granule cells against glutamate-induced neurotoxicity. *J Neurochem.* 1997 Jan;68(1):26-32.
343. Sugita Y, Becerra SP, Chader GJ, Schwartz JP. Pigment epithelium-derived factor (PEDF) has direct effects on the metabolism and proliferation of microglia and indirect effects on astrocytes. *J Neurosci Res.* 1997 Sep 15;49(6):710-8.
344. Yamagishi S, Inagaki Y, Amano S, Okamoto T, Takeuchi M, Makita Z. Pigment epithelium-derived factor protects cultured retinal pericytes from advanced glycation

- end product-induced injury through its antioxidative properties. *Biochem Biophys Res Commun.* 2002 Aug 30;296(4):877-82.
345. Inagaki Y, Yamagishi S, Okamoto T, Takeuchi M, Amano S. Pigment epithelium-derived factor prevents advanced glycation end products-induced monocyte chemoattractant protein-1 production in microvascular endothelial cells by suppressing intracellular reactive oxygen species generation. *Diabetologia.* 2003 Feb;46(2):284-7.
346. Slivka A, Murphy E, Horrocks L. Cerebral edema after temporary and permanent middle cerebral artery occlusion in the rat. *Stroke.* 1995 Jun;26(6):1061-5; discussion 5-6.
347. Pillai DR, Dittmar MS, Baldaranov D, Heidemann RM, Henning EC, Schuierer G, et al. Cerebral ischemia-reperfusion injury in rats--a 3 T MRI study on biphasic blood-brain barrier opening and the dynamics of edema formation. *J Cereb Blood Flow Metab.* 2009 Nov;29(11):1846-55.
348. Sanagi T, Yabe T, Yamada H. Gene transfer of PEDF attenuates ischemic brain damage in the rat middle cerebral artery occlusion model. *J Neurochem.* 2008 Aug;106(4):1841-54.
349. Jinnouchi Y, Yamagishi S, Matsui T, Takenaka K, Yoshida Y, Nakamura K, et al. Administration of pigment epithelium-derived factor (PEDF) inhibits cold injury-induced brain edema in mice. *Brain Res.* 2007 Sep 5;1167:92-100.
350. Zhang SX, Wang JJ, Gao G, Shao C, Mott R, Ma JX. Pigment epithelium-derived factor (PEDF) is an endogenous antiinflammatory factor. *FASEB J.* 2006 Feb;20(2):323-5.
351. Ho TC, Yang YC, Cheng HC, Wu AC, Chen SL, Tsao YP. Pigment epithelium-derived factor protects retinal pigment epithelium from oxidant-mediated barrier dysfunction. *Biochem Biophys Res Commun.* 2006 Apr 7;342(2):372-8.
352. Brea D, Sobrino T, Ramos-Cabrera P, Castillo J. Inflammatory and neuroimmunomodulatory changes in acute cerebral ischemia. *Cerebrovasc Dis.* 2009;27 Suppl 1:48-64.
353. Thorne RG, Hrabetova S, Nicholson C. Diffusion of epidermal growth factor in rat brain extracellular space measured by integrative optical imaging. *J Neurophysiol.* 2004 Dec;92(6):3471-81.
354. Ogawa S, Lee TM, Nayak AS, Glynn P. Oxygenation-sensitive contrast in magnetic resonance image of rodent brain at high magnetic fields. *Magn Reson Med.* 1990 Apr;14(1):68-78.
355. Tombran-Tink J. The neuroprotective and angiogenesis inhibitory serpin, PEDF: new insights into phylogeny, function, and signaling. *Front Biosci.* 2005;10:2131-49.

-
356. Morioka T, Kalehua AN, Streit WJ. Characterization of microglial reaction after middle cerebral artery occlusion in rat brain. *J Comp Neurol*. 1993 Jan 1;327(1):123-32.
357. Denes A, Vidyasagar R, Feng J, Narvainen J, McColl BW, Kauppinen RA, et al. Proliferating resident microglia after focal cerebral ischaemia in mice. *J Cereb Blood Flow Metab*. 2007 Dec;27(12):1941-53.
358. Kushner M, Alavi A, Reivich M, Dann R, Burke A, Robinson G. Contralateral cerebellar hypometabolism following cerebral insult: a positron emission tomographic study. *Ann Neurol*. 1984 May;15(5):425-34.
359. Hovda DA, Yoshino A, Kawamata T, Katayama Y, Becker DP. Diffuse prolonged depression of cerebral oxidative metabolism following concussive brain injury in the rat: a cytochrome oxidase histochemistry study. *Brain Res*. 1991 Dec 13;567(1):1-10.
360. Pappius HM. Dexamethasone and local cerebral glucose utilization in freeze-traumatized rat brain. *Ann Neurol*. 1982 Aug;12(2):157-62.
361. Tsuchiya M, Sako K, Yura S, Yonemasu Y. Local cerebral glucose utilisation following acute and chronic bilateral carotid artery ligation in Wistar rats: relation to changes in local cerebral blood flow. *Exp Brain Res*. 1993;95(1):1-7.
362. Yoshino A, Hovda DA, Kawamata T, Katayama Y, Becker DP. Dynamic changes in local cerebral glucose utilization following cerebral conclusion in rats: evidence of a hyper- and subsequent hypometabolic state. *Brain Res*. 1991 Oct 4;561(1):106-19.
363. Beck T, Goller HJ, Wree A. Chronic depression of glucose metabolism in postischemic rat brains. *Stroke*. 1995 Jun;26(6):1107-13.
364. Kawamata T, Katayama Y, Hovda DA, Yoshino A, Becker DP. Administration of excitatory amino acid antagonists via microdialysis attenuates the increase in glucose utilization seen following concussive brain injury. *J Cereb Blood Flow Metab*. 1992 Jan;12(1):12-24.
365. Hayashi T, Abe K, Suzuki H, Itoyama Y. Rapid induction of vascular endothelial growth factor gene expression after transient middle cerebral artery occlusion in rats. *Stroke*. 1997 Oct;28(10):2039-44.
366. Sun Y, Jin K, Xie L, Childs J, Mao XO, Logvinova A, et al. VEGF-induced neuroprotection, neurogenesis, and angiogenesis after focal cerebral ischemia. *J Clin Invest*. 2003 Jun;111(12):1843-51.
367. Liu HM. Neovasculature and blood-brain barrier in ischemic brain infarct. *Acta Neuropathol*. 1988;75(4):422-6.
368. Dvorak HF, Brown LF, Detmar M, Dvorak AM. Vascular permeability factor/vascular endothelial growth factor, microvascular hyperpermeability, and angiogenesis. *Am J Pathol*. 1995 May;146(5):1029-39.

-
369. Cai J, Jiang WG, Grant MB, Boulton M. Pigment epithelium-derived factor inhibits angiogenesis via regulated intracellular proteolysis of vascular endothelial growth factor receptor 1. *J Biol Chem*. 2006 Feb 10;281(6):3604-13.
370. Zhang SX, Wang JJ, Gao G, Parke K, Ma JX. Pigment epithelium-derived factor downregulates vascular endothelial growth factor (VEGF) expression and inhibits VEGF-VEGF receptor 2 binding in diabetic retinopathy. *J Mol Endocrinol*. 2006 Aug;37(1):1-12.
371. Holash J, Wiegand SJ, Yancopoulos GD. New model of tumor angiogenesis: dynamic balance between vessel regression and growth mediated by angiopoietins and VEGF. *Oncogene*. 1999 Sep 20;18(38):5356-62.
372. Ho TC, Chen SL, Yang YC, Liao CL, Cheng HC, Tsao YP. PEDF induces p53-mediated apoptosis through PPAR gamma signaling in human umbilical vein endothelial cells. *Cardiovasc Res*. 2007 Nov 1;76(2):213-23.
373. Miller AA, Drummond GR, Sobey CG. Reactive oxygen species in the cerebral circulation: are they all bad? *Antioxid Redox Signal*. 2006 Jul-Aug;8(7-8):1113-20.
374. Zheng J, Bird IM, Melsaether AN, Magness RR. Activation of the mitogen-activated protein kinase cascade is necessary but not sufficient for basic fibroblast growth factor- and epidermal growth factor-stimulated expression of endothelial nitric oxide synthase in ovine fetoplacental artery endothelial cells. *Endocrinology*. 1999 Mar;140(3):1399-407.

List of Abbreviations

3D-MPRAGE	3-Dimensional Magnetization Prepared Rapid Acquisition Gradient Echo.
3V	3 rd Ventricle.
4V	4 th Ventricle.
5-HT	5-HydroxyTryptamine (Serotonin).
ABC	ATP-Binding Cassette.
ACA	Anterior Cerebral Artery.
ADC	Apparent Diffusion Co-efficient.
AF	Acceleration Factor.
AF6	Afadin.
AMP	Adenosine Mono Phosphate
AMPA	α -amino-3-hydroxy-5-Methyl-4-isoxazolePropionic Acid.
Ang1	Angiopoetin-1.
Ang2	Angiopoetin-2.
ANOVA	Analysis Of Variance.
APAF	Apoptotic Protease Activating Factor.
AQPs	AQuaPorins.
AR	After Reperfusion.
AT	Acquisition Time.
ATP	Adenosine Tri-Phosphate.
AZT	Azidothymidine.
BBB	Blood Brain Barrier.
BDNF	Brain-Derived Neurotrophic Factor.
bFGF	basic Fibroblast Growth Factor.
BMP	Bone Morphogenetic Protein.
BOLD	Blood Oxygenation Level Dependant.
BR	Before Reperfusion.
BrdU	BromodeoxyUridine.
BTB	Blood Tumour Barrier.
BV	Blood Vessel.
BW	BandWidth.
CASK	Ca ²⁺ -dependent Serine protein Kinase.
CC	Corpus Callosum.
CCA	Common Carotid Artery.
CCD	Charge-Coupled Device.
CM	Cerebellum.
CM ³	Cubic Centimeters.
CNS	Central Nervous System.
CNTF	Ciliary NeuroTrophic Factor.
CP	Caudate Putamen.
CREB	Cyclic AMP Response Element Binding.
CSF	CerebroSpinal Fluid.
DAG	Di-Acyl Glycerol.
DD	Diffusion Direction.

DNA	Deoxyribo Nucleic Acid.
DRG	Dorsal Root Ganglion.
DSV	Diameter of a Spherical Volume.
DW- & PE-EPI	Diffusion Weighted and PERfusion Echo Planar Imaging.
EAAT	Excitatory Amino Acid Transporters.
EB	Evan's Blue.
EC	Endothelial Cell.
ECA	External Carotid Artery.
ECG	Electro CardioGram.
EGF	Epidermal Growth Factor.
EGFR	EGF Receptor.
eNOS	endothelial Nitric Oxide Synthase.
ERK	Extracellular signal Regulated protein Kinase.
ES	Echo Spacing.
ESAM	Endothelial Selective Adhesion Molecule.
ET	Endothelin.
FA	Flip Angle.
FGF	Fibroblast Growth Factor.
FID	Free Induction Decay.
FOV	Field of View.
GABA	γ -Amino Butyric Acid.
GBM	GlioBlastoMa.
Gd-DTPA	Gadolinium DiethyleneTriamine-Penta-acetic Acid.
GDF	Growth Differentiation Factors.
GDNF	Glial cell line Derived Neurotrophic Factor.
GDP	Guanosine Di-Phosphate.
GFR α	GDNF Family Receptor alpha.
GLUT	GLUcose Transporter.
GM & WM	Gray and White matter.
GRAPPA	GeneRALized Auto-calibrating Partially Parallel Acquisition.
GRE	Gradient Recalled Echo.
GTP	Guanosine Tri-Phosphate.
HB-EGF	Heparin Binding-EGF.
HC	HippoCampus.
HCSC	Human Cancer Stem Cell.
HGF	Hepatocyte Growth Factor.
HIF	Hypoxia Inducible Factor.
HT	HypoThalamus.
IM	Image Matrix.
IC	Inferior Colliculus.
IP-3	Inositol 1,4,5-trisPhosphate.
IPR	In-Plane Resolution.
IRS	Insulin Receptor Substrate
IGF	Insulin-like Growth Factor.
ICAM	Inter Cellular Adhesion Molecule.
IFN- γ	InterFeroN- γ .
IL	InterLeukin.
ICA	Internal Carotid Artery.

ISG	Inter-Slice Gap.
ICP	Intra Cranial Pressure
ICH	Intra-Cerebral Haemorrhage.
IV	IntraVenous.
I/R	Ischemia-Reperfusion.
IKK	I κ B-Kinase.
I κ B- α	Inhibitor of NF- κ B.
JACOP	Junction-Associated Coiled-Coil protein.
JAK	JANus protein tyrosine Kinase.
JAM	Junctional Adhesion Molecules.
JNK	c-Jun-N-terminal Kinase.
JNKK	c-Jun N-terminal Kinase Kinase.
LAT	L-system for large neutral Amino acid Transport
LERK	Ligand for Eph Related Kinase.
LIF	Leukemia Inhibitory Factor.
LIFR	LIF Receptor.
LV	Lateral Ventricle.
MAGI	Membrane-Associated Guanylate kinase with Inverted orientation of protein-protein interaction domains.
MAO	Mono-Amine Oxidase.
MAP	Mitogen Activated Protein.
MAPK	MAP Kinase.
MCAO	Middle Cerebral Artery Occlusion.
MEK	MAP kinase kinase/ERK kinase.
MEKK	Mitogen ERK Kinase Kinase.
MHC	Major Histocompatibility Complex.
MM	Molecular Mass.
MMPs	Matrix Metallo-Proteinases.
Mn-SOD	Manganese-SuperOxide Dismutase.
MRI	Magnetic Resonance Imaging.
MRPs	Multidrug Resistance-related Proteins.
MS	MilliSecond.
mSENSE	modified SENSitivity Encoding.
MSM	Multi Slice Mode.
MSP	Macrophage Stimulating Protein.
MUPP	MULTi-PDZ-Protein.
NADP	Nicotinamide Adenine Dinucleotide Phosphate.
NC	Neo-Cortex.
NE	Neutrophil Elastase.
NF	Nuclear Factor.
NGF	Nerve Growth Factor.
NMDA	N-Methyl-D-Aspartate.
NO	Nitric Oxide.
NoA	Number of Averages.
NoM	Number of Measures.
NT	NeuroTrophin.
NTFs	NeuroTrophic Factors.
OB	Olfactory Bulb.

OP	Osteogenic Protein.
P2Y2	Purinergic receptor.
PAR	PARtitioning defective proteins.
PBS	Phosphate Buffered Saline.
PBV	Permeable BBB Volume.
PCA	Posterior Cerebral Artery.
PD	Proton Density.
PDGF	Platelet-Derived Growth Factor.
PDK	Phosphoinositide-Dependent Kinase.
PECAM	Platelet-Endothelial Cell Adhesion Molecule.
PED	Phase Encoding Direction.
PEDF	Pigment epithelium-derived factor.
PGI ₂	Prostacyclin.
Pgp	P-glycoprotein.
PH	Pleckstrin Homology.
PI	Parallel Imaging.
PI RAs	Parallel Imaging Reconstruction Algorithms.
PI(3)K	PhosphoInositide 3-Kinase.
PKC	Protein Kinase C.
PLC γ	PhosphoLipase C γ .
PLI	PhosphatidyLInositol.
PMN	PolyMorpho Nuclear.
PN	Pontine Nuclei.
POS	Phase Over Sampling.
PPAR γ	Peroxisome Proliferator Activated Receptor gamma.
PPM	Parts Per Million.
PR	Post Reperfusion.
PS	PonS.
PTP	Protein Tyrosine Phosphatase.
RA	Reconstruction Algorithm.
Ras-GAP	Ras-GTPase-Activating Protein.
rCBF	regional Cerebral Blood Flow.
RCL	Reactive Center Loop.
rel-CBF & CBV	Relative Cerebral Blood Flow and Blood Volume.
rel-PD	relativ Proton Density.
RF	Radio Frequency.
RGS	Regulator of G-protein Signalling.
ROS	Reactive Oxygen Species.
RPE	Retinal Pigment Epithelium.
RSK	Ribosomal S6 Kinase.
rt-PA	Recombinant tissue type Plasminogen Activator.
SAH	Sub Arachnoid Haemorrhage.
SAPK	Stress Activated Protein Kinase.
SC	Superior Colliculus.
SD	Sprague-Dawley.
SD _{diff}	Standard Deviation difference.
SE	Spin-Echo.
SEM	Standard Error of Mean.

SERPINs	SERine Protease Inhibitors.
SH	Src Homology.
SHP-2	SH2-containing protein tyrosine phosphatase.
SI _{diff}	Signal Intensity difference.
SN	Substantia Nigra.
SNR	Signal-to-Noise Ratio.
SSeCKS	Src-Suppressed C-Kinase Substrate.
ST	Slice Thickness.
STAIR	Stroke Therapy Academic Industry Roundtable.
STAT	Signal Transducer and Activator of Transcription.
TE	Time-to-Echo.
TEER	Trans-Endothelial Electrical Resistance.
TF	Turbo Factor.
TGF	Transforming Growth Factor.
TH	Thalamus.
TIE	Endothelium-specific receptor tyrosine kinase .
TJPs	Tight Junction Proteins.
TJs	Tight Junctions.
tMCAO	transient MCAO.
TNF	Tumor Necrosis Factor.
TR	Time-to-Repeat.
TRP	Transient Receptor Potential.
TRPCs	canonical TRPs.
TSE	Turbo Spin-Echo.
TUNEL	Terminal deoxynucleotidyl transferase dUTP Nick End Labeling.
US-FDA	United States Food and Drug Administration.
VE-Cadherin	Vascular Endothelial cadherin.
VEGF	Vascular Endothelial Growth Factor.
VEGFR	VEGF Receptor.
VIP	Vasoactive Intestinal Peptide.
VRMS	Volume Root Mean Square.
WHO	World Health Organization.
ZO	Zonula Occludens.
ZONAB	ZO-1 associated Nucleic Acid Binding protein.

List of Publications

1) DESCENDANTS OF THIS DISSERTATION WORK.

- 1.1) **Pillai DR**, Heidemann RM, Kumar P, Shanbhag N, Lanz T, Dittmar MS, Sandner B, Beier CP, Weidner N, Greenlee MW, Schuierer G, Bogdahn U, Schlachetzki F. Comprehensive small animal imaging strategies on a clinical 3 T dedicated head MR-scanner; Adapted methods and sequence protocols in CNS pathologies. PLoS One. 2011 Feb 7; 6 (2):e16091.
- 1.2) **Pillai DR**, Dittmar MS, Baladaranov D, Heidemann RM, Henning EC, Schuierer G, Bogdahn U, Schlachetzki F. Cerebral ischemia-reperfusion injury in rats--a 3 T MRI study on biphasic blood-brain barrier opening and the dynamics of edema formation. J Cereb Blood Flow Metab. 2009 Nov; 29(11):1846-55. Epub 2009 Aug 5.

1.3) MANUSCRIPTS IN PREPARATION.

- 1.3.1) **Pillai DR**, Shanbhag N, Mayr J, Dittmar MS, Bogdhan U, Schlachetzki F. Differential effects of pigment epithelium derived factor and epidermal growth factor on ischemia-reperfusion injury in rats; A serial MRI study at 3 T.
- 1.3.2) **Pillai DR**, Mayr J, Shanbhag N, Bogdhan U, Schlachetzki F. Differential effects of pigment epithelium derived factor and epidermal growth factor on the metabolic recovery following ischemia-reperfusion injury in rats; A serial MRI study at 3 T.

2) ADJUNCT WORKS.

- 2.1) Grienberger HJ, **Pillai DR**, Schlachetzki F, Gruber M, Dittmar MS. Detection of free radicals by isolated perfusion of the rat brain following hemorrhagic stroke: a novel approach to cerebrovascular biomarker research. *Exp Brain Res.* 2010 Oct; 206(3):311-7. Epub 2010 Sep 15.
- 2.2) Sandner B, **Pillai DR**, Heidemann RM, Schuierer G, Mueller MF, Bogdahn U, Schlachetzki F, Weidner N. In vivo high-resolution imaging of the injured rat spinal cord using a 3.0 T clinical MR scanner. *J Magn Reson Imaging.* 2009 Mar; 29(3):725-30.
- 2.3) Beier D, Röhl S, **Pillai DR**, Schwarz S, Kunz-Schughart LA, Leukel P, Proescholdt M, Brawanski A, Bogdahn U, Trampe-Kieslich A, Giebel B, Wischhusen J, Reifenberger G, Hau P, Beier CP. Temozolomide preferentially depletes cancer stem cells in glioblastoma. *Cancer Res.* 2008 Jul 15; 68(14):5706-15.

CURRICULUM VITAE

Name : Deepu R. Pillai
Date & Place of birth : 08.03.1971, Thrissur district, Kerala state, India.
Nationality : Indian.
Marital status : Married.

ACADEMIC QUALIFICATIONS

January 2008 - till date : Doctoral student. Department of Genetics and Neurobiology, Julius Maximilians Universität Würzburg, Würzburg, Germany.
October 1999 - September 2001: Master degree in Pharmaceutical sciences (M.Pharm) Rajiv Gandhi University of health sciences, Karnataka. Bangalore, India.
April 1998 : Bachelor degree in Pharmaceutical sciences (B.Pharm) Bangalore University, Bangalore, India.

PROFESSIONAL EXPERIENCE

October 2005 - December 2007 : Research scientist, Department of Neurology, Universität Regensburg, Regensburg, Germany.
September 2001 - September 2005: Research scientist, Department of Pharmacology, Torrent Research Centre, Ahmedabad, India.
January 1999 – October 1999 : Trainee manufacturing chemist with m/s Southern Union Pharmaceuticals. Thrissur, Kerala, India.

Declaration

I hereby solemnly affirm that the work detailed in the presented doctoral dissertation describes my own original research work employing no other resources other than that which are explicitly mentioned within the text of this work. This dissertation work in the present form has not been presented before any other authority and has not been subjected to a review procedure.

In fulfillment of the requirements for receiving the doctoral degree in science, I hereby present my work for the first time at the Bayerischen Julius-Maximilians-Universität Würzburg, Würzburg, Germany.

Date: 28-03-2011

Place: Regensburg

Deepu R. Pillai